SWEEP-FREQUENCY MICROWAVE PULSE COMPRESSION USING A HELICALLY CORRUGATED WAVEGUIDE

Graeme C. Burt

(B.Sc. University of Strathclyde)

Department of Physics

University of Strathclyde

Thesis submitted for the Degree of Ph.D.

September 2004

I would like to dedicate this piece of work to Marianne.

Contents

Acknowledgements

The author wishes to thank his supervisors, Dr A. W. Cross and Prof A.D.R. Phelps, for their guidance, and encouragement. He would also like to thank Dr Sergei Samsonov for his help and for many helpful discussions. The help of Dr K. Ronald with advice in all technical matters was invaluable, as was the advice and discussions of the theory with Dr I.V. Konoplev. The author's colleagues, Dr W. He, Dr A.R. Young, Dr C.G. Whyte, Dr H. Yin have made a number of direct and indirect contributions to the work described in this thesis and the author offers them a sincere thank you. Mr. I.S. Dinwoodie is gratefully thanked for his technical advice and construction of the waveguides and Bob Wylie is thanked for the construction of the helically corrugated waveguide. I would like to thank the ESPRC for the funding of this work.

Finally I would like to acknowledge the help and support of my family during the course of this work.

Abstract

A new type of pulse compressor based on sweep frequency pulse compression has been developed using a helically corrugated waveguide as a dispersive medium. This structure provides selective coupling between a TE_{11} travelling wave and a near cut-off TE_{21} wave, creating an eigenwave where the dispersion characteristics of one mode gradually converts into that of other. As the compressor works far from cut-off the reflections associated with operation close to cut-off are reduced and allows the compressor to be used at the output of a powerful amplifier.

An experimental and theoretical study of swept-frequency based pulse compression as well as a theoretical and experimental investigation of the dispersive properties of a circular waveguide with a helical corrugation on its inner surface was carried out. Measurements of the helically corrugated compressor obtained a maximum optimum power compression ratio of 10.9 for a helically corrugated waveguide of length 208.08cm. A 1 kilowatt input pulse with a frequency sweep from 9.60GHz to 9.35GHz over 70ns was compressed by the helically corrugated waveguide. The compressed pulse had a duration of 3ns and gave a compression efficiency of 44%. The helical compressor experiments conducted were the first of their kind to be carried out and were found to be in good agreement with theory.

A numerical study of the potential of the helically corrugated waveguide to produce multi-GW output pulses using frequency modulation at the falling edge of a microwave pulse produced from a high-power BWO was investigated.

Abbreviation List

ABC	Active Bragg Compressor
AC	Alternating Current
B.P.M	Binary Pulse Multiplication
BWO	Backward Wave Oscillator
CNC	Computer Numerically Controlled
CRM	Cyclotron Resonant Maser
CW	Continuous Wave
DC	Direct Current
FEL	Free Electron Laser
FWHM	Full Width Half Maximum
GVD	Group velocity dispersion
IF	Intermediate Frequency
MWCG	Multi-wave Cherenkov Generators
PIC	Particle-in-cell
RaDAR	Radio Detection And Ranging
ReLS	Resonant Line SLED
RDG	Relativistic Diffraction Generators
RF	Radio Frequency
S.E.S	Switched Energy Storage
S.L.A.C	Stanford Linear Accelerator Centre
SLED	SLAC Energy development
SNA	Scalar Network Analyser
TE	Transverse Electric
TEM	Transverse Electric and Magnetic
TM	Transverse Magnetic
TWT/A	Travelling Wave Tube / Amplifier
VNA	Vector Network Analyser
WFT	Window Fourier Transform

Table of Symbols

E	Electric Field Strength
D	Electric flux density
P	Electric polarisation
ε	Permittivity of a medium
ε_r	Relative permittivity of a medium
ε_0	Permittivity of freespace
B	Magnetic Flux density
H	Magnetic Field Strength
M	Magnetisation
μ	Permeability of a medium
μ_r	relative permeability of a medium
μ_0	Permeability of freespace
J	Current density
J_f	Free current density
J_b	Body current density
i^e	Surface electric current
i^m	Surface magnetic current
ρ	Charge density
ρ_f	Free charge density
S	Poynting's vector
f	Frequency
f_c	Cut-off frequency
f_B	Bragg frequency
ω	Angular frequency
ω_c	Cut-off angular frequency
ω_L	Local oscillator angular frequency
ω_R	Input source angular frequency

ω_{IF}	Intermediate angular frequency
c	Speed of light in a vacuum
φ	Phase
λ	Freespace wavelength
λ_c	Cut-off wavelength
λ_z	Waveguide wavelength
k	Freespace wavenumber
k_z	Axial wavenumber
$k_z^{(0)}$	Real component of the axial wavenumber
$k_{z,A}$	Axial wavenumber of mode A
k_z^+	Axial wavenumber of wave co-rotating with helical corrugation
k_z^-	Axial wavenumber of wave counter-rotating the helical corrugation
k_t	Transverse/Cut-off wavenumber
v_g	Group velocity
v_p	Phase velocity
$v_{1,2}$	Group velocity corresponding to frequencies at the start and end of the input pulse, respectively
ς_{mn}	n^{th} root of the m^{th} Bessel function.
σ_c	Electrical conductivity
δ	Skin depth
Z	Characteristic Impedance
α	Loss coefficient / imaginary component of axial wavenumber
γ	Attenuation coefficient
a_0	Mean radius
a_1	Corrugation amplitude
d	Period of corrugation
$\overline{h}$	Bragg wavevector
$\overline{m}$	Azimuthal wavevector
m_A	Azimuthal indice of mode A

P_L	Power lost through ohmic losses
P_T	Transmitted power
P_0	Input power
P_i	Instantaneous power
P_{ic}	Instantaneous power of the compressed pulse
P_{peak}	Peak power
P_{peakc}	Peak power of the compressed pulse
k_p	Power compression ratio
C	Time compression ratio
η_c	Compression efficiency
τ	Input pulse duration
τ_c	Compressed pulse duration
σ	Coupling coefficient
W_l	Lower/operating eigenwave
W_{ul}	Upper eigenwave
C_A	Amplitude of the partial wave A
C_A	Maximum amplitude of the partial wave A
N	Wave norm
L	Compressor length
L_{tap}	Tapered section length
L_{opt}	Optimum length of compressor
L_c	Optimum length of compressor for a given pulse
$F(\omega)$	Wave amplitude, frequency domain.
u_0	Electric field amplitude of the input pulse, time domain
u	Electric field amplitude of the compressed pulse, time domain
V_0	DC bias voltage
V_{LO}	Local oscillator voltage
V_L	Amplitude of the local oscillator voltage
V_{RF}	Input source voltage
V_R	Amplitude of the input source voltage

1 Introduction

1.1 Background

Microwave radiation sources providing high-power broadband, fast and smooth frequency tuning are used for many important applications. The plasma physics community uses high-power microwaves for plasma heating, plasma current drive[1], plasma diagnostics and in the particle accelerator field microwave amplifiers are used for RF acceleration of electrons[2]. Interest has also been shown in high temperature microwave processing of materials such as sintering of ceramics. High-power microwave sources have opened up a number of possible applications to advanced radars[3]. Future applications of high-power microwaves include, space propulsion and power beaming to spacecraft and production of an artificially ionised layer in the upper atmosphere and stratosphere.[4]

In 1886 Maxwell predicted the existence of electromagnetic waves by making a simple, yet momentous, modification to Ampère's law. This was experimentally verified in 1887 by the pioneering experiments of Hertz, where he produced microwaves by connecting two rods to a LC oscillator. During the 20th century many specific microwave sources have been developed. The first vacuum electronic device developed was the magnetron in 1913[5]. During the Second World War microwave devices went through a renaissance, with the development of higher powers for Radar.

At low power (up to tens of W) there are a number of highly developed solid state sources available (usually oscillators) covering the wavelength range from centimetres to millimetres and beyond. Solid-state microwave sources can be categorised as two-terminal devices (diodes), or three-terminal devices (transistor oscillators). The most common diode sources are the Gunn diode and the IMPATT diode both of which convert DC bias into microwave power. At X-band a Gunn diode can produce ~1W CW and an IMPATT diode can produce ~100W, this power falls of approximately as a function of frequency squared. Transistor oscillators have lower frequency and power capabilities than diodes, but offer a greater flexibility which allows more control of the frequency of operation [6].

At the same time some advanced applications require broadband frequency-controllable microwave sources with high power outputs (kilowatts to megawatts). The most promising method to generate high power levels at high frequencies (>10GHz) is to use the interaction of an electron beam in a vacuum with an electromagnetic wave. A number of discreet oscillators and amplifiers based on this approach are currently used, both broadband such as conventional TWT's and narrowband such as klystrons. The introduction of relativistic electron beams in the 1970's allowed microwave devices to reach much higher powers. At high powers vacuum electronics dominate, and we will concentrate on this research area in this thesis. A review of the main microwave sources which are capable of producing GW power levels are presented in sections 1.2-1.7.

1.2 The Magnetron

The magnetron was the first vacuum microwave device, and was invented by Arthur Hull in 1913. Initial devices in the 1920s reached power levels of 100W. In 1940 the introduction of resonators contained in a solid copper anode block was suggested by Postumus and was independently invented and realised by Boot and Randall[7] and by Alekseev and Malairov[5]. The Boot and Randall magnetron achieved 10kW at S-band.[5]

In the magnetron the potential energy of the electrons is converted into microwave power as the electrons drift from the cathode to the anode. A magnetic field applied along the axis of the magnetron will, in the absence of an electric field, cause the electrons to travel in circular paths and will rotate at the cyclotron frequency. The presence of the alternating electric field causes the electrons to obtain an average velocity component perpendicular to both the electric and magnetic field. The resonant cavities allow the frequency of interaction to be controlled. In the desired mode of operation, some of the magnetic flux lines link the adjacent cavities, this is referred to as the π-mode of operation.[8] Smooth-bore magnetrons can produce 100GHz radiation but at modest powers of a few mW's.

The relativistic magnetron is the high current version of the conventional magnetron where relativistic voltages are required to produce the necessary currents.

The first such device was developed by Bekefi and Orzechowski[9] in 1975 and produced 900MWoperating at a wavelength of 10 cm.

1.3 The Klystron

The klystron was invented by Russell and Sigurd Varian in 1939. A klystron is generally an amplifier and consists of one or more cavities separated by a drift section. First the beam is injected into a bunching cavity which bunches the electrons by modulating the electron velocity using the axial electric fields of the Transverse magnetic mode[10]. Then the beam is passed through an output cavity where currents are present at the same frequency as the RF input or a harmonic there of in the buncher cavity. These fields decelerate the beam and extract energy from it[5].

The klystrons frequency range of operation tends to be from ~100MHz to ~12GHz, however the klystron bunching mechanism has been used to produce optical radiation but relies on the use of a high energy (greater than 10MeV) electron beam which is outwith the scope of this thesis.

Research on klystrons driven by intense relativistic electron beams began in the 1970's with the study of automodulation of an intense relativistic electron beam passing through a set of cavities[11]. Friedman later developed an ultra-high power klystron that relied on an automodulation mechanism similar to that which occurs in a reflex klystron, and produced 1.3GHz frequency monochromatic RF energy at ~1GW with this device[12].

1.4 The Free Electron Laser

The term Free Electron Laser (FEL) is used to describe devices that generate coherent radiation by passing a electron beam through a periodic wiggler field. In 1951 Motz[13] recognised that radiation could be amplified on an electron beam propagating through a magnetic undulator which was the basis for ubitron experiments which used a thermionic cathode electron gun by Philips et al.[14] in the 1960's.

In an FEL an electron beam travelling down the drift tube is given a velocity component perpendicular to the wiggler magnetic field and its motion. As the magnetic field is periodic the electron beam travels in an oscillatory motion. The beating of the radiation with the field of the wiggler causes the electrons to be bunched. The interaction between the beat wave and the bunched electrons is synchronised in phase in order to convert the kinetic energy of the electron bunches to coherent radiation.

In the 1970's experiments using relativistic electron beams were attempted, although, these devices had low efficiencies due to the beams large velocity spread[15]. However, the efficiencies of relativistic FELs has increased with the development of better quality electron beam sources. FELs use relativistic beam technology to upshift the electron 'wiggle'[16]. Since the frequency of interaction is dependant on the beam energy the FEL can be tuned to a wide range of frequencies. Free electron lasers have demonstrated output at a range of frequencies, and in 1970s Madey and co-workers produced a FEL device at infared wavelengths[17]. Since then the frequency range has expanded from the microwave region into the visible and Ultraviolet range.[18]

1.5 The Gyrotron

In gyrotrons electrons move along helical trajectories inside a waveguide immersed in a uniform magnetic field and rely on the CRM instability for their operation, the interaction occurs between the negative energy cyclotron mode of a gyrating electron beam and an electromagnetic wave. Because the electrons cyclotron frequency depends on their energy through the relativistic mass the action of the wave on the gyrating electrons modifies their frequency depending on whether they are accelerated or decelerated. The perturbed electron beam forms phase bunches and if the phase velocity of the radiation exceeds that of the beam then the bunches move naturally into decelerating phase giving amplification to the radiation.

R.Q. Twiss was the first to recognize an amplifying mechanism for free electron gyroradiation in 1958[19]. While Twiss did not actually evaluate the formula for conditions appropriate to an amplifying device he did point out that the formula

predicts amplification for Cerenkov radiation and for cyclotron radiation, but not for bremsstrahlung.

Then in 1959, evidently without knowledge of Twiss's work, Schneider[20] and Gaponov[21] each published calculations which specifically treated the stimulated emission of relativistic monoenergetic electrons in a magnetic field; Schneider's approach was quantum mechanical, while Gaponov's was classical.

In 1959, R.H.Pantell verified this in what was perhaps the first experimental work involving the electron cyclotron maser mechanism[22]. In this experiment radiation at 2.5-4.0GHz was produced from a 1-kV 3 μA electron beam drifting through a varying magnetic field. Pantell suggested that the radiation was caused by the coupling of the TE_{11} waveguide mode to the backwards travelling cyclotron wave.

In 1964 I.B. Bott reported the generation of radiation[23] between 2.2mm and .95mm using a 10kV, 50mA beam in a spatially converging pulsed magnetic field.

It was Hirshfield and Wachtel who performed the first experiment that definitely confirmed the existence of the electron cyclotron maser mechanism[24] in 1964. In this early work the cyclotron maser was operated both as an oscillator and as an amplifier at millimeter wavelengths. The radiated power achieved in these experiments was as high as 1kW. Nonpulsed low-current electron beams were used through-out the early experiments.

The gyrotron operates through the fast cyclotron wave interaction ($v_p>c$) unlike most conventional microwave sources where the interaction circuit is constructed so that the group velocity of the electromagnetic wave is slowed to the electron beam velocity. Gyrotrons therefore have an advantage over conventional microwave sources in that the radiation wavelength is not determined by the characteristic size of the interaction region enabling operation at high frequencies 10GHz to 300GHz and high powers ~1MW.[25]

1.6 The Travelling Wave Tube

At frequencies between 10 GHz and 30 GHz, intermediate powers (100 Watt at 30 GHz to 1kilowatt at 10GHz) can be achieved with slow-wave (Cherenkov type)

linear beam TWTs driven by low power oscillators. The travelling wave tube was first proposed in 1942 by Rudolf Kompfner[26], where a slow wave structure was used to reduce the waves phase velocity so that it is equal to the beam velocity[27].

In the Cherenkov interaction coupling occurs between a negative energy (slow) space charge wave of a rectilinear electron beam and an electromagnetic wave, where the axial component of the electric field in the transverse magnetic mode causes bunching in the electron beam. If the electrons are initially faster than the wave, more electrons are decelerated than accelerated and there is a net transfer of energy to the wave. In order for such coupling to be possible some measures are taken to reduce the phase and group velocity of the radiation so that it's dispersion interacts with that of the electron beam. A complex periodic metallic structure is often used to provide this 'slow wave'. At high Ka-band (26.5 to 40.0GHz) and W-band (75-110GHz) frequencies it is difficult to manufacture TWTs due to the size of the microwave structure, cavity or waveguide being directly proportional to the wavelength of operation. This restricts the total power capacity to ~10kW at X-band because of the need to observe the limits in the amount of heat dissipated in the structure and the electric field strengths near various components.

At lower X-band (8.2-12.4GHz) frequencies, a relativistic coupled cavity TWT amplifier producing 400MW was first reported in 1990 by Shiffler and Nation[10].

1.7 The Backwards Wave Oscillator

Very high power microwaves can be realised using Relativistic BWO's and other related devices. In the BWO the internal feedback mechanism makes it possible to excite oscillations over a wide range of beam parameters making these devices relatively insensitive to electron velocity spread.[29,10].

The backward wave oscillator (BWO) was the first microwave device to be driven by a relativistic electron beam[28]. In 1970 Nation used relativistic electron beam technology to produce 10MW at 0.05% efficiency[29]. The BWO was also the first truly-high power microwave device, producing 400MW. It is now possible for BWO's to produce powers in excess of a Gigawatt at X-band frequencies.[5,30]

Relativistic diffraction generators (RDGs) and multi-wave Cherenkov generators (MWCGs) have generated the highest levels of power at X-band, with ~15GW at ~10GHz reported. In these devices an annular relativistic electron beam passes through a pair of rippled wall sections in an overmoded cylindrical waveguide and interacts either with the volume or surface wave of the structure. [10]

1.8 Microwave pulse compression

Microwave pulse compression is a technique of generating short high-peak power pulses by compressing low-power pulses of longer duration. Applications of high-peak-power radiation include accelerating gradients for linear accelerators, plasma diagnostics and advanced radar applications. The concept of compressing RF pulses in time in order to increase their peak power is not new and references go back to the 60's[31,32,33]. Microwave pulse compression has been used for many years at low power levels for radar[33]. The common motivation to use microwave pulse compression is that it is easier to generate lower peak power at longer pulse lengths, since this can be done using lower current and voltage electron beams, and requires lower circuit RF fields. The main methods used for pulse compression are switched energy storage (SES), SLED (SLAC Energy development), binary power multiplication (BPM) and passive pulse compressors based on resonators and delay lines[5,10].

In SES a resonant cavity is used to store up microwave energy generated over a long time and rapidly switch it out by changing the cavity Q. However because the size of the cavity is proportional to the radiation wavelength small sized components can lead to RF breakdown at high frequencies. The most common type of Switched Energy Storage uses a plasma discharge to switch the energy stored in a superconducting resonator to an external load. In this resonator-switch configuration an H-plane T section is connected to the output of the cavity at a distance of $\lambda/2$ from the end wall. This creates a voltage null at the output branch leading to the load.

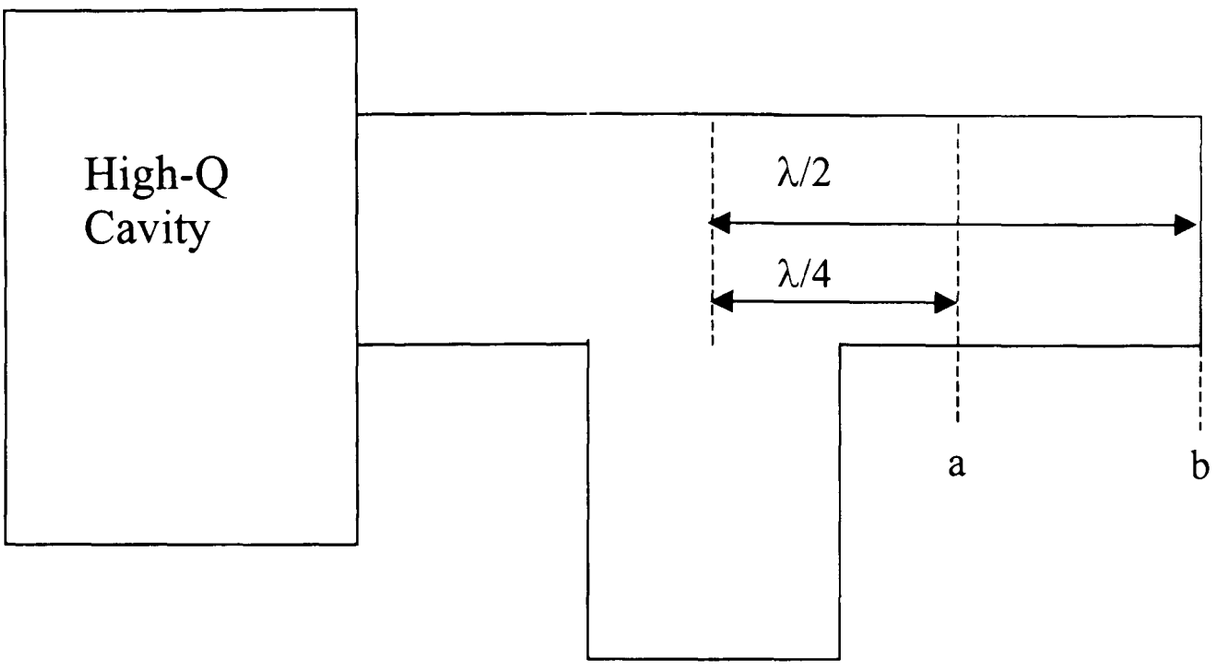

Figure 1-1 Cavity-switch circuit

The triggering occurs when a plasma discharges at λ/4 from the main wall, shown in Figure 1-1. This reflects the incident microwaves producing a maximum field at the output branch leading to the load. The energy in the cavity then couples strongly to the load. Alvarez et al reports a maximum compression ratio of 35.[31,32,34,35]

Switching can also be performed by phase reversal. In the SLED method of pulse compression, a klystron is used to build up the fields in two high-Q cavities, connected by a 3-dB coupler. The emitted waves from the cavities add in phase at the output port and are opposite in phase from the wave from the klystron. The reversal in the phase of the klystron causes the cavities to rapidly empty, as the waves add in phase at the output port. Following the phase reversal, the fields in the cavities decrease rapidly as the cavities try to charge up to a new field level of opposite phase. This gives SLED a sharply decaying exponential output pulse and limited power compression ratio of 3.18.[36]

In SLED II, long lengths of oversized circular waveguide terminated in a short circuit, replace the cavities, forming a Resonant Line SLED (ReLS). The waveguide is coupled to the source via a coupling network. The distance between the coupling network and the short must be multiples of λ/2 and the final pulse duration is given by the round trip delay. This produces a flat pulse, this means that ReLS can be used in stages to give a greater peak power gain. Dissipation losses are minimised

by using the low loss TE_{01} mode. However the compression efficiency decreases sharply with time compression ratio, giving SLED II a power compression ratio 6 at a time compression ratio of 12 and a power compression ratio of 8.6 at a time compression ratio of 252. [37]

An active variation of SLED II can be created to improve the efficiency using a high power switch to change the coupling coefficient during the discharging phase. Phase reversal is still needed to reduce the burden on the switch. A 3-port network is used, with a piece of semiconductor in the third arm. An external stimulus can induce an electron-hole plasma layer at the surface of the semiconductor, changing its dielectric constant. The propagation constant of RF signals through the active arm changes due to this and consequently the coupling between the other two ports also changes. This gives the compressor a power compression ratio of 11 at 29% efficiency.[38]

In Binary Pulse Multiplication (BPM) 3dB couplers are combined with phase encoding to produce stages of power doubling. Each step doubles the input power and halves the pulse duration. Two phase modulated klystrons are connected to one or more pulse compression stages. Each stage consists of a 3dB coupler with one output port connected to a delay line, with a delay equal to half the input pulse duration, with the other end connected to a zero delay transmission line. Each stage coverts its two coded inputs into two compressed outputs appropriately coded for the next stage.[39]

An active pulse compressor can be constructed using a Bragg structure containing a system of gas discharge tubes in the output Bragg reflector for Q-modulation. The Active Bragg Compressor (ABC) has a maximum compression ratio of 11-12 at 50% compression efficiency.[40,41]

Linear frequency modulation can also be used for passive pulse compression using diffraction gratings[42] or dispersive lines[33]. A Quasi-optical pulse compressor uses a high-Q three-mirror resonator and an excitation system. The resonator consists of two focusing mirrors and the third mirror with a fine corrugation on its surface. The corrugation provides coupling of the operating mode with the wave beam formed by the excitation system. A power compression ratio of 3 can be obtained at 75% compression efficiency in a single pass.[43] A chain of these resonators can be

used to produce a high compression ratio.[44] An active pulse compressor can also be formed. To achieve this, for energy storage, the grating should provide branching of a small portion of the incident power by diffraction to couple the resonator with the feeding line. Then to extract the energy the grating should be switched quickly into a state where most of the energy is diffracted. This can be achieved by using a gas-discharge plasma to change the distribution of the electromagnetic field on the grating. A power compression ratio between 15-30 is reported at 50% compression efficiency.[43]

1.8.1 Sweep-frequency based pulse compression

Some advanced applications require the use of frequency-controllable microwave sources with higher power. One method of achieving higher power is the realization of passive pulse compression based on fast frequency sweeps and the use of a dispersive medium.

Consider a wavepacket, much longer than the period of the oscillations, which has its oscillation frequency gradually swept from a low frequency, ω_1, at the beginning of the pulse to a higher frequency, ω_2, at the end of the pulse, as shown in Figure 1-2.[33]

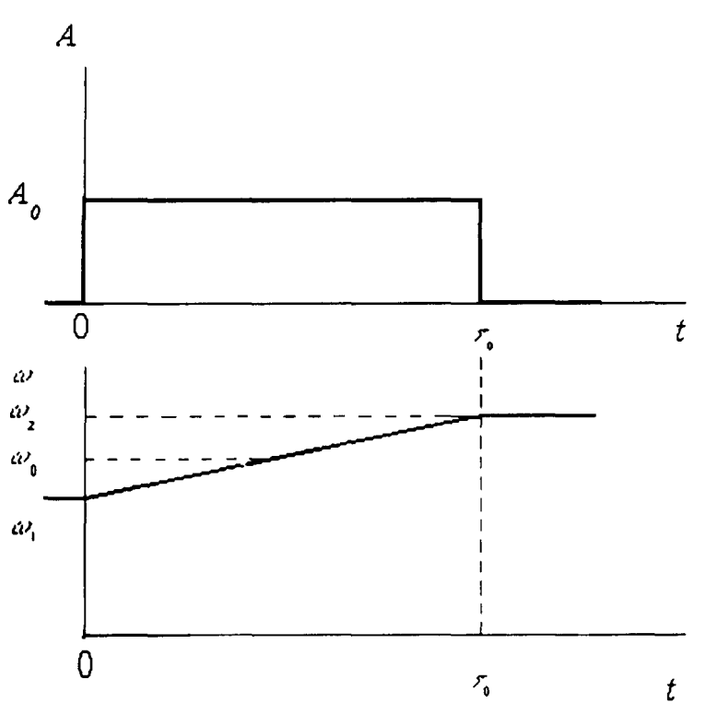

Figure 1-2 Amplitude and frequency of the initial wave packet used in sweep-frequency pulse compression.

This pulse is then propagated down a dispersive medium in which the group velocity of the wave is a function of frequency only.

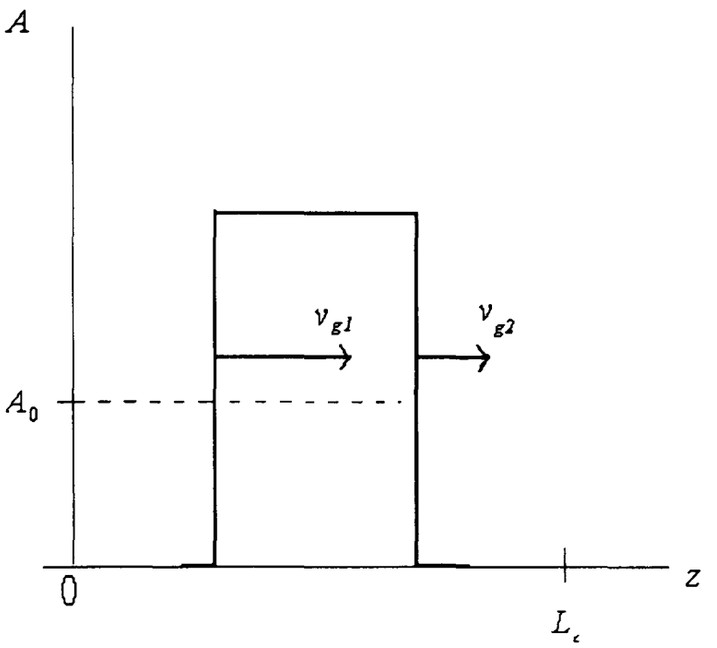

Figure 1-3 Illustration of the principle of sweep-frequency based pulse compression.

If the group velocity of the higher frequency wave, ω_2, was slower than the group velocity of the low frequency wave, ω_1, then the end of the pulse would move towards the start of the pulse to overtake it and the pulse would be compressed. This leads to the pulse duration decreasing and a corresponding growth in the pulse amplitude, as shown in Figure 1-3. The optimum length, L_c, is the distance to the point where the tail of the pulse overtakes the start.

Year	Technique	Author	kp
1967	Sweep-frequency	Bromley	10
1974	SLED	Farkas	3.18
1977	SES	Birx	16
1981	SES	Alvarez	35
1986	BPM	Farkas	8
1990	SLED II	Farkas	8.6
1997	Active SLED II	Tantawi	11
1999	ABC	Virkharev	12
2002	Active Quasi optical	Virkharev	15-30

Table 1-1 Comparison of Pulse compression techniques

A comparison of the maximum power compression ratio for each of the methods discussed, is shown in Table 1-1

1.9 Linear beam sources as input devices for sweep-frequency based pulse compression

In order to have coupling between a beam and a wave the beam dispersion must intersect the dispersion of the wave on a ω-k_z diagram. One method of doing so is to use a slow wave structure to reduce the phase velocity of the wave to match the beam velocity. A slow wave structure is typically a waveguide with a periodic corrugation on its inner surface[45]. This gives rise to a series of spatial harmonic waves each differing in axial wavenumber by the Bragg periodicity vector, $\bar{h} = 2\pi/d$, where d is the period of the corrugation. The most common microwave tubes of this type are the travelling-wave tube and the backwards wave oscillator. The travelling-wave tube is an amplifier, in which the input wave is amplified by the electron beam through a convective instability. Great care is undertaken in designing these devices to avoid any parasitic oscillations, where the beam couples to another mode through an absolute instability, hence drawing energy from the beam. Reflections at the output from the amplifier can result in the excitation of spurious modes, hence high reflections at the output are to be avoided[46]. Placing a near-cut-off waveguide, such as the type used in sweep-frequency based pulse compression, at the output of a travelling-wave tube can cause parts of the pulse to be reflected back into the tube. As RF isolation using unidirectional elements is impossible at high powers (>1MW), it is clear that for pulse compression at high powers another method must be used. For passive compression of microwave pulses, an oversized circular waveguide with a helical corrugation on it's inner surface was proposed. The first spatial harmonic of a TE_{11} wave passing through the waveguide is coupled to a TE_{21} near-cut-off mode by the corrugation. This can create a region with a low group velocity far from cut-off, if the correct parameters are chosen for the corrugation, pulse compression can take place without the reflections associated with operation near cut-off.

Feedback resulting in oscillations can be used to create a backwards-wave oscillator (BWO). In a BWO the electron beam couples to a wave travelling in the

opposite direction, as the waves phase velocity is in the same direction as the beam velocity.[47]

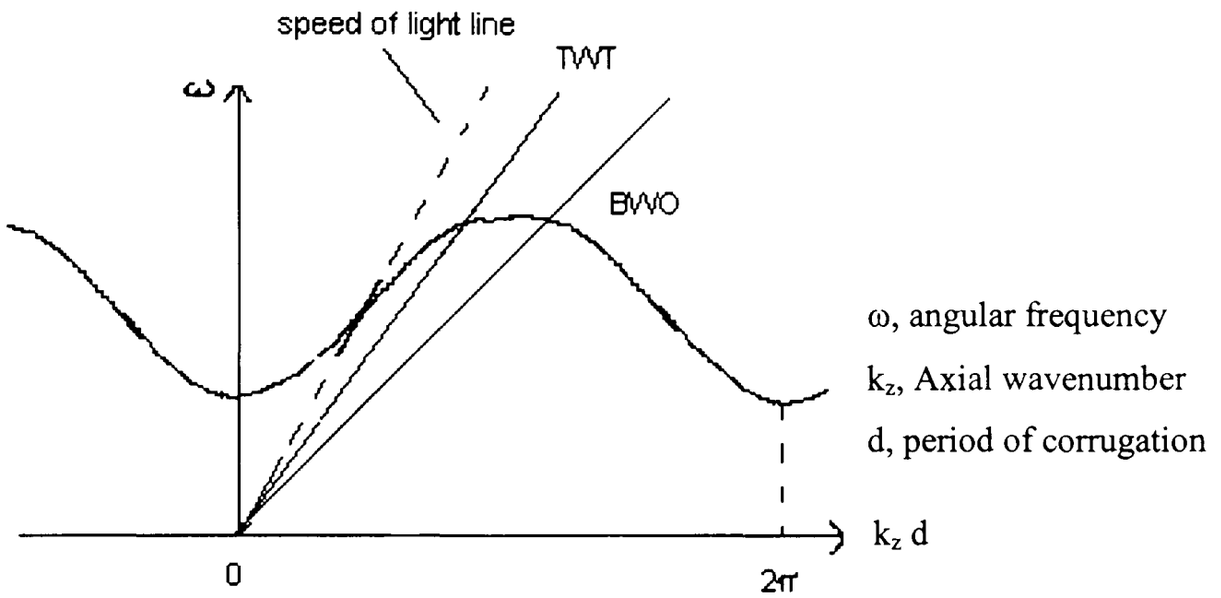

Figure 1-4 Intersection of the beamline and wave dispersion for linear beam devices.

As can be seen in Figure 1-4 the frequency of interaction is usually an inverse function of beam voltage. In order to have the beamline intersect the waves dispersion high beam voltages are required. For a smooth-bore pulse compressor the frequency sweep required would need a voltage sweep that increases with time. When operating at voltages in the region of hundreds of kilovolts, such a sweep is extremely difficult to realise. A helically corrugated compressor, however, would require a voltage sweep that decreases with time, which is much easier to produce at high voltages and can be produced naturally with the decay of a Marx bank generator.

In this work, the theory for such an experiment was developed and experimental measurements of compression were made. A helically corrugated waveguide was developed to provide a very flexible and controllable wave dispersion which can be used to produce a large change in group velocity over a small frequency bandwidth. This allowed the length of the pulse compressor to be dramatically reduced and hence to also significantly reduce losses.

1.10 Previous research at the University of Strathclyde using helically corrugated waveguides

Metal hollow waveguides with various types of periodic corrugation are used widely in high-power microwave electronics. One such structure that has recently attracted considerable interest consists of a helical corrugation in the wall of a circular cylindrical waveguide, which involves both an axial and azimuthal periodicity. This provides asymmetry of the wave dispersion for circularly polarized modes resulting in additional mode selection. These properties make waveguides with a helical corrugation attractive for a large number of applications. In particular, they have been used as slow-wave interaction structures in relativistic Cherenkov devices[30], Bragg reflectors[48] and as mode converters[41] etc. Helically corrugated waveguides have recently been successfully used as interaction regions in gyro-TWTs and gyro-BWOs[49].

In 1998 a new type of amplifier known as a Gyrotron Travelling Wave Tube with a helically corrugated interaction region was invented at the University of Strathclyde in collaboration with scientists from the Institute of Applied Physics, Russia[50,51,52,53]. The novelty of this research lay with the use of a helical corrugation on the inner surface of a cylindrical waveguide to radically modify the wave dispersion. Instead of the normal cut-off scenario in the region of near infinite phase velocity, the corrugation gives rise to some eigenmodes with constant finite group velocity. Such dispersion may be readily matched to that of a gyrating electron beam allowing an efficient convective high gain beam-wave interaction using the CRM mechanism to occur over a wide frequency band, as shown in Figure 1-5.

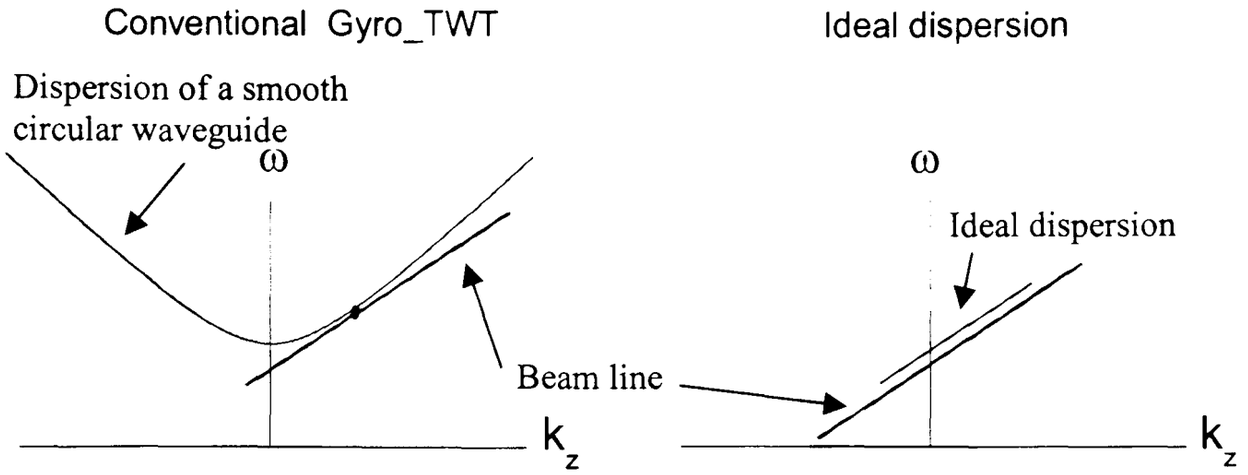

Figure 1-5. Dispersion diagram for a conventional smooth cylindrical metal waveguide compared to the helically corrugated waveguide. In the ideal dispersion diagram of the helically corrugated waveguide, (RHS) as the axial wavenumber tends to and passes through zero, the operating eigenwave has a constant and finite gradient which can be matched to the electron beam drift velocity over a broad frequency range.

The simplest method of analysing the CRM mechanism is to examine the interaction of a single beamlet, or ensemble of electrons with the electric field. The beam in a cyclotron wave device can be built up from an overlapping distribution of many such beamlets[54]. Initially the electrons in a beamlet are uniformly distributed along a single helical path prior to interaction with the RF field. The rotation of the electrons is dependant on the direction of the longitudinal magnetic field. The electrons are assumed to rotate in the clockwise direction if the electrons propagate in the same direction as the magnetic field, when viewed in the direction of e-beam propagation [8]. The electron will orbit the centre at a constant Larmor radius r_L given by

$$r_L = v_\perp / \omega_c \qquad \textbf{Equation 1-1}$$

where ω_c is the relativistic cyclotron frequency.

$$\omega_c = e B_0 / m_0 \gamma = e B_0 / m \qquad \textbf{Equation 1-2}$$

Gyrotrons rely on relativity for their operation where electron mass is larger than its rest mass with bunching arising due to the dependence of the electron cyclotron frequency on beam energy..

The transverse electromagnetic field of a TE mode in a circular waveguide will decelerate electrons travelling towards it's peak and accelerate electrons travelling away from it's peak. In Figure 1-6a) electrons 1-5 are accelerated and electrons 6-10 are decelerated by the electric field. The decelerated electrons will

lose energy, this causes the electron to lose relativistic mass (γm) due to relativity. The reduced mass causes the cyclotron frequency to increase. The accelerated electrons gain energy which causes the cyclotron frequency to decrease. The increase in cyclotron frequency of electrons 6-10 and decrease in the cyclotron frequency of electrons 1-5 causes the electrons to bunch at the peak of the field shown in Figure 1-6b). No energy exchange has taken place as the number of electrons losing energy is the same as those gaining energy.[55]

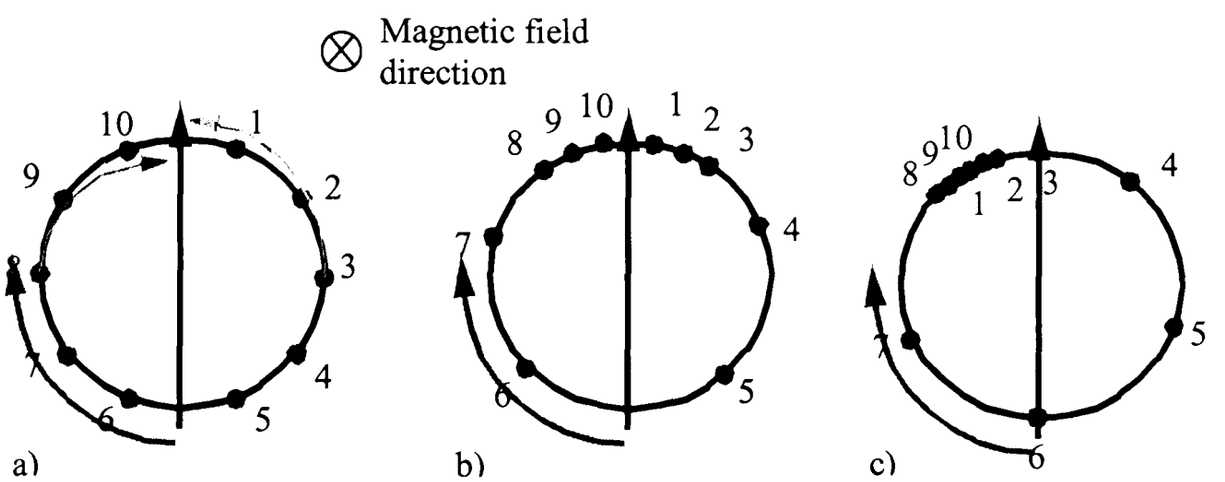

Figure 1-6 Phase Bunching in CRM devices. a) shows the intial position of the electrons, b) shows the interaction between the beam and the wave and c) shows the result of phase slippage between the beam and the electric field.

However, if the cyclotron frequency is lower than the frequency of the RF field, the position of the bunches along the helical orbit is delayed with respect to the phase of the electric field as can be seen in Figure 1-6c). This is done by setting

$$B/B_{sync} < 1 \qquad \textbf{Equation 1-3}$$

where B is the longitudinal dc magnetic field and B_{sync} is the B-field value that would produce exact synchronism between the rotating electric field and the gyrotron motion of the electrons.[56]

As a result of the phase slippage between the particles and the field the net kinetic energy of the particles will decrease. To satisfy energy conservation the amplitude of the wave increases. As the electron bunches rotate in near synchronism with the alternating RF field they continue to give up energy on each half cycle of rotation.[8]

In the case of a gyro-TWT with a smooth circular waveguide as its interaction region, the parasitic gyrotron self excitation forces the operating wave to have a relatively large axial wavenumber in order to provide the stable amplification regime. This gives the interaction a much broader frequency band but causes significant Doppler frequency shift which makes the interaction sensitive to the spread in the electron velocity resulting in low interaction efficiency. The most attractive wave dispersion is when the wave group velocity is constant and equal to the electron beam velocity in the region of near-infinite phase velocity, as shown in Figure 1-5.

Operation of the first Gyro-TWA with a helically corrugated interaction region resulted in world record performance where 1MW output power in the frequency range of 9.2 to 10.2GHz corresponding to a saturated gain of 37dB and an efficiency of 30% was measured.[53]

1.11 Research pursed in this thesis

The theoretical and experimental work in this thesis was concerned with the use of an oversized circular waveguide with a helical corrugation on its inner surface for the application of sweep-frequency based passive pulse compression. Theoretical simulations and experiments were developed to investigate the advantages of using a helically corrugated waveguide instead of a standard cylindrical waveguide with a uniform circular cross-section. The performance of the helical compressor was compared to that of a normal cylindrical waveguide compressor. The results obtained in this thesis can be summarized as follows:

1. The method of perturbations in Maxwell's equations were used in order to find the dispersive characteristics of the helically corrugated waveguides. This approach was also used to find the ohmic losses in the helix.
2. A Particle-in-cell code was used to find the dispersive characteristics of a helically corrugated waveguide. Two methods were used, one that measures the polarisation rotation of a linearly polarised mode in the helically corrugated waveguide and another method that directly measures the

wavelength of the eigenwave in the helical waveguide using a Fourier transform.

3. A simple kinetic approximation for the optimum power compression ratio, due to a frequency swept pulse propagating through a length of waveguide was derived.
4. A theoretical simulation of a pulsed chirped (frequency swept) signal propagating through a dispersive medium was constructed. This was based on a numerical Fourier transform of the input signal and a numerical inverse Fourier transform of the result taking the spatial component of the wave, waveguide dispersion and losses into account. Using this technique simulations of passive compression of a frequency swept microwave pulse in a helically corrugated waveguide were obtained.
5. The dispersion of the helically corrugated waveguide was found by measuring the angle of rotation of a linearly polarised wave passed through the waveguide.
6. A novel technique for measuring the dispersive characteristics of the operating eigenwave was developed by measuring the change in phase produced by introducing a helically corrugated waveguide between two sections of circular X-band waveguide carrying a circularly polarised wave.
7. The ohmic losses in the helical waveguide were measured.
8. The compression of 1kW chirped pulses in 3 separate helically corrugated waveguides and various lengths of smooth circular waveguide were measured.
9. A frequency-swept BWO for use as an input source for a helically corrugated compressor was designed and simulated.

2 Waveguide Theory

2.1 Introduction

The use of waveguides, of rectangular or circular cross-section, as frequency dispersive media for microwave pulse compression was first studied in 1967[33]. In this thesis a new type of frequency swept microwave compressor, which uses a helically corrugated waveguide as a frequency dispersive element, is presented. However the general waveguide theory is applicable to both types of compressor and is reviewed in chapter 2. In section 2.2 Maxwell's equations and the wave equation in free space are presented. In sections 2.3, 2.4 and 2.5 the theory of rectangular waveguides, the different modes that can be supported and the equations that govern the frequency of operation are reviewed. In section 2.6 the theory of circular waveguides, which requires the use of polar co-ordinates and Bessel functions, are presented. In sections 2.7, 2.8, 2.9 and 2.10 1) the dispersion relation 2) the phase, group and signal velocities and 3) the power flow and the factors that govern losses in waveguides are presented. In section 2.11 more specialised concepts such as periodically loaded waveguides are discussed. Finally in section 2.12 the principle behind microwave pulse compression for a conventional circular waveguide are introduced.

2.2 Electromagnetic waves

In 1865 Maxwell made a small modification to Ampère's Law that predicted the existence of electromagnetic waves that propagate at the speed of light. Shown below is all the fundamental equations in electromagnetism. These four equations are collectively known as Maxwell's equations.

$$\nabla . B = 0$$ **Gauss's Law for magnetic fields, Equation 2-1**

$$\nabla \times B = \mu_0 J + \mu_0 \varepsilon_0 \frac{\partial E}{\partial t}$$ **Amperè-Maxwell Law, Equation 2-2**

$$\nabla . E = \frac{\rho}{\varepsilon_0}$$ **Gauss's Law, Equation 2-3**

$$\nabla \times E = -\frac{\partial B}{\partial t}$$ **Faraday's Law, Equation 2-4**

Where E is the Electric field strength, B is the Magnetic Flux density, J is the volume current density, μ_0 is the permeability of the free space, ε_0 is the permittivity of the free space and ρ is the volume charge density. Most electromagnetic phenomena and the main principles behind the operation of free electron radiation sources can be described by Maxwell's equations, the Lorentz force equation and the conservation of charge.[57]

In the presence of dielectric materials an electric field can force charges bound to atoms to move a minute distance creating an electric polarisation, P, proportional to the electric field strength given by

$$P = \varepsilon_0 \chi_e E$$ **Equation 2-5**

where χ_e is the electric susceptibility. Hence the electric flux density, D, is given by

$$D = \varepsilon_0 E + P = \varepsilon_0 (1 + \chi_e) E = \varepsilon E$$ **Equation 2-6**

where ε is the permittivity of the medium, given by $\varepsilon_r \varepsilon_0$, where $\varepsilon_r = 1 + \chi_e$ is the relative permittivity of the medium.

All atoms contain spinning electrons which give rise to magnetic fields. Magnetic materials, when properly orientated, can give a net magnetic moment or magnetisation, M, given by

$$M = \mu_0 \chi_m H$$ **Equation 2-7**

where χ_m is the magnetic susceptibility and H is the magnetic field strength.
This gives the magnetic flux density as

$$B = \mu_0 (H + M) = \mu_0 (1 + \chi_m) H = \mu H$$ **Equation 2-8**

where μ is the permeability of the medium, given by $\mu_r \mu_0$, where $\mu_r = 1 + \chi_m$ is the relative permeability of the medium.

In the presence of matter, Maxwell's equations 2-2 and 2-3 can be reformulated as

$$\nabla \times B = \mu_0 \left(J_f + \frac{\partial P}{\partial t} + \nabla \times M \right) + \mu_0 \varepsilon_0 \frac{\partial E}{\partial t}$$ **Equation 2-9**

$$\nabla . E = \frac{\rho_f - \nabla . P}{\varepsilon_0}$$

where J_f is the free current density and ρ_f is the free charge.

Electromagnetic waves can be guided in a direction by waveguides. In this thesis the guiding of electromagnetic radiation by waveguides in air was studied where the relative permittivity and permeability are close to freespace at X-band. There are many types of waveguide. Hollow metallic waveguides operate at high power but are lossy. The electromagnetic wave propagates down a hollow metallic tube by reflection on the inner surfaces and operate at frequencies of the order of 10^9 hertz and higher. The general wave equations for the propagation of electric and magnetic fields down such a waveguide can be derived from Maxwell's equations.

$$\nabla^2 E = \mu\varepsilon \frac{\partial^2 E}{\partial t^2}$$ **Equation 2-10**

$$\nabla^2 B = \mu\varepsilon \frac{\partial^2 B}{\partial t^2}$$ **Equation 2-11**

The complete solutions to these equations are subject to the boundary conditions imposed by the walls of the waveguide. With any type of electromagnetic wave, E vanishes inside a perfect conductor. Due to the continuity of the tangential component of E at an interface, the tangential component of E is zero close to the walls of the guide, $E_{\|} = 0$, and the normal component of B, close to a perfectly conducting guide is zero, $B_{\perp}=0$, and $\frac{\partial H_z}{\partial n} = 0$, where H is the magnetic field strength and n is normal to the waveguide walls. Due to these boundary conditions it is impossible for a TEM wave to propagate down a hollow conducting tube.[58]

The general properties of an electromagnetic wave propagating in a straight line are

1. The medium of propagation is homogeneous, isotropic, linear, and stationary (HILS)

2. It is nonconducting. This does not exclude metallic guides, because the wave propagates along a metallic guide.
3. The free charge density is zero.
4. Propagation occurs in a straight line, in the positive direction of the z-axis. There is no reflected wave travelling in the –z direction.
5. The wave is sinusoidal.
6. There is zero attenuation. If the guide is metallic, then its conductivity must be infinite to avoid ohmic losses.

The wave equation for cylindrical waveguides is given by,

$$\left(\nabla_t^2 + \mu\varepsilon\omega^2 - k_z^2\right)\begin{Bmatrix} E \\ B \end{Bmatrix} = 0 \qquad \textbf{Equation 2-12}$$

where ω is the angular frequency, k_z is the axial wavenumber and ∇_t^2 is the transverse part of the Laplacian operator, $\nabla_t^2 = \nabla^2 - \frac{\partial^2}{\partial z^2}$.

Waveguides come in a variety of different physical structures subject to their use and operational bandwidth. The most common structures are rectangular and cylindrical hollow metal waveguides.

2.3 Rectangular waveguides

For microwaves the most common shape for a waveguide is rectangular. It has the simplest equations for electric and magnetic fields.

Consider two electromagnetic plane waves of the same wavelength moving across each other having their magnetic fields in the plane of the paper and the electric wave perpendicular to the paper as shown in Figure 2-1.

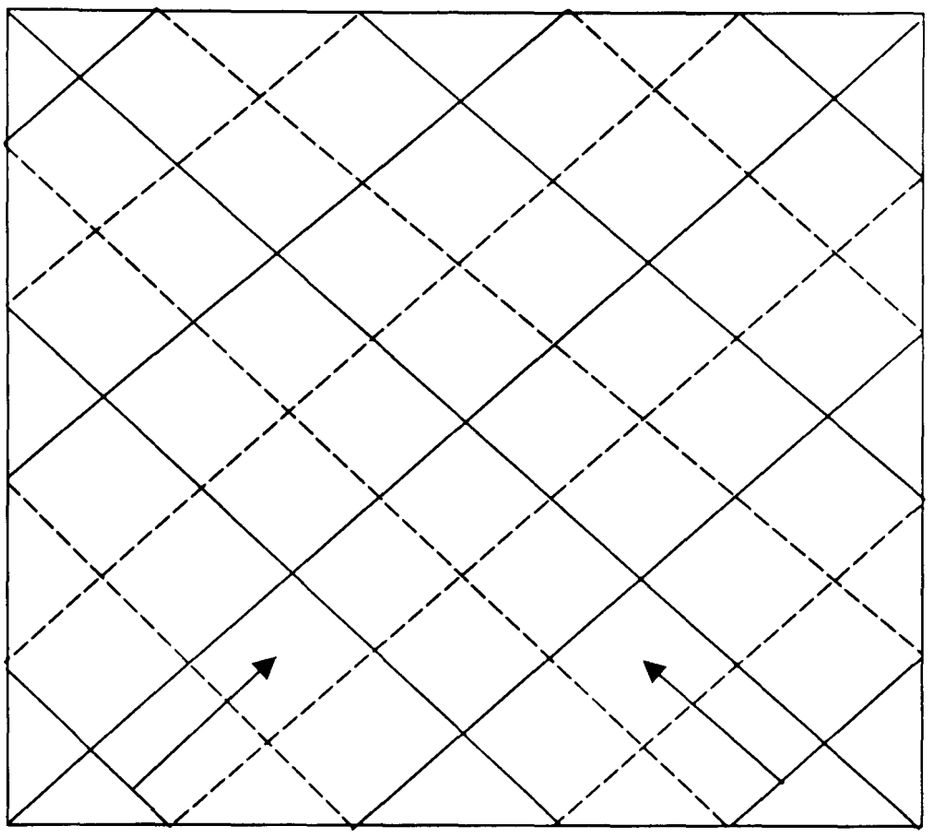

Figure 2-1 Two electromagnetic plane waves propagating perpendicular to each other.

The full lines represent the peaks of the electric field and the dashes represent the troughs. When the two waves are superimposed on each other it can be seen at certain points the peak of one wave coincides with the trough of another. At these points there is no electric field. This means that two sheets of metal placed along each of these lines will not influence the pattern in anyway. This means that the waves will propagate between those sheets.[59]

Along the centre lines of the pattern, the electric field adds, producing a maximum disturbance which is twice the amplitude of any single disturbance. The distance between any parallel full lines is the freespace wavelength of the electromagnetic field. Similarly the distance between the points of interception of any two lines is the distance between two peaks of maximum disturbance and so is the wavelength of the composite wave made up of adding the two separate waves. Which is known as the waveguide wavelength.

2.4 Modes

The transverse electromagnetic field patterns that propagate down a waveguide are called modes. There are an infinite number of possible modes of propagation of

electromagnetic waves in waveguides, but they can be classified into three basic types;

1. transverse electric (TE)
2. transverse magnetic (TM)
3. transverse electric and magnetic (TEM)

The TE mode has no component of E in the z direction, but the magnetic field has a component along the z direction. The propagation of a TE mode in a hollow rectangular waveguide can be depicted by considering a high frequency oscillator connected to the walls of a rectangular tube. At one instant the oscillator will cause a surplus of electrons on the top wall of the tube and a deficiency on the bottom wall. This causes a potential difference between the top and bottom walls of the waveguide. The potential difference causes currents to flow which in turn create magnetic fields trying to circle around the currents. The walls of the waveguide prevent the magnetic fields from completely encircling the currents and cause them to join up instead. Then as the oscillator slowly reverses its polarity new currents are created further along the waveguide by induction which in turn create new E and B fields (Figure 2-2). This makes it appear as if the E vector has moved forward down the tube. [59]

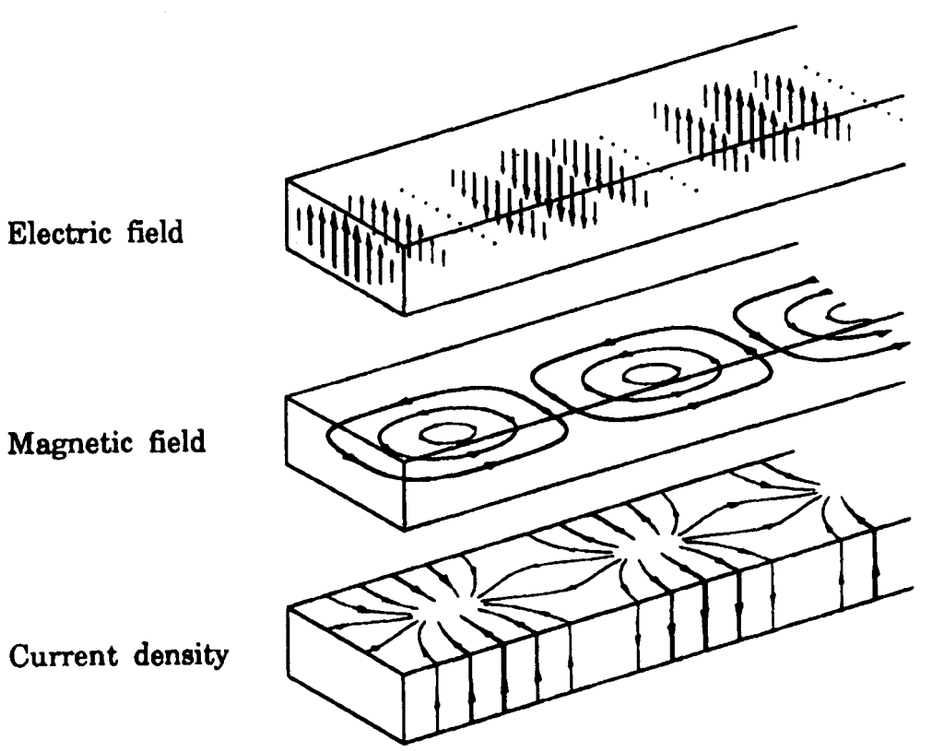

Figure 2-2 Field and current patterns of the TE_{01} mode of a rectangular conducting waveguide from reference 62.

The TM mode has no component of B in the z direction, but has an electric field component in the z direction. The TEM mode has no component of E or B in the z direction. A TEM wave cannot be propagated in a hollow conducting tube.

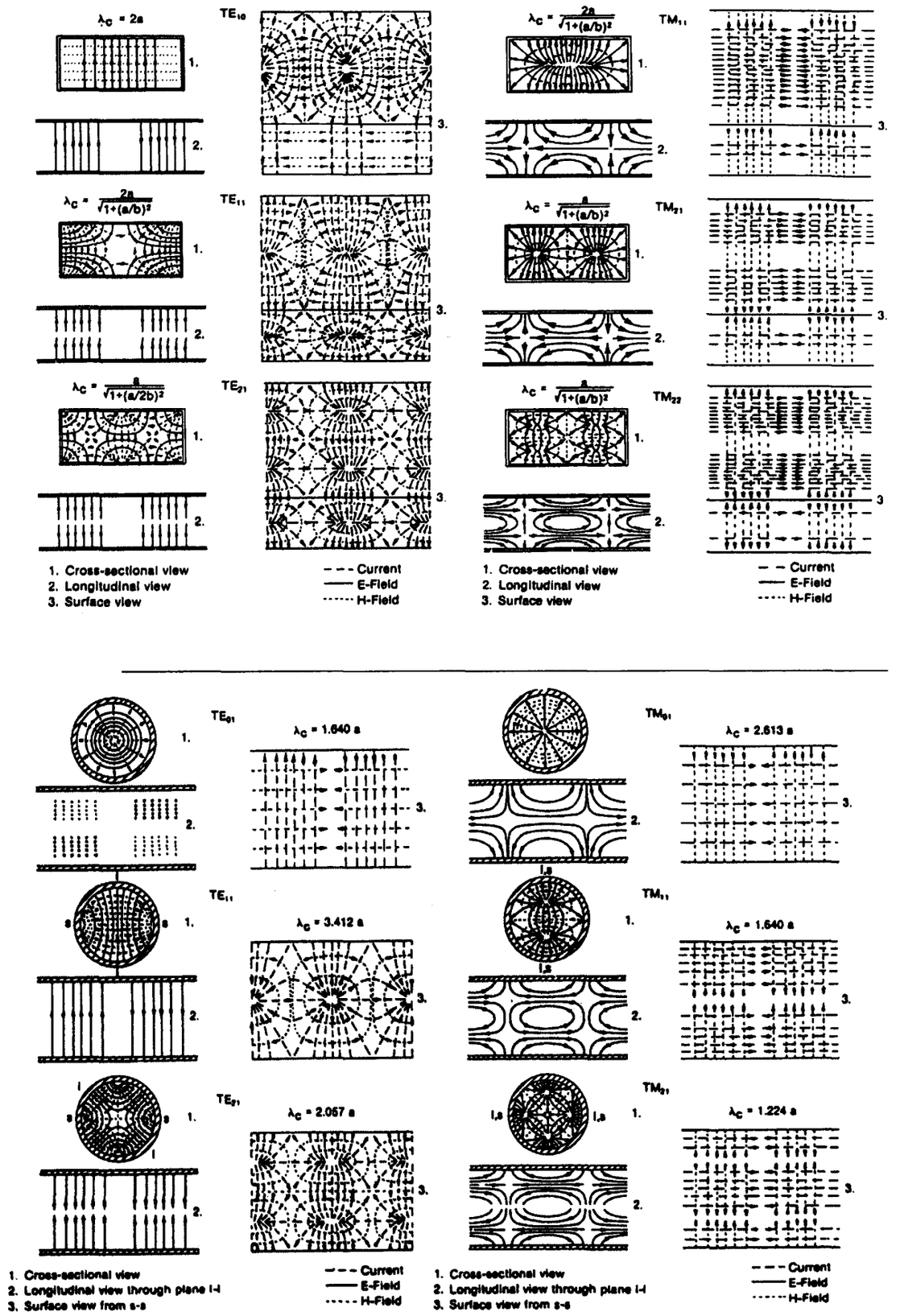

Figure 2-3 Field distribution of TE and TM modes in rectangular and circular waveguides from reference 4.

The TE and TM modes are characterized by two indices m and n. m represents the number of half wave variations of the electric field over the width of a rectangular waveguide and the number of full wave variations of the radial electric field in the azimuthal direction in a circular waveguide. n represents the number of half wave variations of the electric field over the height of a rectangular waveguide and the number of half wave variations of the azimuthal electric field in the radial direction in a circular waveguide (Figure 2-3).[4]

2.5 Cut-off frequencies

The propagation of a given mode in a waveguide is determined by its cut-off frequency. This is directly related to the geometry of the waveguide and is the lowest frequency which can propagate.

The cut-off frequency, ω_c, can be calculated for a waveguide using the freespace dispersion relation $\omega=ck$ (where $k= 2\pi/\lambda$).

Taking $k = \sqrt{k_x^{\,2} + k_y^{\,2} + k_z^{\,2}}$ **Equation 2-13**

where k is the wavenumber in the direction denoted by the subscript

c is the speed of light

λ is the wavelength associated with k

This can be rewritten as $k = \sqrt{k_t^{\,2} + k_z^{\,2}}$ **Equation 2-14**

where k_t is the wavenumber transverse to the direction of propagation.

If you consider the two electromagnetic waves from Figure 2-1 again it can be seen that the waveguide wavelength, λ_g, is longer than the freespace wavelength, λ_0, since

$$\lambda_0 = \lambda_g \cos\theta \qquad \textbf{Equation 2-15}$$

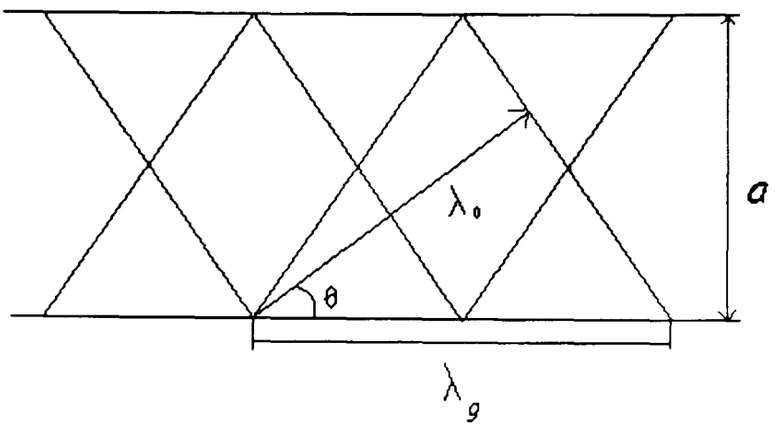

Figure 2-4 The wave in the waveguide formed by the superposition of the coherent radiation

If you now imagine that λ_0 is now larger than 2a shown in Figure 2-4, it can be seen that the constructive interference between the reflected waves does not occur and it is impossible to find an angle, θ, for propagation. Therefore the constructive interference only occurs for wavelengths, $\lambda_0 < 2a$.[60] .

Hence the cut-off wavenumber is,

$$k_t = \left[\left(\frac{m\pi}{a}\right)^2 + \left(\frac{n\pi}{b}\right)^2\right]^{1/2} \qquad \textbf{Equation 2-16}$$

for a rectangular waveguide where a is the waveguide height and b is the waveguide width.

The cut-off frequency is the lowest frequency at which a mode can propagate down a waveguide. The propagation of a given mode in a waveguide is given by its cut-off frequency. Below this frequency, k_z is imaginary and the wave decays exponentially in amplitude as it enters the waveguide. The dominant mode in a wave guide is the one with the lowest cut-off frequency. For a rectangular waveguide the dominant mode is always the TE_{10} mode. Up to a certain frequency above this cut-off, wave propagation is single mode.

2.6 Circular waveguides

Treatment of the propagation of microwaves in a circular waveguide is more complex than that of a rectangular guide as it requires the use of cylindrical polar co-ordinates for the wave equations due to the circular geometry. If we let ψ represent E_Z for TM modes and H_Z for TE modes then,

$$\left[\frac{1}{r}\frac{\partial}{\partial r}\left(r\frac{\partial}{\partial r}\right)+\frac{1}{r^2}\frac{\partial}{\partial \varphi^2}+\mu\varepsilon\omega^2-k_z^{\,2}\right]\psi=0 \qquad \textbf{Equation 2-17}$$

Separating variables and applying a periodic boundary condition to the azimuthal component, we find $\psi = R_m e^{\pm im\varphi}$, with m an integer. The radial function R_m satisfies Bessel's equation whose general solution is

$R_m=A_1\ Jm(k_t\ r)+A_2\ N_m(k_t\ r)$ **Equation 2-18**

Where $k_t^{\,2}=\mu\varepsilon\omega^2-k_z^{\,2}$. Since R_m must be well behaved at r=0, we set the expansion constant A_2 to zero giving[61]

$$\psi = A_1 J_m(k_t r)e^{\pm im\varphi} \qquad \textbf{Equation 2-19}$$

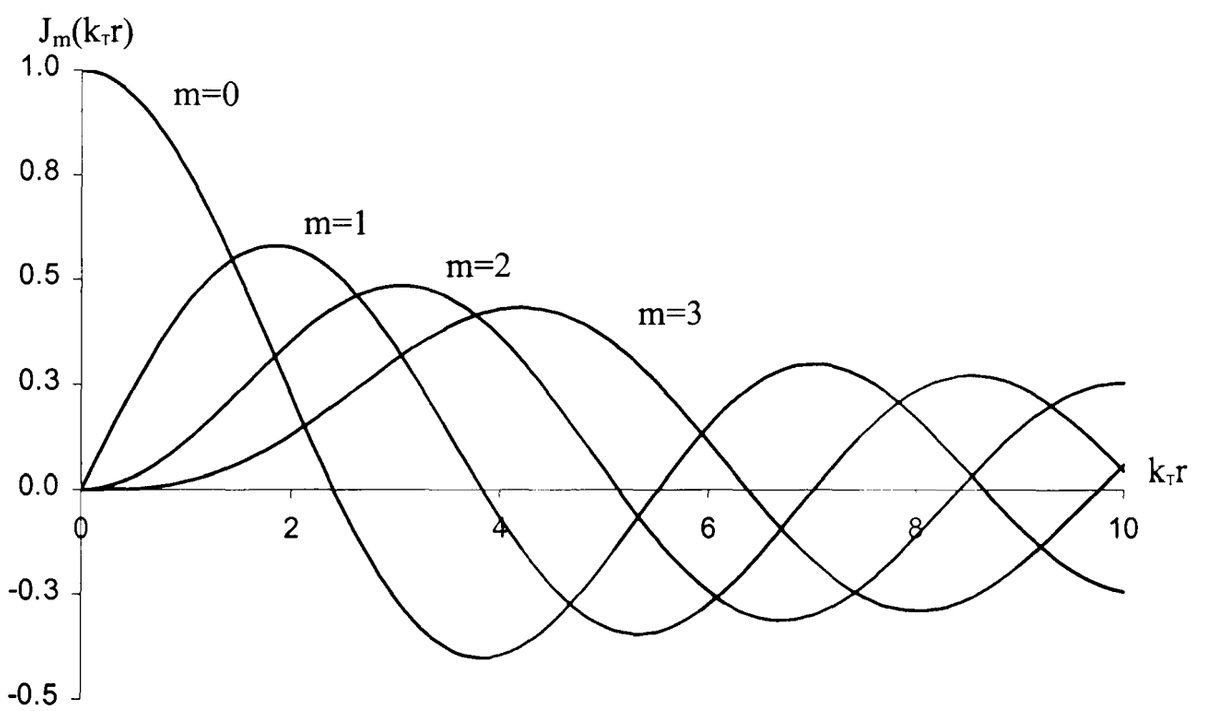

Figure 2-5 First four Bessel functions.

For TM modes at r = a, the waveguide wall, $E_{||}$ must vanish implying that $J_m(k_T a) = 0$ and that $k_t a$ must be a root of J_m, the nth root is designated $\varsigma_{m,n}$. This gives the z component of the electric field as,

$$E_z(r,\varphi)=A_1 J_m\left(\frac{\varsigma_{m,n} r}{a}\right)e^{\pm im\varphi} \qquad \textbf{Equation 2-20}$$

and from Maxwell's equations the transverse fields E_t and H_t. can be derived to be,

$$E_t=\frac{ik_z a^2}{\varsigma_{m,n}^2}\nabla_t E_z \qquad \textbf{Equation 2-21}$$

$$H_t = \frac{i\varepsilon\omega a^2}{\varsigma_{m,n}^2}(\hat{z} \times \nabla_t E_z)$$ **Equation 2-22**

where H is the magnetic field strength.

TE modes have $E_z = 0$ and $H_z = AJ_m(k_t r)e^{\pm im\varphi}$ and the boundary condition $\frac{\partial H_z}{\partial n} = 0$ at r = a, where n is normal to the waveguide wall. This implies that $J_m'(k_t a) = 0$ therefore $k_t a$ must be a root of J'_m, the nth root designated by $\varsigma'_{m,n}$. The z component of the magnetic field strength is given by[5]

$$H_z(r,\varphi) = A_1 J_m\left(\frac{\varsigma'_{m,n} r}{a}\right)e^{\pm im\varphi}$$ **Equation 2-23**

and the transverse fields are given by,

$$H_t = \frac{ik_z a^2}{\varsigma'^2_{m,n}}\nabla_t H_z$$ **Equation 2-24**

$$E_t = -\frac{i\mu\omega a^2}{\varsigma'^2_{m,n}}(\hat{z} \times \nabla_t H_z)$$ **Equation 2-25**

For cylindrical waveguides of radius a, the cut-off wavenumbers are given by

$k_t = \varsigma'_{mn} / a$, for a TE mode and, **Equation 2-26**

$k_t = \varsigma_{mn} / a$, for a TM mode **Equation 2-27**

where ς'_{mn} is the n_{th} root from the origin of the differentiated m_{th} order Bessel function (Figure 2-5) and ς_{mn} is the n_{th} root from the origin of the m_{th} order Bessel function. Each root of the Bessel function plot corresponds to a transverse mode of the system.[62]

2.7 The dispersion relation of cylindrical waveguide

The relationship connecting the angular frequency, ω, and wavenumber, k_z, is known as the dispersion relation.

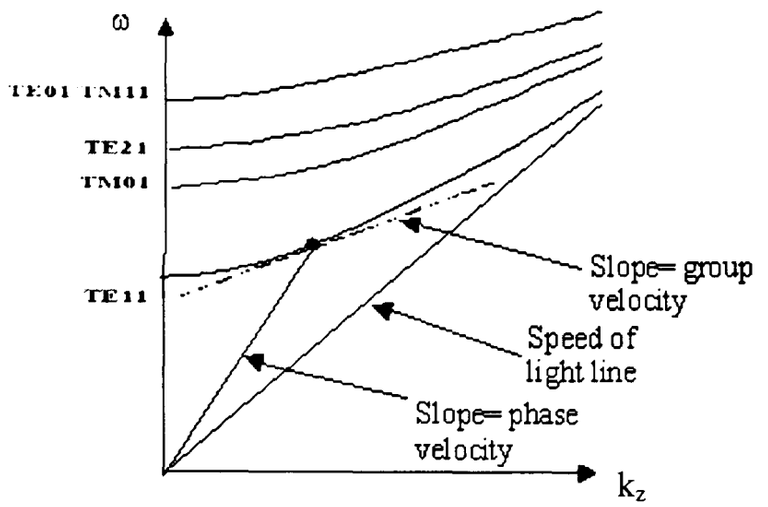

Figure 2-6 Dispersion diagrams for modes in circular waveguides, where the x-axis is the axial wavenumber and the y-axis is angular frequency.

Figure 2-6 shows a plot of ω against k_z. The cut-off frequency can be found from this plot, and hence the dominant mode, and the phase velocity and the group velocity of each mode at any frequency. The frequency range for which the waveguide has single mode operation can also be found.

The dispersion is of the form.

$$\omega^2 = \frac{k_z^2}{\mu\varepsilon} + \omega_c^2 \qquad \textbf{Equation 2-28}$$

where ω_c is the angular cut-off frequency, and $k_t^2=\mu\varepsilon\omega_c^2$.

The group velocity is the gradient at the point on the dispersion curve and the phase velocity at any point is the gradient of a line from the origin to that point.

There are an infinite number of modes for any value of ω, however some of the modes will have a cut-off frequency above ω, the rest will have an imaginary value of k_Z.

For a circular waveguide the dominant mode is the TE_{11} mode. The mode with the next lowest cut-off frequency is the TM_{01} mode.

2.8 The phase, group and signal velocities

The phase velocity is the velocity at which the phase propagates down the guide. This is always greater than the speed of light in a smooth walled waveguide as the TE wave is a superposition of the two plane waves.

When the wave-front moves down a waveguide in free space at speed c the point A moves to the right at speed greater than c (Figure 2-7) this is the phase velocity.

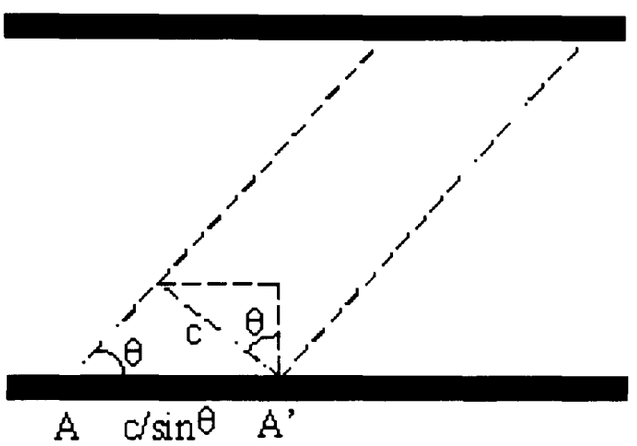

Figure 2-7 Velocity of a wavefront travelling in a waveguide

Although the phase velocity is greater than the speed of light, the signal proceeds down the line at speed $v_g = c \sin \theta$ this is the group velocity which is always less than the speed of light. The relation between the phase velocity, v_p, and group velocity, v_g, in a smooth walled waveguide is given by[58]

$$v_g \cdot v_p = c^2 \qquad \textbf{Equation 2-29}$$

and is maintained for all modes.

Using the dispersion relation, Equation 2-23, the group velocity can be found to be

$$v_g = \frac{\partial \omega}{\partial k_z} = c\sqrt{1 - \left(\frac{\omega_c}{\omega}\right)^2} \qquad \textbf{Equation 2-30}$$

and the phase velocity is found to be,

$$v_p = \frac{\omega}{k} = \frac{c^2}{v_g} \qquad \textbf{Equation 2-31}$$

2.9 Power flow

The Poynting vector, $S = E \times H$, defines the rate at which energy flows through a unit area normal to the direction of propagation. The time-averaged Poynting vector is given by $S_{av} = \frac{1}{2}\mathrm{Re}(E \times H^*)$. Integrating the Poynting vector across the cross section of a waveguide gives the total power, P, flowing out of that cross section $P = \int_S (E \times H) \cdot dA$.[58]

2.10 Losses

The power lost in a waveguide is due to ohmic losses. Real waveguides have a finite conductivity and the electric fields can penetrate a short distance into the conductor, known as the skin depth. In the process of guiding electromagnetic waves, conductors dissipate part of the wave energy in the form of ohmic heating, because the wave induces electric currents in the guide. Near the surface, the electric field in the conductor, E_c, is related to the eddy current density by Ohm's law, $J=\sigma_c E_c$, where σ_c is the electrical conductivity, leading to a power loss in the waveguide. As an electromagnetic wave propagates down a waveguide by multiple reflections of a plane wave, the number of reflections per metre of waveguide increases as the group velocity of the wave decreases. The losses in a waveguide are dependent on cross-sectional area, waveguide length, group velocity of the wave, the ratio of the operating frequency to the cut-off frequency of the waveguide and the waveguide conductivity.[58]

As the power lost is relative to the incident power the attenuation is exponential. The loss coefficient, α, is the imaginary part of the axial wavenumber where $k_z = k_z^{(0)} + i\alpha$ where $k_z^{(0)}$ is the real part of the axial wavenumber. It is also useful to define an attenuation coefficient, γ, where $\gamma=2\alpha$. The transmitted power, P_T, is given by

$$P_T = \exp(-2\alpha\Delta z)\, P_0 \qquad \textbf{Equation 2-32}$$

where Δz is the length of the guide and P_0 is the input power.[58] Hence the loss coefficient is given by

$$\alpha = \frac{1}{2P_T}\frac{\partial P_L}{\partial z} \qquad \textbf{Equation 2-33}$$

where P_L is the power lost due to ohmic heating. The power lost per unit length can be found by integrating the time averaged Poynting vector around the surface contour,

$$\frac{\partial P_L}{\partial z} = \frac{1}{2}\oint E \times H^* dl \qquad \textbf{Equation 2-34}$$

The ratio of the electric field strength to the magnetic flux density is given by the characteristic impedance, Z. The characteristic impedance of a good conductor is given by

$$Z = \frac{E}{H} = \sqrt{\frac{\omega\mu}{\sigma_c}}\exp\frac{i\pi}{4} \qquad \textbf{Equation 2-35}$$

and E leads H by $\pi/4$ radians. As the electric field in the conductor is related to the tangential magnetic field at the surface, the power loss can be presented as a function of the conductor surface current, $i^e = n \times H$ [63].

$$\frac{\partial P_L}{\partial z} = \frac{1}{2\sigma_c \delta}\oint \left|i^e\right|^2 dl \qquad \textbf{Equation 2-36}$$

where δ is the skin depth.

In a cylindrical waveguide of any cross-section in free space, the loss coefficient is given by,

$$\alpha = \sqrt{\frac{\varepsilon_0 \omega_c}{2\sigma_c}}\left(\frac{C}{2A}\right)\frac{\left(\frac{\omega}{\omega_c}\right)^{1/2}}{\sqrt{1-\left(\frac{\omega_c}{\omega}\right)^2}}\left[\xi_c + \eta_c\left(\frac{\omega_c}{\omega}\right)^2\right] \qquad \textbf{Equation 2-37}$$

where C is the circumference, A is the area of cross section and ξ_c and η_c are dimensionless numbers of the order unity.

For a TE mode of a circular waveguide in free space, α , is given by

$$\alpha = \frac{1}{a}\sqrt{\frac{\omega\varepsilon_0}{2\sigma_c}}\left[\frac{m^2}{\varsigma'_{mn}{}^2 - m^2} + \left(\frac{f_c}{f}\right)^2\right]\frac{1}{\sqrt{1-\left(f_c/f\right)^2}} \qquad \textbf{Equation 2-38}$$

where a is the waveguide radius, σ_c is the conductivity, f_c is the cut-off frequency, and m is the number of full wave variations in the radial electric field in the azimuthal direction.

However, this result fails at cut-off but can be solved by using k_z^2, where $k_z^2 = k_z^{(0)2} - \alpha^2 + i2k_z^{(0)}\alpha$. For small losses where, $\alpha^2 << k_z^{(0)2}$, it can be assumed that $i2k_z^{(0)}\alpha - \alpha^2 = (1+i)\,2k_z^{(0)}\alpha$, where,

$$2k_z^{(0)}\alpha = \sqrt{\frac{2\omega\varepsilon_0}{\sigma_c}}\left(\frac{m^2}{\varsigma'_{mn}{}^2 - m^2} + \left(\frac{\omega_c}{\omega}\right)^2\right)\frac{k}{a} \qquad \textbf{Equation 2-39}$$

in this case $2k_z^{(0)}\alpha$ is finite when $k_z^{(0)}=0$. [64,65] The value $2(i+1)k_z\alpha$, will henceforth be known as ϖ.

2.11 Periodically loaded waveguide

Any perturbation in a waveguide that produces a change in impedance is said to load the waveguide. Any change in impedance causes part of the propagating wave to be reflected. For a waveguide with equally spaced obstacles along its length, separated by a distance L, a wave propagating in the waveguide is reflected off each obstacle. The reflections will destructively interfere and the propagating wave will be cut-off, if the wavelength of the propagating wave is twice the distance between the obstacles, $k_zL = \pi$, as shown in Figure 2-8.[66] If this waveguide is infinitely long, then complete reflection will occur.

Spatial harmonics appear due the periodic obstacles and the axial wavenumber of a spatial harmonic is given by $k_z = k_z^0 + n\bar{h}$ where $\bar{h} = \frac{2\pi}{L}$ is the Bragg wavevector, n is the harmonic number and k_z^0 is the axial wavenumber in a smooth waveguide.

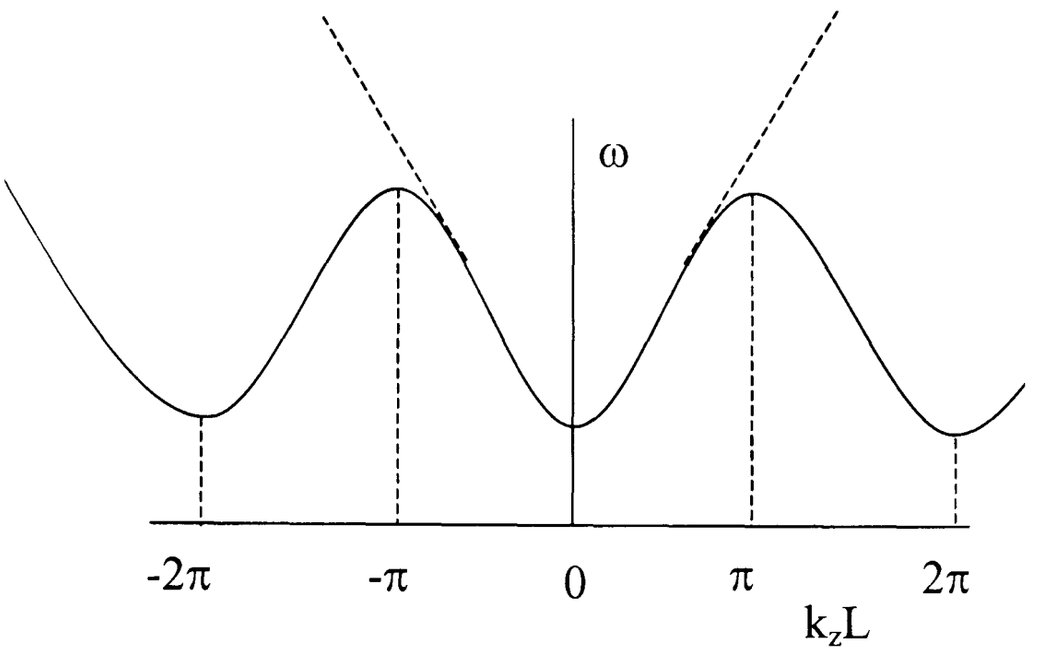

Figure 2-8 Dispersion diagram for a periodically loaded waveguide

2.12 Pulse compression

If a pulse of full width half maximum (FWHM) pulse duration τ is propagated down a waveguide then its Energy, E, is given by

$$E = \int_0^{\tau_0} P_i.dt \qquad \textbf{Equation 2-40}$$

where P_i is the instantaneous power of the initial pulse.

If this pulse is somehow compressed to a shorter pulse duration, τ_c, the energy in the pulse will remain constant due to the law of conservation of energy and the maximum power will increase (Figure 2-9). This is related by a time compression ratio, C, for input and output pulses,

$$C = \frac{\tau}{\tau_c} \qquad \textbf{Equation 2-41}$$

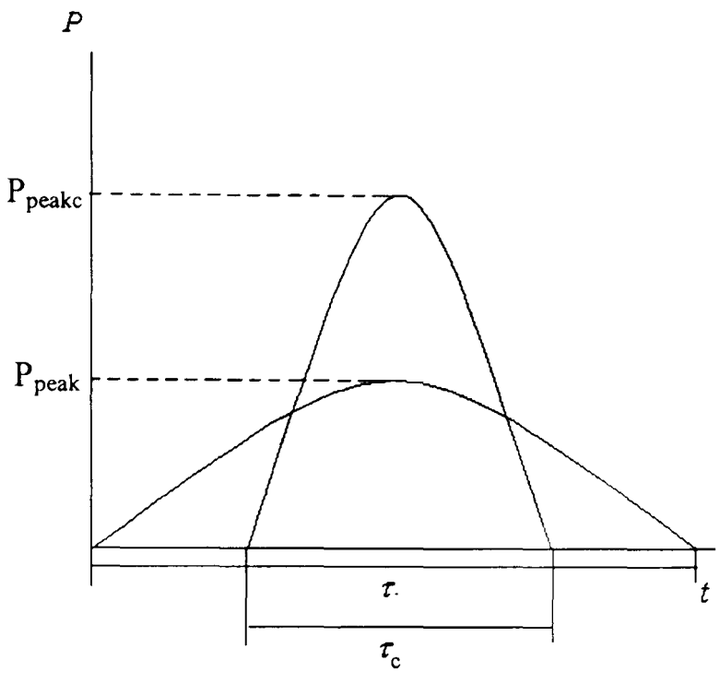

Figure 2-9 Principle of pulse compression.

If a reliable method of pulse compression was found for microwaves then very high peak powers could be realized.

However due to losses incurred in the method of compression the input energy is higher than the output energy, and the peak power compression ratio is lower than the time compression ratio. The peak power compression ratio, k_p, is given by

$$k_p = \frac{P_{peak}}{P_{peakc}} \qquad \textbf{Equation 2-42}$$

where P_{peak} and P_{peakc} are the values of peak power for the initial and compressed pulse respectively.

The compression efficiency, η_c, is given by,

$$\eta_c = \frac{k_p}{C} \qquad \textbf{Equation 2-43}$$

However, it should be noted that this is a ratio of energy contained in the useful part of the pulse to the input energy, and not the actual efficiency, which is given by,

$$\eta = \frac{\int_0^{\tau_c} P_{ic}\,dt}{\int_0^{\tau_0} P_i\,dt} \qquad \textbf{Equation 2-44}$$

where P_{ic} is the instantaneous power of the compressed pulse.

When a circular waveguide is used as a pulse compressor, the greatest change in group velocity with frequency occurs close to cut-off and hence optimum operation is close to cut-off. However, if this compressor was used at the output of a HPM amplifier then any part of the pulse below cut-off would be reflected back towards the microwave source. It is inevitable that the low frequency part of the amplification band of a high-power amplifier will be below the cut-off, resulting in this part of the wave being reflected from the compressor back to the amplifier. An upshot of this is that a conventional waveguide cannot be used as a pulse compressor at the output of a high-power amplifier, as RF isolation using unidirectional elements is limited to powers of less than 1MW. A major problem that limits the upper frequency of operation and the peak power capability of TWTs is backward wave oscillations. At certain frequencies the electrons can interact with the first-order spatial harmonic of the backwards wave which has a negative group velocity but a positive phase velocity equal to that of the electron beam velocity. Due to the nearly linear dispersion characteristics of the helical structure the opportunity for parasitic backward wave oscillation is intrinsic in the helix TWT. Because of the high gain of these devices, small levels of reflection are important hence a smooth-bore circular waveguide compressor is not suitable for use at the output of a TWT. [46]

3 Helically corrugated waveguides

3.1 Introduction

As discussed in Section 2.12, circular waveguide microwave compressors are not suitable for use at the output of high power microwave amplifiers due to the problem of reflections close to cut-off affecting the stability of the amplifier. A helically corrugated waveguide, however, has a more optimum dispersion for use at the output of high power amplifiers. In section 3.2 the use of helically corrugated waveguides as pulse compressors is reviewed. In sections 3.3 and 3.4 the coupling of waves due to the Bragg conditions and the calculation of the dispersion characteristics of the helix using the method of perturbation is discussed. Sections 3.5 and 3.6 examine the surface currents and the coupling coefficient. The three structures designed for use as compressors are discussed in Section 3.7. Sections 3.8, 3.9, and 3.10 consider special structures such as helical tapers and elliptical shaped polarisers required to convert the linearly polarised TE_{11} mode of a smooth circular waveguide into the eigenwave of the helically corrugated waveguide.

3.2 Helically corrugated waveguide as a pulse compressor

The ideal dispersion for a swept-frequency based pulse compressor would have a significant change in group velocity with frequency at a point far from cut-off, as shown in Figure 3-1.

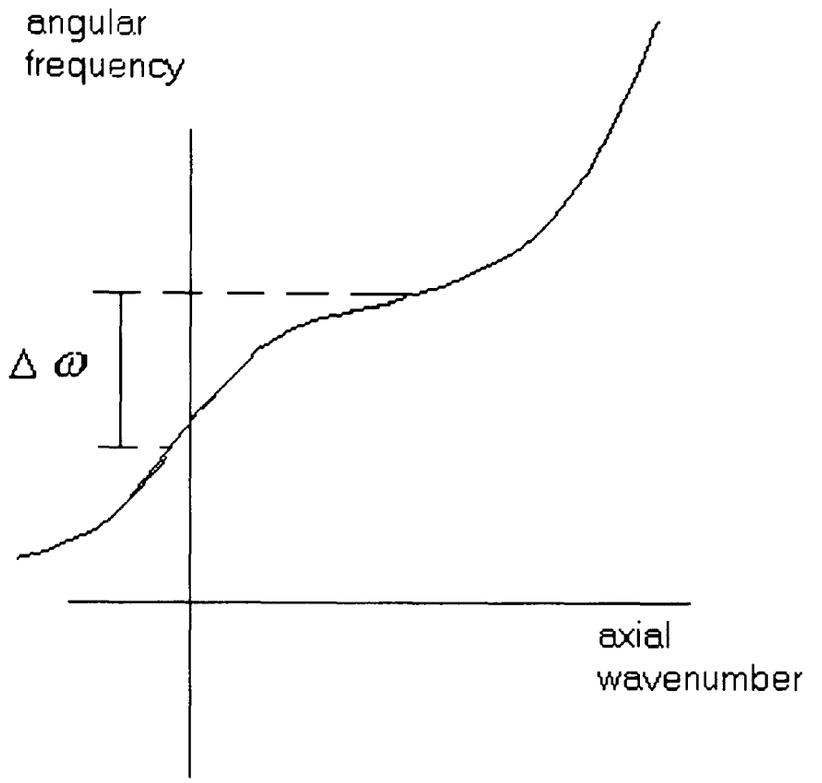

Figure 3-1 Ideal dispersion for a pulse compressor

Such a dispersion is possible by radically altering the circular waveguide geometry by placing a special helical corrugation along its inner surface, which acts to change the dispersion characteristics of the waveguide in order to have a far from cut-off travelling wave with a large change in group velocity over a short frequency change. The helical symmetry allows the frequency regions with zero or negative group velocity of the eigenwave to be avoided, which ensures good RF matching of the compressor with the input source over a sufficiently wide frequency band. The helically corrugated waveguide provides very flexible and controllable wave dispersion, which enables the dispersion to be matched to the output frequency sweep of a microwave source. In addition the large change in group velocity over a small frequency range allows shorter lengths of waveguide to be used which acts to reduce ohmic losses as compared to a conventional circular waveguide.

3.3 Helically corrugated waveguide

A helical corrugation on the inner surface of a circular waveguide can provide selective coupling between a near to cut-off upper mode and a far from cut-off lower mode to produce a wave dispersion with a finite and nearly constant group velocity in the region of near infinite phase velocity. Greater flexibility of a waves dispersion characteristics can be realized. The desired change of the dispersion will be achieved if the corrugation couples two partial rotating waves of a waveguide with a radius of a_0; one partial wave is near-cut-off, mode (A), and has a small axial wavenumber, $k_{z,A} << k$, where $k=\omega/c$, while the other partial wave, a travelling wave (B), has a large axial wavenumber, $k_{z,B} \sim k$. The B wave rotates against the helix and is perturbed in a similar manner to a periodically loaded waveguide creating spatial harmonics of the wave at intervals of $\pm 2n\pi/$ the period of the helix which is defined as $\bar{h}$, while the A wave rotates in the same direction as the helical corrugation and is not significantly perturbed by the structure. In a periodically corrugated waveguide the electromagnetic field can be represented as a superposition of the spatial harmonics, which, at negligibly small corrugation amplitude, possess dispersion characteristics of the smooth waveguide modes (partial modes) shifted along the axial-wavenumber axis by an integer number of the Bragg periodicity vector $\bar{h}$. At non-zero amplitude of the corrugation resonant coupling between the modes occurs when their axial and azimuthal wavenumbers satisfy the Bragg conditions: $k_{z,A} - k_{z,B} = \bar{h}$; $m_A - m_B = \bar{m}$

The helical structure can couple together the 1st spatial harmonic of the B wave and the A wave, Figure 3-2, with cut-off frequencies ω_0 and ω_{0B} respectively. The resonant coupling of the waves corresponds to the intersection of their dispersion curves.

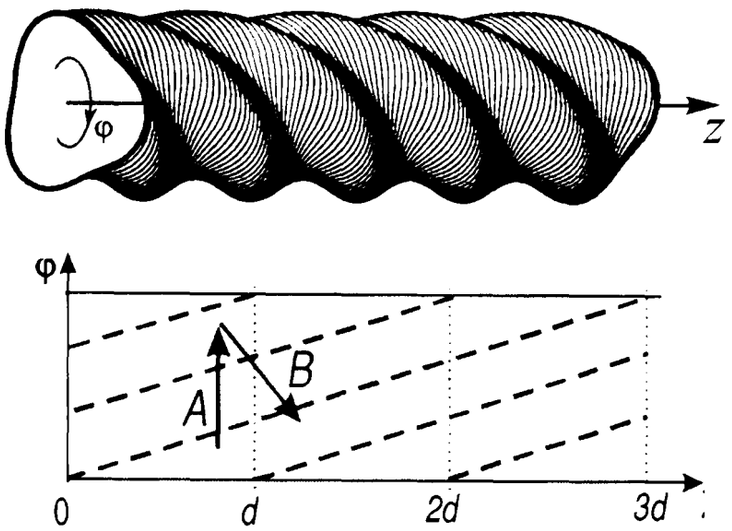

Figure 3-2 Schematic diagram of 3-fold helically corrugated waveguide showing mode propagation along the structure.

3.4 Perturbation theory

An approximation of the dispersion characteristics of a helically corrugated waveguide can be found using perturbation theory. If the corrugation amplitude a_1 is small compared with the wavelength and the waveguide is long enough, the field structure and dispersion characteristics of the helically corrugated waveguide can be calculated by means of the method of perturbation. For the method of perturbation the ratio of corrugation depth to mean radius should be much smaller than 1, $\frac{a_1}{a_0} << 1$.

The surface of the helically grooved waveguide can be represented in cylindrical coordinates r, φ, z as follows:

$$r(\varphi,z) = a_0 + a_1 \cos(\overline{m}\varphi + \overline{h}z), \qquad \textbf{Equation 3-1}$$

where a_0 is the waveguide mean radius, a_1 is the amplitude, and $\overline{m}$ and $\overline{h} = 2\pi/d$, are the azimuthal and axial components of the Bragg periodicity vector respectively, and d is the corrugation period.

The resonant coupling of the waves corresponds to the intersection of their dispersion curves on the dispersion diagram. For the desired dispersion they are mode A, $\vec{E} = \vec{E}_A(r)(C_{A+}e^{-ik_{z,A}z} + C_{A-}e^{ik_{z,A}z})e^{i(\omega t - m_A\varphi)}$ and the first spatial harmonic of

wave B, $\vec{E} = \vec{E}_{B1}(r)C_B e^{-ik_{z,B1}z} e^{i(\omega t + m_B \varphi)}$ where $k_{z,B1} = k_{z,B} - \bar{h}$. For negligibly small corrugation depth these modes satisfy the following unperturbed dispersion equations

$$k^2 - k_0{}^2 - h_A{}^2 = 0$$
$$k^2 - k_{0B}{}^2 - (k_{z,B1}{}^2 + \bar{h})^2 = 0 \qquad \textbf{Equations 3-2}$$

where k_0 and k_{0B} are wavenumbers corresponding to the cut-off frequencies of modes A and B.

If these fields are inserted into the general wave equation for the propagation of electric fields in a waveguide

$$\nabla^2\psi + \omega^2\varepsilon\mu\psi = 0 \qquad \textbf{Equation 3-3}$$

and introduce the corrugation as a small perturbation in the permativity, ε, the eigenwaves W_{u1}, W_{u2} and W_1 which arise as a result of coupling the partial waves can be found. We consider the amplitude of the partial waves, C_A and C_B as functions of the axial coordinate z, which are described by a set of coupled wave linear differential equations consisting of one second order and one first order equation.

$$\frac{\partial C_B}{\partial z} + i\left(k_{z,B} - \bar{h}\right)C_B = \frac{-i}{k_{z,B}}\sigma C_A \qquad \textbf{Equation 3-4}$$

$$\frac{\partial^2 C_A}{\partial z^2} + k_{z,A}{}^2 C_A = 2\sigma C_B \qquad \textbf{Equation 3-5}$$

where $C_A = C_{A+}(z) + C_{A-}(z)$ and σ is the coupling coefficient.[51]

Putting the eigenwaves in the form of $C_B = C_B e^{-ik_z z}$ the dispersion equation is obtained.

$$\left(\frac{\omega}{c^2}^2 - (k_z^- + \bar{h})^2 - \left(\frac{\varsigma'_{11}}{a_0}\right)^2\right)\left(\frac{\omega}{c^2}^2 - k_z^{-2} - \left(\frac{\varsigma'_{21}}{a_0}\right)^2\right) = 4\sigma^2 \qquad \textbf{Equation 3-6}$$

where ς'_{11} and ς'_{21} are the first roots of the differentiated first and second order Bessel functions respectively and ω_0 is the cut-off frequency of the partial wave A and k_z^- is the axial wavenumber of the eigenwave.

When parameters of the corrugation are properly chosen, the wave W_1 has the desirable dispersion. The relative frequency gap between W_1 and "spurious" waves W_{u1} at "zero" axial wavenumber is of the order of the coupling coefficient of the

waves σ, which is proportional to the relative amplitude of the corrugation l/a_0 and depends also on the azimuthal and radial indices of the partial waves.

If the complex axial wavenumbers are used we find

$$(k^2-(k_z^- +\bar{h})^2-\left(\frac{\varsigma'_{11}}{a_0}\right)^2+\varpi_1)\,(k^2-k_z^{-2}-\left(\frac{\varsigma'_{21}}{a_0}\right)^2+\varpi_2)=4\sigma^2 \qquad \textbf{Equation 3-7}$$

This equation has four roots, the forwards propagating W_{u1} wave, the backwards propagating W_{u1} wave, the forward propagating W_1 wave and the fourth root is the backwards propagating W_{-1} wave. Figure 3-3 shows the forwards and backwards W_{u1} waves, the W_1 wave and their second spatial harmonics W_{u2} and W_2, as well as the second and third harmonics of the W_{-1} wave, W_{-2} and W_{-3}, respectively.

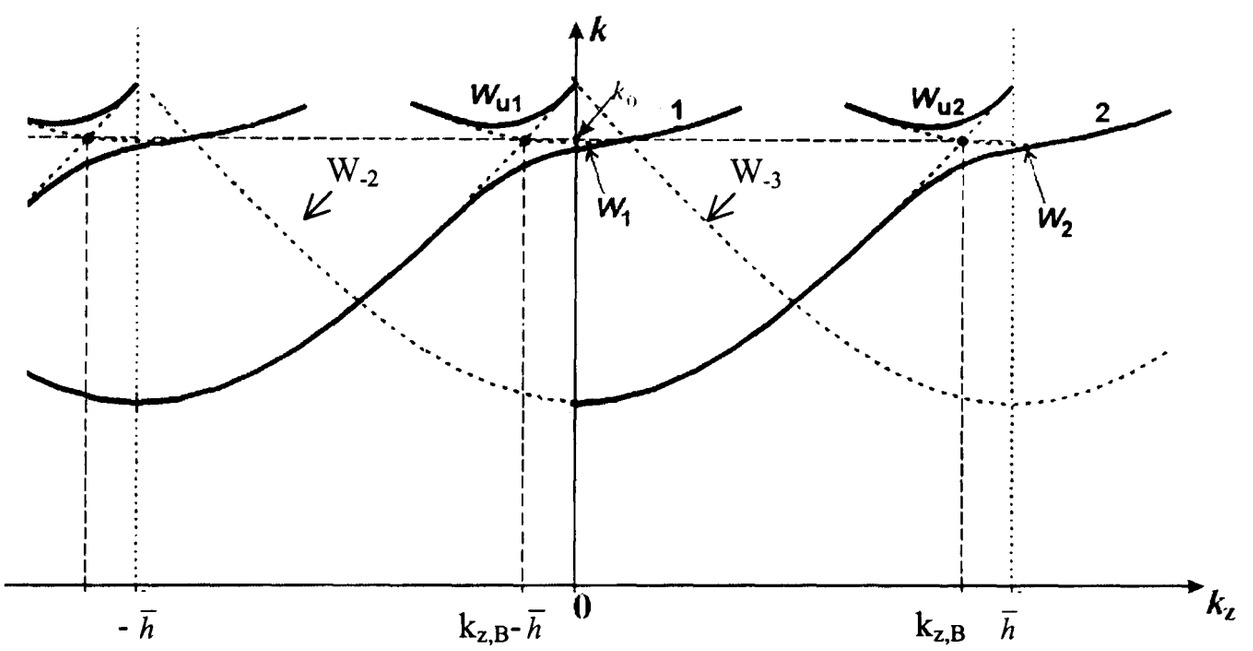

Figure 3-3 Dispersion diagram of a helically corrugated waveguide showing spatial harmonics.

Further analysis will be concentrated on properties of the forward propagating wave W_1 which perturbation theory dispersion $k(k_z)$ or $f(k_z)$ ($f=kc/2\pi$ is the frequency) represents a numerically found selected root of Eq.(4) plotted with sufficiently small interval over the k_z axis. In this case, the eigenwave group velocity shown in the diagrams is numerically derived using the following expression:

$$v_g = c\frac{dk}{dk_z}. \qquad \textbf{Equation 3-8}$$

3.5 Surface currents

If we consider an electromagnetic field in a loop at the boundary between a conductor and free space in the n-τ plane, as shown in Figure 3-4, where n is normal to the conductor surface.

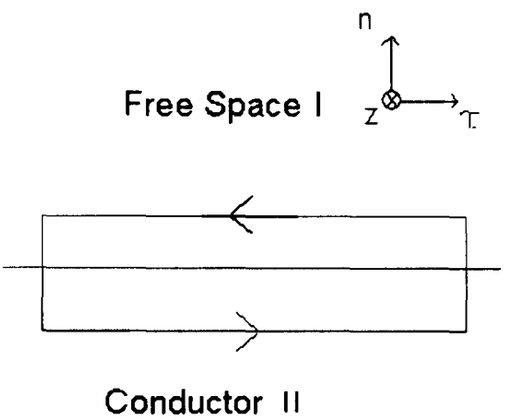

Figure 3-4 Magnetic field loop around a contour at a surface boundary

Taking the integral form of $\nabla \times H = i\omega\varepsilon_0 E + J_f$ and considering the free current density consists of a body current density, J_b, and a surface electric current density, $i^e(\tau,z)$ to obtain.

$$\oint H.dl = \int i\omega\varepsilon_0 E + J_b.dA + \int -i_z^e dl \qquad \textbf{Equation 3-9}$$

as the width of this loop tends towards zero then,

$$\int \left(H_\tau^{II} - H_\tau^{I}\right) d\tau = -\int i_z^e d\tau \qquad \textbf{Equation 3-10}$$

by repeating this for a loop in the n-z plane the equation for the surface electric current is obtained[63]

$$i^e = n \times \left(H^I - H^{II}\right) \qquad \textbf{Equation 3-11}$$

By considering a surface magnetic current due to a tangential electric field, we can show that the surface magnetic current density is given by,

$$i^m = n \times E_\tau \qquad \textbf{Equation 3-12}$$

however as the electric field tangential to the waveguide surface is zero, the surface magnetic current density in a waveguide is zero.

3.6 Coupling coefficient

In order to represent the fields in the helically corrugated waveguide in terms of the modes in a smooth circular waveguide the coupling coefficients of the waves needs to be found. To achieve this the method of fictitious sources can be used to derive the coupling between modal coefficients so that the total field satisfies the boundary conditions at the modified wall surface. In the helix the individual field eigenmode solutions of the unperturbed waveguide will no longer match the boundary conditions of the new system. However these boundary conditions can be enforced provided that additional electric and magnetic currents are assumed to exist in the walls of the new structure to screen the residual tangential Electric and Magnetic fields.

Such electric currents can exist, but are effectively short circuited by the metallic wall. That is, they will flow in the walls of the waveguide to screen the nonzero tangential magnetic fields, but will not excite other modes. However magnetic currents are not physical and are in this sense fictitious. Therefore, equal and opposite magnetic surface currents must be introduced to give a net physical magnetic current of zero, and these currents act as sources to excite other modes.

To calculate the surface magnetic current density we first find an equivalent boundary condition on the surface before the deformation, on the surface S_0, to the boundary condition $E \cdot \tau = 0$ after the deformation, on the surface S. To do so we apply the integral form of Faradays's equation to the boundary ABCD in, Figure 3-5, where n is a unit vector normal to the surface and τ is tangential to the surface.

$$\oint E_\tau dl = -\int \nabla \times E_n \cdot dA - \int i\omega B \cdot dA \qquad \textbf{Equation 3-13}$$

taking into account that the usual boundary condition is valid on S[67].

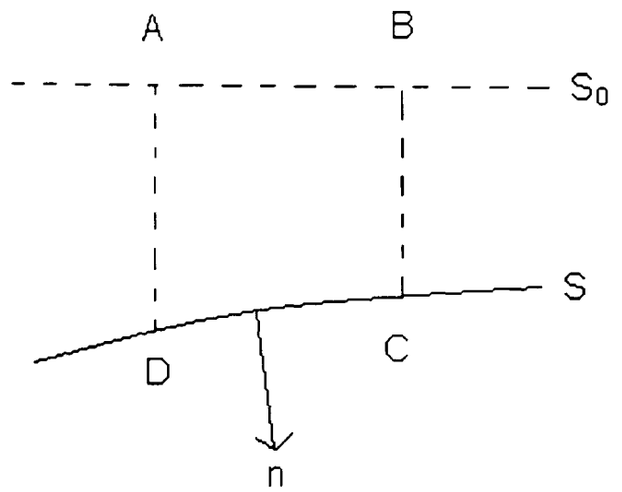

Figure 3-5 The surface boundary in the helically corrugated waveguide.

If the distance between S and S_0 is small and the angle between them is small the equivalent boundary condition on S_0 is given by,

$$E.\tau = \nabla(lE.n).\tau + \tau.i\omega l(n \times B) \qquad \textbf{Equation 3-14}$$

where l is the distance between the corresponding points of S and S_0, and the sign of l is negative[68].

The application of the boundary condition instead of the deformation is in fact the introduction of additional magnetic surface currents into the problem. From the formal point of view, the field perturbation connected with the deformation is caused by those currents[50,69]

$$\frac{\partial C_s}{\partial z} - ik_z C_s = -\frac{1}{N_s}\oint \vec{i}_m \vec{B}_{-s} dl = \frac{i\sigma}{k_{z,s}} C_s \qquad \textbf{Equation 3-15}$$

where the integration is carried out over the contour of the unperturbed waveguide, and

$$N_s = 2\int E_s^0 B_{-s}^0 dA \qquad \textbf{Equation 3-16}$$

are the norms of the interacting waves[70].

Inserting this into Equation 3-15 gives the coupling coefficient, between mode 1 and mode 2.

$$\sigma = \frac{k_{z,1}\omega}{N_1}\oint l_{-p}\left(B_{2,\tau}^0 B_{-1,\tau}^0 + \frac{E_{2,n}^0 E_{-1,n}^0}{c^2}\right)dl \qquad \textbf{Equation 3-17}$$

and solving this gives[50,71]

$$\sigma = \frac{1}{2}\frac{\varsigma'_A{}^2\,\varsigma'_B{}^2 - m_A m_B a_0{}^2\left(k_{tB}{}^2 + \bar{h}.k_{z,B}(f_B)\right)}{\left(\varsigma'_A{}^2 - m_A{}^2\right)^{1/2}\left(\varsigma'_B{}^2 - m_B{}^2\right)^{1/2}}\frac{a_1}{a_0{}^3} \qquad \textbf{Equation 3-18}$$

where f_B is the frequency where the Bragg conditions are satisfied and $k_{z,B}(f_B) = \dfrac{\left(k_{tA}{}^2 - k_{tB}{}^2 + \bar{h}^2\right)}{2\bar{h}}$.

If the condition, $k_{z,B} < \sigma L$, is satisfied then the helically corrugated waveguide can be considered to be of infinite length for the purposes of the method of perturbation, otherwise the theory for finite length waveguides must be used, which shall not be covered in this thesis.

3.7 3-fold helically corrugated compressors

Three such helically corrugated waveguides were developed for use as pulse compressors in the X-band (8.4-12.0GHz). All three were chosen to have a 3-fold helical corrugation (m=-3) with the same period of 28.9mm, resonantly coupling the 1st spatial harmonic of the TE_{11} (m_B=-1) and the near cut-off TE_{21} (m_A=2) partial modes of a corresponding smooth waveguide. The vector diagram of this coupling is shown in Figure 3-6.

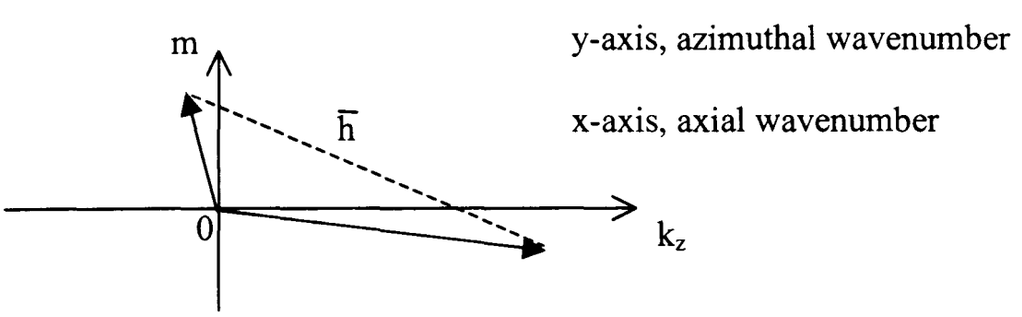

Figure 3-6 Vector diagram of the wave coupling in the helically corrugated waveguides.

Coupling also occurs between the co-rotating TE_{11} mode (m_B=1) and the TE_{41} mode (m_A=4), however as the Bragg conditions are not satisfied near the frequency band of operation, this wave is weakly coupled and the dispersion is not significantly perturbed from that of a TE_{11} mode in a smooth circular waveguide. All the waveguides studied, were chosen to have a right-handed rotation. The waveguides

were designed to have the lowest possible minimum group velocity and a large change in group velocity in the operational bandwidth. The optimum frequency sweep for each helix was also taken into account. It is difficult to synthesize a complex frequency sweep using a microwave source, hence it was important to design a helix that requires an optimum frequency sweep that was as close to linear as possible.

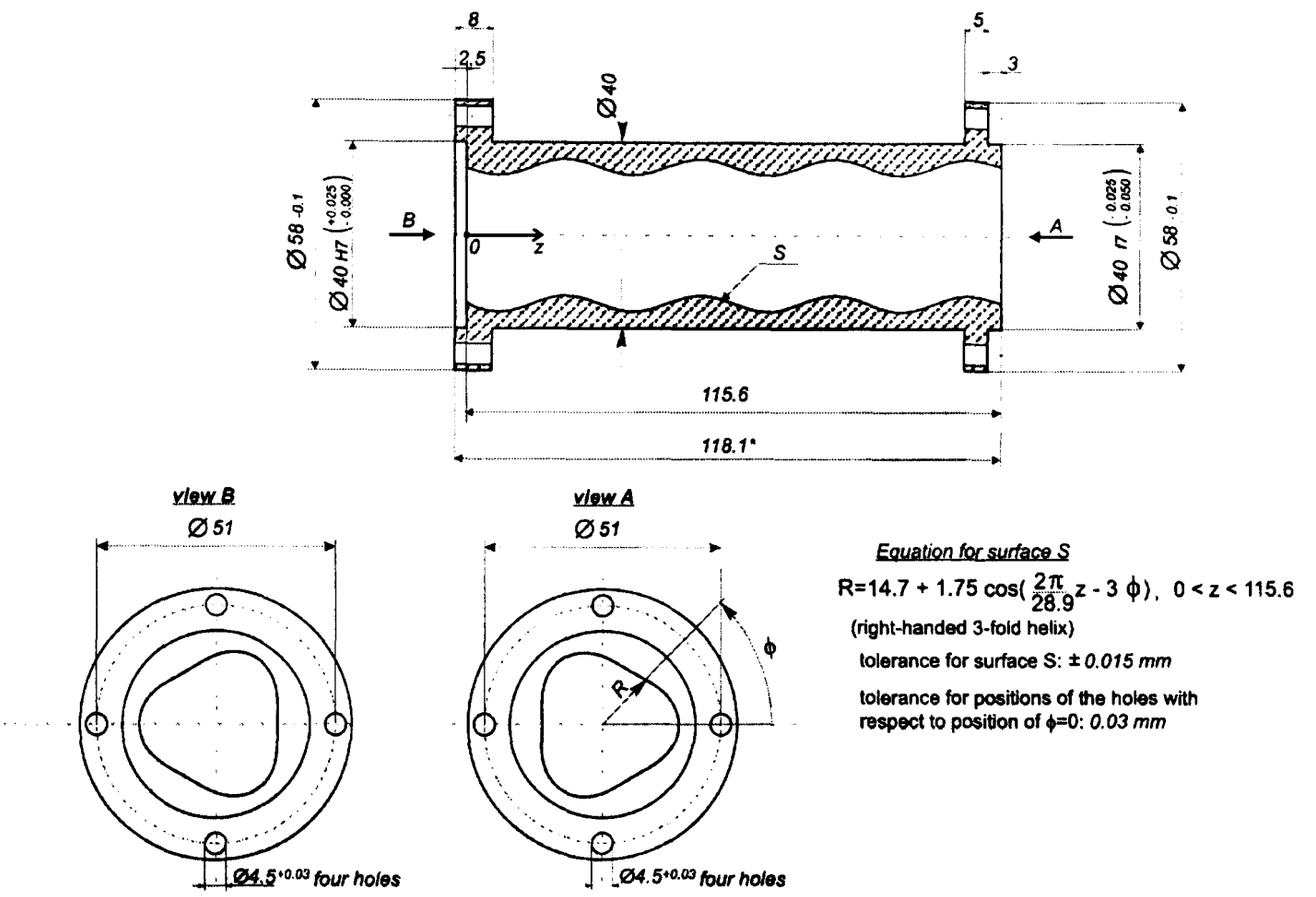

Figure 3-7 Technical drawing of the aluminium helically corrugated waveguide.

The first waveguide, Figure 3-7, herein after known as the aluminium waveguide, had a mean diameter of 29.4mm, a corrugation depth of 1.75mm, and a coupling coefficient of 4212m^{-2}, these parameters gave the desired wave dispersion for an operating frequency range within the band of interest. The method of perturbation was used to calculate the minimum group velocity for the aluminium helix (Figure 3-8).

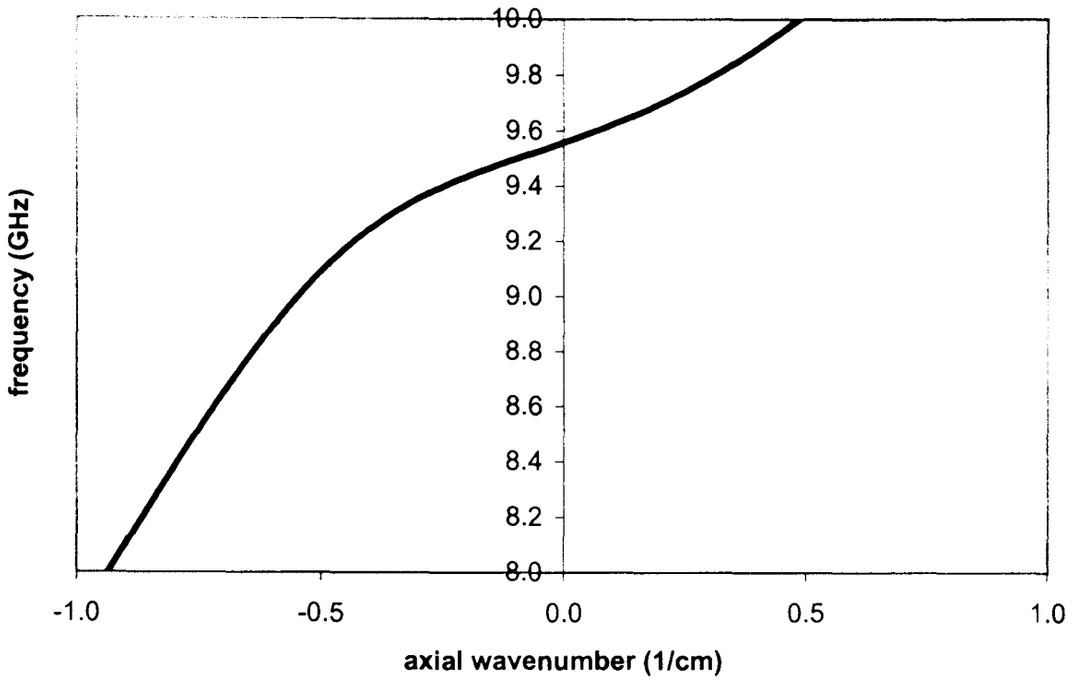

Figure 3-8 Dispersion characteristics of the aluminium helix calculated using the method of perturbations.

The minimum group velocity was found to be 3.78cm/ns at a frequency of 9.53GHz. The cut-off frequency of the W_{u1} eigenwave was calculated to be 10.94GHz, which was well above the maximum frequency of operation for this waveguide, given by the frequency of the wave with the minimum group velocity in X-band. However due to its large corrugation depth there was a discrepancy between the dispersion calculated using the method of perturbation and the experimentally measured dispersion (see Chapter 6). The imaginary part of the axial wavenumber can also be found using the perturbation of Maxwell's equations.

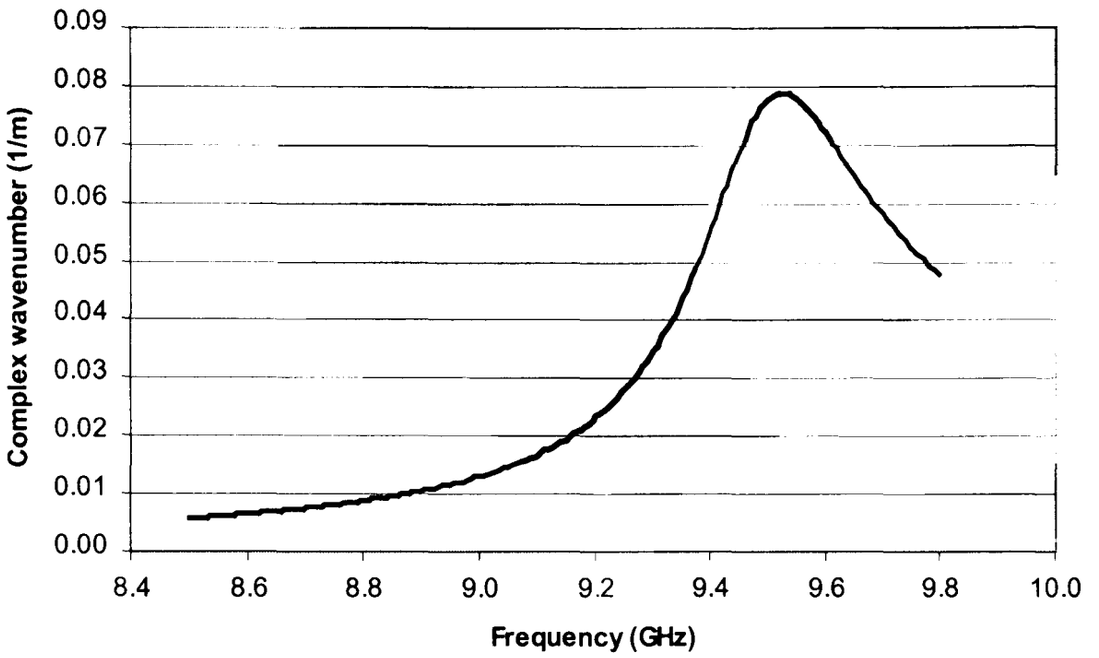

Figure 3-9 The loss coefficient as a function of frequency for the aluminium helically corrugated waveguide, calculated using the method of perturbations.

In Figure 3-9 the complex part of the axial wavenumber is shown. This was calculated using an electrical conductivity of 3.54×10^{7} siemens/metre. The maximum loss coefficient was $0.079m^{-1}$ at a frequency of 9.53GHz.

The second helix was created by boring a circular hole of diameter 27.68mm down the inside of the aluminium helical waveguide, shown in Figure 3-10. This waveguide will be referred to as the modified helix.

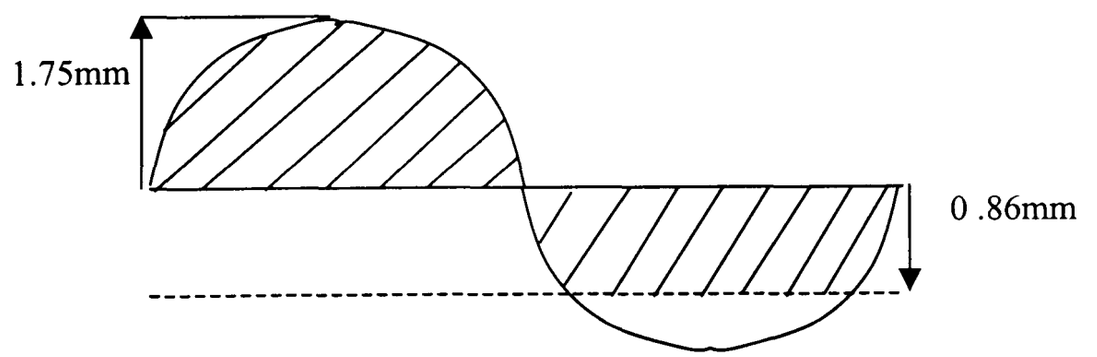

Figure 3-10 Modification to the helically corrugated waveguide to reduce the coupling coefficient

This reduced the corrugation depth, however the mean diameter was increased and the corrugation no longer had a sinusoidal shape, but gave the helix a smaller coupling coefficient of the helix. The new mean radius was calculated to be 14.89mm, and the depth of the corrugation, a_1, was calculated to be 1.4mm using a

Fourier transform taking the corrugation depth to be the amplitude of the first Fourier harmonic. This gave the modified helix a coupling coefficient of $3259m^{-2}$, which was much smaller than the aluminium waveguide. The method of perturbation, (Figure 3-11), calculated the minimum group velocity of the modified helix as 2.1cm/ns at 9.53GHz. As the coupling coefficient was smaller than for the unmodified aluminium helix the W_{u1} eigenwave had a lower cut-off frequency, which was calculated to be 10.66GHz. This frequency was still much higher than the frequency of the wave with the minimum group velocity.

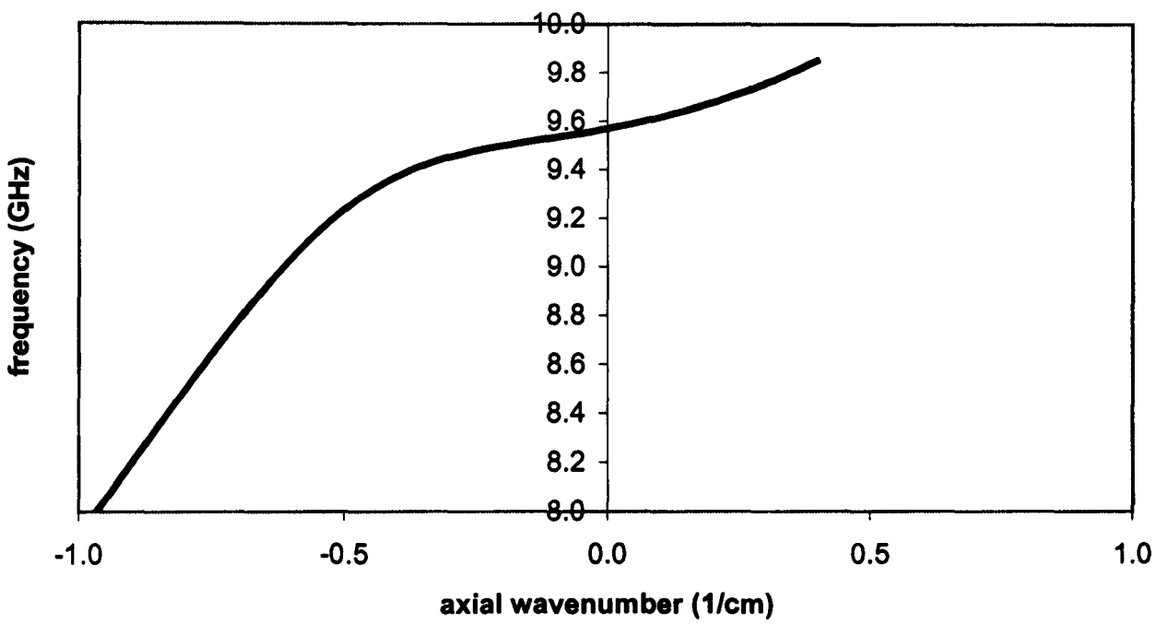

Figure 3-11 Dispersion characteristics of the modified helix calculated using the method of perturbations.

The imaginary part of the axial wavenumber as a function of frequency was calculated using a electrical conductivity of 3.54×10^{7} siemens/meter, shown in Figure 3-12. The maximum value of the loss coefficient occurred at 9.53GHz, and had a value of $0.139m^{-1}$.

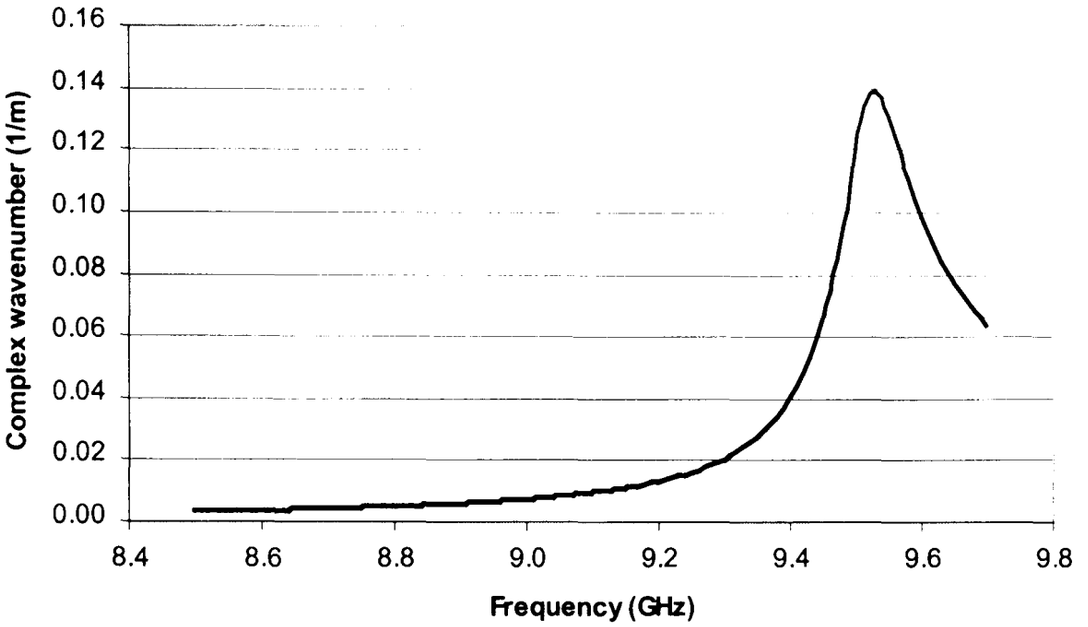

Figure 3-12 The loss coefficient as a function of frequency for the modified helically corrugated waveguide, calculated using the method of perturbations.

The third helix, known as the copper helix, was designed to have the same mean radius (14.7mm) as the aluminium helix but with a smaller corrugation depth (1.4mm). This helix had a normalised coupling coefficient which was similar to the modified aluminium compressor of 3370m^{-2}. The method of perturbations was used to calculate its dispersion characteristics, as shown in Figure 3-13.

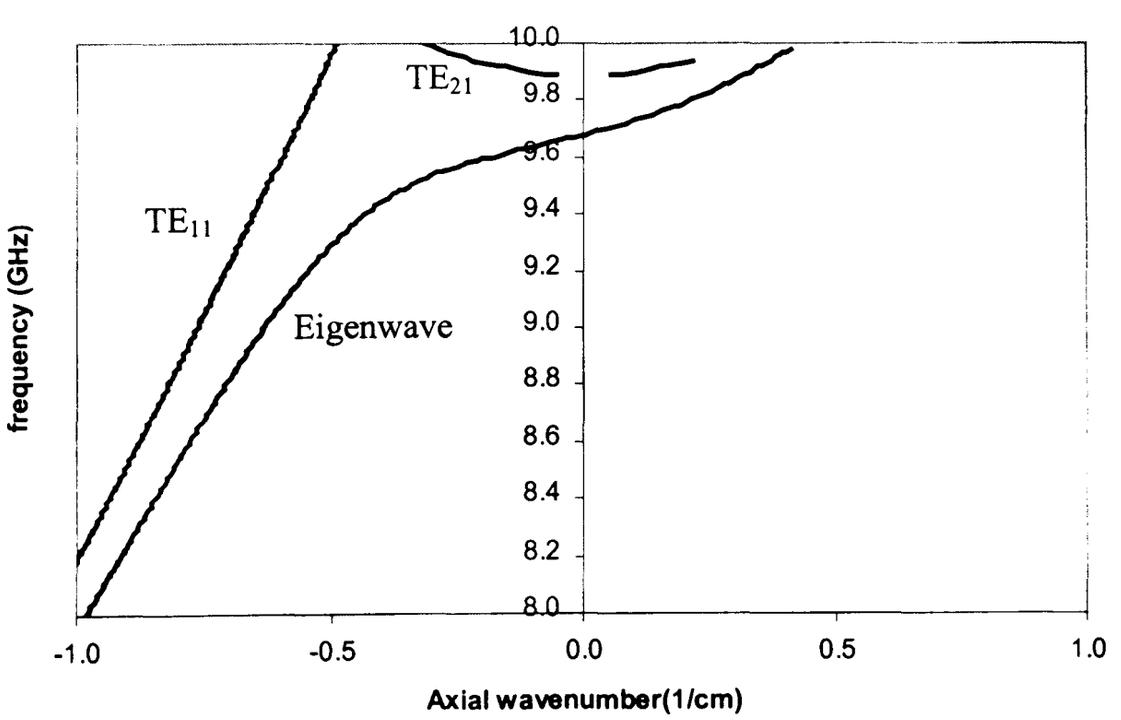

Figure 3-13 Dispersion characteristics of the copper helix calculated using the method of perturbations.

The cut-off frequency of the W_{u1} eigenwave was calculated to be 10.78GHz. This gave the helix a minimum group velocity of 2.49cm/ns at 9.64GHz. as shown in Figure 3-15.

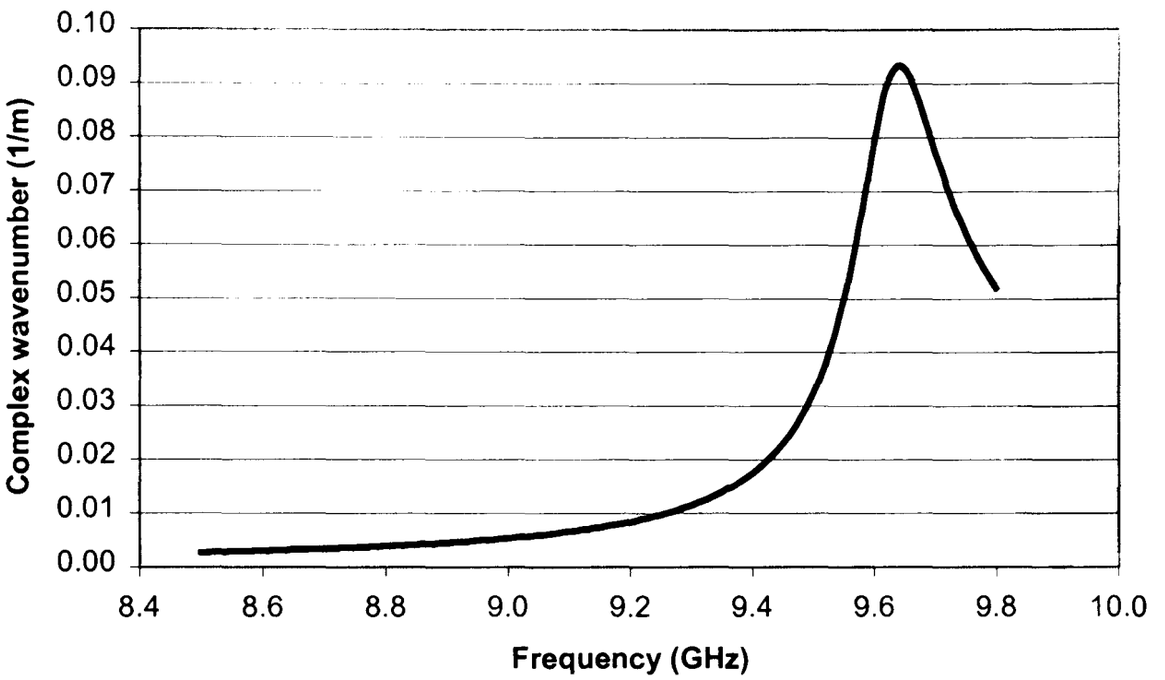

Figure 3-14 The imaginary part of the axial wavenumber as a function of frequency for the copper helically corrugated waveguide, calculated using the method of perturbations.

The maximum value of the loss coefficient, α, was found to be $0.0934m^{-1}$ at 9.64GHz, calculated using a conductivity of 5.8×10^{7} siemens/metre (Figure 3-14). As the compression of the microwave pulse is determined by the group velocity of the wave, more insight can be achieved by looking at the group velocity dispersion (GVD) of the helically corrugated waveguides, as shown in Figure 3-15.

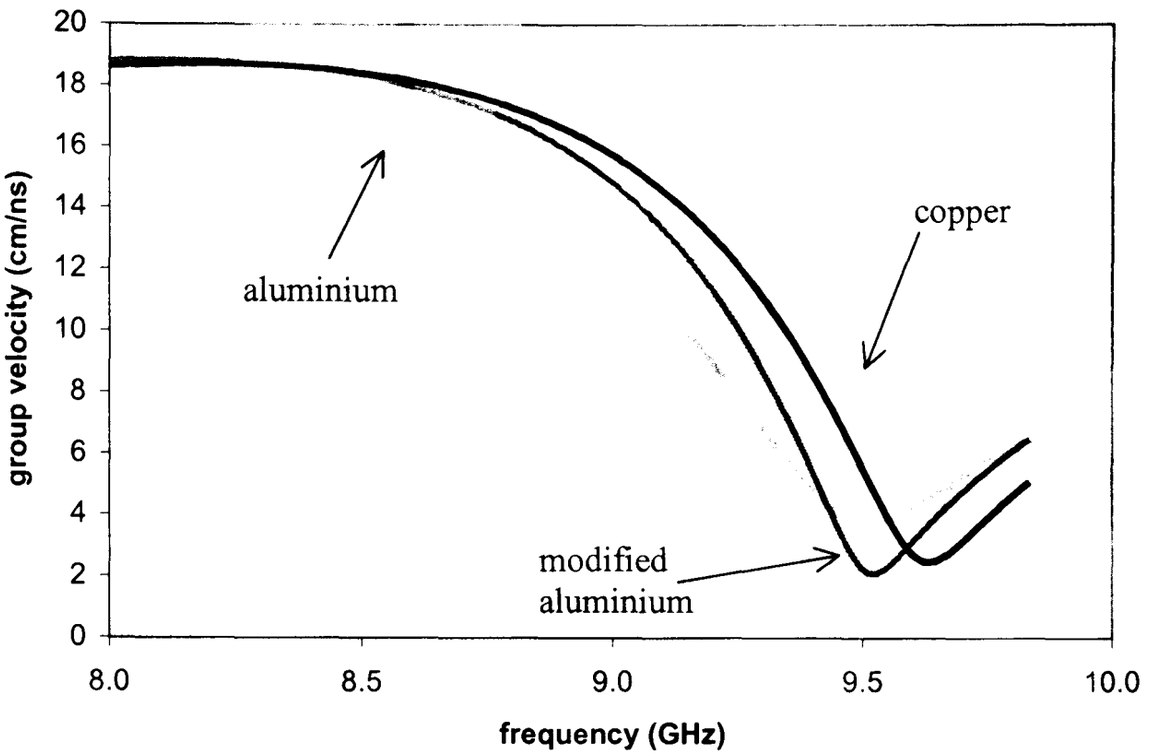

Figure 3-15 Group velocity dispersion curve of all three helices calculated using the method of perturbations

The method of perturbations predicted that the modified aluminium helix would provide the best group velocity dispersion for a pulse compressor, however the method of perturbation for this helix was only an approximation due to its complicated shape. The copper helix was found to have the better dispersion characteristics of the two sinusoidal helical corrugations.

3.8 Helical tapers

In order to convert the $TE_{-1,1}$ wave into the eigenmode W_1 tapered sections, which changed the compressor cross-section from circular to helical, were designed and constructed. Each of these tapers had a linear increase in the corrugation amplitude over 4 periods so that they had circular cross-section at one end and a helical cross-section at the other. Left-handed TE_{11} waves (designated as k_z^-) were transformed completely into the W_1 eigenmode whereas right-handed $TE_{1,1}$ remained practically unperturbed ($k_z^+ \approx k_{zTE1,1}$). These tapers also provided an impedance match between the circular section and the corrugated waveguide to reduce reflections.

A pair of helical tapers were made using a CNC lathe with the corrugation parameters of the aluminium helical compressor at one end which was tapered to a smooth circular waveguide of diameter 1.47cm at the opposite end. These tapers were used for experiments involving the unmodified aluminium helix. For the modified aluminium and copper helically corrugated waveguide experiments a 13.84mm radius hole was bored down the centre of each taper, the cross section at each end of the helical taper is shown in Figure 3-16. Although this resulted in a variation in the average radius along the length of the tapered section, the modification resulted in improved matching to the modified aluminium and copper helix.

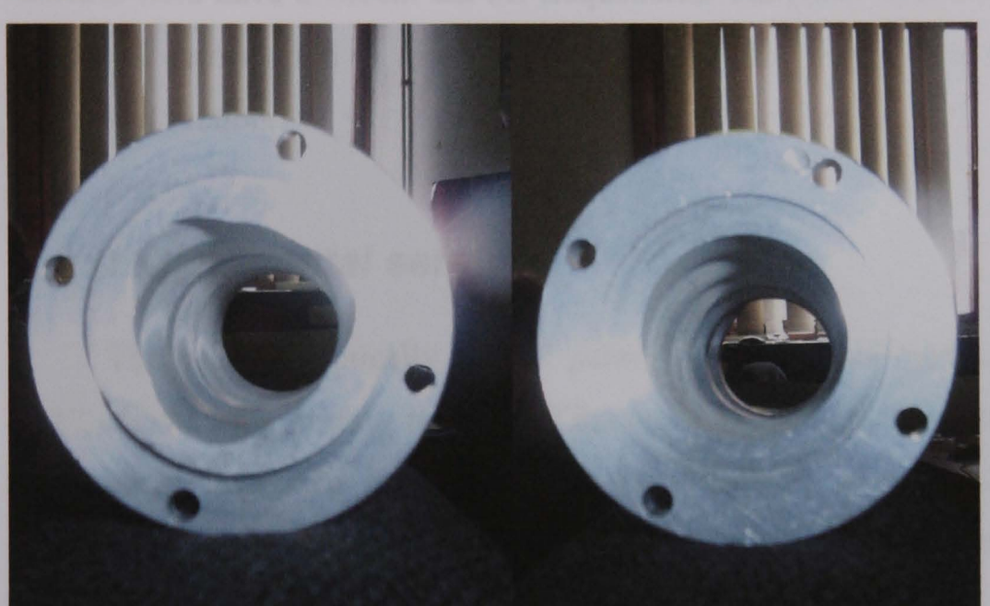

Figure 3-16 The cross-section at either end of the modified aluminium helical taper, the helical cross section is shown on the left and the circular cross-section is shown on the right.

3.9 Elliptically deformed waveguide polariser

In order to ensure that the entire wave was in the operating eigenmode a polariser was used to circularly polarise the wave before it entered the helically corrugated waveguide. To polarise the wave an elliptically deformed section of waveguide was inserted before the helix.

A wave is right-circularly polarized if the transverse electric field component can be presented as

$$E_{right} = \mathrm{E}_0(\vec{e}_y \cos(k_{z1}z - \omega t) - \vec{e}_x \sin(k_{z2}z - \omega t)) \qquad \textbf{Equation 3-19}$$

and left-circularly polarized if

$$E_{left} = \mathrm{E}_0(\vec{e}_y \cos(k_{z1}z - \omega t) + \vec{e}_x \sin(k_{z2}z - \omega t)) \qquad \textbf{Equation 3-20}$$

where E_0 is the electric field amplitude and $\vec{e}_y$ and $\vec{e}_x$ are unit vectors.

The general form for the linear polarized wave can be represented by

$$E_{lin} = E_0(\vec{e}_x \pm \vec{e}_y)\cos(k_z z - \omega t) \text{ or } E_{lin} = E_0(\vec{e}_x \pm \vec{e}_y)\sin(k_z z - \omega t) \qquad \textbf{Equation 3-21}$$

Therefore to circularly polarise the wave the electric field in either the x or y plane must be shifted in phase by $\pi/2$. In the circular waveguide modes $k_{z1}=k_{z2}$, however, in the elliptical waveguide $k_{z1}\neq k_{z2}$ and the eigenmodes with the x and y component of electric field have different cut-off frequencies. The phase difference created by the elliptical deformation is given by, $\varphi = \int(k_{z1}-k_{z2})dL$, where L is the length of the deformed section.

3.10 Experimental set-up

The use of elliptically shaped polarisers and helical tapers, shown in Figure 3-17, allowed the linearly polarised TE_{11} wave of a smooth circular waveguide to be completely converted into the operating eigenwave of the helically corrugated waveguide at the compressor input, and converted back to a linearly polarised TE_{11} wave at the output.

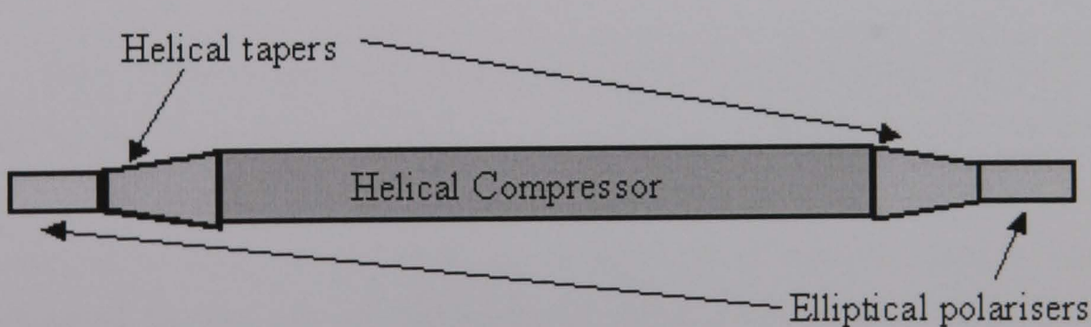

Figure 3-17 Experimental set-up of the helically corrugated waveguide including elliptically shaped polarisers and helical tapers.

The elliptically shaped polarisers were connected to a smooth circular waveguide and converted the linearly polarised wave to a circularly polarised wave. The polarisers were connected to the helical tapers, which provided good matching to the helical compressor, and reduced reflections. At the output of the helically

corrugated waveguide the tapers converted the eigenwave of the helix back to the circularly polarised TE_{11} wave of the smooth circular waveguide. The taper was then connected to the elliptical shaped polariser to convert the circular polarisation into a linear polarisation.

4 Numerical simulations

4.1 Introduction

As was mentioned in section 3.4 the method of perturbation can only be used if the corrugation amplitude a_1 is small compared with the wavelength. If the helical corrugation has deep grooves another method must be used to calculate the dispersive characteristics of the helical waveguide. One method of calculating the dispersion curve of a helically corrugated waveguide is to use a numerical Particle-in-cell (PIC) code.

In Section 4.2 the PIC code used is introduced and in Section 4.3 a method for calculating the dispersion curves of the helically corrugated waveguide using a PIC code is presented. This method was based on the fact that the dispersion characteristics of a circularly polarised TE_{11} mode propagating in a helical waveguide strongly depends on its direction of polarisation. In Section 4.4 a 2^{nd} method was proposed in which a spatial Fourier transform of a wave with a defined frequency was used to find the axial wavenumber associated with that frequency.

4.2 Particle in Cell code's

For a relatively small corrugation depth, when the corrugation depth $a_1 << a_0$ it was found that the method of perturbation provides good agreement with microwave measurements (see Chapter 6). For larger corrugation depths a discrepancy arises between perturbation theory and experimental measurements, which can be circumvented by the use of Particle-in-cell (PIC) code modelling. To find the dispersion for larger corrugation depths the propagation of a TE_{11} wave propagating through the helical waveguide was simulated using the PIC code MAGIC. The electric fields were calculated as they evolve in time and space from some defined initial configuration using a finite-difference method. Time and 3-D space were divided into a finite grid and from some known initial state, time was advanced by adding a single time step. At each new value of time, Maxwell's equations were

solved throughout space to advance the electromagnetic fields in time. The continuity equation was solved to map charge and current densities onto the grid, which were then used as sources for Maxwell's equations on the next time step.

4.3 MAGIC

The PIC code MAGIC[72] was used to find the dispersion characteristics of all three helically corrugated waveguides. MAGIC is an electromagnetic particle-in-cell code, i.e., a finite-difference, time-domain code for simulating processes that involve space-charge and electromagnetic fields. The full set of Maxwell's time-dependant equations are solved to obtain electromagnetic fields.

The dispersion characteristics of a helically corrugated waveguide can be found from the angle of rotation caused by the helix similar to the experimental approach described by Denisov[51], which henceforth will be labelled as the SNA MAGIC simulations. Classically, a linearly polarized wave in an axis-symmetrical waveguide can be synthesized by the coherent superposition of equal amounts of left and right circularly polarized waves. For a linearly polarized wave the orientation of its electric field is constant, although its magnitude and sign vary in time. The electric field therefore resides in what is known as the plane of vibration.

Because the dispersion characteristics of the left and right circularly polarized TE_{11} wave in the helical waveguide strongly depends on the direction of polarization i.e. where the circularly component rotating against the helix is perturbed this allowed dispersion measurements of the helical structure to be carried out. Inside the helical waveguide a wave co-rotating with the helix is weakly coupled and its dispersion is close to that of a normal smooth circular waveguide and can be used as a reference wave, while a wave counter rotating against the corrugation will be coupled to a co-rotating mode similar to the TE_{21} mode of a circular waveguide, and will propagate in the operating eigenmode of the helix. This causes the rotating wave to have different axial wavenumbers and causes the wave to rotate along the inside of the helix with axial wavenumber equal to half the difference in axial wavenumber between the oppositely rotating waves, Δk_z, as can be seen below. When the wave exits into the circular waveguide the eigenmode will convert to the fundamental

mode of the cylindrical waveguide counter-rotating with respect to the helix. Hence, the output radiation from the helix will become linearly polarised at an angle, $\Delta\theta=\Delta k_z L$, to its input polarisation due to its rotation inside the helix.

E_{in} is the electric field at the input to the helix and is linearly polarised along the y-axis and made up of equal amounts of oppositely circularly polarised waves.

$$E_{in} = \left(\vec{i}\frac{E}{2}\sin(kz+\omega t)+\vec{j}\frac{E}{2}\cos(kz+\omega t)\right)+\left(-\vec{i}\frac{E}{2}\sin(kz+\omega t)+\vec{j}\frac{E}{2}\cos(kz+\omega t)\right)$$

Equation 4-1

At the output of the waveguide the wave that is counter-rotating with respect to the helix is perturbed and is ϕ radians out of phase. This causes the output wave to have its linear polarisation to be rotated.

$$\begin{aligned} E_{out} &= \vec{i}\frac{E}{2}\sin(kz+\omega t)+\vec{j}\frac{E}{2}\cos(kz+\omega t) \\ &-\vec{i}\frac{E}{2}[\sin(kz+\omega t)\cos(\phi)+\cos(kz+\omega t)\sin(\phi)] \\ &+\vec{j}\frac{E}{2}[\cos(kz+\omega t)\cos(\phi)-\sin(kz+\omega t)\sin(\phi)] \end{aligned}$$

Equation 4-2

When the phase shift of the eigenwave is equal to π radians the output wave has its polarisation rotated by $\pi/2$ radians.

$$E_{out} = \vec{i}E\sin(kz+\omega t)$$

Equation 4-3

The plane of vibration of the linearly polarised input wave at the output is perpendicular to the input plane of vibration.

When the phase shift of the eigenwave is equal to 2π radians the plane of vibration of the linearly polarised input wave at the output is parallel to the input plane of vibration.

$$E_{out} = \vec{j}E\cos(kz+\omega t)$$

Equation 4-4

The change in phase of the linearly polarised wave caused by the helically corrugated waveguide is the angle of rotation in radians plus $2\pi n$, where n is the number of full rotations of the wave in the helix. Hence by measuring the angle of rotation of a linearly polarised wave propagated through a helically corrugated waveguide the dispersive characteristics of the eigenwave can be found.

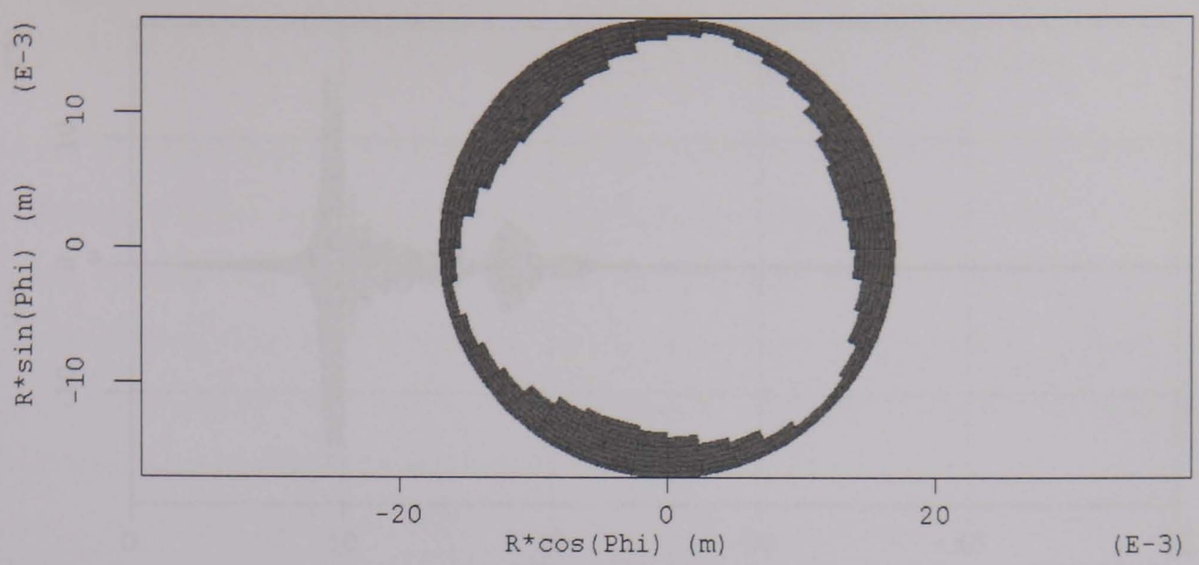

Figure 4-1 Cross section of the copper helically corrugated waveguide from MAGIC.

A simulation of a linearly polarised TE_{11} wave with a wide bandwidth in the region of interest propagating in the helix was run using MAGIC. In order to obtain the correct time profile for the pulse, an inverse Fourier transform was performed on a square spectral profile from 8 to 10GHz. In the simulation the wave was injected into a circular waveguide, where the mode structure and phase velocity was well known. In order to find the rotation of the wave in the helix the radial electric field along lines, parallel and perpendicular to the input polarisation in the circular section at the output of the helix (Figure 4-2) was measured. A fast Fourier transform was performed on the electric field as it varied with time along each of these lines, shown in Figure 4-3. In order to simplify the modelling of the helical waveguide surface, a cylindrical coordinate system was used in MAGIC. This excluded from the analysis the electromagnetic fields on the z-axis (r=0), and therefore a temporal Fourier transform of the radial electric field at a position slightly shifted from the axis was used as an equivalent to the SNA frequency scan (Figure 4-3) which was then processed in the same way to obtain the dispersion diagram.

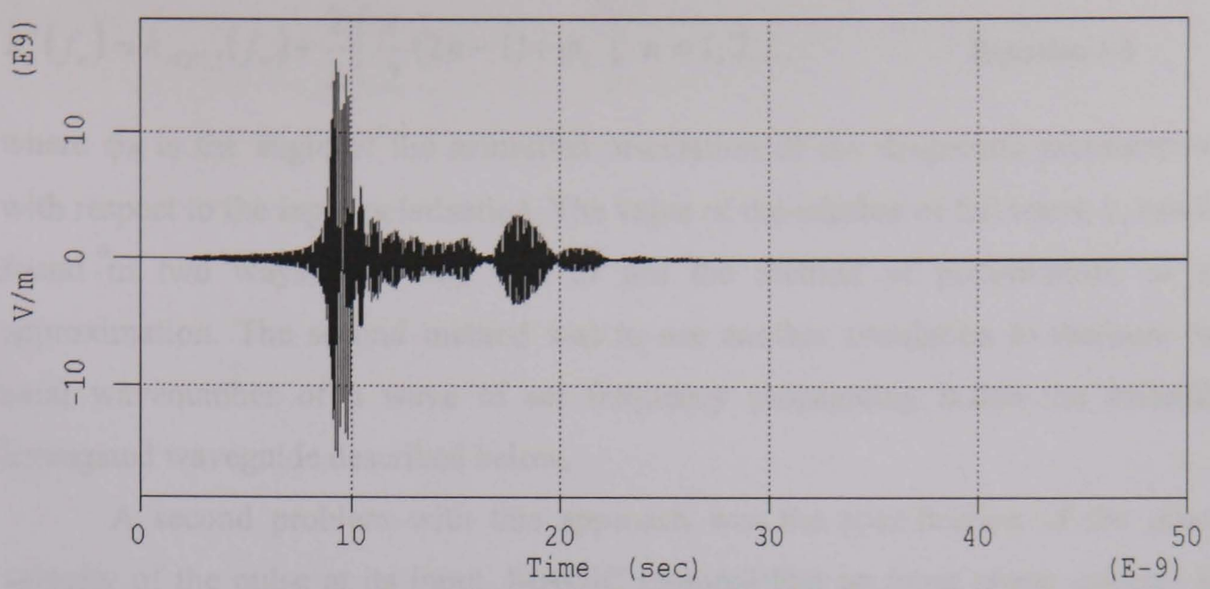

Figure 4-2 Radial electric field at the output of the copper helix, measured parallel to the input polarisation in MAGIC.

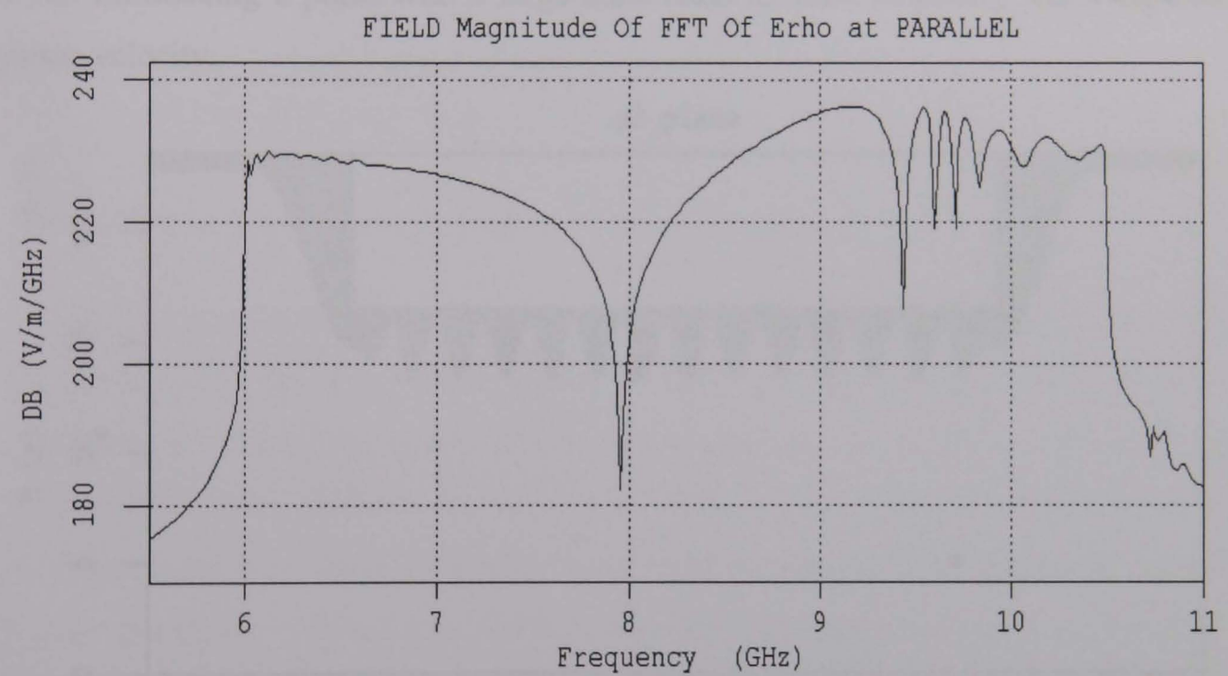

Figure 4-3 Fourier transform of the radial electric field at the output of the copper helix, measured parallel to the input polarisation from MAGIC.

The frequencies that coincide with minima on the FFT correspond to a wave polarisation perpendicular to the measurement polarisation at the output of the helix due to Malus's law[61]. The angle of rotation can be calculated from the minima as the angle of rotation is an increasing function of frequency. The frequencies of the minima, f_n, sharply indicated on a logarithmically scaled MAGIC plot were accurately measured and the points for the dispersion diagram were calculated as follows:

$$k_z^-(f_n) = k_{zTE1,1}(f_n) + \frac{2}{L}\left(\frac{\pi}{2}(2n-1) + \varphi_R\right);\ n = 1, 2, \ldots \qquad \textbf{Equation 4-5}$$

where φ_R is the angle of the azimuthal orientation of the diagnostic measurement with respect to the input polarisation. The value of the number of full turns, n, can be found in two ways, one way was to use the method of perturbations as an approximation. The second method was to use another simulation to measure the axial wavenumber of a wave of set frequency propagating inside the helically corrugated waveguide described below.

A second problem with this approach was the specification of the phase velocity of the pulse at its input. MAGIC required that an input phase velocity be specified in the code to impedance match the waveguide. This caused a problem when introducing a pulse with a large bandwidth as each frequency has a separate phase velocity.

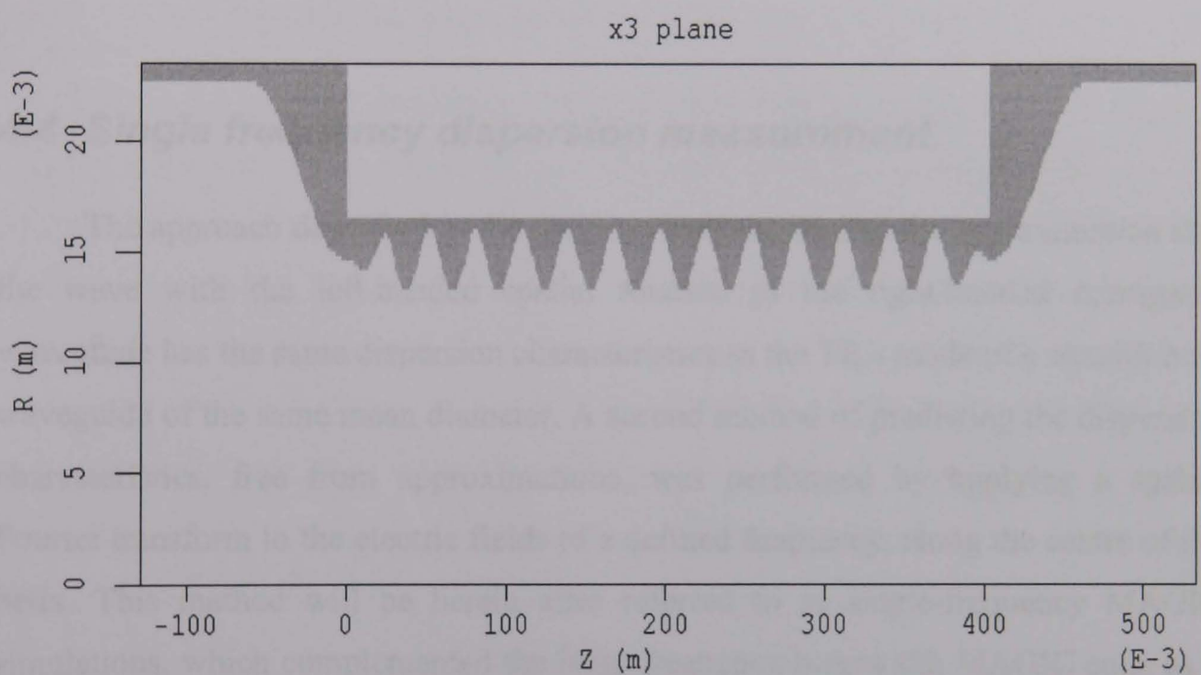

Figure 4-4 Geometry used in the simulation for the measurement of dispersion in the SNA MAGIC simulation for the copper helically corrugated waveguide.

To avoid this problem a large diameter circular waveguide was simulated at the input and output so that the wave propagated far from cut-off, as shown in Figure 4-4. When operating far from cut-off the phase velocity becomes approximately constant with a phase velocity equal to the speed of light, c.

The circular section was slowly tapered to the cross-section of the helix (Figure 4-1), using helical tapers with a linear increase in the corrugation depth along

their length, to reduce reflections at the entrance port, and the helix was slowly tapered back to a smooth circular waveguide at the output.

The tapered sections introduce additional rotation to the wave. To compensate for this half the length of the tapers was added to the length of the helix (this is shown to be accurate in Chapter 6).

The dimensions of the MAGIC cells required to ensure good agreement with results of the measurements were as follows: $dr=a_1/7$, $d\varphi= 8°$, $dz=d/30$ A further decrease in all cell dimensions by a factor of 1.5 resulted in a very small shift (less than 0.35%) of frequencies of the minima, which proved the numerical simulations had good convergence and reliability. An advantage of this method was that one MAGIC run allowed a wide frequency region to be instantly analysed but in this case it was difficult to extract information about the electromagnetic field distribution over the volume (selected plane or line) at a defined frequency.

4.4 Single frequency dispersion measurement

The approach described in the previous section requires the approximation that the wave with the left-handed spatial rotation in the right-handed corrugated waveguide has the same dispersion characteristics as the TE_{11} mode of a smooth bore waveguide of the same mean diameter. A second method of predicting the dispersion characteristics, free from approximations, was performed by applying a spatial Fourier transform to the electric fields of a defined frequency, along the centre of the helix. This method will be herein after referred to as single-frequency MAGIC simulations, which complemented the large frequency bandwidth MAGIC code as it would be used to find the axial wavenumber of a given frequency in the helix within a small range, due to the finite length of the helix. To obtain the axial wavenumber corresponding to a wave of set frequency propagating through the helix in the operating eigenmode, a circularly polarised wave was used.

In the simulation a TE_{11} wave was circularly polarised using an elliptically shaped polariser and was propagated through the helically corrugated waveguide rotating against the helical corrugation in order to excite the operating eigenwave.

The helix was tapered to a circular section at both ends using the helical tapers (Figure 4-5).

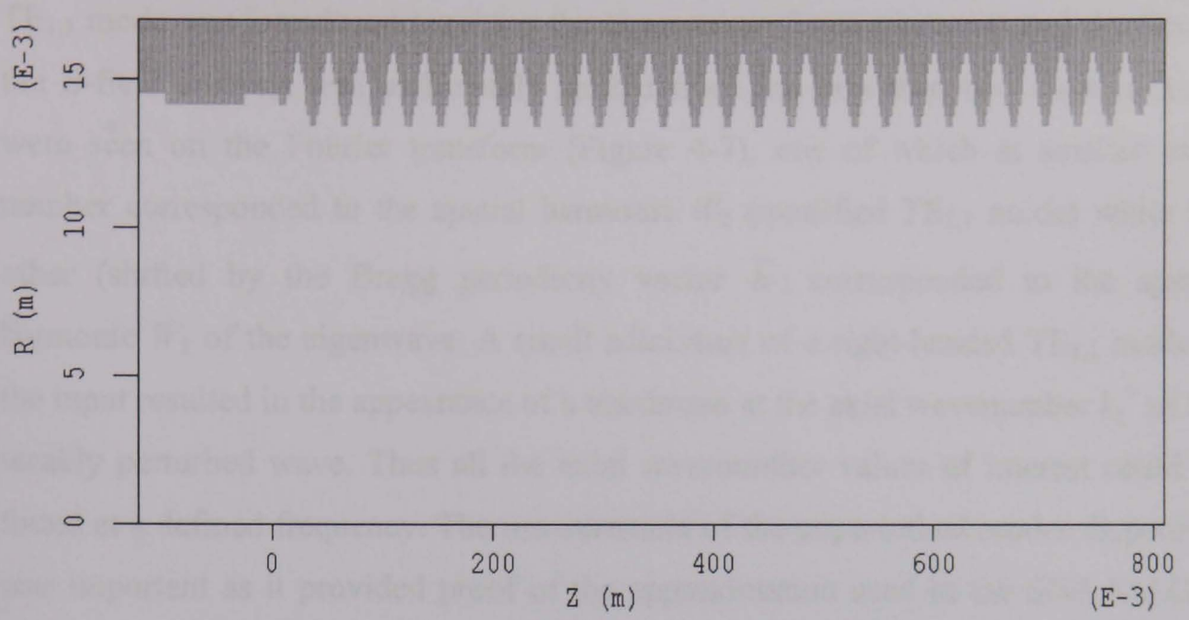

Figure 4-5 Cross section of the copper helical waveguide used in the single frequency MAGIC simulation.

The electric field was measured in one plane along the helix. Measuring the radial electric field along a line that was off centre allowed the axial variation along one polarisation to be measured. The radial electric field was only measured inside the helically corrugated waveguide, as shown in Figure 4-6, to ensure that the tapers did not produce any uncertainty in the measurement.

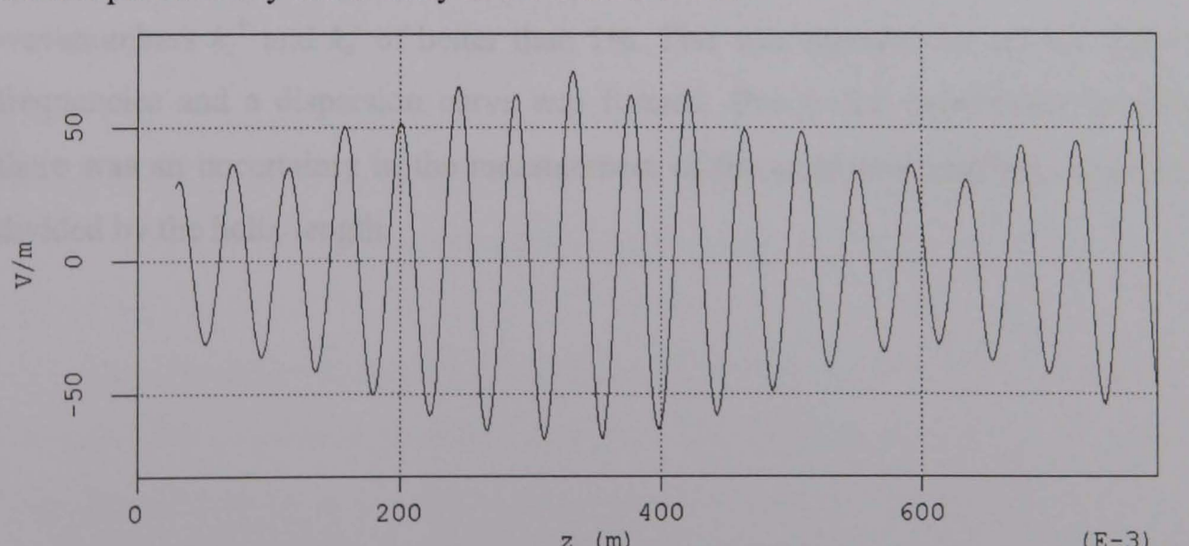

Figure 4-6 Axial variation of radial electric field inside the copper helical waveguide simulated in MAGIC.

After a sufficiently long time to ensure that the electromagnetic field was established over all the structure a snap shot of the radial electric field distribution

along a line parallel to the z-axis was taken and its spatial Fourier transform for a region with constant amplitude of the corrugation was performed. If a left-handed $TE_{1,1}$ mode was introduced (exciting the eigenwave of main interest) and the line of the E-field analysis was sufficiently shifted from the axis then two clear maxima were seen on the Fourier transform (Figure 4-7), one of which at smaller axial number corresponded to the spatial harmonic W_2 (modified $TE_{2,1}$ mode) while the other (shifted by the Bragg periodicity vector $\bar{h}$) corresponded to the spatial harmonic W_1 of the eigenwave. A small admixture of a right-handed $TE_{1,1}$ mode at the input resulted in the appearance of a maximum at the axial wavenumber k_z^+ of the weakly perturbed wave. Thus all the axial wavenumber values of interest could be found at a defined frequency. The measurement of the unperturbed modes dispersion was important as it provided proof of the approximation used in the SNA MAGIC simulation that the unperturbed mode had the same dispersion characteristics as a TE_{11} mode in a smooth circular waveguide of the same mean radius. In addition, important information about the field magnitudes and its distribution was obtained using this method. The accuracy of these simulations for determining the axial wavenumbers improved with increasing length of the helical structure. In the single-frequency MAGIC simulations performed, structures with an operating length of more than 30 periods were analysed, which ensured a relative accuracy for the axial wavenumbers k_z^+ and k_z^- of better than 1%. This was repeated for several different frequencies and a dispersion curve was formed. Due to the fast Fourier transform there was an uncertainty in the measurement of the axial wavenumber, equal to 2π divided by the helix length.

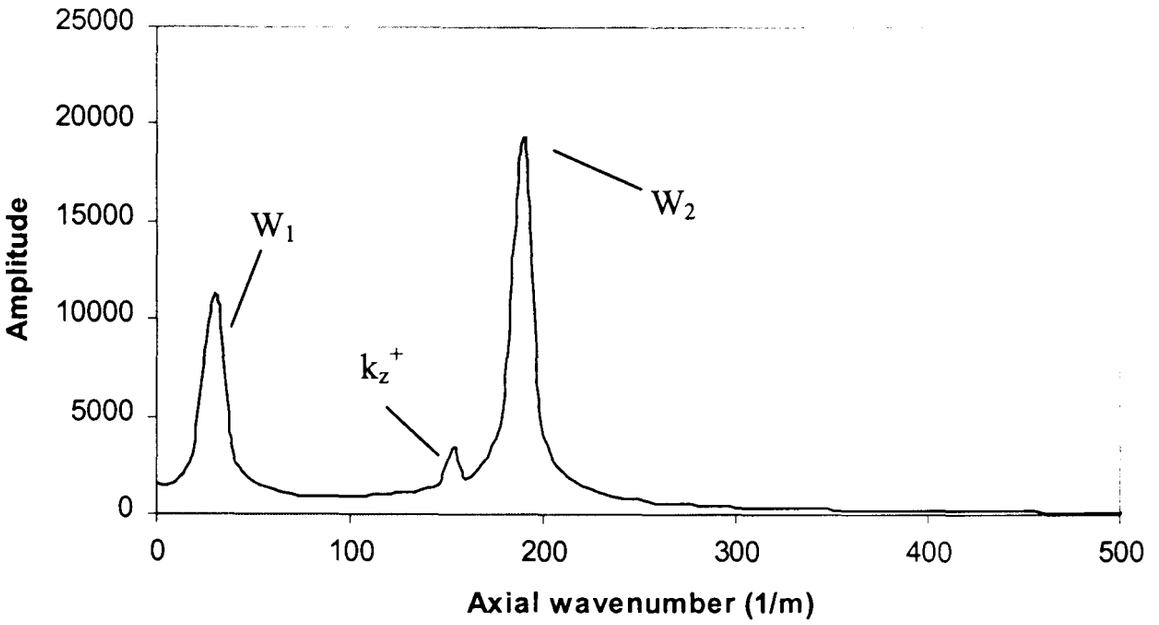

Figure 4-7 FFT of the axial variation of the radial electric field in the copper helical waveguide simulated in MAGIC.

The frequency used was chosen to correspond to one of the points given in the previous simulation so that the axial wavenumber of that frequency could be found within a small uncertainty. This allowed the number of full rotations caused by the helix in the previous simulation to be ascertained by matching the values for the axial wavenumber and was more accurate than the previous method as the phase velocity of the wave was single valued in the smooth circular waveguide.

A 184.96cm length of aluminium helix bounded by two 11.56cm aluminium tapers, was simulated using the SNA MAGIC technique. A length of 104.04cm was simulated using the single-frequency MAGIC technique for all 3 helix each with two 2.89cm long tapers with the same parameters as used in the regular helical section (Figure 4-8).

The dispersion calculated using the method of perturbation was compared to the numerical simulation by finding the frequencies where the axial wavenumbers were the same as those obtained using the numerical SNA simulation. To find the average standard deviation of the results for each helix, the standard deviation was found as a percentage for each pair of frequencies (theoretical and numerical simulation), and the mean standard deviation for each helically corrugated waveguide was calculated. However because the standard deviation was so small it was more illuminating to find the mean standard deviation of the group velocity. To

do so the group velocity for both methods at discrete frequency values was calculated.

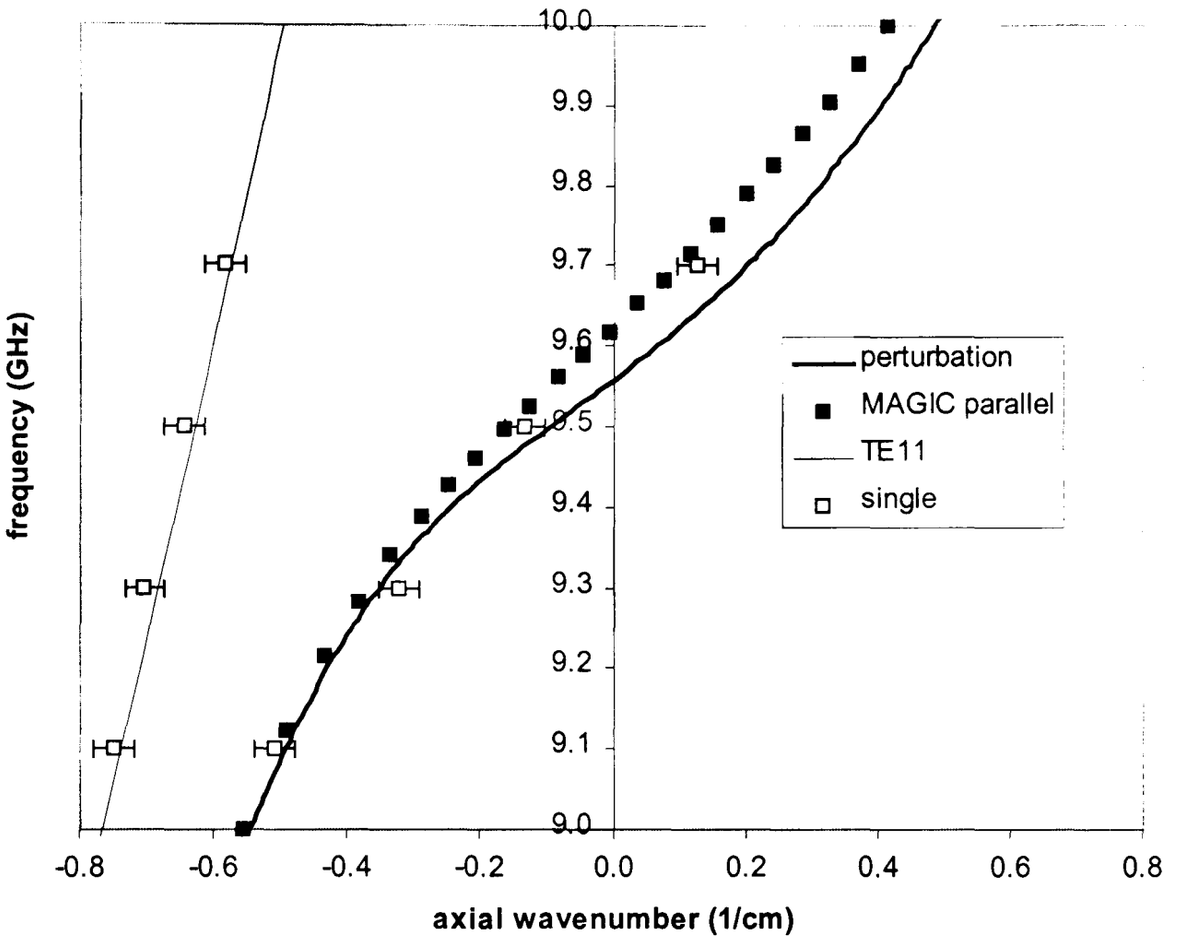

Figure 4-8 Dispersion curve of the modes inside the Aluminium waveguide, calculated using both MAGIC codes and the method of perturbations.

The frequencies found using MAGIC were found to vary by a mean standard deviation of 0.51% from the frequencies calculated using the method of perturbations, for the aluminium helix.

A minimum group velocity of 4.56cm/ns at 9.59GHz was calculated for the aluminium helix using the data obtained from MAGIC, shown in Figure 4-9. The mean standard deviation of the group velocities in the operating bandwidth was found to be 8.19% for the aluminium helix.

The dispersion characteristics of the unperturbed wave found using the single-frequency MAGIC simulation gave good agreement with the dispersion of a TE_{11} mode in a smooth circular waveguide of the same mean radius.

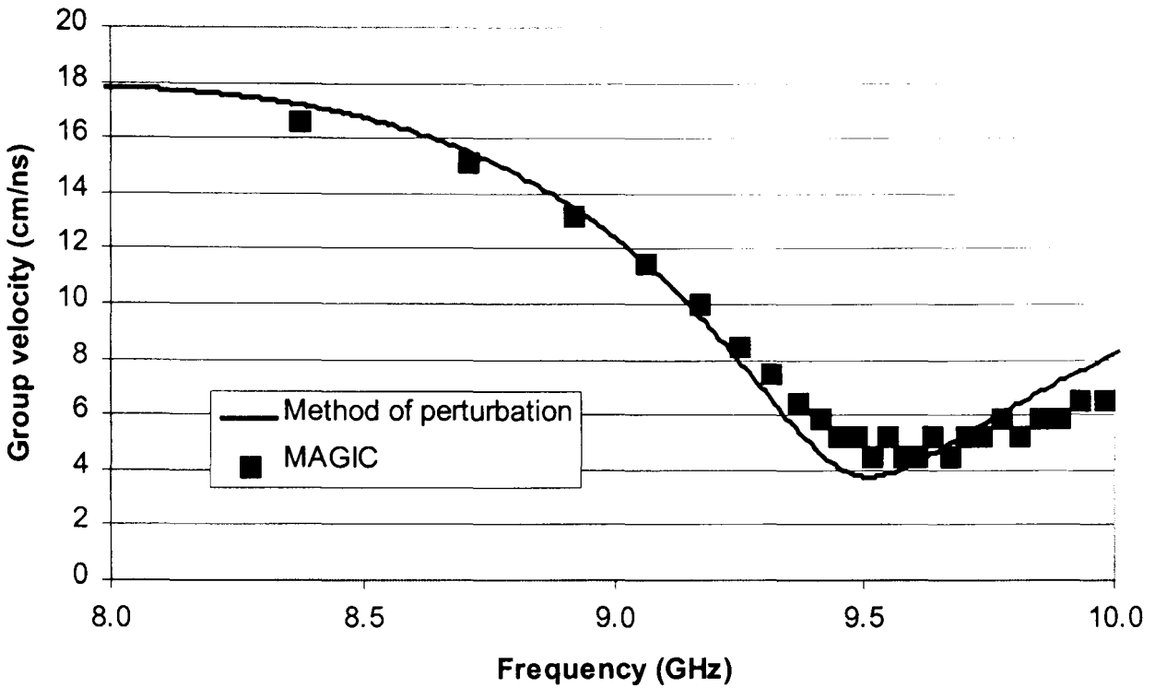

Figure 4-9 Group velocity dispersion of the operating eigenwave in the Aluminium Waveguide measured using SNA MAGIC simulation and the method of perturbations.

For the modified helix the cross-section was defined by first creating the 1st helix structure then cutting out a circular cylinder to give the modified structure. This gave the exact cross-section, as opposed to the approximation used in perturbation theory and hence the MAGIC simulation was more likely to give better agreement with the measured dispersion characteristics of the waveguide. A section of the modified helix 64 periods in length was used in the simulation using SNA MAGIC simulation bounded by two 4 period modified tapers, the results of which are shown in Figure 4-10.

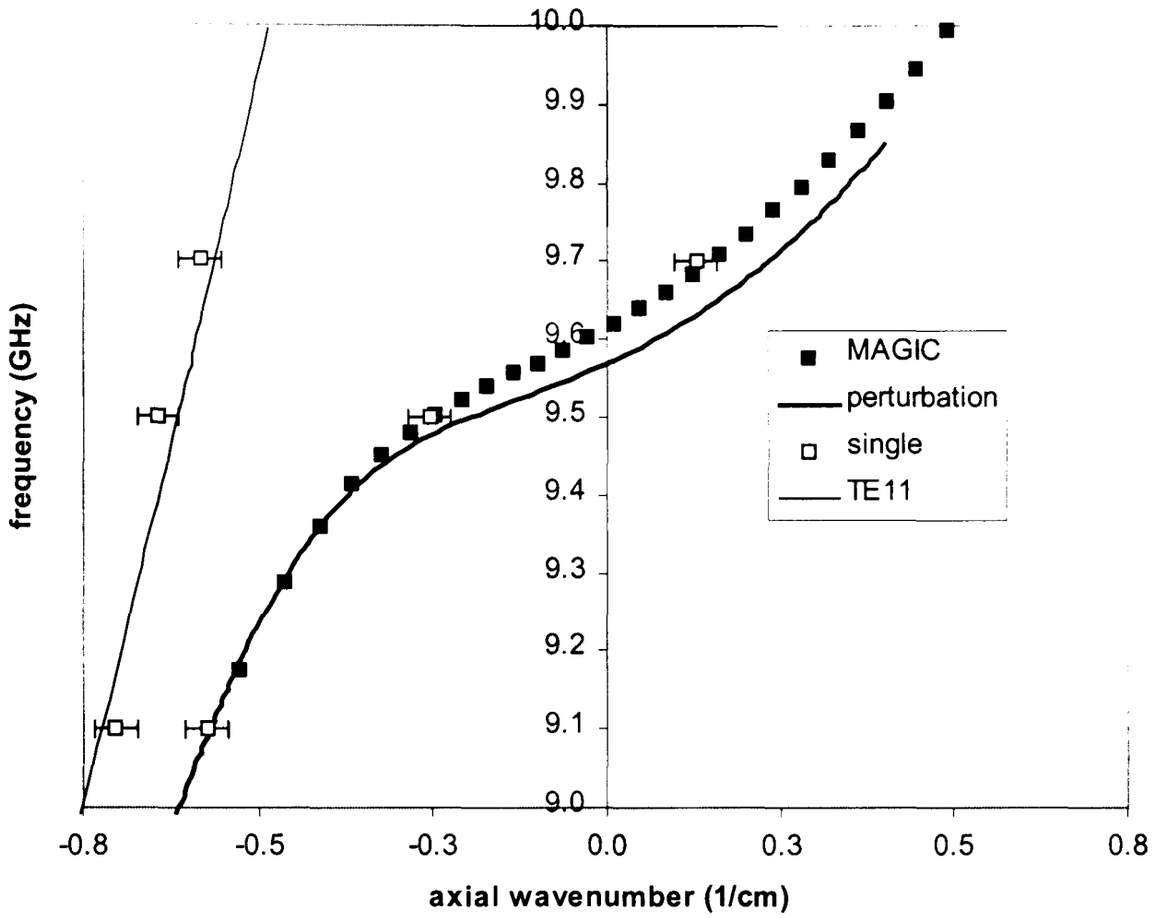

Figure 4-10 Dispersion curve of the modes inside the modified aluminium waveguide, calculated using both MAGIC codes and the method of perturbations.

The mean standard deviation of the frequencies for the modified helix was calculated to be 0.33%. The approximation that the unperturbed mode has the same dispersion characteristics as a TE_{11} mode of a smooth circular waveguide was confirmed for the modified helix using the single-frequency MAGIC simulation.

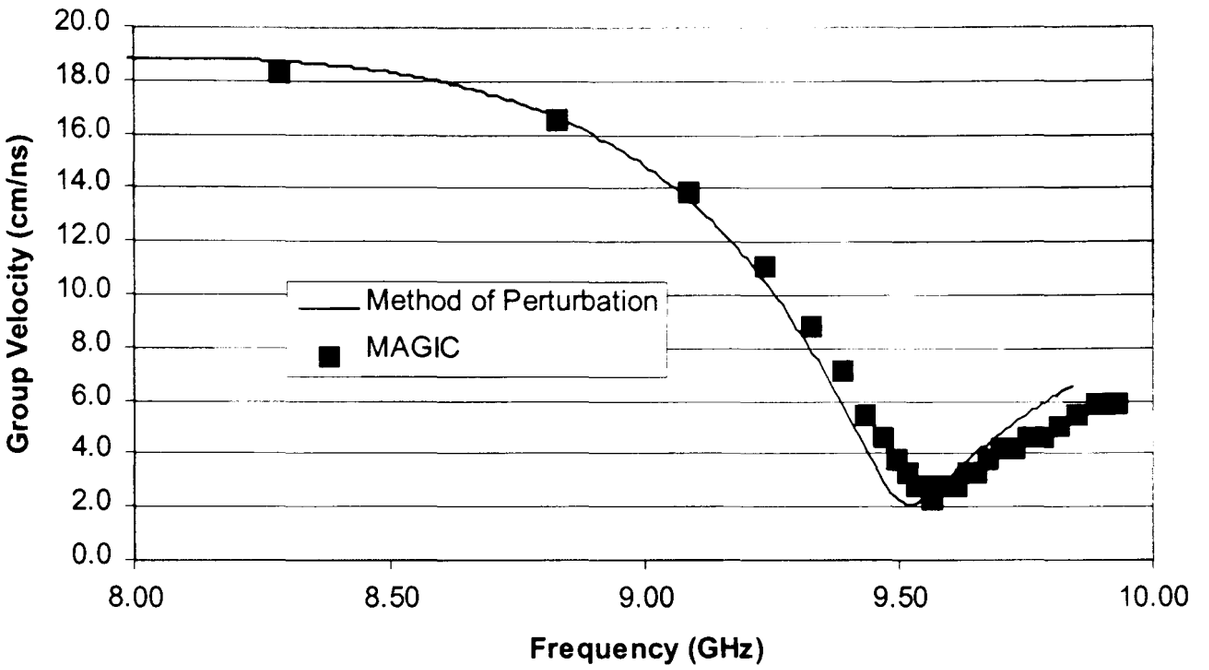

Figure 4-11 Group velocity dispersion of the operating eigenwave in the Modified aluminium waveguide measured using the SNA MAGIC simulation and the method of perturbations.

The modified aluminium helix had a minimum group velocity of 2.5cm/ns at a frequency of 9.59GHz, as can be seen in. Figure 4-11. The mean standard deviation of the group velocities was calculated to be 11.11%.

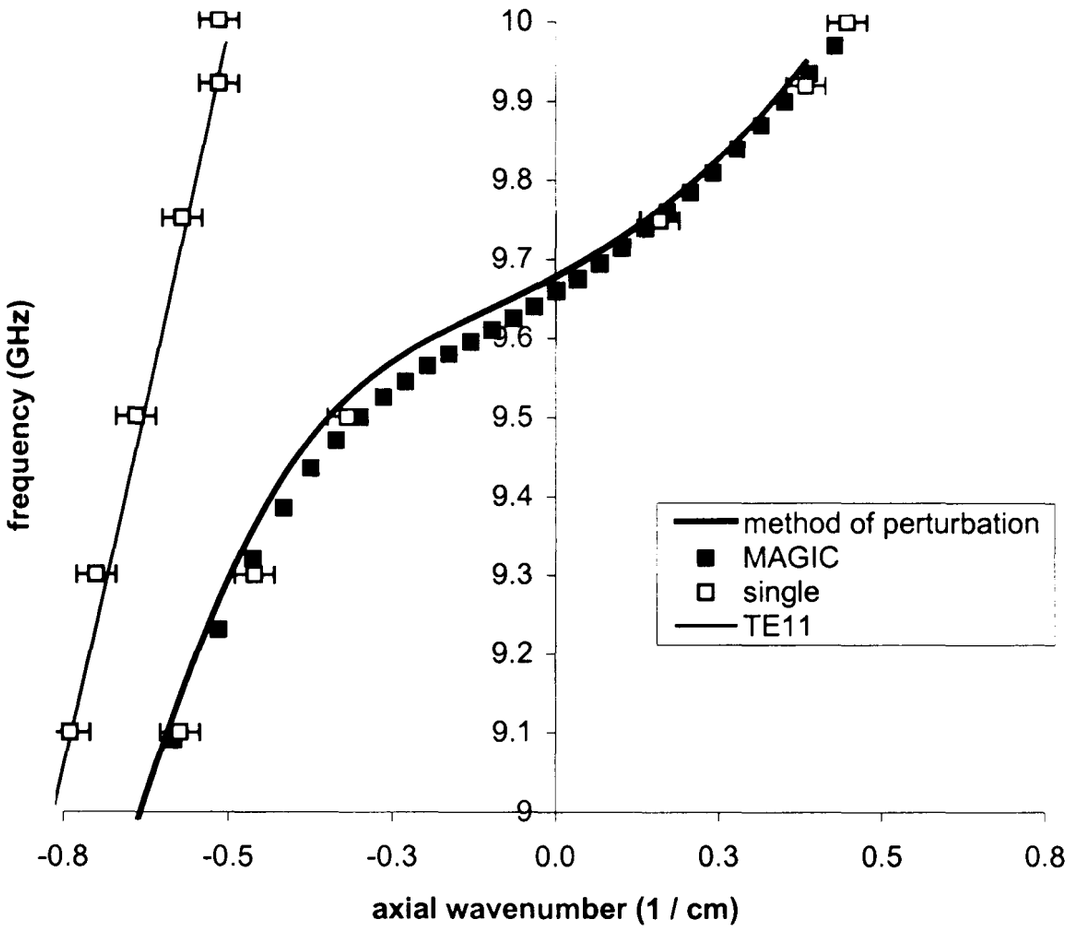

Figure 4-12 Dispersion curve of the modes inside the copper helical waveguide, calculated using both MAGIC codes and the method of perturbations.

A copper helix of length 208.08cm was used in the simulation with two 11.56cm tapers with the same parameters as the copper helix. The mean standard deviation of the frequencies in the band of operation for this helix was found to be 0.11%. As can be seen from Figure 4-12, the dispersion curve of the unperturbed wave was similar to the dispersion of the TE_{11} mode of a smooth circular waveguide for the copper helix.

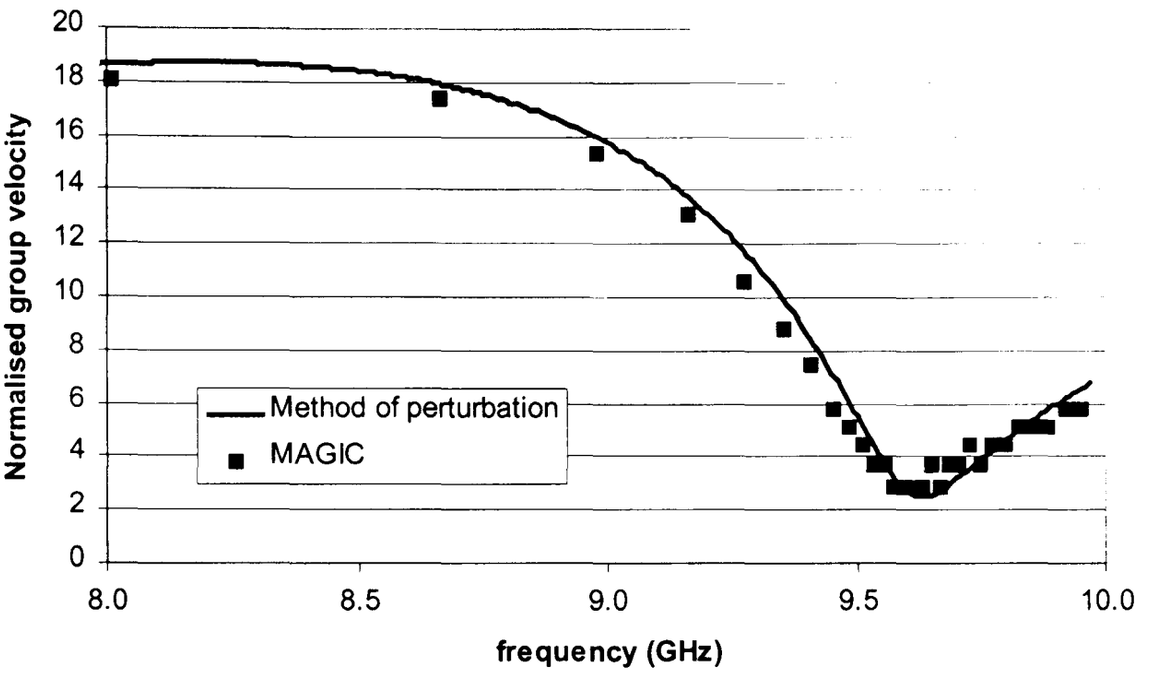

Figure 4-13 Group velocity dispersion of the operating eigenwave in the Copper helical waveguide measured using the SNA MAGIC simulation and the method of perturbations.

The results from MAGIC were used to calculate the minimum group velocity of the copper helix. The waveguide was found to have a group velocity of 3.0cm/ns at 9.62GHz, as shown in Figure 4-13. The mean standard deviation of the group velocities was calculated to be 8.2%.

The numerical PIC code can also be used to look at the electric field lines inside the helically corrugated waveguides. A circularly polarised TE11 mode, counter rotating with respect to the helix, was injected into the helix through a helical taper to convert the fundamental mode of a smooth circular waveguide into the operating eigenmode of the helical waveguide. Figure 4-14 shows the electric field pattern of the aluminium helix at 10GHz.

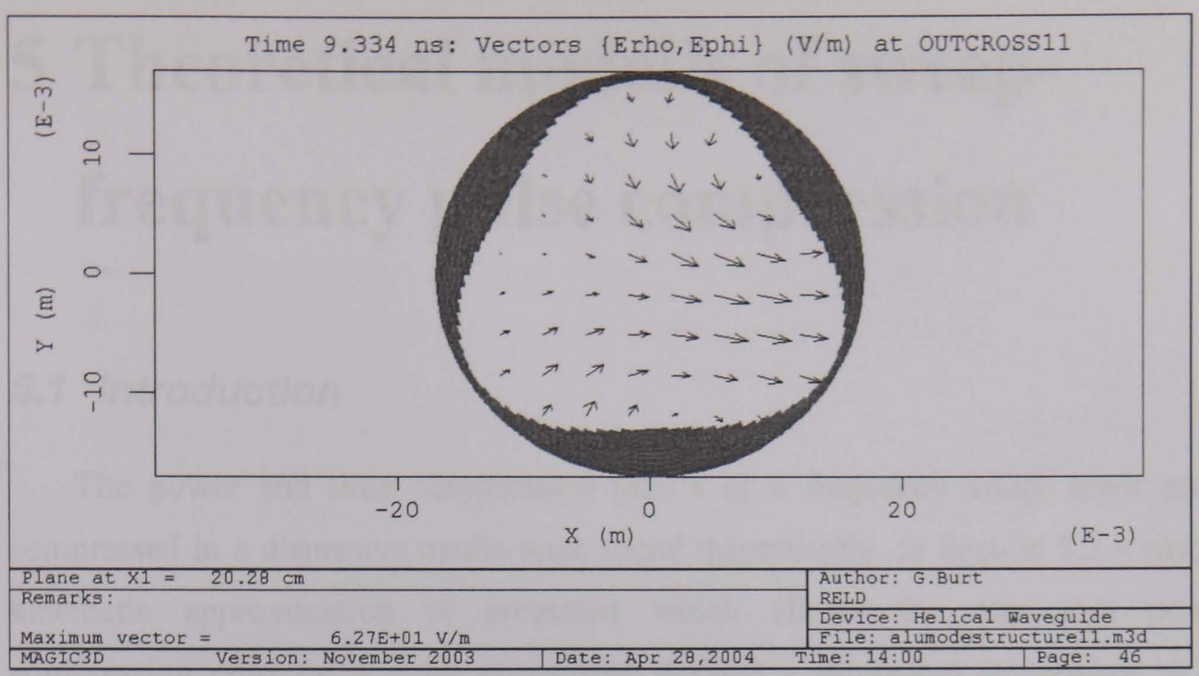

Figure 4-14 Electric field pattern of the aluminium helix, at a frequency of 10GHz, plotted from the numerical PIC code MAGIC.

4.5 Discussion

In this chapter the numerical calculation of the dispersion characteristics of the operating eigenwave of a helically corrugated waveguide was investigated. Two methods of calculating the dispersion relation of the eigenwave were devised using the PIC code MAGIC. One method used the polarisation rotation of a linearly polarised wave propagating through the helix while the other measured the radial electric field variation of the eigenwave along the helix. Both these methods gave good agreement with each other, as well as agreeing with the Method of Perturbations, if a helically corrugated waveguides with a shallow corrugation amplitude, such as the copper helix was used, where a minimum group velocity of 3.0 cm/ns was calculated. For helix with deeper corrugation amplitudes, such as the aluminium helically corrugated waveguide the dispersion curve deviated from the method of perturbations, where the group velocity varied by 8.19%. For the modified aluminium helix the real geometry was able to be simulated in MAGIC as opposed to the sinusoidal variation used in the method of perturbations, which resulted in an 11.11% standard deviation in the calculation of the group velocity.

5 Theoretical model's of sweep-frequency pulse compression

5.1 Introduction

The power and time compression ratio's of a frequency swept input pulse compressed in a dispersive media were found theoretically. In Section 5.2 a simple kinematic approximation is presented which allows the maximum power compression ratio for a pulse propagated through a dispersive compressor to be calculated as a function of the start and stop frequencies of the frequency sweep. In Section 5.3 the optimum frequency sweep for a pulse to be compressed in a given dispersive media is shown. In Section 5.4 a Fourier optics simulation of microwave pulse compression is presented, where the compressed pulse was calculated from the input pulse and dispersive media used for compression.

5.2 Approximation

A simple kinematic approximation for the compression of a pulse may be obtained by considering a rectangular input pulse comprising of a train of particles having different velocities and entry times. However for this approach, at optimum compression the pulse width is zero. Any pulse of finite duration in the time domain, τ, has a spectral bandwidth, Δf, in the frequency domain. The minimum spectral bandwidth is related to the pulse length by

$$\Delta f \geq \frac{1}{\tau} \qquad \textbf{Equation 5-1}$$

Hence it can also be shown a pulse of a given spectral width in the frequency domain has a minimum pulse duration in the time domain, τ_c. When a frequency-swept pulse is compressed the minimum achievable pulse duration, τ_c, is inversely proportional to the spectral bandwidth of the input pulse.

If there are no losses in the compression, the compression ratio, k_p, is given by

$k_p = P_{max} / P_0 \sim \tau_0 / \tau_c \sim \Delta f \tau_0$ **Equation 5-2**

However, significant losses are associated with pulse compression in a dispersive line due to ohmic losses in the waveguide. When losses are included

$$K_p = |u_{\max}|^2 / A_0^2 = \Delta f \, \tau_0 e^{-\bar{\gamma} L}$$ **Equation 5-3**

where $\bar{\gamma}$ is the averaged attenuation coefficient between the frequency sweep. In the range of interest, the imaginary part of the axial wavenumber can be approximated by a linearly growing function of the inverse group velocity for smooth bore waveguides. At optimum modulation, when the inverse group velocity is a linear function of time, this approximation gives simply: $\bar{\gamma} = (\alpha_1 + \alpha_2)$, where $\alpha_{1,2}=\alpha(\omega_{1,2})$ for the start and final frequency, respectively.

Using a simple kinematic approach the optimum length of dispersive medium, L_c, for maximum compression of a pulse of initial duration, τ_0, is $L_c = \tau_0 U$ where,

$$U = v_{gr1} v_{gr2} / (v_{gr2} - v_{gr1})$$ **Equation 5-4**

This allows the optimum power compression ratio for a compressor to be found as a function of frequency sweep, the start and tail group velocities, the averaged attenuation constant and the compressor length,

$$K_p = \frac{\Delta f \, L}{U} e^{-\bar{\gamma} L}$$ **Equation 5-5**

By differentiating Equation 5-5 with respect to compressor length and finding its roots the optimum compressor length was ascertained.

$$L_{opt} = 1/\bar{\gamma}$$ **Equation 5-6**

Thus, for a chosen mode and optimum modulation, the maximum power compression can be estimated by the analytical function of two variables, ω_1 and ω_2.

Hence, $K_{p\max} = \frac{\Delta f \, e^{-1}}{\bar{\gamma} U}$ **Equation 5-7**

In this case the maximum energy efficiency is e^{-1}, or 33%.

Contour plots showing the approximated compression ratio as a function of start and stop frequencies for optimum sweeps are shown for each of the three helical compressors. Contour plots are also presented for the case where the optimum length of each compressor helix was used. The dispersive properties and losses were calculated in two ways. In the first method dispersion and losses were calculated using the method of perturbation. In this case the conductivity was assumed to be 35.4 M siemens/metre for aluminium and 58.0 M siemens/metre for copper and all losses were assumed to be ohmic losses. In the second method the dispersion was calculated using the numerical code MAGIC and the loss coefficient was calculated from transmission measurements, presented in Chapter 6, assuming that all losses were due to ohmic heating and leakage. The use of transmission measurements to calculate the loss coefficient was more accurate and closer to the experiments as it included losses due to both ohmic heating and leakage from connections.

The plots show frequencies from 9GHz. Although higher compression ratios can be obtained with stop frequencies below 9GHz, the sweep rate required to maintain the optimum sweep below 9GHz was greater than 100MHz/ns, which was much faster than could be obtained using the equipment available in the laboratory.

Four contour plots are presented for each helix. The first is the maximum compression ratio as a function of frequency for the helical compressor used in the experiment, the second shows the same plots for an optimised length of helix. The third and fourth sets of contour plots show the maximum compression ratio as a function of frequency for the helical compressor used in the experiment and an optimised length of helix, respectively, calculated using the dispersion found from the numerical code MAGIC.

Figure 5-1 shows maximum power compression ratio as a function of the maximum and minimum frequencies of the sweep for the aluminium helically corrugated compressor of length equal to 64 periods plus two 4 period tapers. The dispersion was calculated using the method of perturbation and the conductivity was assumed to be 35.4 M siemens/metre. A maximum compression ratio of 17.45 was estimated.

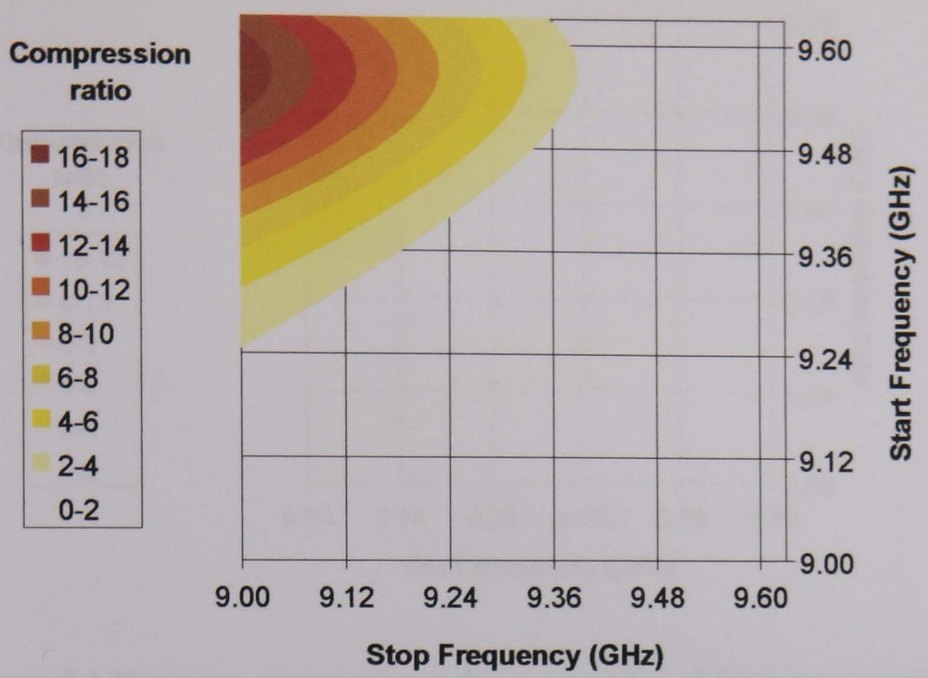

Figure 5-1 Maximum compression ratio as a function of frequency bandwidth for a 68 period long length of aluminium helically corrugated waveguide, using the dispersion found from the method of perturbations.

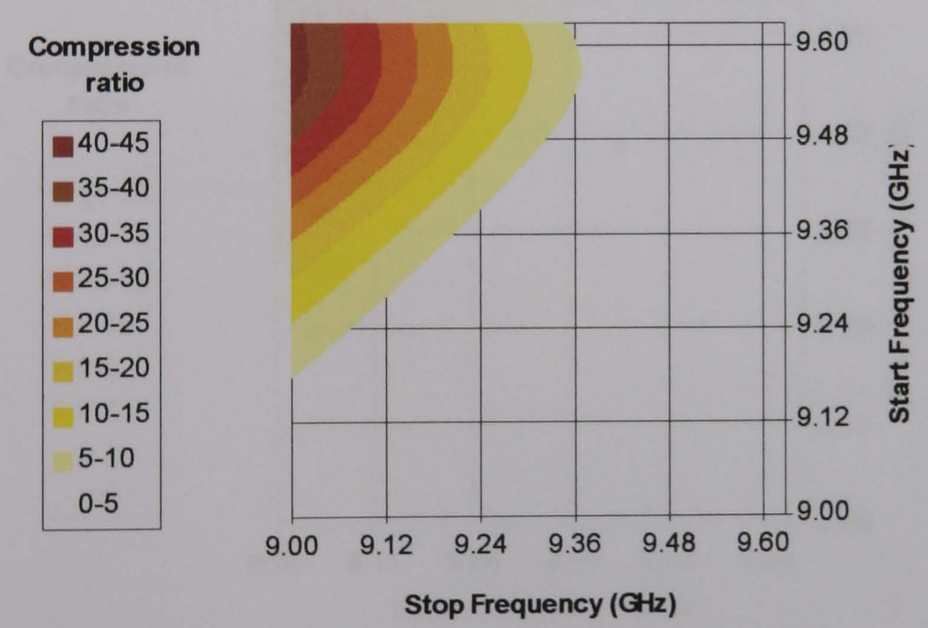

Figure 5-2 Maximum compression ratio, as a function of frequency bandwidth, for the optimum length of aluminium helically corrugated waveguide, using the dispersion found from the method of perturbations.

The approximated power compression ratio's for the optimum length of aluminium helical compressor is shown in Figure 5-2. A maximum compression ratio of 42.47 was calculated, corresponding to a 5.43m length of waveguide.

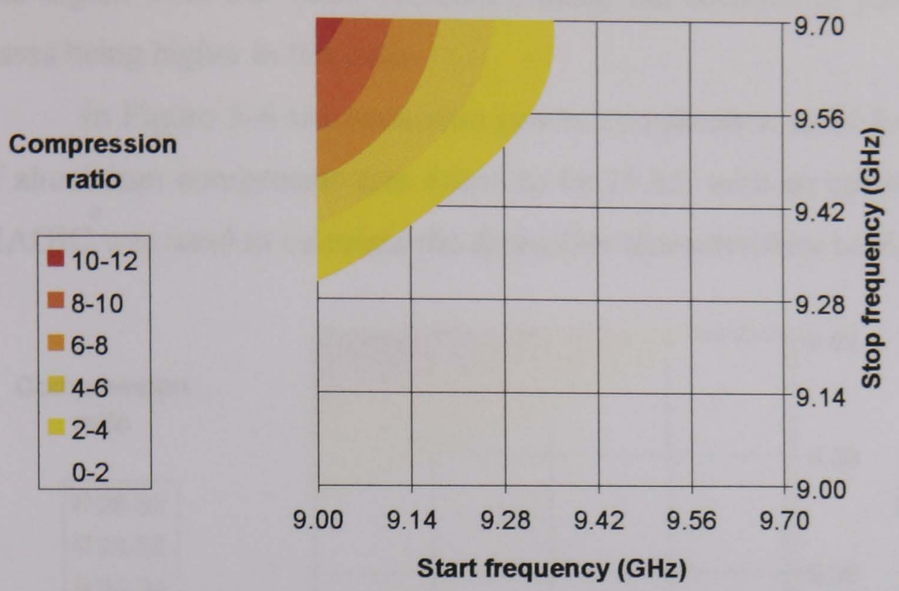

Figure 5-3 Maximum compression ratio as a function of frequency bandwidth for a 68 period long length of aluminium helically corrugated waveguide, using the dispersion found from the numerical PIC code MAGIC.

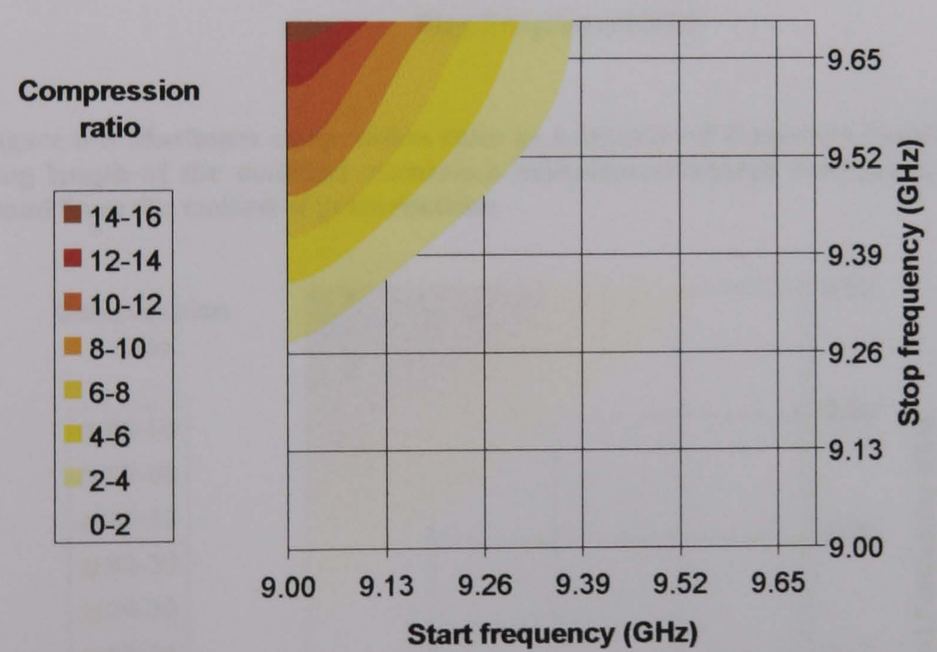

Figure 5-4 Maximum compression ratio, as a function of frequency bandwidth, for the optimum length of aluminium helically corrugated waveguide, using the dispersion found from the numerical PIC code MAGIC.

Figure 5-3 shows the power compression ratios approximated for the aluminium compressor where the dispersion was calculated using the numerical code MAGIC. A maximum power compression ratio of 10.7 was obtained. The power compression ratio was lower than the previous plot as the minimum group velocity

was higher than the value calculated using the method of perturbation, as well as losses being higher in this case.

In Figure 5-4 the maximum power compression ratio for the optimum length of aluminium compressor was found to be 15.85, with an optimum length of 4.07m. MAGIC was used to calculate the dispersive characteristics used in this plot.

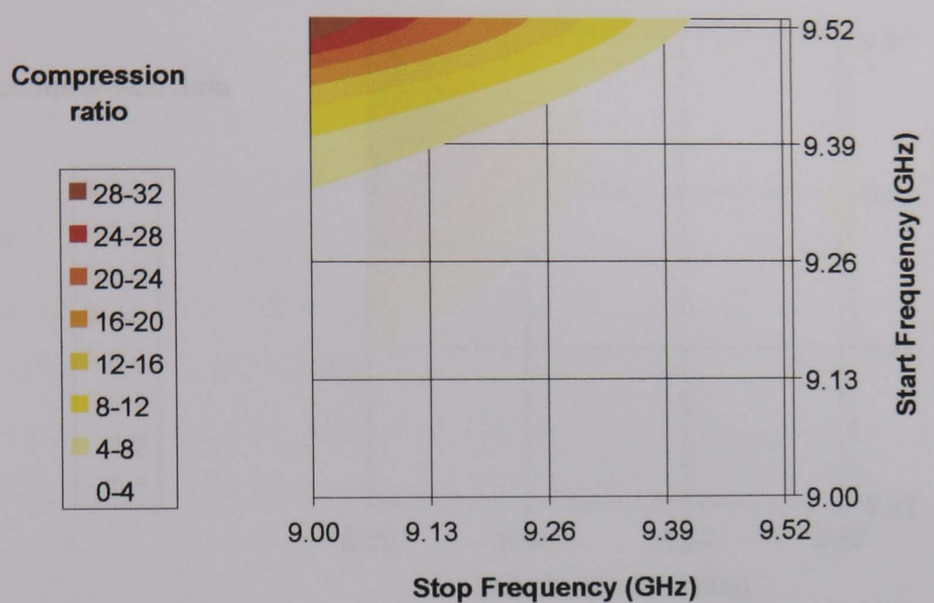

Figure 5-5 Maximum compression ratio as a function of frequency bandwidth for a 68 period long length of the modified aluminium helically corrugated waveguide, using the dispersion found from the method of perturbations.

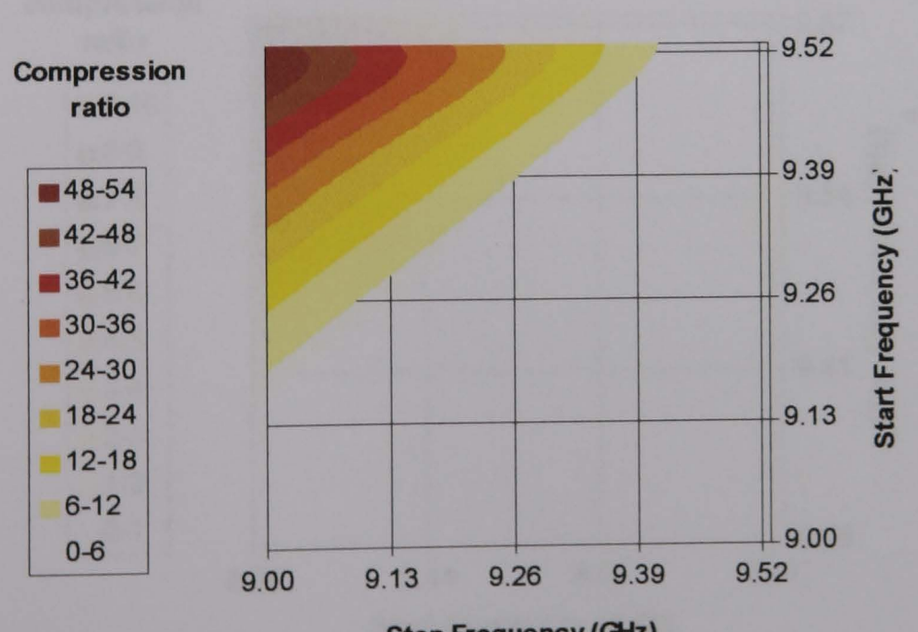

Figure 5-6 Maximum compression ratio, as a function of frequency bandwidth, for the optimum length of the modified helically corrugated waveguide, using the dispersion found from the method of perturbations.

Figure 5-5 shows a maximum power compression ratio of 31.94 for the modified aluminium compressor helix of 64 periods length with two 4 period tapers. The method of perturbation was used to calculate the compression ratio's, and a maximum power compression ratio of 53.83 was calculated for an optimum length of modified compressor of 3.42m, as shown in Figure 5-6.

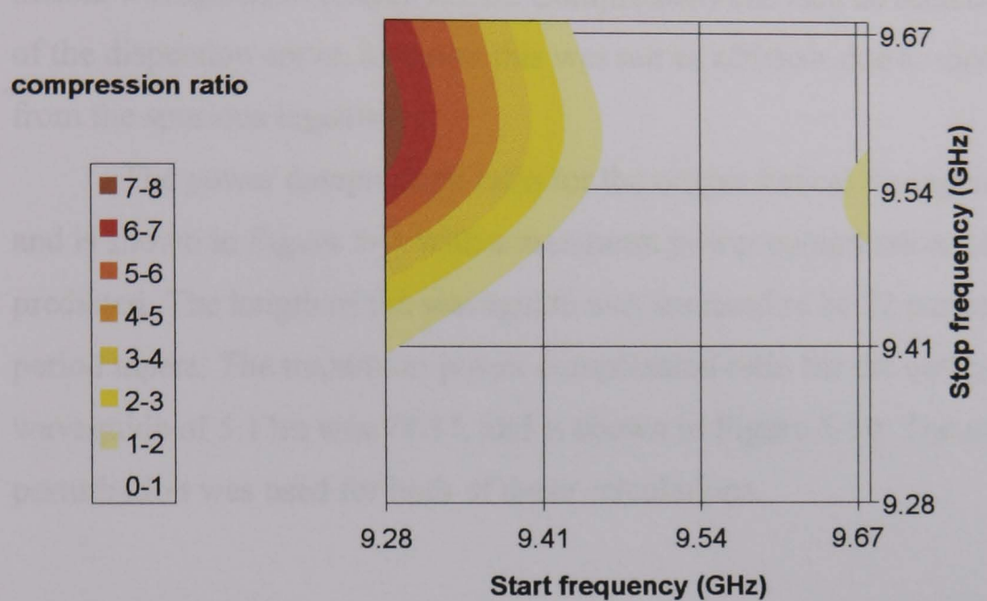

Figure 5-7 Maximum compression ratio as a function of frequency bandwidth for a 68 period long length of the modified aluminium helically corrugated waveguide, using the dispersion found from the numerical PIC code MAGIC.

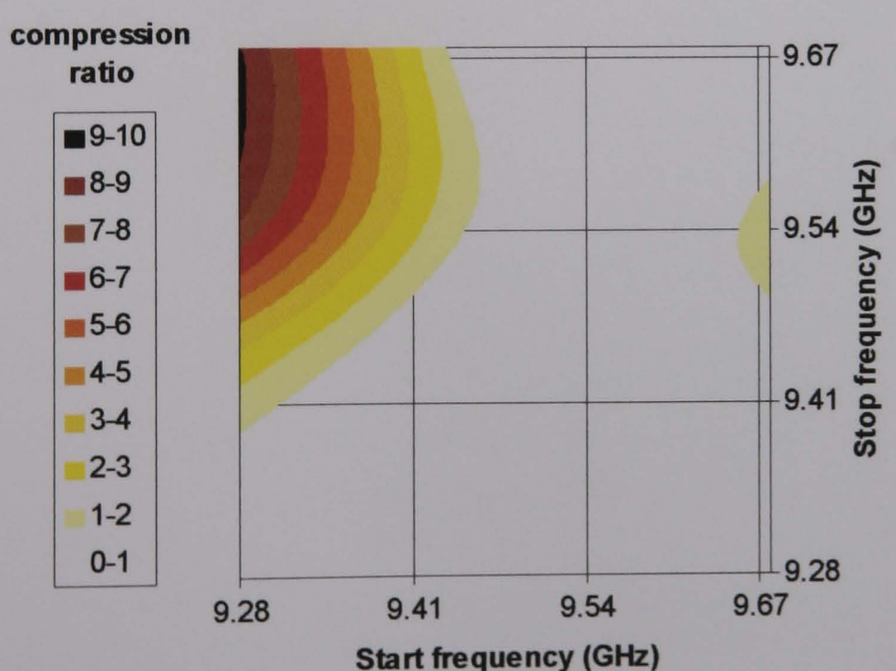

Figure 5-8 Maximum compression ratio, as a function of frequency bandwidth, for the optimum length of the modified aluminium helically corrugated waveguide, using the dispersion found from the numerical PIC code MAGIC.

For the case where MAGIC was used, a maximum power compression ratio of 7.58 was calculated for a frequency sweep with a stop frequency of 9.28GHz, as shown in Figure 5-7. The compression using the optimum length of compressor is shown in Figure 5-8, where a maximum power compression ratio of 9.33 was found for a helical waveguide of length 4.63m. Compression can also be seen on the other side of the dispersion curve, however this was not as efficient due to mode competition from the spurious eigenwave.

The power compression ratio for the copper helical waveguide was calculated and is shown in Figure 5-9, with a maximum power compression ratio of 36.19 predicted. The length of the waveguide was assumed to be 72 periods and had two 4 period tapers. The maximum power compression ratio for the optimum length of waveguide of 5.13m was 74.17, and is shown in Figure 5-10. The method of perturbation was used for both of these calculations.

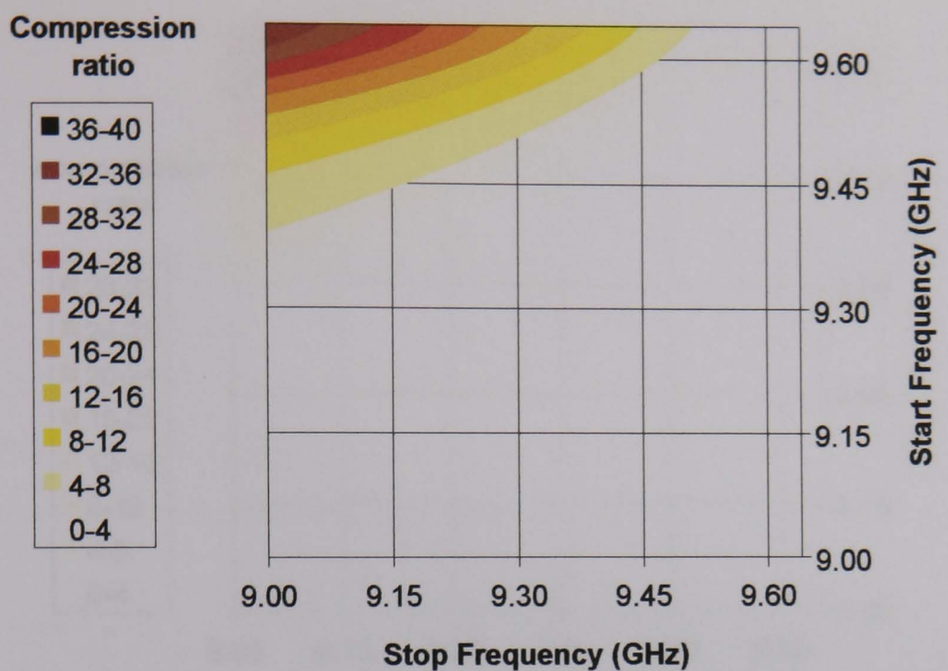

Figure 5-9 Maximum power compression ratio as a function of frequency bandwidth for a 68 period long length of the copper helically corrugated waveguide, using the dispersion found from the method of perturbations.

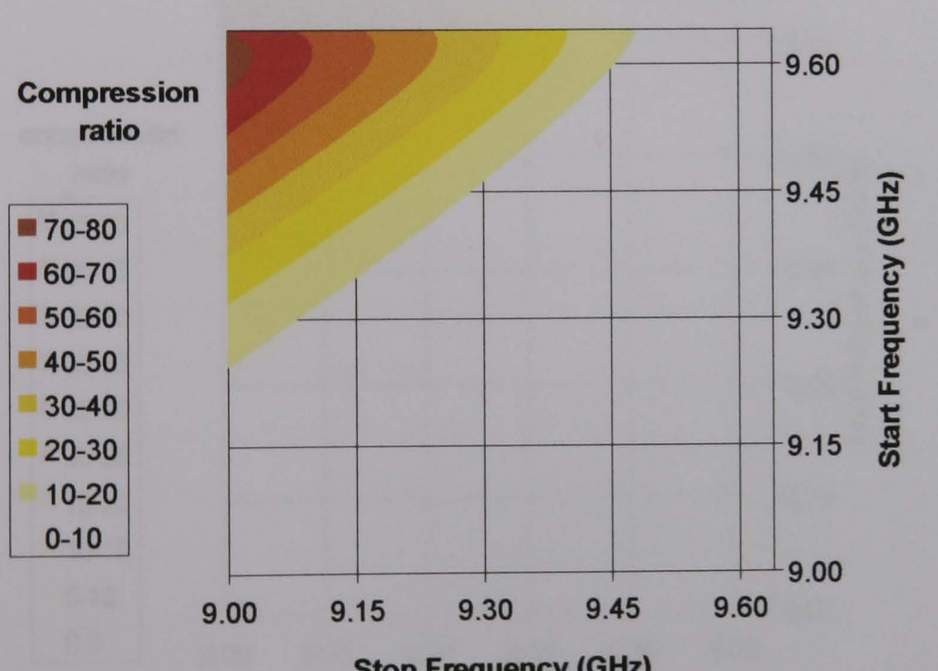

Figure 5-10 Maximum power compression ratio, as a function of frequency bandwidth, for the optimum length of the copper helically corrugated waveguide, using the dispersion found from the method of perturbations.

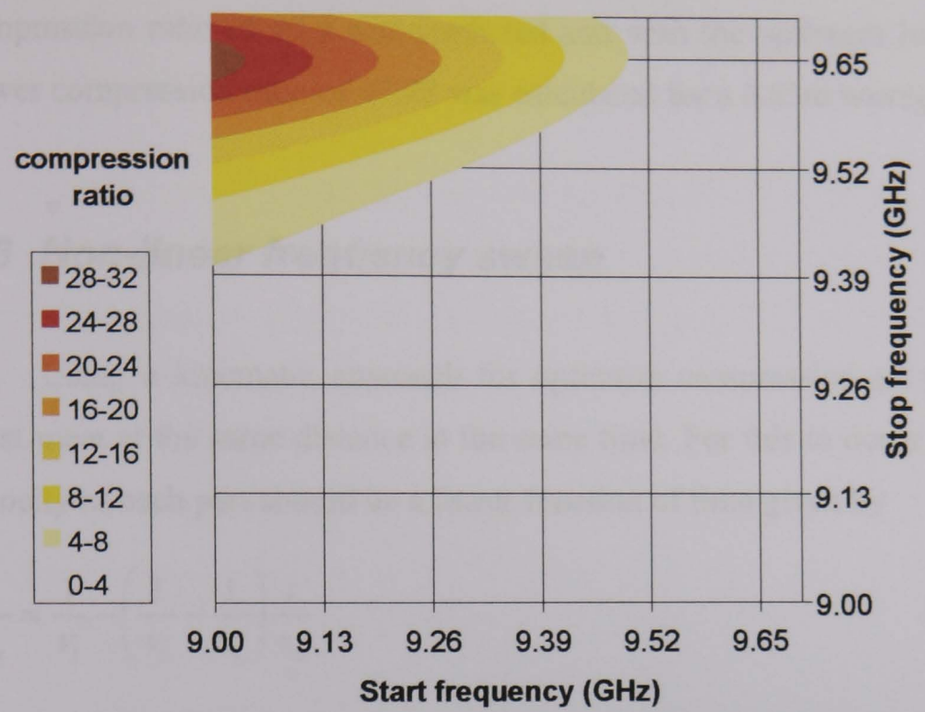

Figure 5-11 Maximum power compression ratio as a function of frequency bandwidth for a 68 period long length of the copper helically corrugated waveguide, using the dispersion found from the numerical PIC code MAGIC.

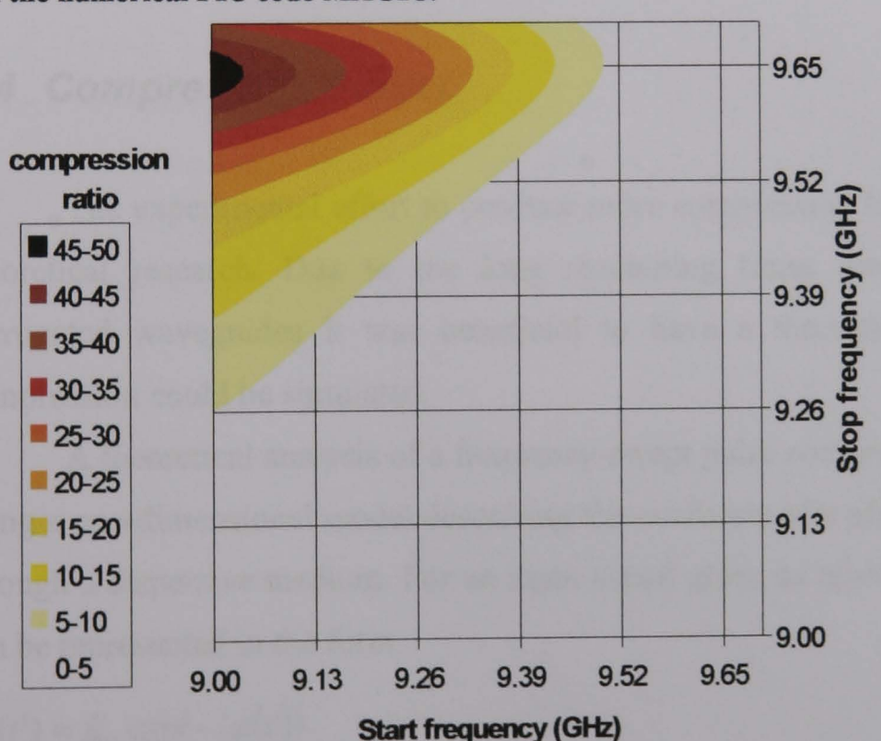

Figure 5-12 Maximum power compression ratio, as a function of frequency bandwidth, for the optimum length of the copper helically corrugated waveguide, using the dispersion found from the numerical PIC code MAGIC.

The calculated pulse compression in the copper helix using MAGIC is shown in

Figure 5-11 and Figure 5-12. For a length of 208.08cm, a maximum power compression ratio of 29.9 was predicted and with the optimum length, a maximum power compression ratio of 47.78 was calculated for a 6.85m waveguide.

5.3 Non-linear frequency sweep

Using a kinematic approach for optimum compression all parts of the pulse must meet at the same distance at the same time. For this to occur the inverse group velocity of each part should be a linear function of time given by

$$\frac{1}{V_{gr}} = \frac{1}{V_1} - \left(\frac{1}{V_1} - \frac{1}{V_2}\right)\frac{t}{\tau_0} \qquad \textbf{Equation 5-8}$$

where $v_{1,2}=v_{gr}(\omega_{1,2})$ are the group velocities corresponding to the frequencies of the pulse at the beginning and end of the pulse, respectively and τ_0 is initial pulse width.

5.4 Compression model

The experimental effort to produce pulse compression has been supported by theoretical research. Due to the long machining times associated with helical corrugated waveguides it was beneficial to have a theoretical model in which compression could be simulated.

A theoretical analysis of a frequency-swept pulse compression was performed using a one-dimensional model describing the evolution of a plane wave propagating through a dispersive medium. For an input signal given as $u(z=0,t')=u_0(t')$ a solution can be represented in the form

$$u_0(t') = E_0 \exp(-i\varphi(t')) \qquad \textbf{Equation 5-9}$$

where $\varphi(t')$ is the phase of the electric field and is given by

$$\varphi(t') = \int_0^{t'} \omega.dt' \qquad \textbf{Equation 5-10}$$

this allows the frequency sweep to be controlled, with respect to time.

The Fourier transform of the input wave is given by

$$F(\omega) = \frac{1}{2\pi i}\int_{-\infty}^{\infty} u_0(t')e^{i\omega t'}dt' \qquad \textbf{Equation 5-11}$$

Each Fourier component in time corresponds to a spatial wavenumber. In a linear media the equations of motion for electromagnetic waves are linear and so any linear combination of waves is also a solution. Hence by the principle of superposition the resultant disturbance at any point in a medium is the algebraic sum of the separate constituent waves. Thus using a 1-D Fourier optics approach[73], the pulse as a function of time and space leads to

$$u(z,t) = \frac{1}{2\pi i}\int_{-\infty}^{\infty}\int_{-\infty}^{\infty} d\omega.dt' u_0(t')\exp[-i\omega(t-t') + ik(\omega)z] \qquad \textbf{Equation 5-12}$$

Using the dispersion relations this integral can be solved using a numerical integration technique. The losses in the system due to ohmic losses are accounted for in the model by the use of an imaginary component of the axial wavenumber.

Using this approach, the compression of several pulses with frequency sweeps corresponding to the optimum kinematic sweep in helically corrugated compressors, were simulated, and compared to the simple kinematic approximation. It was found that one of the major limitations to the maximum power compression ratio was the maximum sweep rate of the input source used.

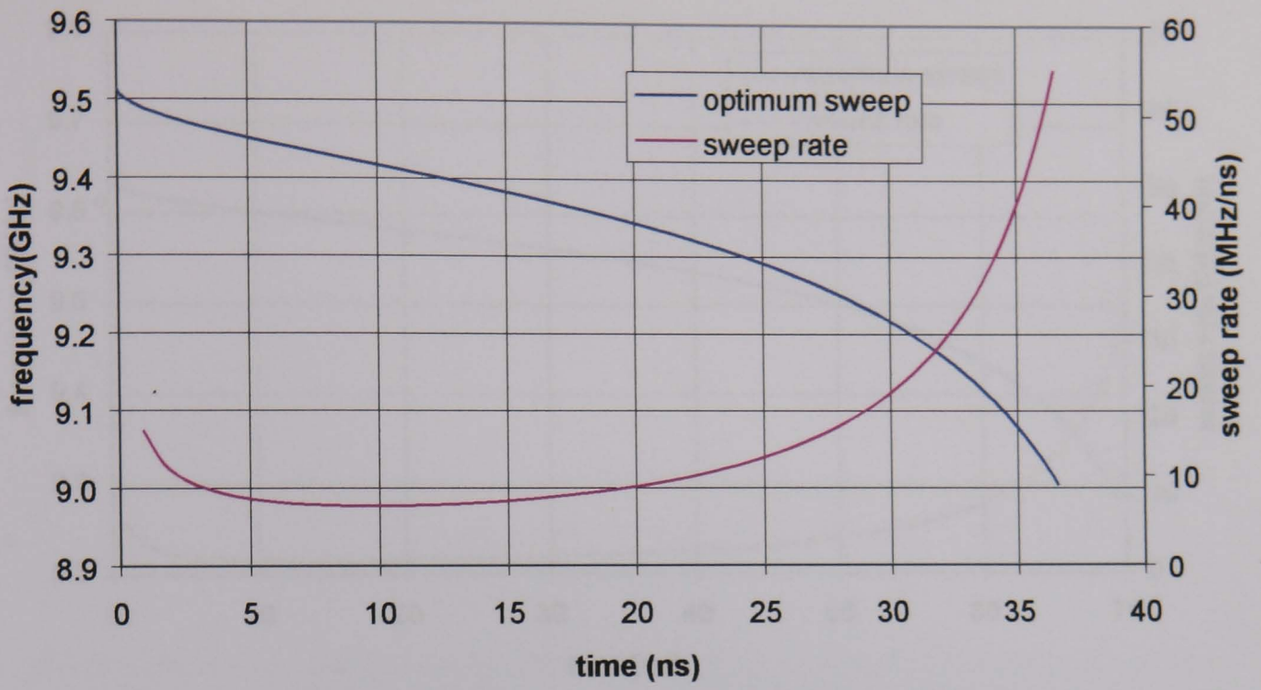

Figure 5-13 Optimum kinematic frequency sweep and sweep rate for a pulse to be compressed in the full length of the aluminium helical waveguide.

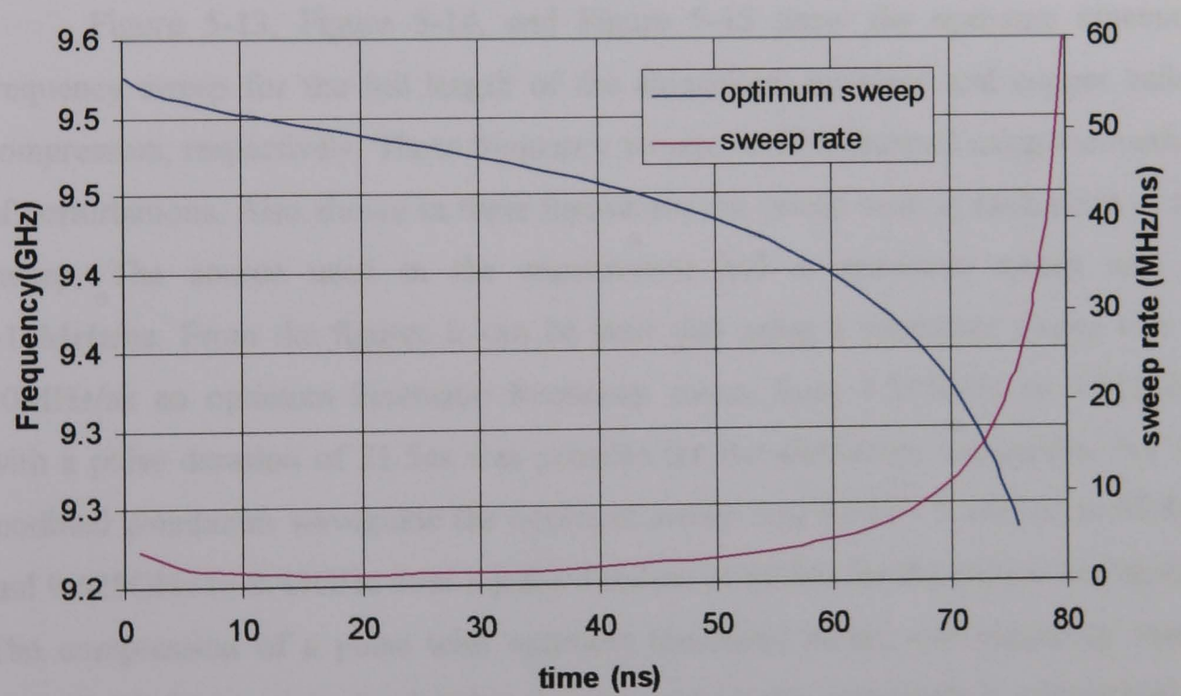

Figure 5-14 Optimum kinematic frequency sweep and sweep rate for a pulse to be compressed in the full length of the modified aluminium helical waveguide.

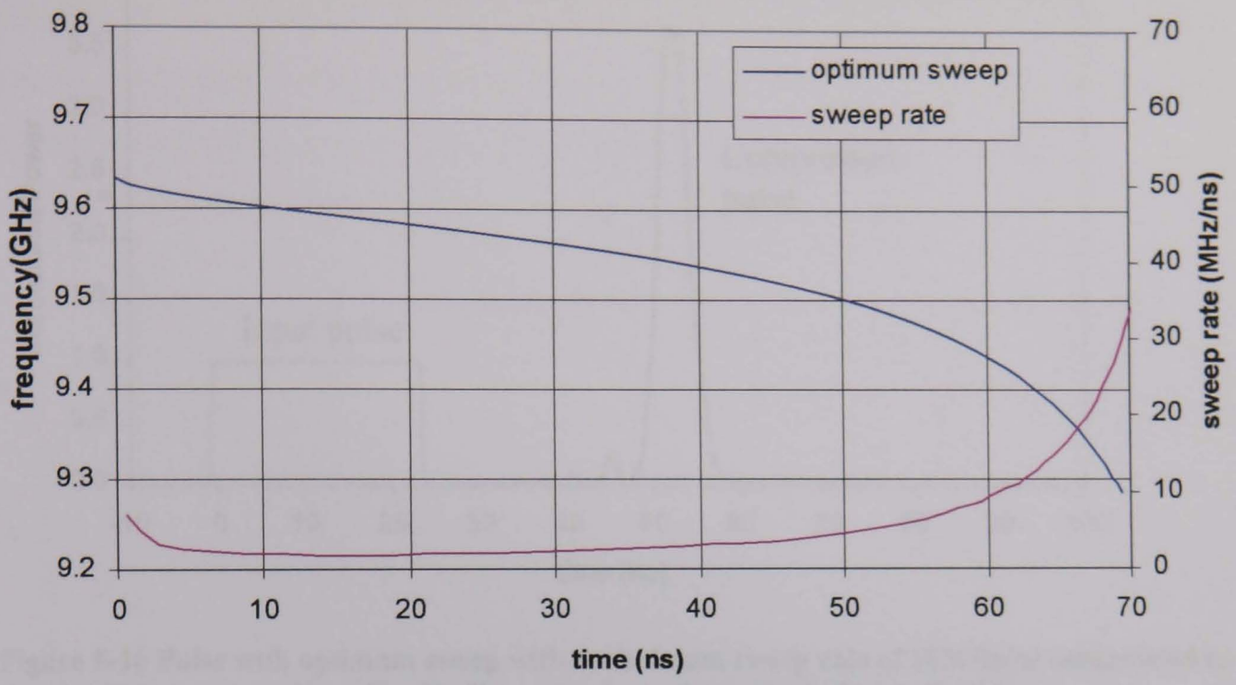

Figure 5-15 Optimum kinematic frequency sweep and sweep rate for a pulse to be compressed in the full length of the copper helical waveguide.

Figure 5-13, Figure 5-14, and Figure 5-15 show the optimum kinematic frequency sweep for the full length of the aluminium, modified and copper helical compressors, respectively. These frequency sweeps were calculated using the method of perturbations. Also shown in these figures are the sweep rates at each point of the sweep. The source used in the experiments had a maximum sweep rate of ~10MHz/ns. From the figures it can be seen that using a maximum sweep rate of 10MHz/ns an optimum kinematic frequency sweep from 9.505GHz to 9.315GHz with a pulse duration of 21.5ns was possible for the aluminium waveguide. For the modified aluminium waveguide the optimum sweep was 9.525 - 9.34GHz in 68.8ns, and 9.625GHz to 9.43GHz over a pulse duration of 68.8ns for the copper waveguide. The compression of a pulse with optimum kinematic sweep and maximum sweep rate of 10MHz/ns was simulated and compared to the compression calculations in section 5.1, for each helical compressor.

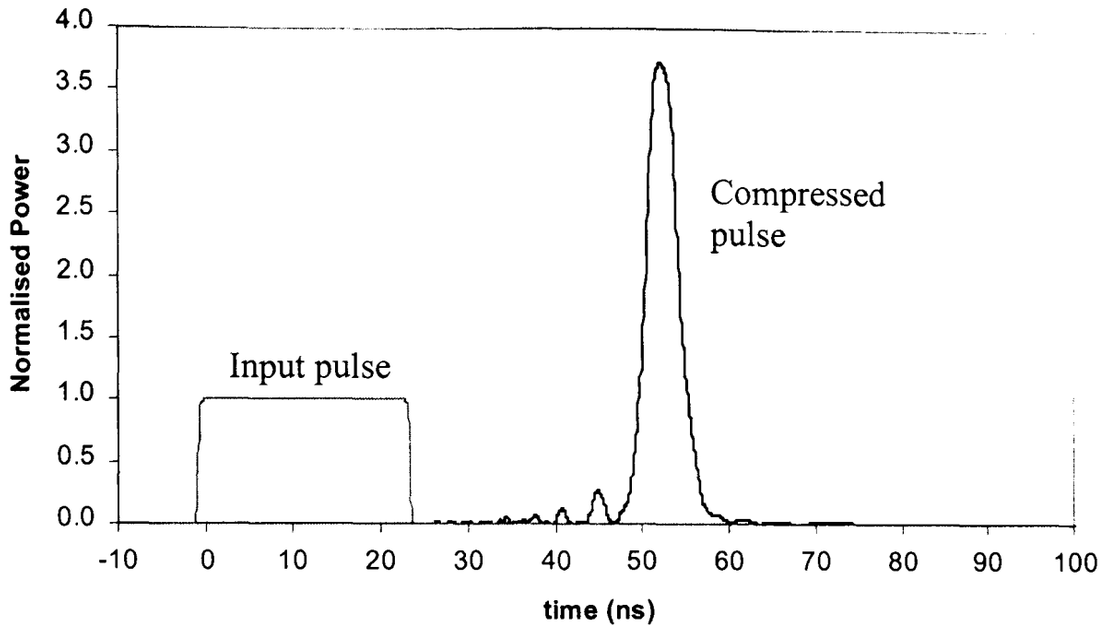

Figure 5-16 Pulse with optimum sweep with a maximum sweep rate of 10MHz/ns compressed in the aluminium waveguide using the dispersion from the method of perturbation.

The simulation predicted a power compression ratio of 3.735 for a 68 period section of the aluminium waveguide (64 regular sections plus two 4 period tapers), as shown in Figure 5-16, and a compressed pulse duration of 4.4ns. This gives a time compression ratio of 4.89 and an efficiency of 76%. The simple kinematic approximation gave a power compression ratio of 3.425.

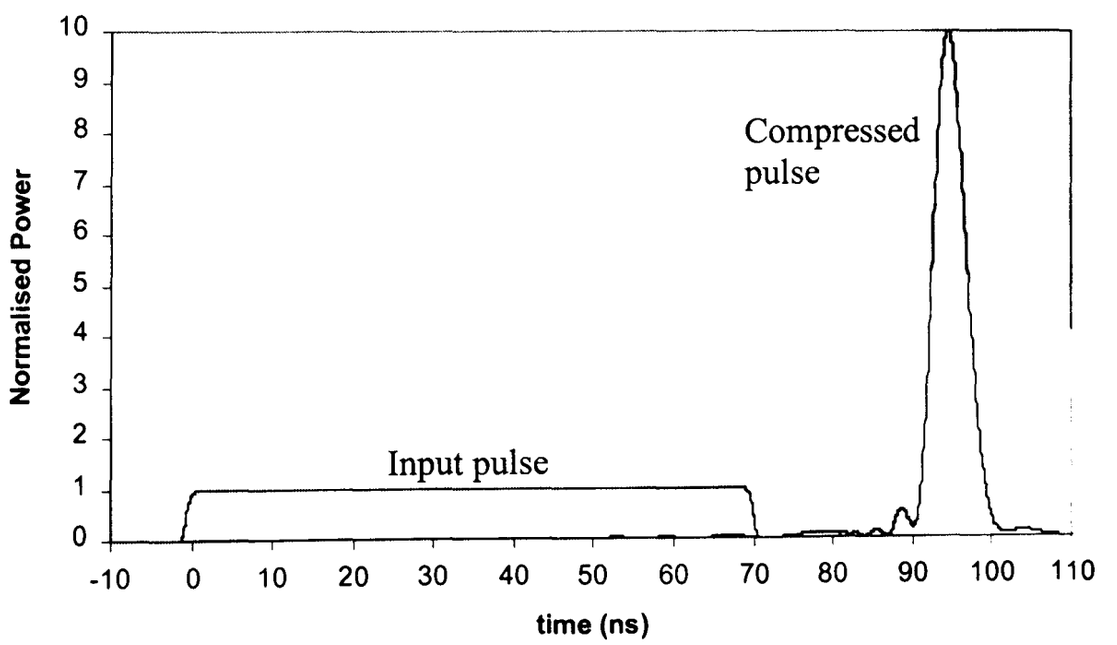

Figure 5-17 Pulse with optimum sweep with a maximum sweep rate of 10MHz/ns compressed in the modified waveguide using the dispersion from the method of perturbation.

The simulation predicted a power compression ratio of 10 for a 68 period section of the modified aluminium waveguide, shown in Figure 5-17, and a compressed pulse duration of 4.9ns. This gives a time compression ratio of 14.0 and a compression efficiency of 71%. The simple kinematic approximation gave a power compression ratio of 9.7.

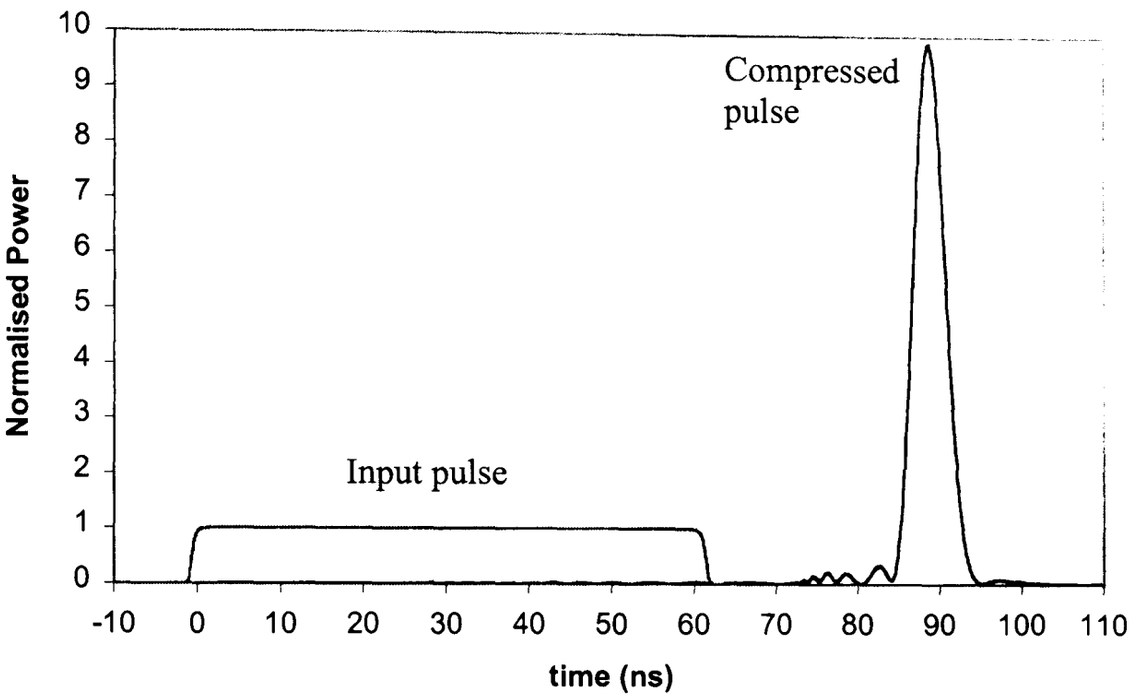

Figure 5-18 Pulse with optimum sweep with a maximum sweep rate of 10MHz/ns compressed in the copper waveguide using the dispersion from the method of perturbation.

The simulation predicted a power compression ratio of 9.87 for a 76 period section of the copper waveguide, shown in Figure 5-18, and a compressed pulse duration of 4.5ns. This gave a time compression ratio of 13.5 and a compression efficiency of 73%. The simple kinematic approximation gave a power compression ratio of 9.5.

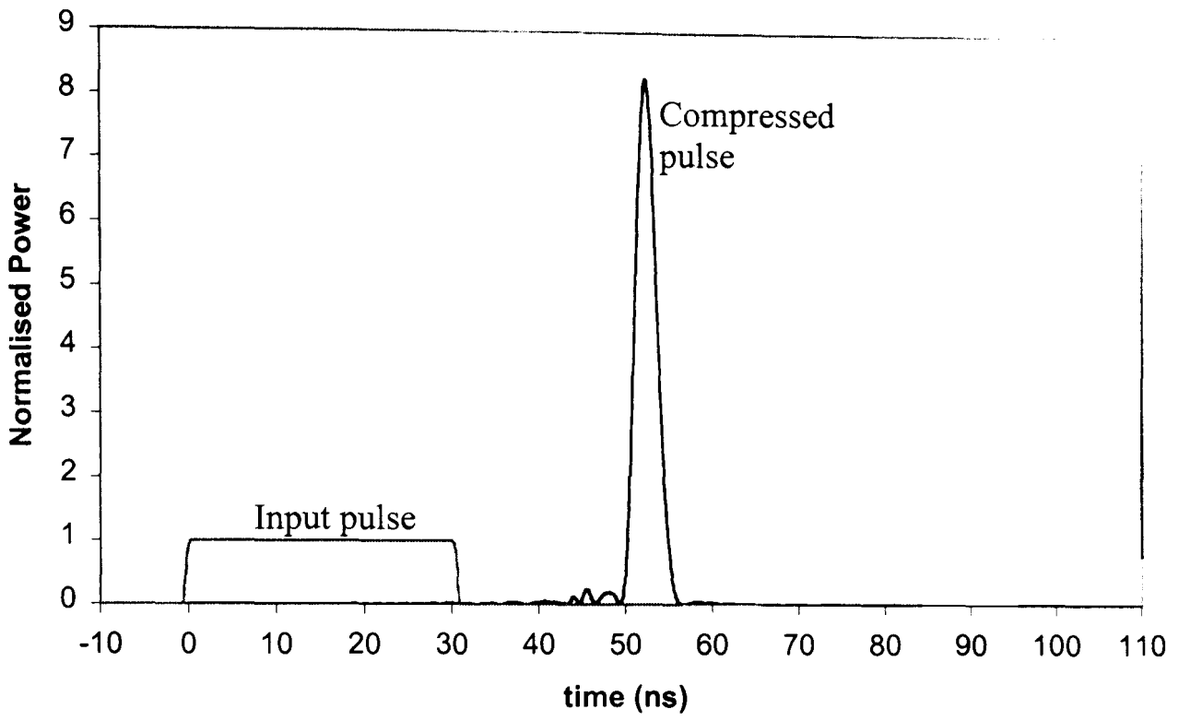

Figure 5-19 Pulse with optimum sweep with a maximum sweep rate of 20MHz/ns compressed in the aluminium waveguide using the dispersion from the method of perturbation.

With an improved sweep rate of 20 MHz/ns the optimum frequency sweep between 9.505 and 9.215 GHz with a pulse of duration of 30.3ns was calculated for the aluminium compressor. Figure 5-19 shows the simulated compression of a pulse with optimum frequency sweep in the aluminium compressor with a maximum sweep rate of 20MHz/ns. A maximum power compression ratio of 8.28 and a compressed pulse duration of 2.9ns was calculated. This gives a time compression ratio of 10.45 and hence a compression efficiency of 79%. The simple kinetic approximation gave a power compression ratio of 8.6 for the same case.

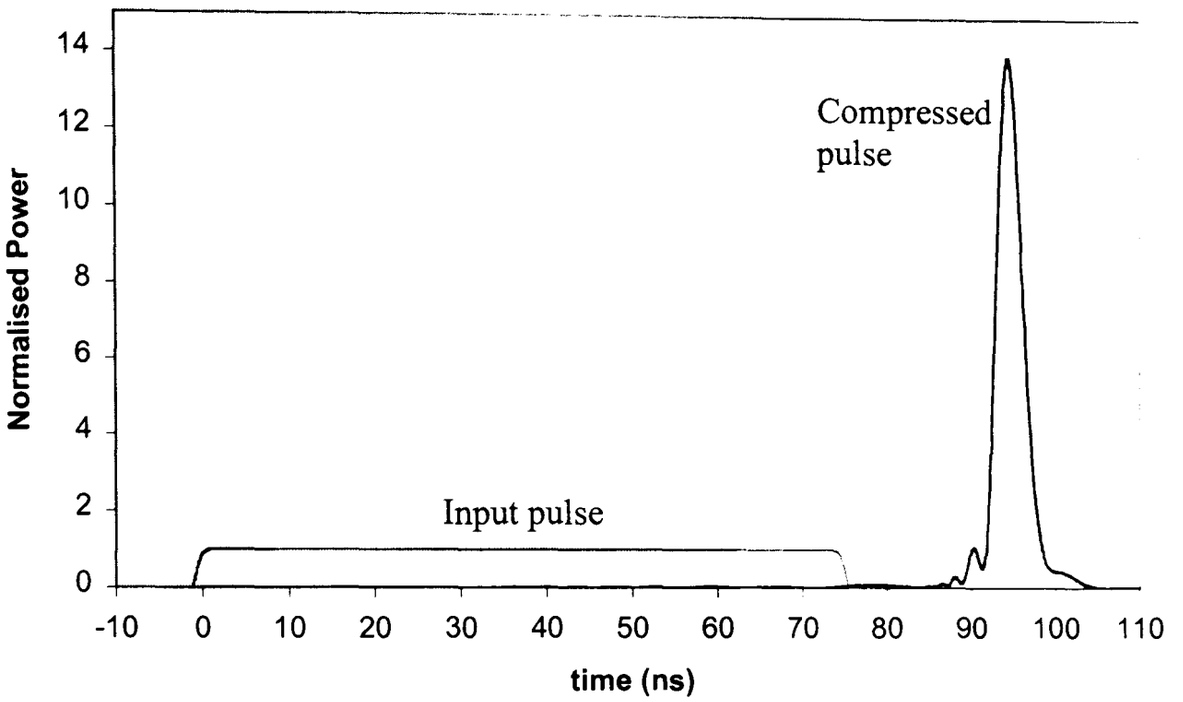

Figure 5-20 Pulse with optimum sweep with a maximum sweep rate of 20MHz/ns compressed in the modified waveguide using the dispersion from the method of perturbation.

With an improved sweep rate of 20 MHz/ns an optimum frequency sweep from 9.525 to 9.26GHz in 74.6ns was calculated for the modified aluminium compressor. Simulation of the modified compressor gave a power compression ratio of 14 and a compressed pulse duration of 3.5ns, shown in Figure 5-20. A time compression ratio of 21.3 and an efficiency of 66% was calculated. The approximation gave a power compression ratio of 14.08.

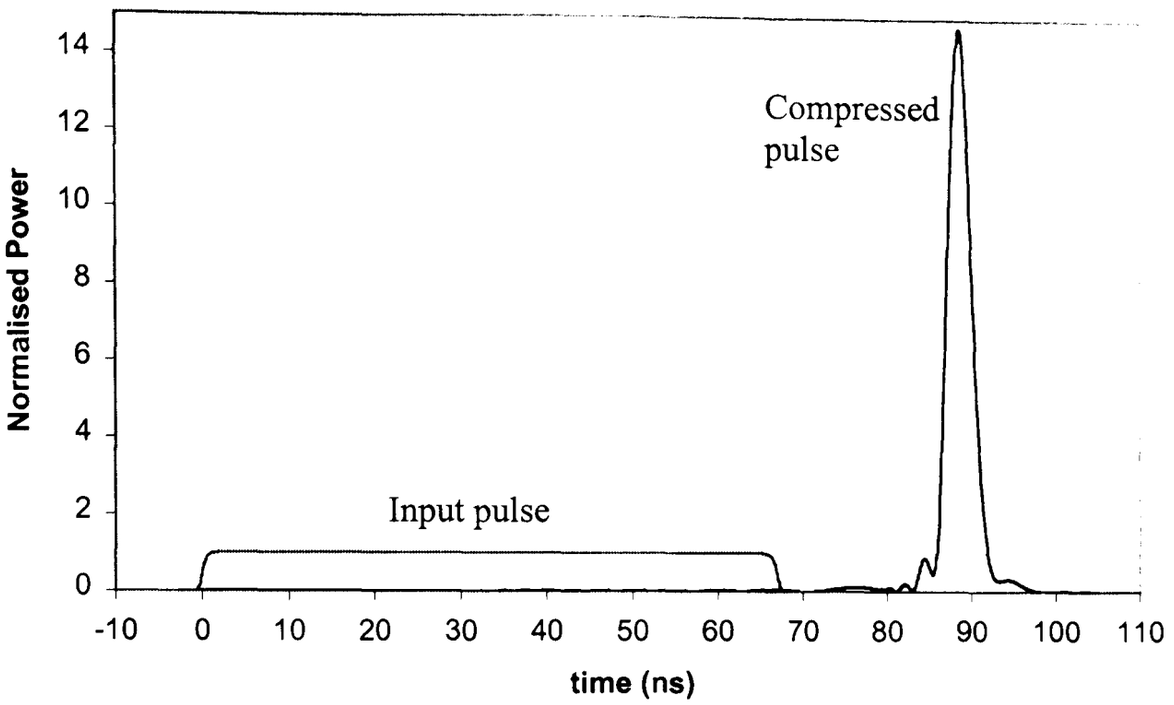

Figure 5-21 Pulse with optimum sweep with a maximum sweep rate of 20MHz/ns compressed in a copper waveguide using the dispersion from the method of perturbation.

With an improved sweep rate of 20 MHz/ns the optimum frequency sweep between 9.625 and 9.345 GHz over 67ns for the copper compressor was calculated, resulting in a power compression ratio of 14.77. A compressed pulse duration of 3.7ns and a time compression ratio of 18.1 were obtained. This gave an efficiency of 81.6%, the input and compressed pulses are shown in Figure 5-21. The simple approximation gave a similar result of 14.6 for the power compression ratio.

The dispersion characteristics simulated using MAGIC was used in the compression model along with the measured losses (see Chapter 6) to give better agreement with experiment. As the dispersion calculated using MAGIC varies slightly from the method of perturbations, new optimum sweeps must be calculated, hence the largest frequency sweep possible due to the maximum sweep rate was recalculated.

Using a maximum sweep rate of 10MHz/ns an optimum frequency sweep between 9.58-9.266GHz over 18.6ns was possible for the 68 period aluminium helix. This pulse gave an optimum power compression ratio of 3.55, a minimum pulse duration of 2.7ns, and the compressed pulse had a compression efficiency of 51.5%. The simple kinematic approximation gave a power compression ratio of 3.3 for this frequency sweep, in this waveguide.

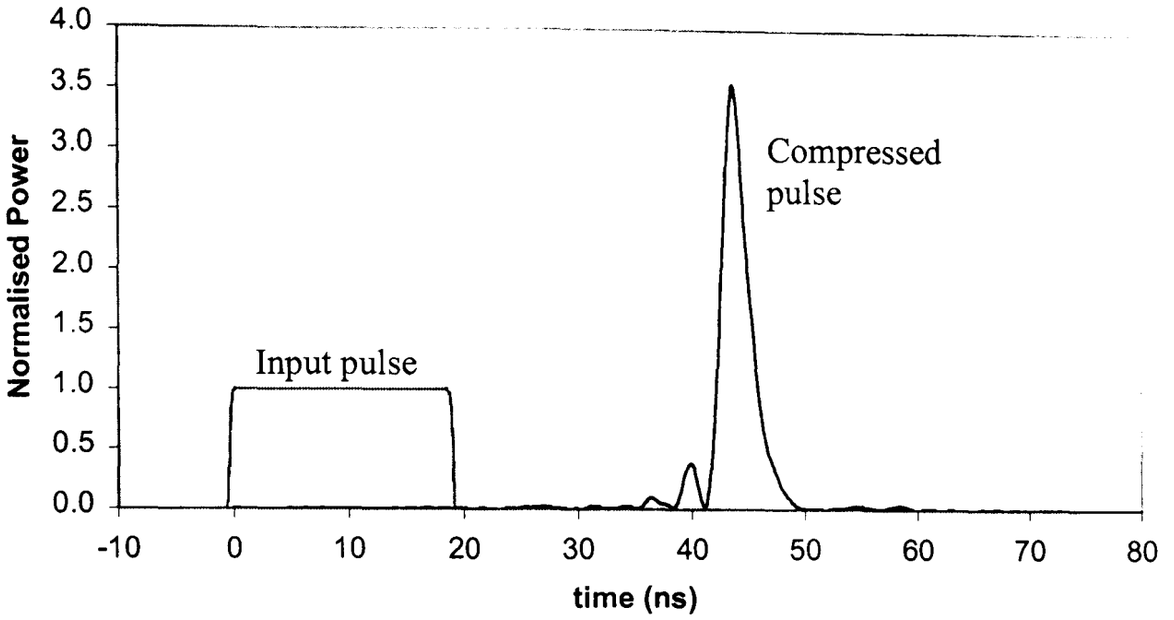

Figure 5-22 Pulse with optimum sweep with a maximum sweep rate of 10MHz/ns compressed in the aluminium waveguide using the dispersion from the numerical PIC code MAGIC.

The maximum frequency sweep for an optimum sweep for the 196.52cm modified helix was 9.57-9.335GHz. This gave an optimum pulse duration of 45.2ns and a minimum pulse duration of 4.3ns. The compressed pulse had a power 5.12 times greater than the input pulse and the duration was 10.15 times shorter giving a compression efficiency of 48.7%. It was calculated that 60% of the input energy was in the output from the waveguide, with the remaining 11.3% emerging as a sidelobe that appears ~14ns before the main pulse. The approximation predicted a power compression ratio of 5.18.

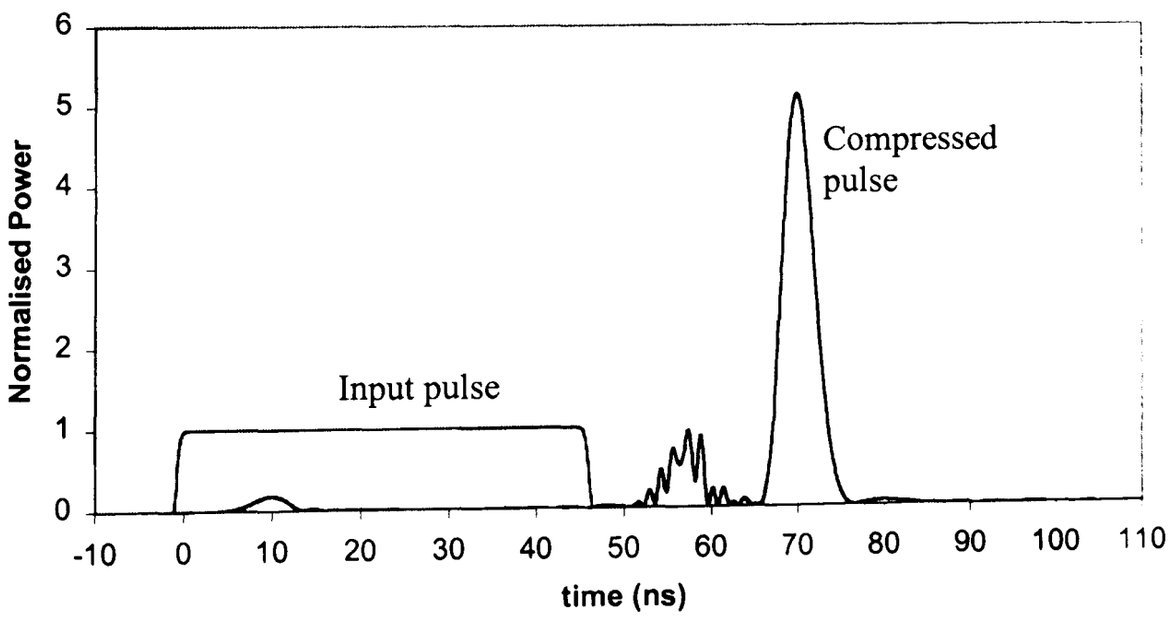

Figure 5-23 Pulse with optimum sweep with a maximum sweep rate of 10MHz/ns compressed in the modified waveguide using the dispersion from the numerical PIC code MAGIC.

The 219.64cm copper helically corrugated waveguide had an optimum power compression ratio of 6.75, using the maximum frequency sweep between 9.635-9.425GHz. The input pulse was 60.73ns long and the compressed pulse was 4.4ns long. This gave a time compression ratio of 13.8 and a compression efficiency of 47.6%. The simple approximation gave a similar power compression ratio of 6.83.

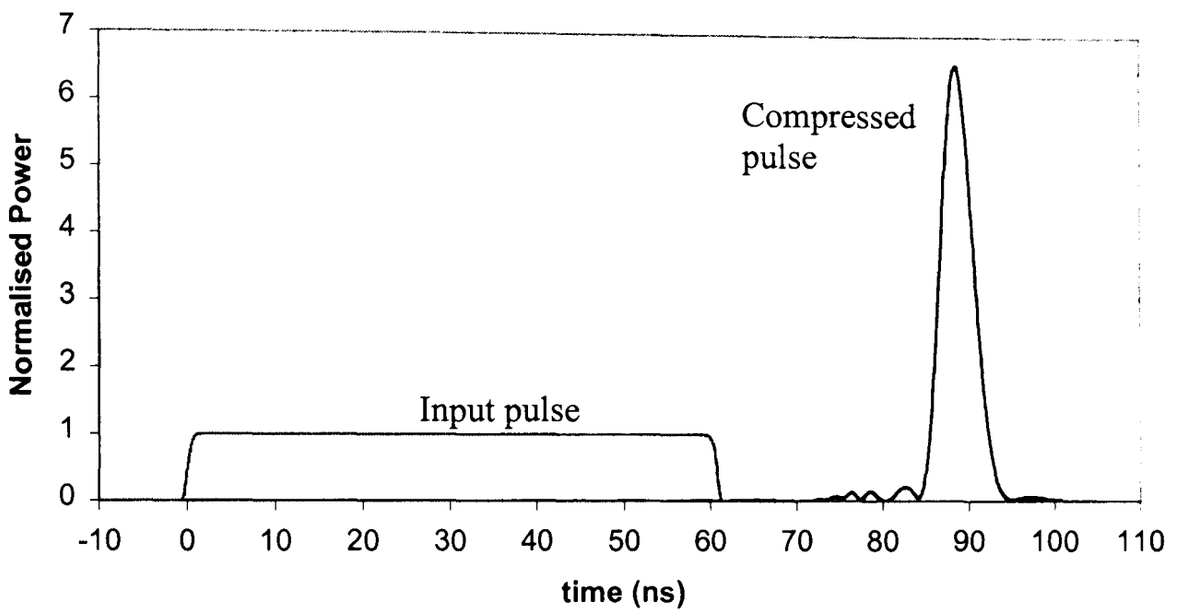

Figure 5-24 Pulse with optimum sweep with a maximum sweep rate of 10MHz/ns compressed in the copper waveguide using the dispersion from the numerical PIC code MAGIC.

Using a sweep rate of 20MHz/ns the power compression ratios increase to 5.37 for the aluminium helix, 6.45 for the modified helix, and 9.63 for the copper helix.

The difference in maximum compression ratio between the model and the simple approximation did not exceed ±16%. Thus, the approach developed can be used effectively for sufficiently precise analysis and optimisation of the pulse compression in a medium with known dispersion and losses.

5.5 Discussion

In this chapter two theoretical models of pulse compression were investigated. The first model was a simple kinematic model, where the input pulse was considered as a train of particles having different velocities and entry times. Using this model the maximum power compression ratio as a function of start and tail frequencies was calculated for each of the helically corrugated waveguides. The

second model used a Fourier optics approach to model the compressed pulse, from the input pulse.

For both methods, the dispersion characteristics were calculated first using the method of perturbations and then using the PIC code MAGIC. Table 5-1 shows a comparison of the maximum compression ratios calculated by each method for each of the helically corrugated waveguides. The Fourier optics simulation used a maximum sweep rate of 10MHz/ns and the simple kinematic approximation used the same start and tail frequencies as the Fourier optics frequency sweep.

	Method of Perturbations		MAGIC	
	Kinematic	Fourier optics	Kinematic	Fourier optics
aluminium	3.425	4.89	3.3	3.55
modified aluminium	9.7	10	5.18	5.12
copper	9.5	9.87	6.89	6.75

Table 5-1 Calculated maximum power compression ratios for each of the helically corrugated waveguides.

Using the method of perturbations the modified aluminium helix gave the highest power compression ratio, while using the MAGIC dispersion the highest power compression ratio was obtained for the copper helix. This is because the method of perturbations gave a better dispersion, from the point of view of pulse compression, than MAGIC for the modified aluminium helix. The Fourier optics simulation is the more accurate of the two methods (as will be shown in Chapter 7). The difference in maximum power compression ratio between the kinematic and Fourier optics approach never exceeded 16%.

6 Waveguide Experiments

6.1 Introduction

In order to design a helically corrugated waveguide to act as a dispersive media for pulse compression, the dispersive characteristic of the waveguide must be well known. In this chapter the experimental measurement of the dispersion curves of the helically corrugated waveguides are presented and compared to previous theoretical and numerical dispersion curves (Chapter 3 and 4 respectively).

In section 6.2 the construction of the three helically corrugated waveguides is discussed. The experimental methods of dispersion measurement are presented in section 6.3. Two methods are proposed for the measurement of dispersion, the first involves the use of a Scalar Network Analyser and is discussed in section 6.3.1. Section 6.3.2 provides details of a second method using a Vector Network Analyser and gives the experimental results of both methods. The measurements of losses in both smooth and helically corrugated waveguides are presented in Section 6.4. A comparison between the experimental results from this chapter and theoretical results from Chapters 3 and 4 are presented in Sections 6.5, 6.6 and 6.7. The experimental results of dispersion are compared to both the method of perturbation and the numerical model, and the losses are compared to the losses calculated from the method of perturbation.

6.2 Construction of the helix

6.2.1 1st aluminium

The length of the waveguide was 184.96m and was constructed out of aluminium consisting of 64 individual sections each equal to one period in length for ease of manufacture, with a period of the corrugation 28.9mm (shown in Figure 6-1). Entrance tapers each equal to 4 periods in length were placed at the input and output

of the compressor where the amplitude of the corrugation was tapered linearly to meet the smooth input/output waveguides.

This was designed and manufactured at the University of Strathclyde using a CNC (Computer Numerically Controlled) Mill.

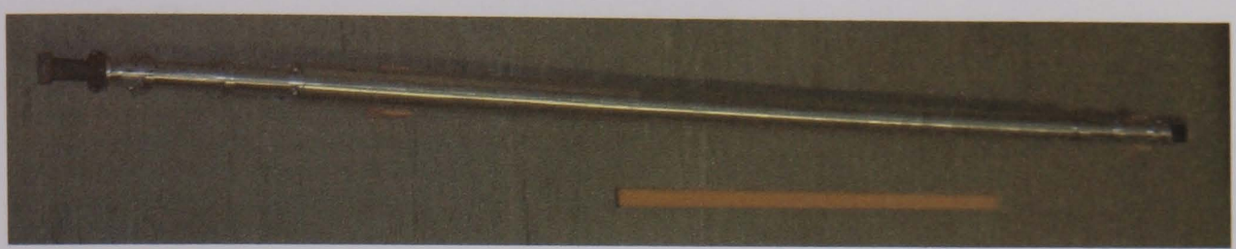

Figure 6-1 Aluminium helically corrugated waveguide including helical tapers, elliptically shaped polarisers and rectangular-to-circular converters with metre stick shown for perspective.

6.2.2 Modified aluminium

The 1st aluminium helix was modified by boring a circular hole of diameter 27.68mm down the inside of the helical waveguide which had a mean diameter of 29.4mm and a corrugation depth of 1.75mm. The cross section of this waveguide is shown in Figure 6-2. The same technique was applied to the tapered sections.

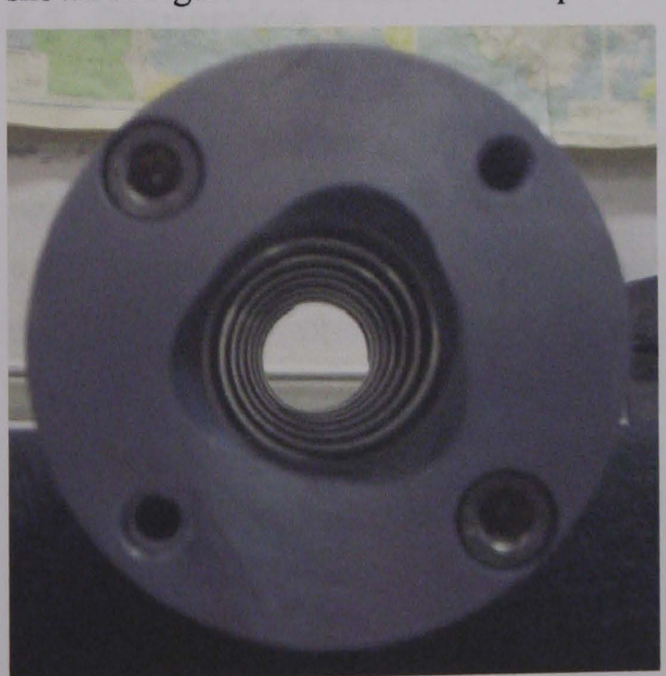

Figure 6-2 Digital photo of the modified aluminium helically corrugated waveguide.

6.2.3 Copper

A 3rd helix was created using copper electroforming. Using electroforming a thick layer of metal was built up over an aluminium base by electro chemical deposition[74]. Copper has a higher electrical conductivity than aluminium and hence has less joule losses when used as a waveguide. The copper helix also had fewer sections, consisting of 9 electroformed copper sections each 8 periods long, one of these sections is shown in Figure 6-3. Which resulted in fewer connections where reflections could occur.

Figure 6-3 Digital photo's of the copper helically corrugated waveguide.

6.3 Dispersion

The dispersion characteristics of rotating waves in a waveguide with a helical corrugation strongly depends on the direction of their rotation, the dispersion of the wave counter rotating with respect to the helix is significantly modified, while the dispersion of the wave co-rotating with the helix is practically unperturbed. This phenomena was used to devise two methods of measuring the dispersion characteristics of the helically corrugated waveguide based on two different measurement instruments, the first used a Scalar Network Analyser (SNA) and the second a Vector Network Analyser (VNA).

6.3.1 Measurement of the dispersion characteristics of the helically corrugated waveguide using a SNA

In order to obtain the dispersion curve of the operating eigenwave of the helical compressor the angle of rotation was measured for the linearly polarized TE11 wave when passed through the waveguide. The difference in their axial wavenumbers, $\Delta k_z = k_z^- - k_z^+$, results in the rotation of the polarization vector of the initial linearly polarized wave by the angle $\Delta\varphi = \Delta k_z L/2$, where L is the effective length of the helical structure (this effect is well known for gyrotropic media in optics[61]). The change in axial wavenumbers results in a change of phase of the wave rotating against the helix at the output equal to $\Delta k_z L$, where L is the length of the helical waveguide. The change in phase corresponds to double the angle of rotation of the polarisation vector.

To measure the angle of rotation, the output of the helix was connected to a piece of standard rectangular X-band waveguide using a circular-to-rectangular waveguide converter, where only the fundamental mode of the waveguide was above cut-off in the frequency region of operation. As this mode has a clearly defined polarisation, only waves with an identical polarisation can propagate in the waveguide. The waves entered and exited into the helically corrugated waveguide via helically corrugated tapers which were used to reduce reflections.

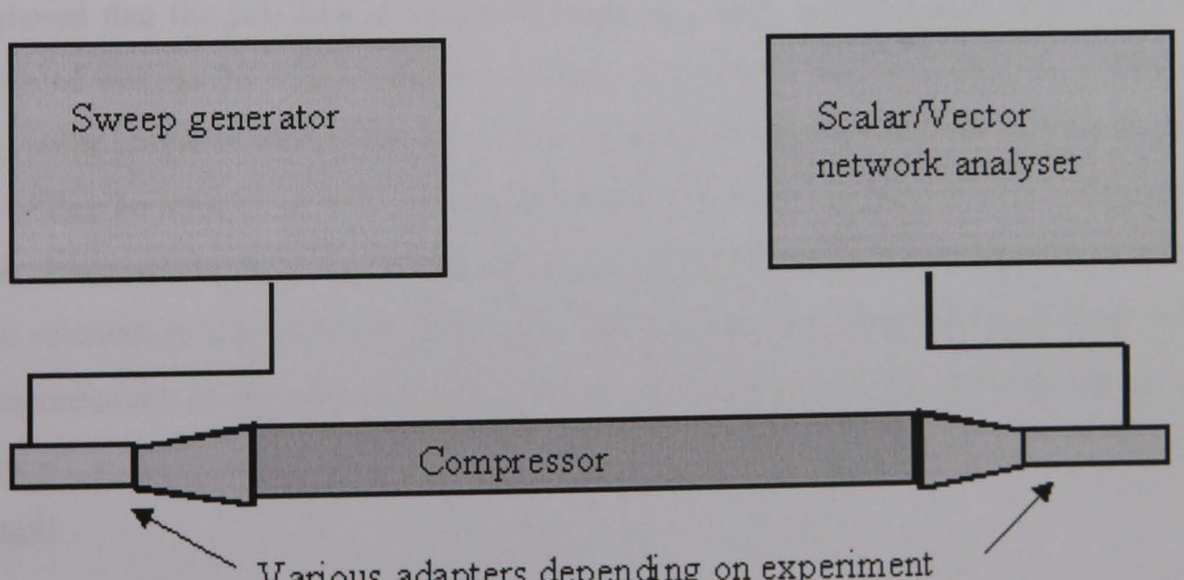

Figure 6-4 Experiment set-up for dispersion measurement.

A scalar network analyser (SNA) and a synthesized sweep generator were used to measure the radiation transmitted through the helix as a function of frequency, the helix was connected between the launching and detecting waveguide which consisted of two identical X-band waveguide components as described in the previous paragraph, as shown in Figure 6-4. It is clear from a qualitative analysis that the difference in the axial wavenumbers Δk_z and, hence, the polarization rotation $\Delta\varphi$ was an increasing function of frequency, therefore when using a sufficiently long helical structure and a fixed orientation of the receiving port an SNA frequency scan represented a number of minima (almost zeros) and maxima which corresponded to polarizations of the output radiation perpendicular or parallel to the polarization of the receiving port, an example of which is shown in Figure 6-5 for the copper waveguide. The frequencies of the minima, f_n, sharply indicated by a rapid decrease in transmission, were measured by the SNA and plotted on a logarithmic scale, and were accurately measured using the cursor function on the SNA with the points for the dispersion diagram calculated as follows:

$$k_z^-(f_n) = k_z^+(f_n) + \frac{2}{L}\left(\frac{\pi}{2}(2n-1) + \varphi_R\right);\ n = 1, 2, \ldots \qquad \textbf{Equation 6-1}$$

where φ_R is the angle of the azimuthal orientation of the rectangular waveguide in the receiving port with respect to that in the launching port. It was assumed that the two helical tapers of length L_{tap} each acted together like a single piece of waveguide with a regular corrugation of length L_{tap}, i.e. $L=L_{reg}+L_{tap}$, where L_{reg} is the length of the section which has a regular corrugation. By varying the angle φ_R within an interval of $\pi/2$, a sufficient number of points for the dispersion diagram was measured (in the measurements of long structures for the pulse compressor only one orientation was needed). When the experimental equipment did not allow the measurements of the minimal frequency, f_1, the number of 180° polarization turns (integer n in Equation 6-1) was ascertained by measuring structures of different length.

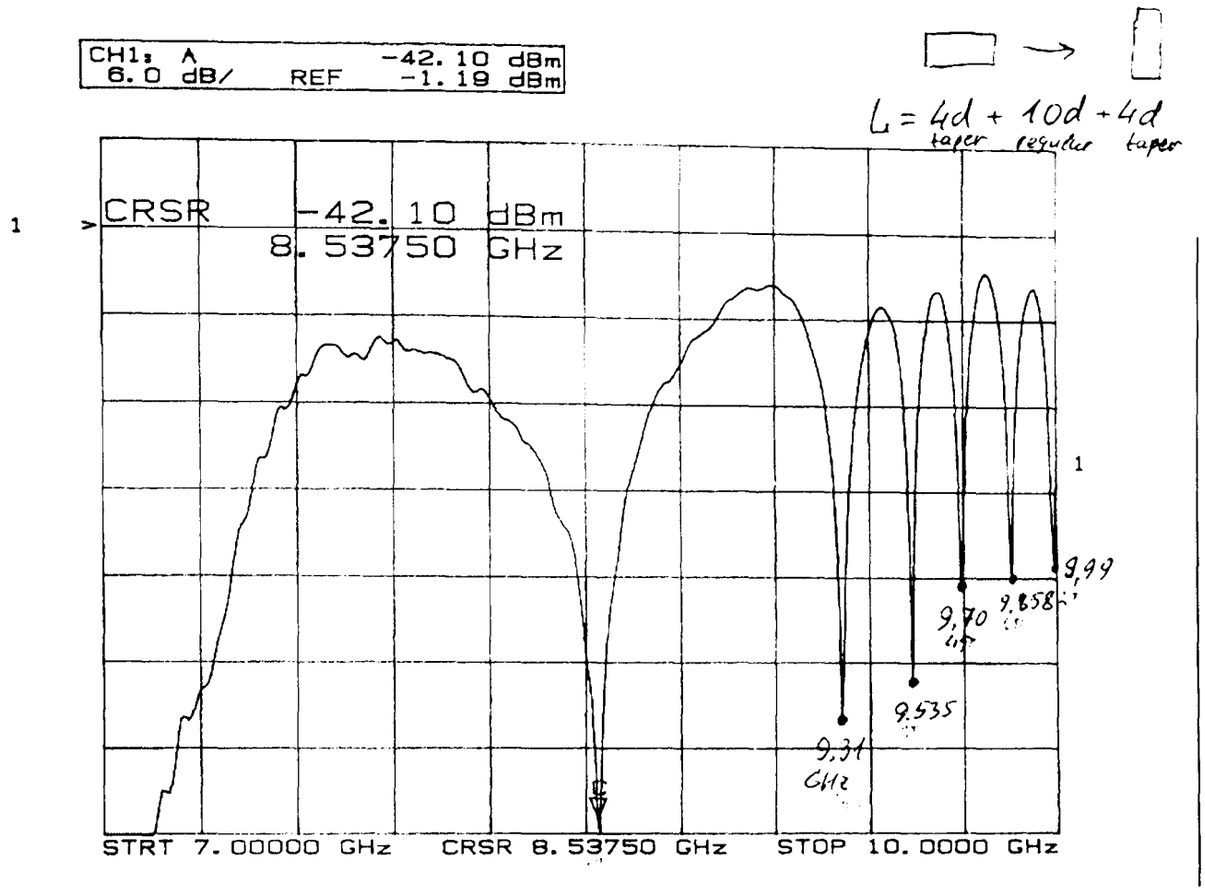

Figure 6-5 Amplitude measurement of a linearly polarised TE11 wave at the output of a 10 period section of the 1st aluminium helix, including both 4 period tapers, using a SNA.

The experimental approach for the eigenwave dispersion measurement discussed relied on the approximation that the left-handed wave in the helical structure has the same dispersion relation as the $TE_{1,1}$ mode of the smooth circular waveguide. However a large corrugation amplitude can result in a considerable change in the dispersion and therefore lead to systematic inaccuracy. Another source of inaccuracy of this method is the inexact assumption of the effective length of the structure. It was found that the inaccuracy occurring due to the estimation of the effective length $L=L_{reg}+L_{tap}$ was diminished by increasing the length of the regular corrugation section with respect to the length of the tapers.

6.3.2 Measurement of the dispersion characteristics of the helically corrugated waveguide using a VNA

In order to experimentally measure the dispersion characteristics of a helically corrugated waveguide free from the sources of inaccuracy associated with the SNA

approach, a vector network analyser (VNA) has been used to directly and accurately measure the difference between the phases of the signal at the input and output calibration planes as a function of the frequency. If an experimental set-up provides excitation of a sufficiently pure eigenwave and a waveguide with a constant or periodically changing cross-section along its axis is used then the axial wavenumber of the eigenwave, k_z, remained constant along the axis, and a phase difference, $\Delta\psi$, between the eigenwave electromagnetic fields taken at two different cross-sections separated by length, L, could be determined as follows: $\Delta\psi=k_zL$. Therefore, by measuring the phase $\Delta\psi$, the eigenwave axial wavenumber k_z can be measured in a piece of regularly corrugated waveguide of length, L.

Two special elliptically shaped polarisers have been employed so that circularly polarised waves are introduced to the helix providing excitation of a pure eigenmode in a piece of regular helically corrugated waveguide. A circularly polarized $TE_{1,1}$ mode (right- or left-handed) was converted from a linearly polarized wave by passing through a broad-frequency-band polarizer having in the middle an elliptical cross-section azimuthally oriented by +45° or -45° with respect to the polarization vector of the incident wave.

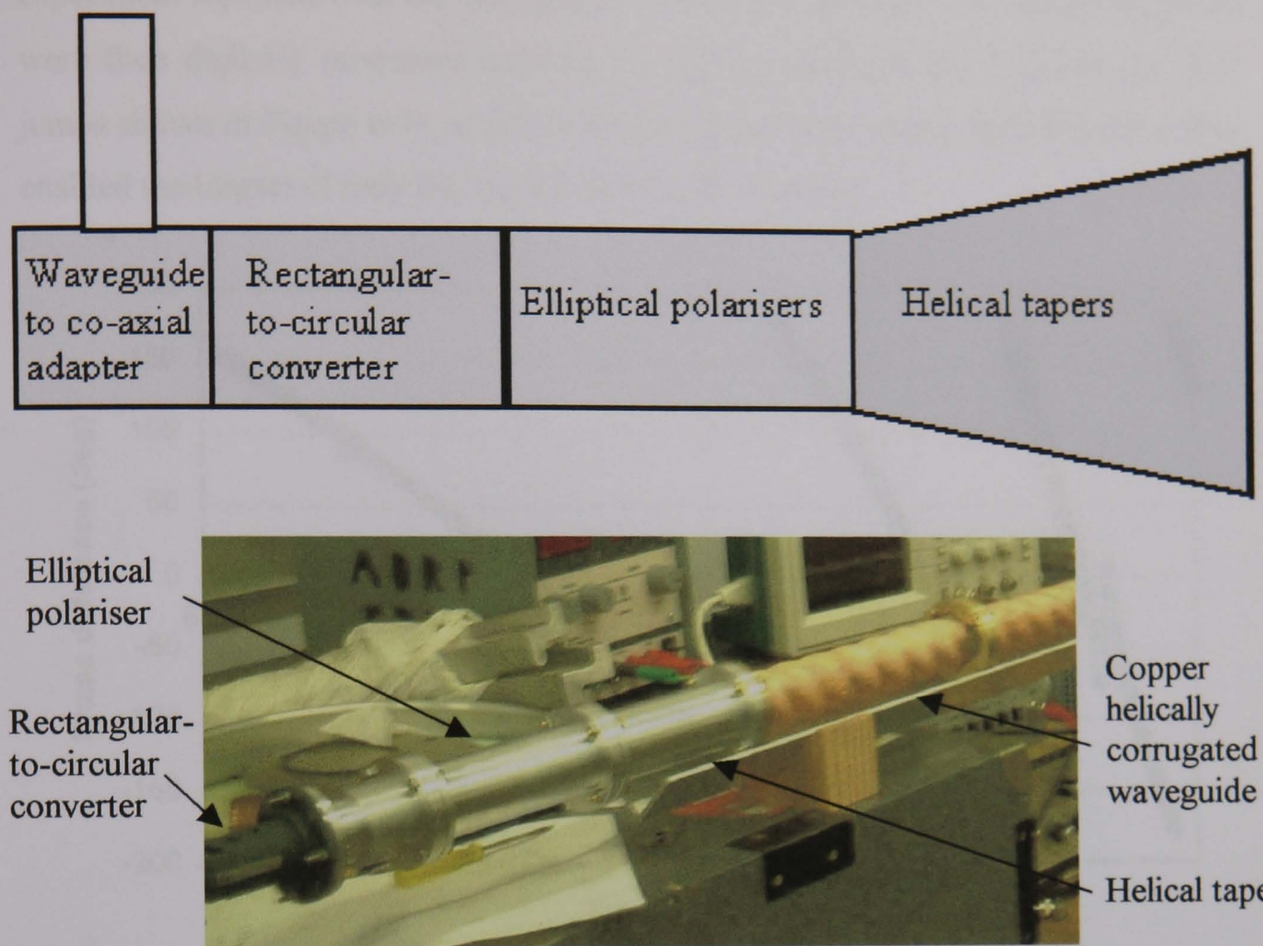

Figure 6-6 Adapters required to inject the wave from the co-axial cable to the helical waveguide.

A co-axial to waveguide adapter, connected to port 1 and 2, respectively, of the VNA, was required to inject the signal in to the waveguide. The waveguide had a rectangular cross-section, which was tapered up to a circular waveguide using a rectangular to circular waveguide converter. The circular waveguide had a radius chosen so that only the fundamental TE11 mode of a circular waveguide could propagate. The elliptical polarisers were used to convert the linearly polarised wave to a circularly polarised wave with the correct rotation to interact with the helix. The circular cross-section was slowly converted to a helical cross-section, by tapering the corrugation depth over 4 periods, to improve the impedance matching which minimises reflections, as shown in Figure 6-6. The VNA was calibrated using a 10 term, Line-Reflect-Line calibration that excluded isolation[75]. The calibration planes were each set to be at the connection planes between the elliptical polarizer and the helical taper at each end of the experimental set-up. For the phase evolution of the helically corrugated waveguide to be measured, first, the phase evolution of the corrugated waveguide bounded by two 4 period tapers was measured with the

experiment repeated with the corrugated waveguide removed. The measured phases were then digitally processed resulting in continuous functions (without the 360° jumps shown in Figure 6-7), which were subtracted, from each other. This procedure enabled the impact of only the regular helix to be selected.

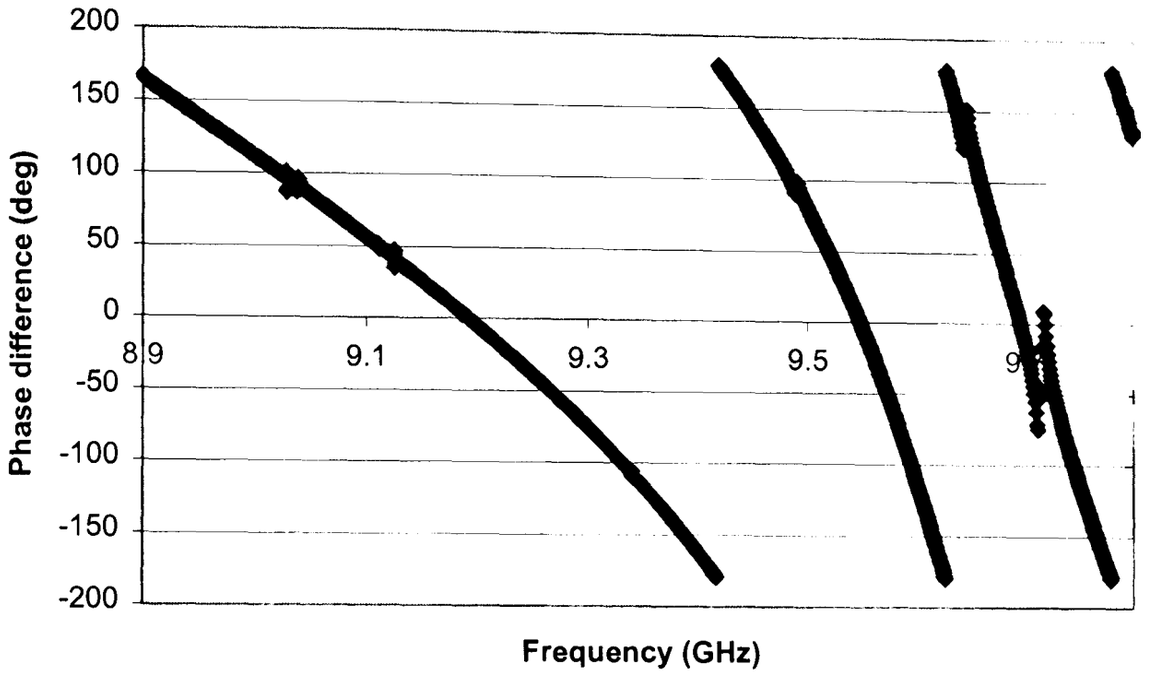

Figure 6-7 Change in phase due to an 8 period section of the copper helix measured using a VNA.

The phase value measured by the VNA was proportional to the waveguide length L and the wave longitudinal wavenumber k_z i.e. $k_zL=\varphi+2\pi n$ where φ is the principal value of the phase change and n is an integer. The length of the waveguide has been chosen such that for the start frequency the change in phase is given by, $\varphi_0=k_zL\leq 2\pi$ where k_z is estimated using either coupled wave theory or MAGIC. This allowed $n=0$ at the start frequency and the exact value of k_z to be measured.

Rotating the polarisers by 90 degrees can alternate the rotation of the mode propagating through the helix. The co-rotating circularly polarised TE_{11} dispersion was measured and compared to a normal TE_{11} mode in a circular waveguide of the same mean radius as the helix. Any difference can be attributed to the weak influence of the helix on the wave, which is ignored by the coupled wave approximation.

Using the same techniques as described above the dispersion diagram of the eigenwave has been evaluated for the aluminium (Figure 6-8), modified aluminium (Figure 6-9) and copper helix (Figure 6-10). The small level of noise in the

experimental graph was due to imperfect connections in the experimental set up but this did not affect the final results.

The aluminium helically corrugated waveguide was analysed with the SNA using its full 64 period length with both 11.56cm aluminium tapers.

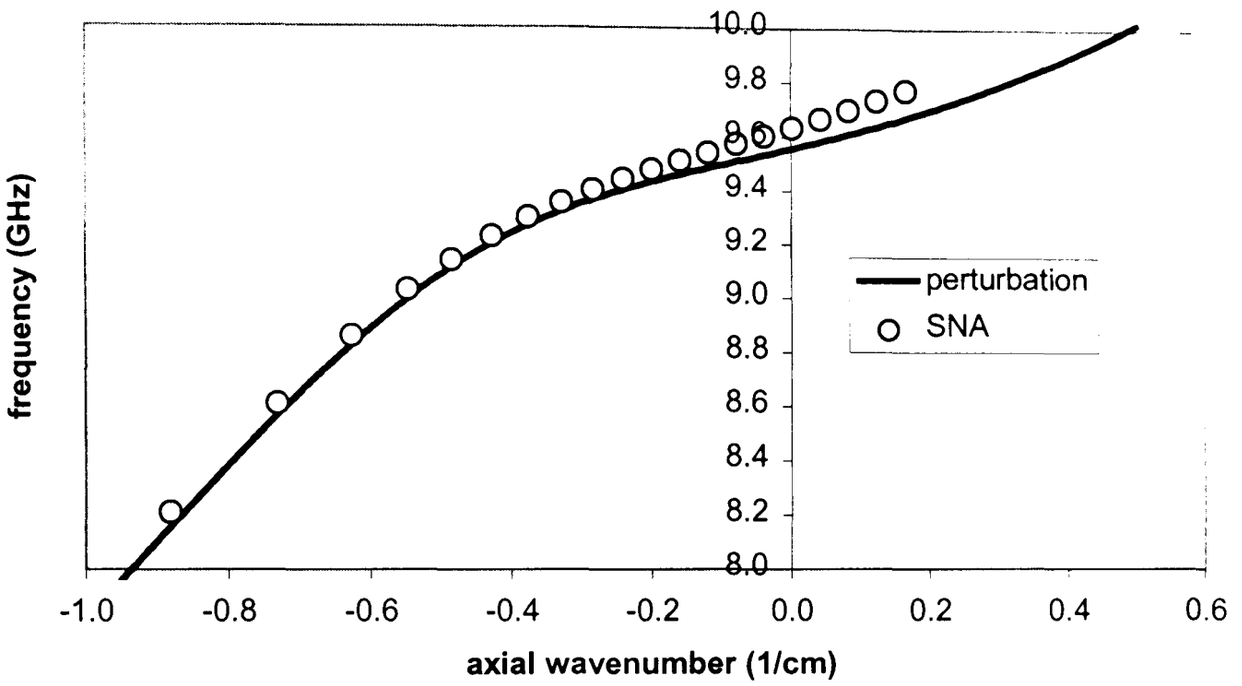

Figure 6-8 SNA measurement of dispersion and perturbation theory of the aluminium helix.

The Group velocity dispersion of the aluminium helical waveguide was, measured using the SNA approach and had a minimum group velocity of 4.56 cm/ns at 9.57GHz. There was no measurement of the aluminium helix using the VNA, as it was modified before the VNA was obtained.

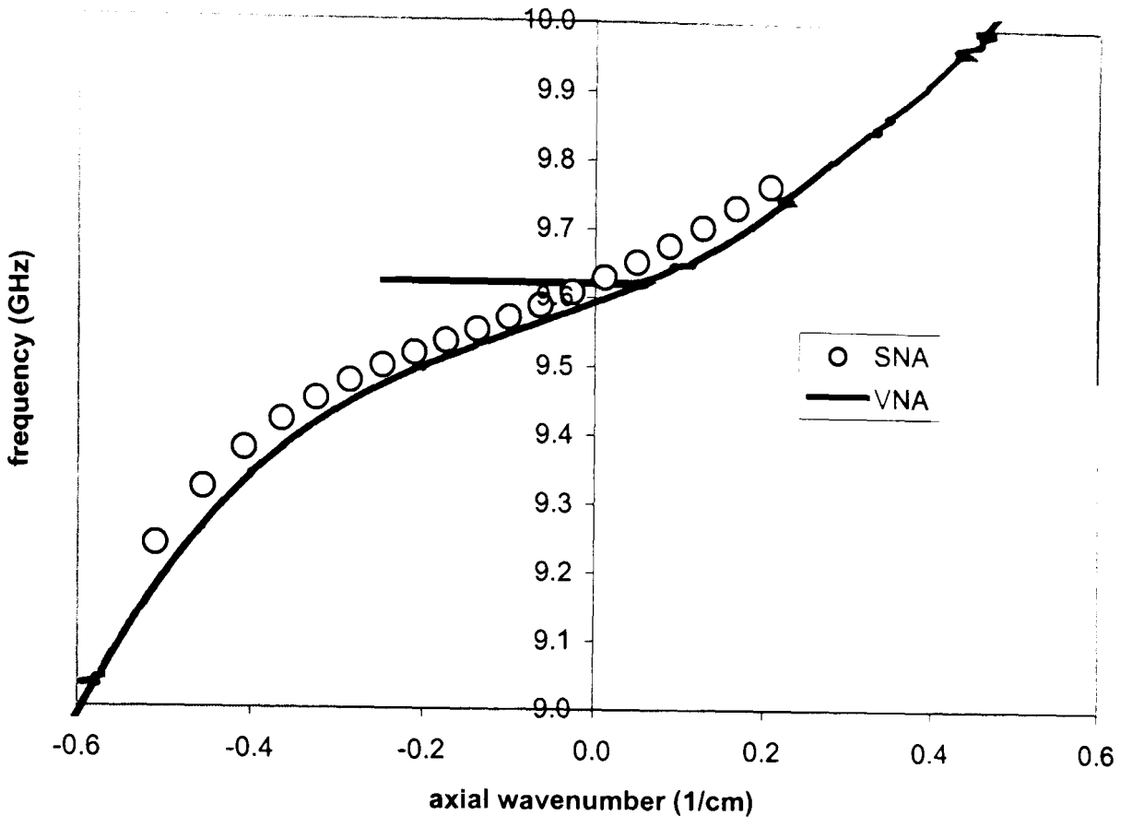

Figure 6-9 Dispersion measured using the SNA and VNA techniques for the modified aluminium waveguide.

The modified helically corrugated waveguide was analysed using both the SNA and VNA. The SNA was used to investigate the polarisation rotation in the full 184.96cm length of modified helix with both 4 period modified tapers. The VNA approach used a 7 period section of modified waveguide. The minimum group velocity found from the SNA approach was 2.94 cm/ns at a frequency of 9.54GHz while the VNA approach gave a minimum group velocity of 2.96 cm/ns at 9.56GHz. The dispersion of the unperturbed mode deviated slightly from the dispersion of a TE_{11} mode in a smooth circular waveguide of the same mean radius. This was due to the complicated structure of the modified helically corrugated waveguide and the mean radius, which was calculated using a Fourier approach.

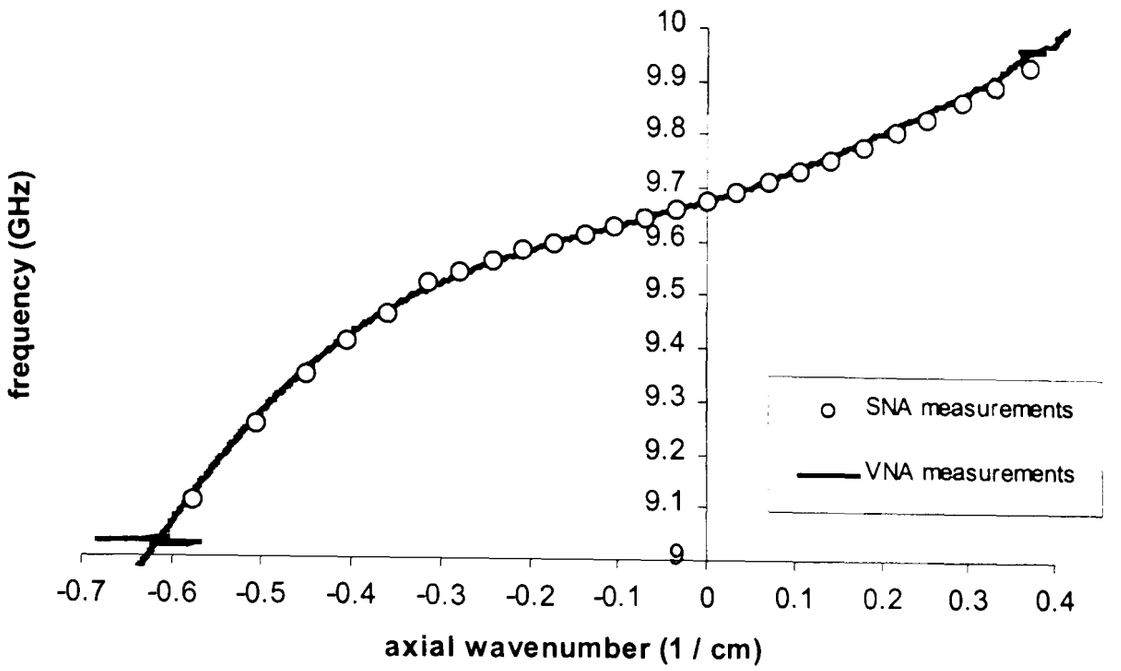

Figure 6-10 Comparison of the two experimental techniques for measuring the dispersion characteristics of the copper helically corrugated waveguide.

The full 72 period length of copper helix with both 11.56cm modified tapers were used in the SNA approach and one 23.12cm section of copper waveguide was used in the VNA experiment. The copper helix was found to have a minimum group velocity of 3.1cm/ns at a frequency of 9.58GHz by the SNA approach and a minimum group velocity of 2.9cm/ns at 9.62GHz using the VNA technique. As can be seen in Figure 6-11 the VNA approach does not give a clear plot of the GVD. This was due of the large number of data points in the dispersion plot, where a small error in the phase measurement can create a large error in the gradient between two adjacent points. However the outline of the GVD curve follows the same general trend as the SNA GVD plot. If a GVD is required a best-fit polynomial of the dispersion curve can be found, and the GVD can be derived from the derivative of the angular frequency with respect to axial wavenumber.

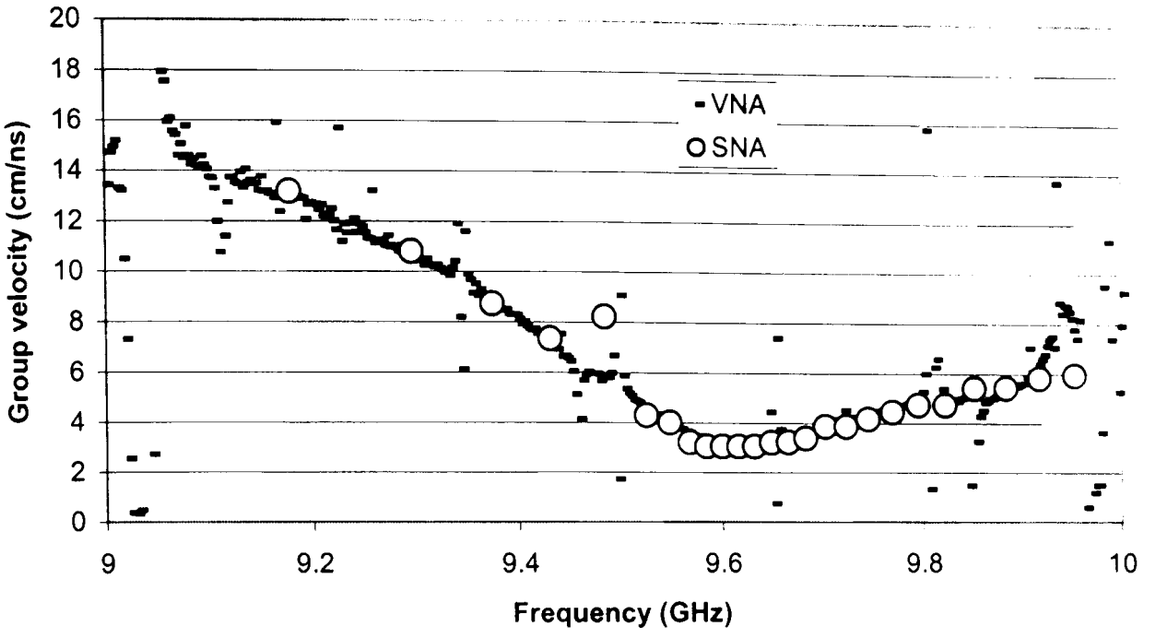

Figure 6-11 Group velocity dispersion calculated from the SNA and VNA techniques for the copper helix.

The unperturbed wave in the copper helically corrugated waveguide was found to give good agreement with the dispersion of a TE_{11} mode in a smooth circular waveguide of the same mean radius.

The VNA approach can also be used to show that the polarisation rotation of a linearly polarised TE_{11} wave due to a linearly tapered section of helically corrugated waveguide is roughly equal to the polarisation rotation due to half it's length of regular helically corrugated waveguide. If the change in phase due to the operating eigenwave propagating through 8 periods length of tapered section and 4 periods length of regular helical section, we can find the polarisation rotation by subtracting the change in phase due to a wave with opposite circular polarisation.

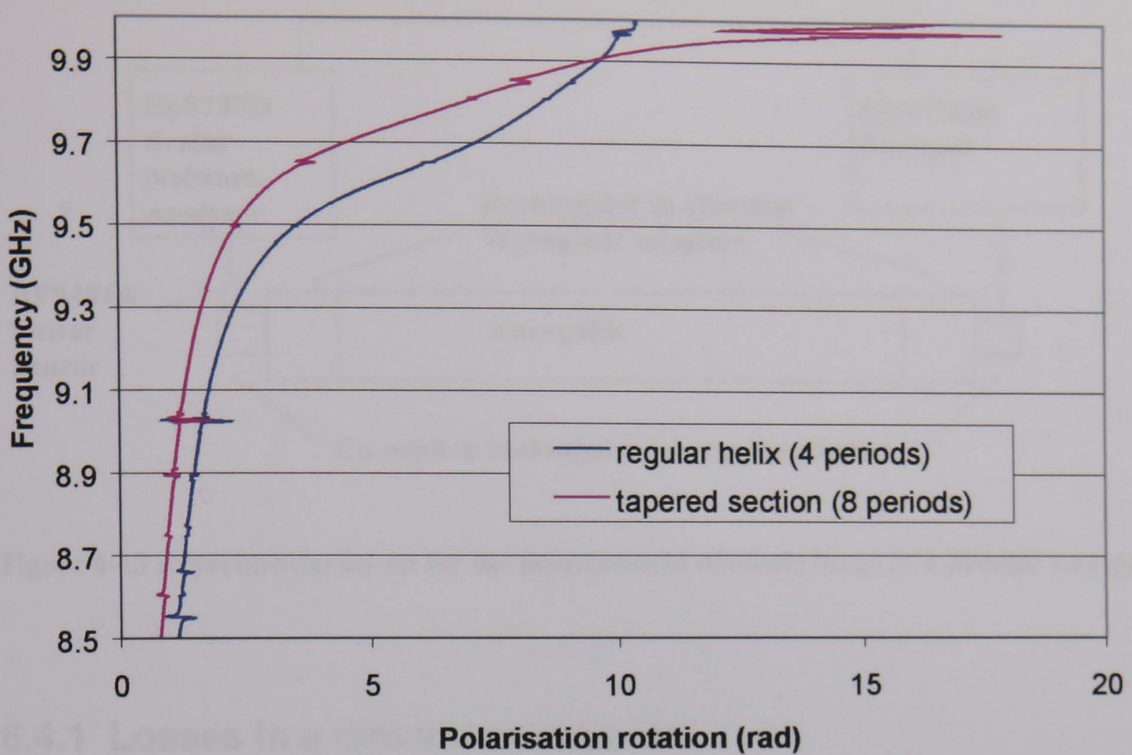

Figure 6-12 The polarisation rotation of a linearly polarised TE_{11} wave propagating through a 4 period length of regular helically corrugated waveguide compared to the polarisation rotation due to an 8 period length of taper.

In Figure 6-12 it is shown that the polarisation rotation due to the two sections are roughly in agreement between the frequency range 8.5GHz to 9.9 GHz.

6.4 Losses

The ohmic losses in the waveguide play an important role in the final compression ratio. To have an accurate value for the ohmic losses the imaginary component of the axial wavenumber was measured as a function of frequency. With the transmission coefficient of a wave propagating through the compressors measured as a function of frequency. This was achieved using a sweep generator and a scalar network analyser as shown below in Figure 6-13.

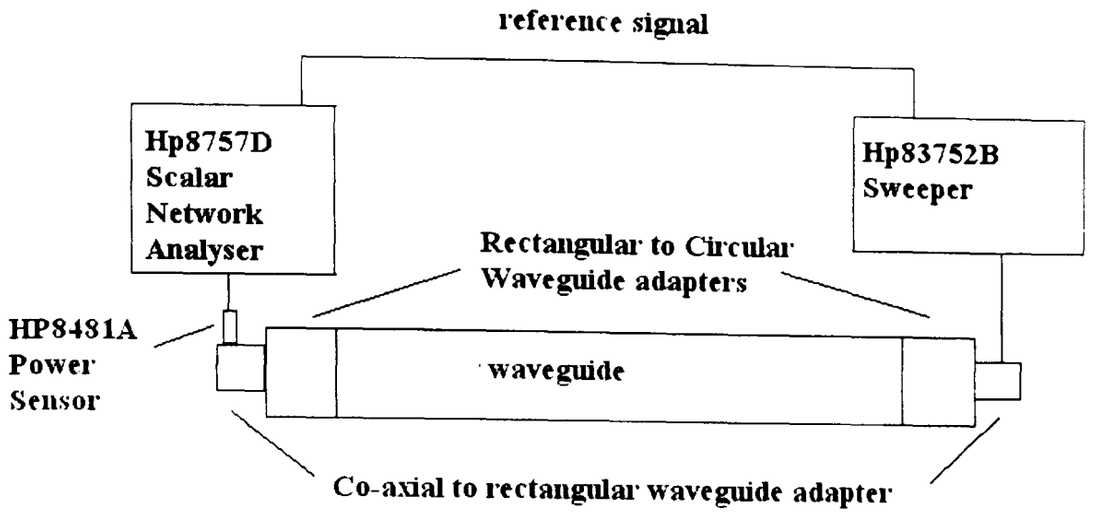

Figure 6-13 Experimental set-up for the measurement of ohmic losses in a circular waveguide.

6.4.1 Losses in a circular waveguide

HP 8481A detectors, which are part of the scalar network analyser (SNA) system, were used. A through calibration was performed and saved, where the input and output waveguides were connected directly without the circular waveguide present, this allowed the output power to be measured as a ratio of the input power. The circular waveguide was then placed between the input and output waveguides and the ratio of the power detected with and without the circular waveguide was displayed against the frequency sweep.

To find the electrical conductivity of the waveguide material, the measured curve was fitted to a curve obtained by analytical calculation. The best fit occurred with an electric conductivity for the circular waveguide equal to $1.95*10^7$ siemens/ metre, shown in Figure 6-14. (1 siemens is 1 ampere/volt)

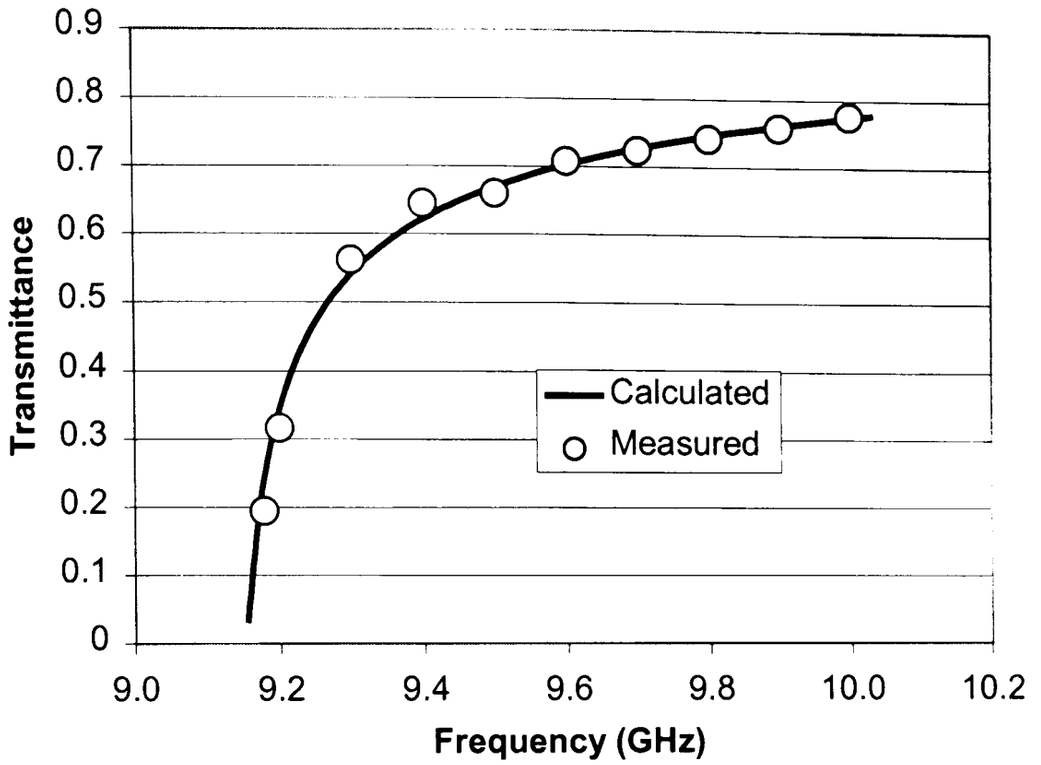

Figure 6-14 Transmission as a function of frequency in a 3.3 metre length of circular waveguide.

6.4.2 Losses in a helical waveguide

The losses in the waveguide were found by measuring the transmittance of the operating eigenmode as a function of frequency using a Scalar network analyser. The elliptical polarisers were used so that all of the energy passed through the waveguide in the operating eigenwave. The scalar network analyser was calibrated so that only losses due to the helix were measured.

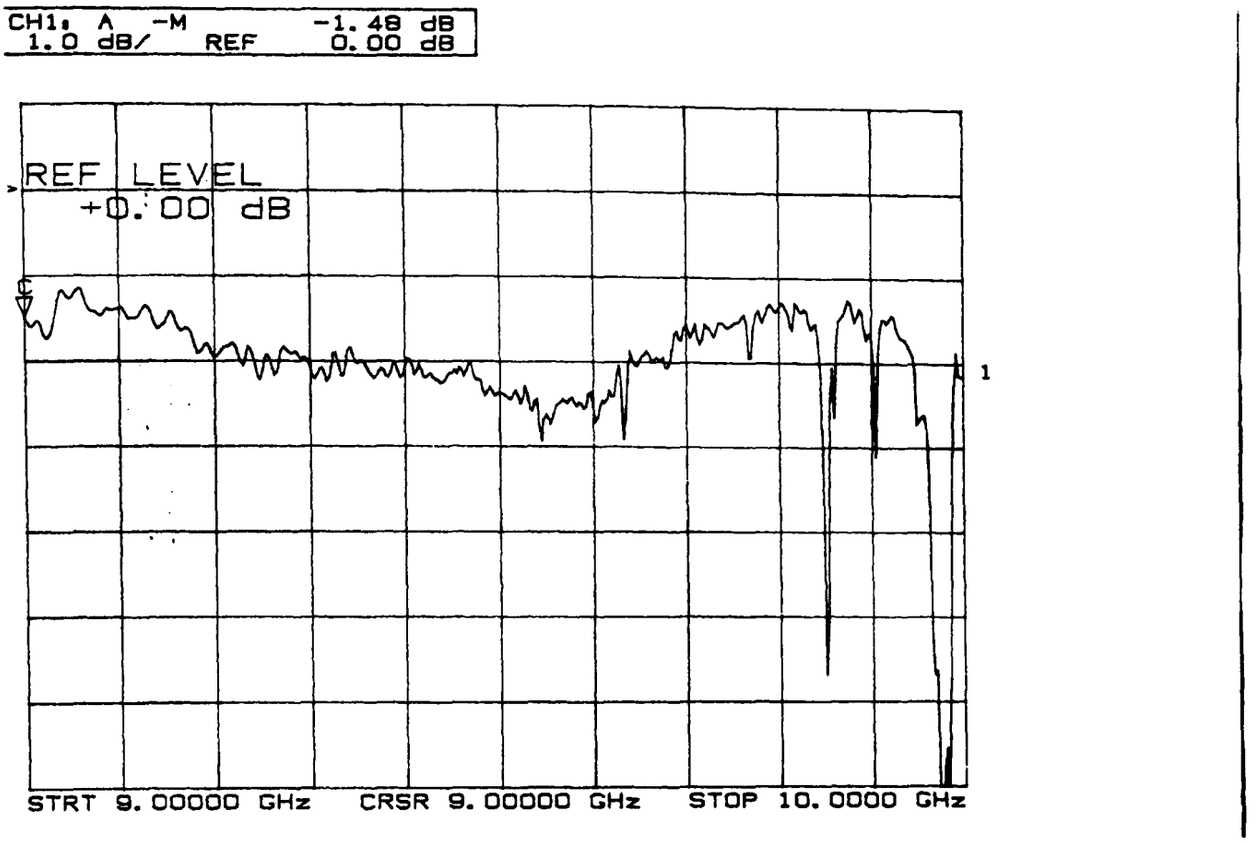

Figure 6-15 Transmission coefficient of the eigenwave in the 64 period aluminium helix measured using a SNA.

Between the frequency bandwidth of 9.0GHz to 10.0GHz the transmission coefficient of a 64 period aluminium helix was found to vary between -1.11dB and -2.56dB. Figure 6-15 shows the minimum transmission occurring at 9.55GHz.

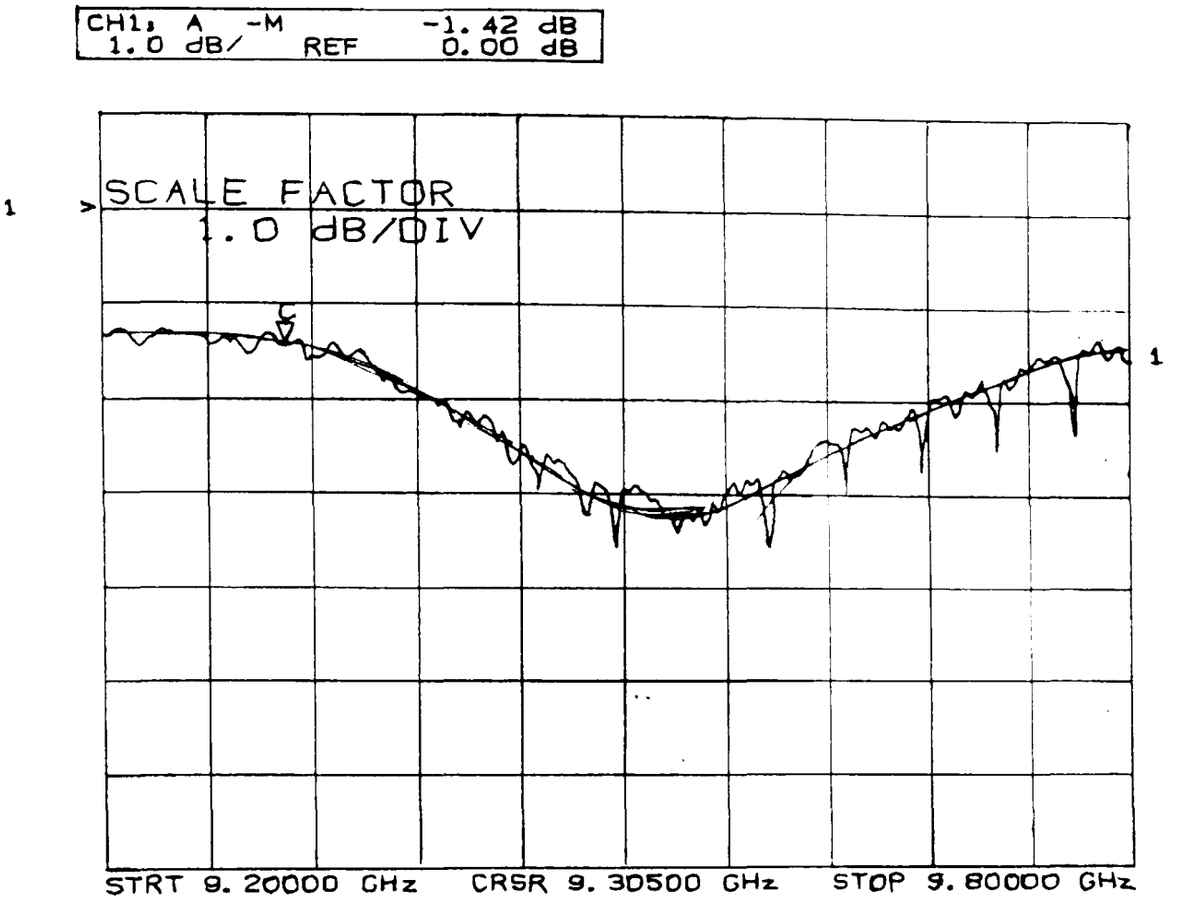

Figure 6-16 Transmission coefficient of the operating eigenwave in the 64 period modified aluminium helix measured using a SNA.

The transmission of a 64 period modified aluminium helix was found to vary between –1.28 to -3.22dB within the frequency range between 9.2 to 9.8GHz, as shown in Figure 6-16.

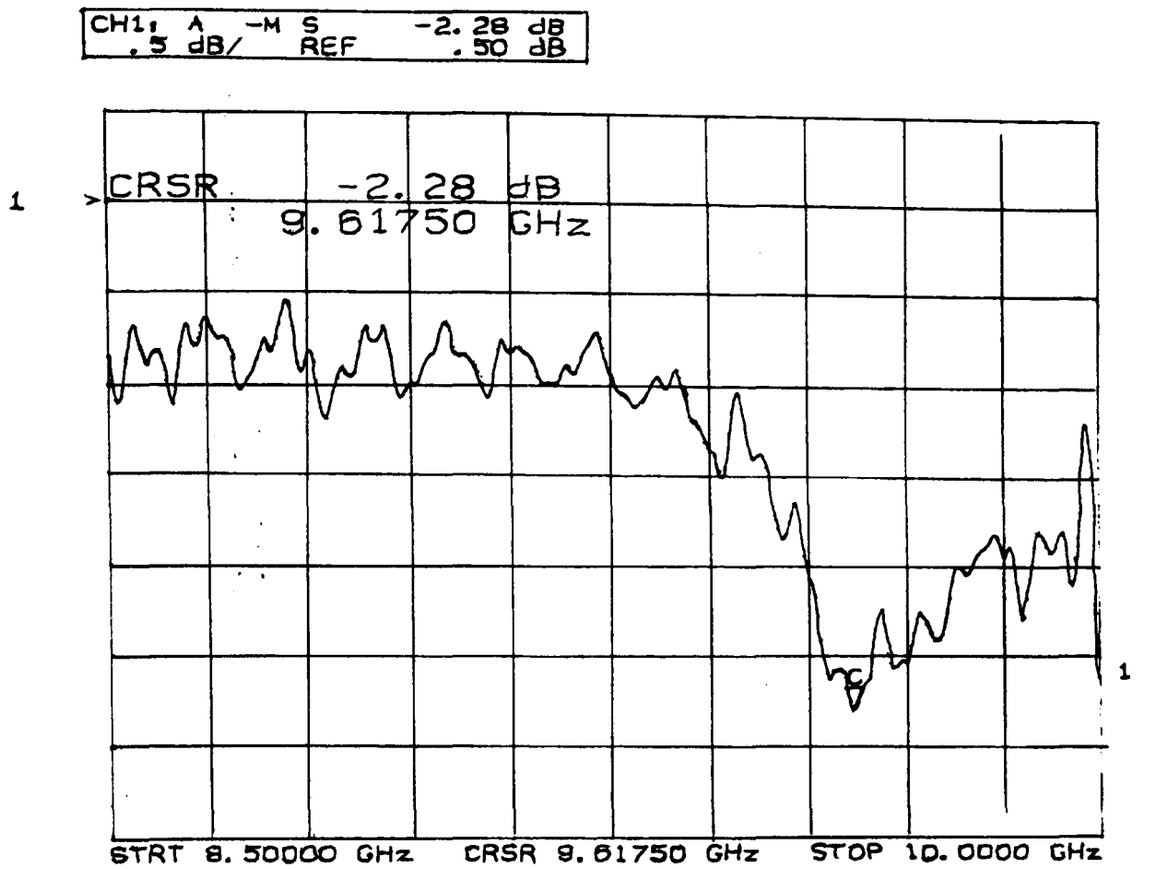

Figure 6-17 Transmission coefficient of the operating eigenwave in the 72 period copper helix measured using a SNA.

The 72 period length of copper helically corrugated waveguide was found to have losses between -0.278 and -2.28dB in its operating bandwidth of 8.5 to 10.0GHz, shown in Figure 6-17.

In real waveguides not all of the losses are due to ohmic heating in the waveguide walls. In the helically corrugated waveguides some of the input pulse is reflected as it enters the helical waveguide. The use of helical tapers reduces this, by varying the cross section along the waveguide. As a through-calibration was performed before the transmission of the waveguides were measured, losses due to reflections should be small enough to be neglected. Another source of losses was leakage of microwave energy through the connections between sections. As the losses due to leakage increases exponentially with length of waveguide, losses due to leakage can be taken into account by including it in the imaginary part of the axial wavenumber. The loss coefficient, α, can then be found using

$$\alpha = -\frac{Ln(T)}{2L} \qquad \textbf{Equation 6-2}$$

where T is the transmittance and L is the length of waveguide.

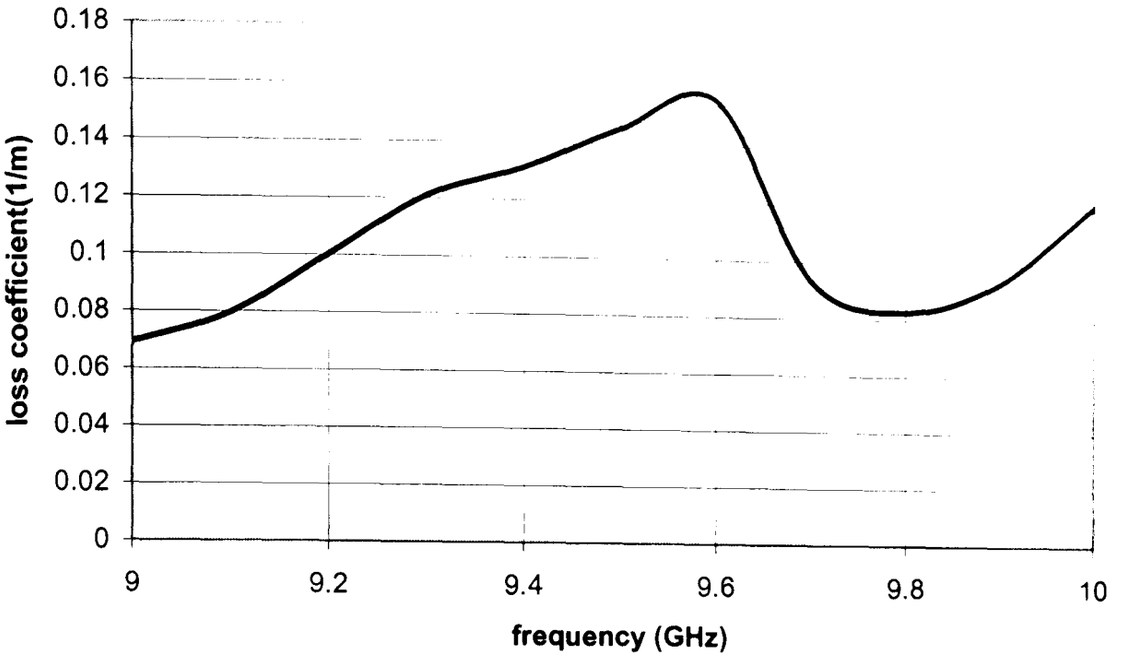

Figure 6-18 The loss coefficient for the operating eigenwave of the aluminium helical waveguide as a function of frequency, calculated from the experimental transmittance.

The imaginary part of the axial wavenumber, α, for the aluminium compressor varied between 0.069 and 0.159m^{-1}, as shown in Figure 6-18, within the frequency range of 9.0-10.0GHz, with the maximum value of α occurring at 9.55GHz.

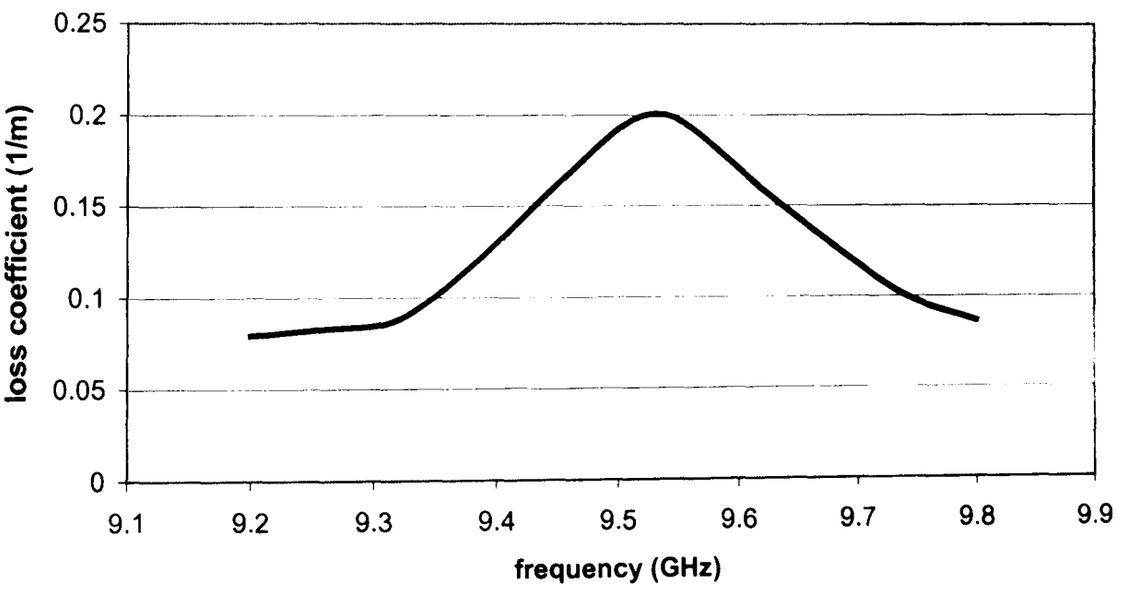

Figure 6-19 The loss coefficient for the operating eigenwave of the modified aluminium helical waveguide as a function of frequency calculated from the experimental transmittance.

The modified aluminium compressor had a maximum value of the loss coefficient, α, at 9.53GHz shown in Figure 6-19, equal to 0.20m^{-1}. The value of α at 9.20GHz was found to be 0.08m^{-1}.

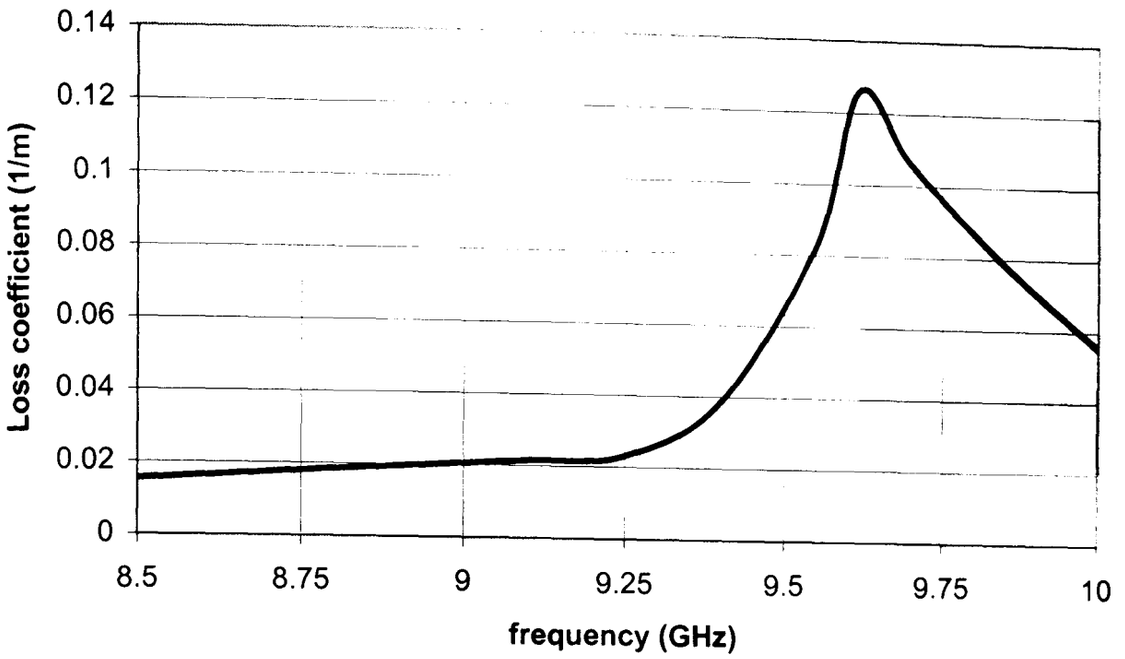

Figure 6-20 The loss coefficient for the operating eigenwave of the copper helical waveguide as a function of frequency calculated from the experimental transmittance.

The value of α in the copper compressor had a maximum of $0.126m^{-1}$ at 9.62GHz and a minimum $0.015m^{-1}$ at 8.5GHz for the frequency bandwidth between 8.5-10GHz, shown in Figure 6-20.

6.5 Comparison between perturbation theory and experiment

The dispersion calculated using the method of perturbation was compared to the experimental SNA results by finding the frequencies where the axial wavenumber was the same as the axial wavenumber calculated using the experimental SNA results. To find the average standard deviation of the frequencies for each helix, the standard deviation was found as a percentage for each pair of frequencies (experiment and numerical simulation) with the mean standard deviation found for each helically corrugated waveguide.

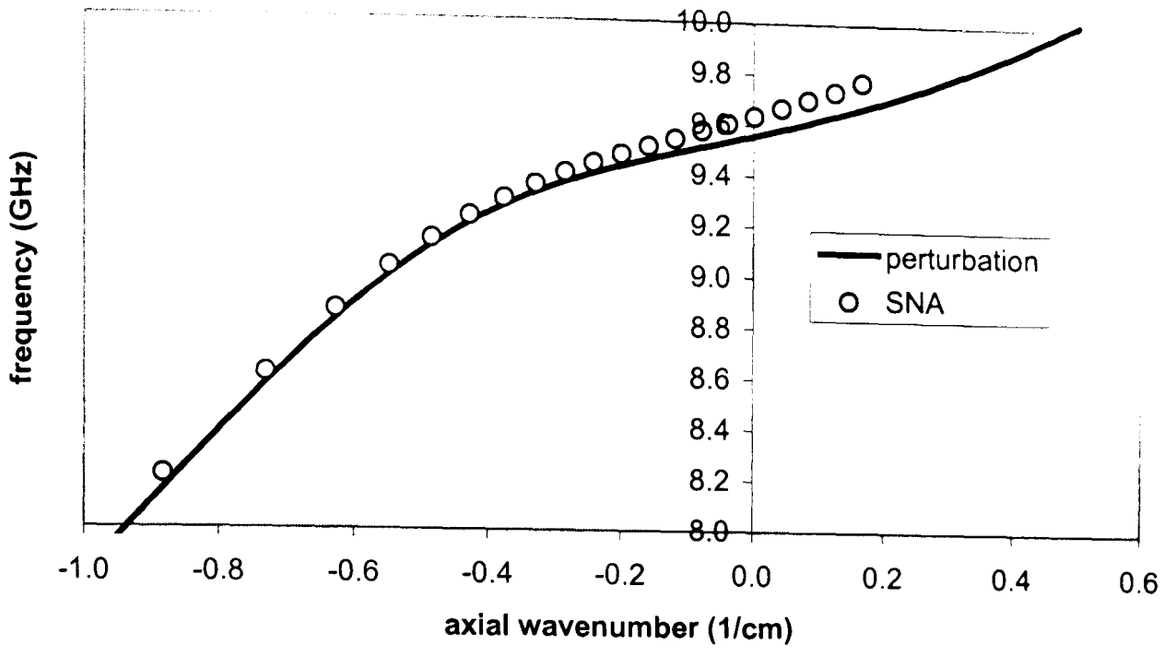

Figure 6-21 Dispersion plots of the aluminium helix showing the experimental SNA plot and the method of perturbation plot.

The dispersion of the aluminium helix calculated using the method of perturbation disagreed slightly with the experimental results due to its relatively deep corrugation, shown in Figure 6-21. The mean standard deviation of the frequency was 0.49% and the mean standard deviation of the group velocity between the experiment and the method of perturbation was 9.92%.

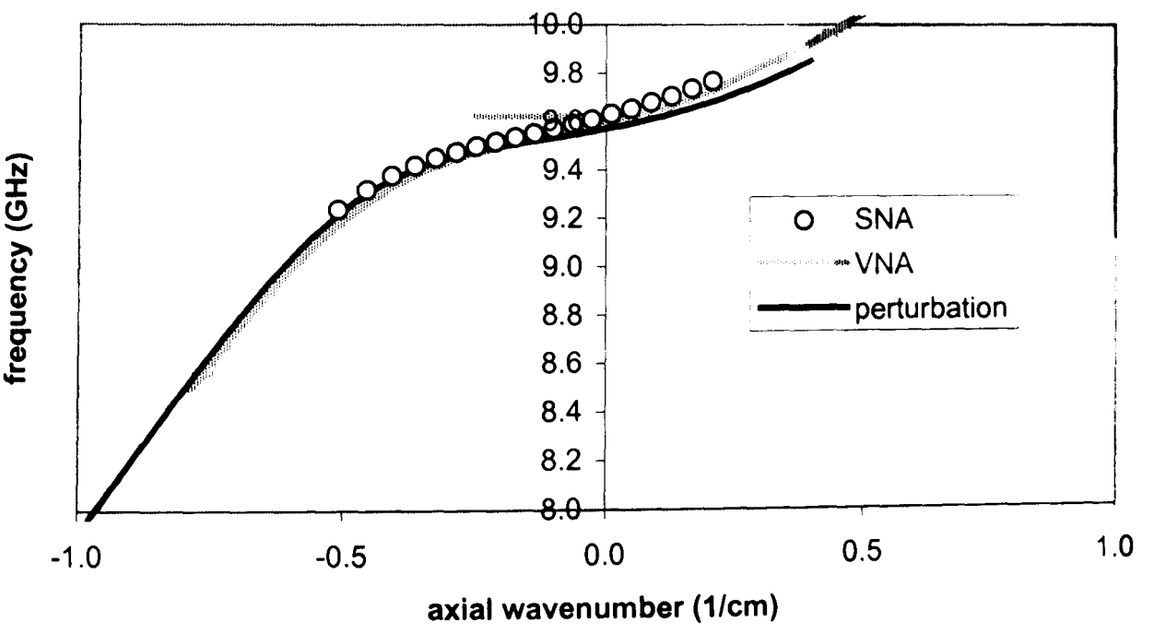

Figure 6-22 Dispersion plots of the modified aluminium helix showing the experimental SNA and VNA plots and the method of perturbation plot.

The modified helix had a slight deviation in the dispersion plots calculated from the experiment and the theory, due to the approximation of the helix shape used in the method of perturbations, as shown in Figure 6-22. The mean standard deviation between the SNA experiment and the method of perturbation was 0.37% for the frequency and 10.07% for the group velocity, respectively.

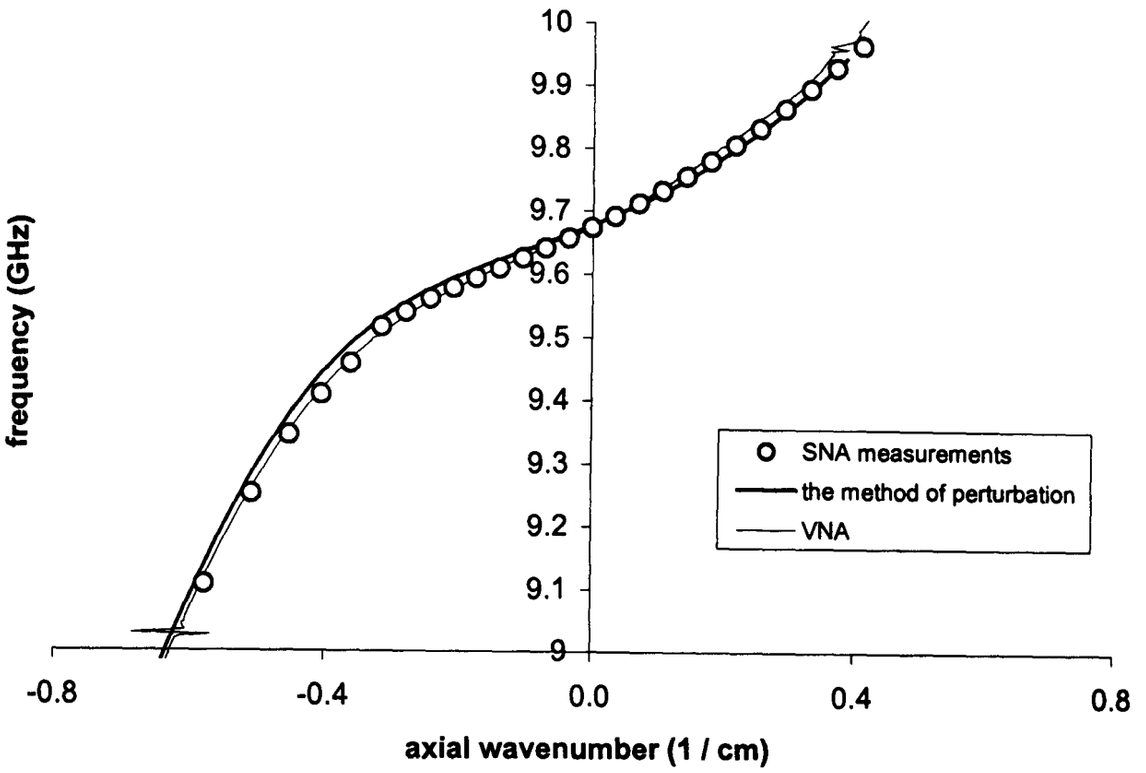

Figure 6-23 Dispersion plots of the copper helix showing the experimental SNA plot and the method of perturbation plot.

The copper helix gave good agreement between experiment and theory due to its shallow corrugation depth, as shown in Figure 6-23. The mean standard deviation of the frequencies for the copper helix was calculated to be 0.10%, while the mean standard deviation of the group velocities was calculated to be 6.25%.

Perturbation theory was found to give good agreement with experiment for small corrugation depths. The 3rd copper helix compared well with experimental results however the dispersion curves for the two aluminium helix deviated from the measured dispersions. The modified helix deviated significantly from the experiments as the shape was approximated by a sinusoidal variation.

6.6 Comparison between MAGIC and experiment

To investigate the accuracy of MAGIC, the SNA MAGIC simulation was used to model the experimental SNA results. The same length of helically corrugated waveguide and helical tapered sections as used in the experiment were inserted into the model. This allowed the approximation that the helical tapered section was equal to half its length of regular helically corrugated waveguide. MAGIC gave good agreement with the experiments for all corrugation depths.

A 64 period section of aluminium helix was used in both the simulation and experiment and two 4 period sections of helical taper were used to reduce reflections in each case. Figure 6-24 shows the dispersion characteristics calculated from the experimental measurement of the transmission of a linearly polarised TE_{11} wave through a aluminium helically corrugated waveguide and from the numerical PIC code, MAGIC. These results gave good agreement with each other, however it was more illuminating to compare the group velocity dispersion plots.

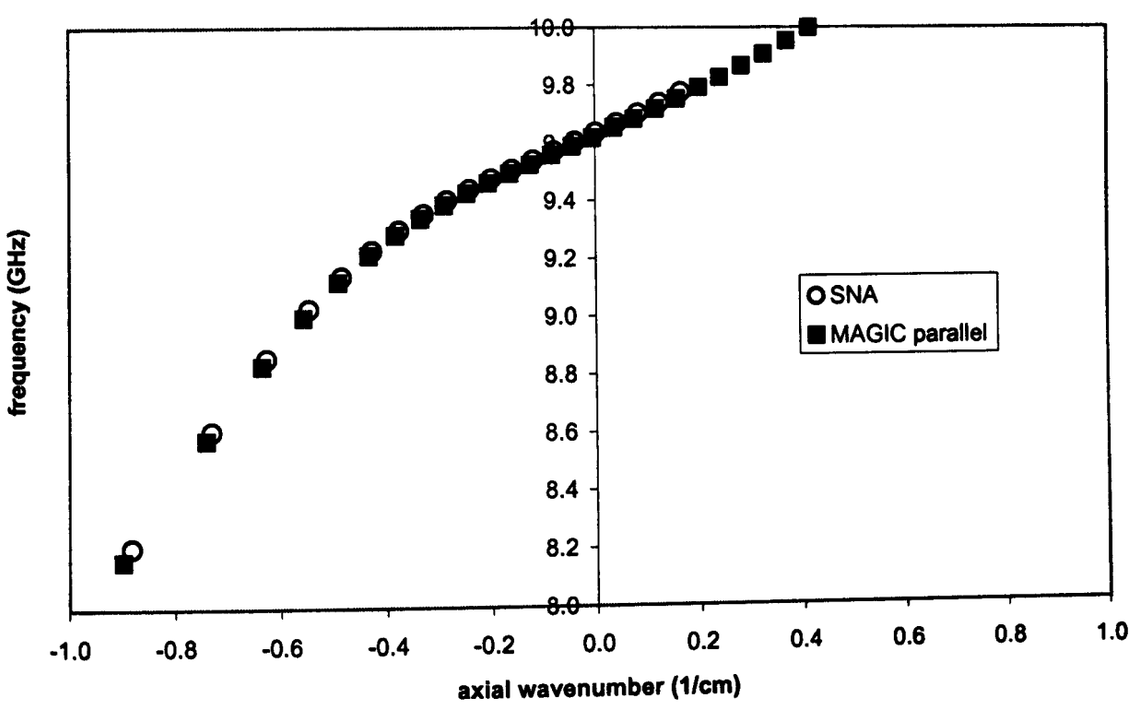

Figure 6-24 Dispersion plots of the aluminium helix showing the experimental SNA plot and the SNA MAGIC plot.

Figure 6-25 shows the group velocity dispersion calculated using MAGIC compared to the GVD calculated using the experimental SNA measurements.

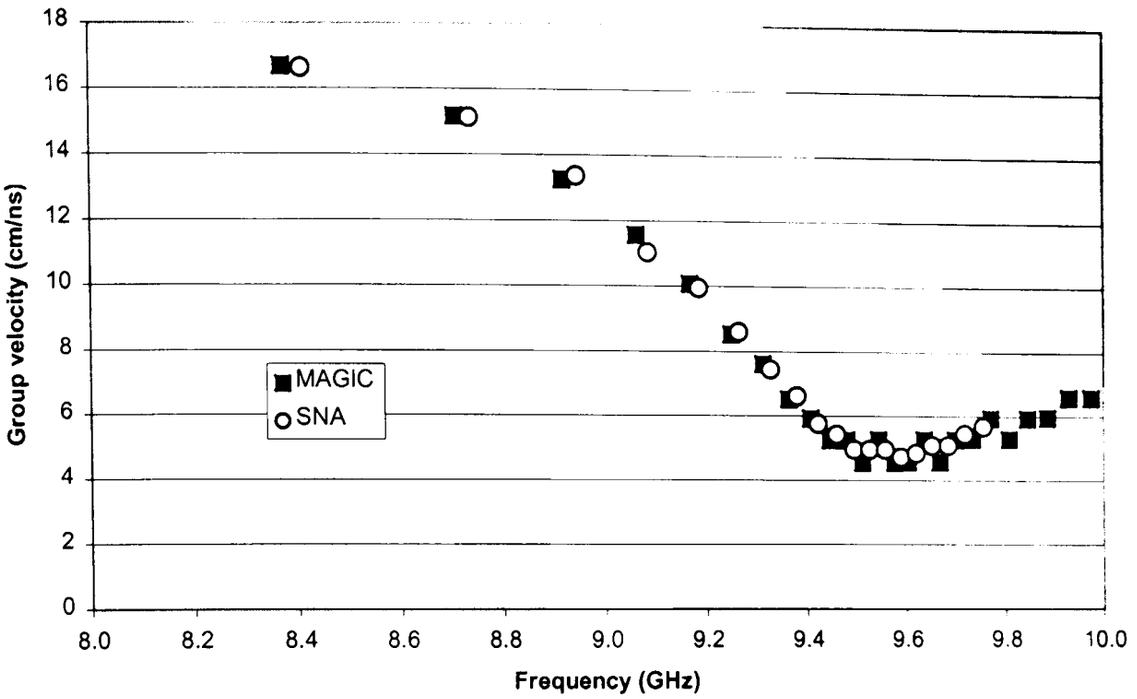

Figure 6-25 Group velocity dispersion plot for the Aluminium helix showing the group velocity versus frequency curves calculated using the experimental SNA, and SNA MAGIC techniques.

The frequencies, when the polarisation turn was equal to an integer times pi radians were measured and compared to the experimental results. To find the average standard deviation of the results for each helix, the standard deviation was found as a percentage for each pair of frequencies (experiment and numerical simulation) and the mean standard deviation for each helically corrugated waveguide was calculated. The frequency bandwidth was between 7.0 GHz and 9.8GHz and was split up into two plots (7.0GHz to 9.2GHz and 9.2GHz to 9.8GHz) in order to get better resolution.

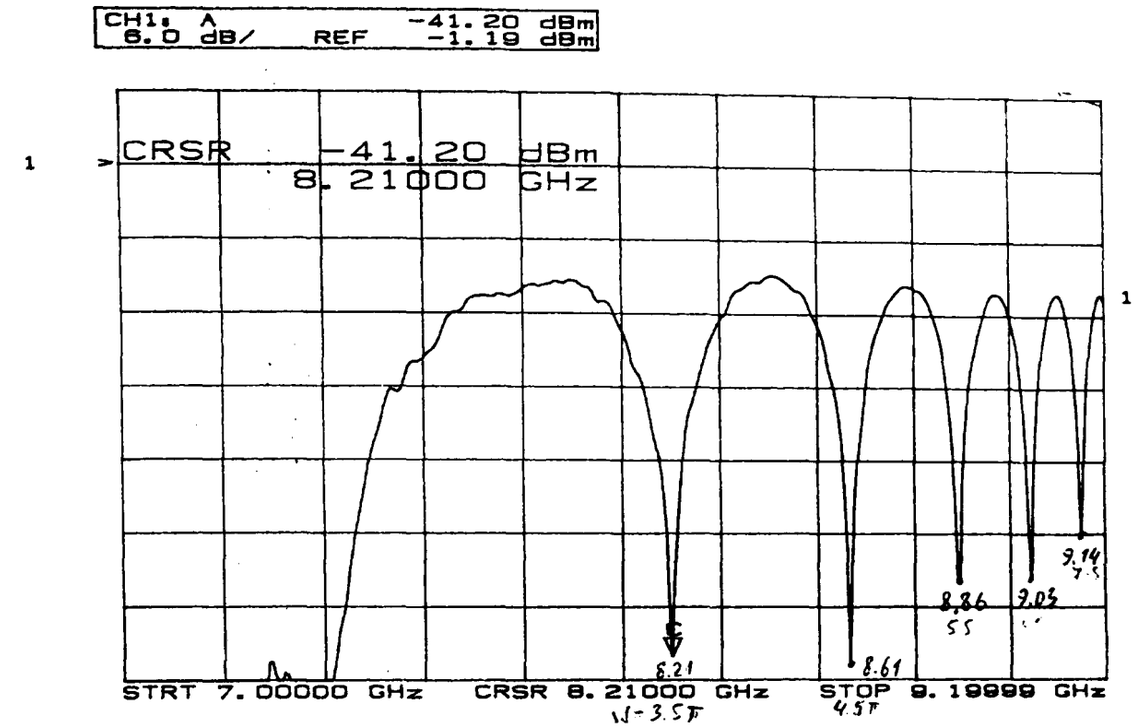

Figure 6-26 Transmission measurement of a linearly polarised wave propagating through a 64 period length of aluminium helix with two 4 period tapers, between 7.0 and 9.2GHz, measured using a scalar network analyser.

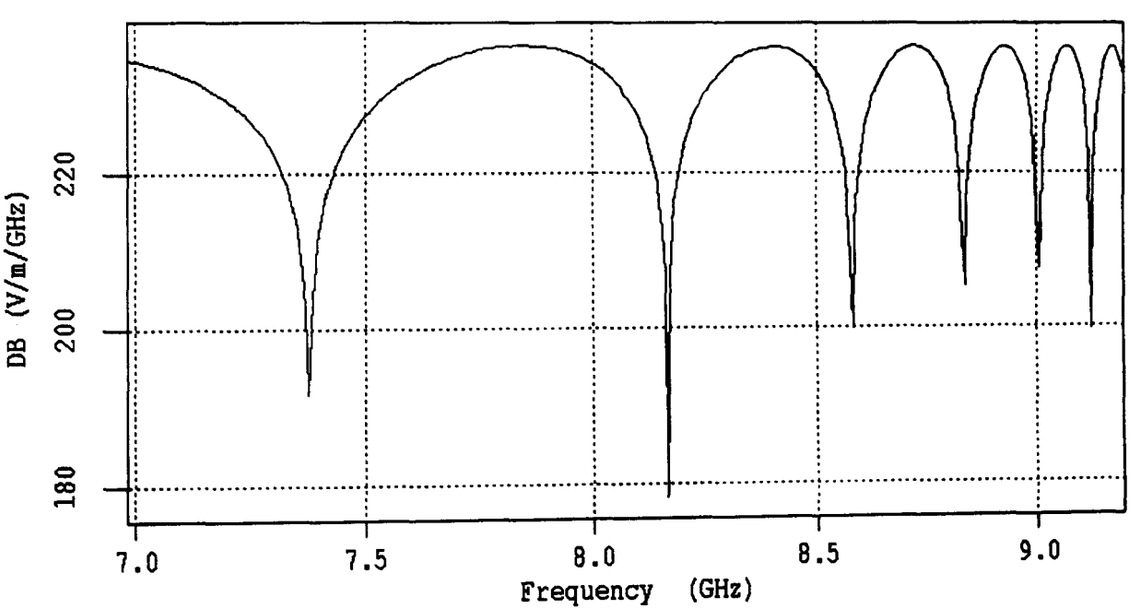

Figure 6-27 Fourier transform of a radial electric field measurement of a linearly polarised wave propagating through a 64 period length of aluminium helix with two 4 period tapers, between 7.0 and 9.2GHz, obtained using MAGIC.

Figure 6-26 and Figure 6-27 show the experimental and numerical SNA plots respectively and cover the frequency bandwidth between 7.0GHz and 9.2GHz. Figure 6-28 and Figure 6-29 also show the experimental and numerical SNA plots respectively but these cover the frequency bandwidth from 9.2GHz to 9.8GHz. The mean standard deviation of the frequencies at which minima occur for the aluminium

helix was calculated to be 0.14% and the maximum standard deviation was 32MHz (0.39%). Although there may be a small variation in the frequency of the minima between the experimental and numerical approach, the dispersion curves calculated from these results were in good agreement.

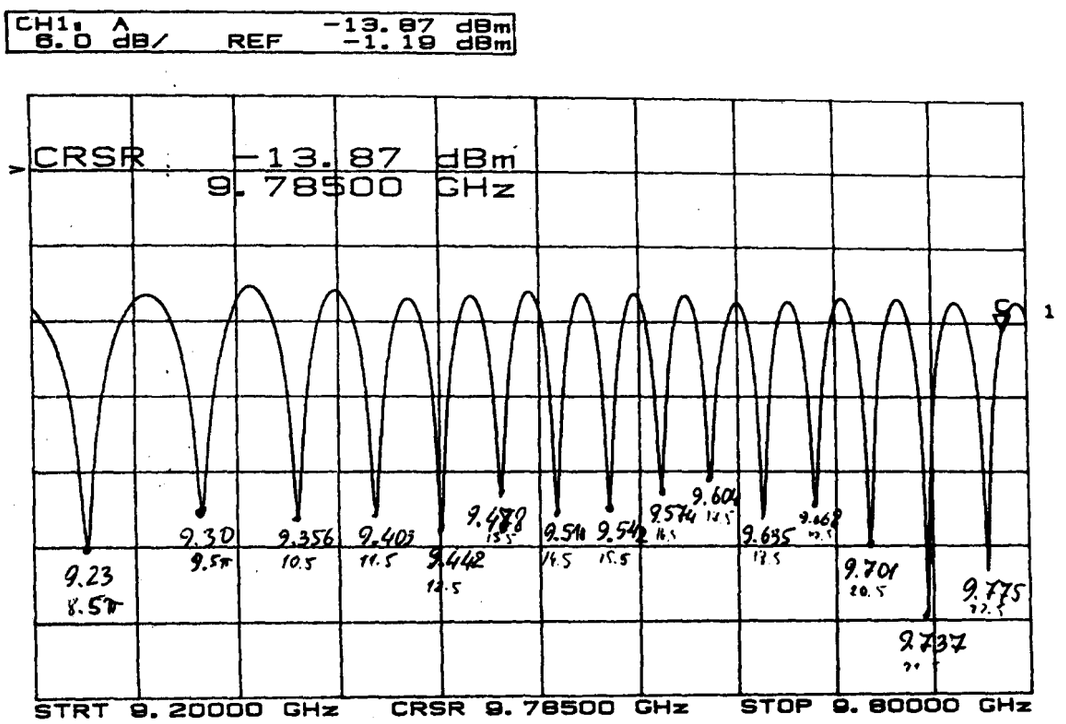

Figure 6-28 Transmission measurement of a linearly polarised wave propagating through a 64 period length of aluminium helix with two 4 period tapers, between 9.2 and 9.8GHz, measured using a scalar network analyser.

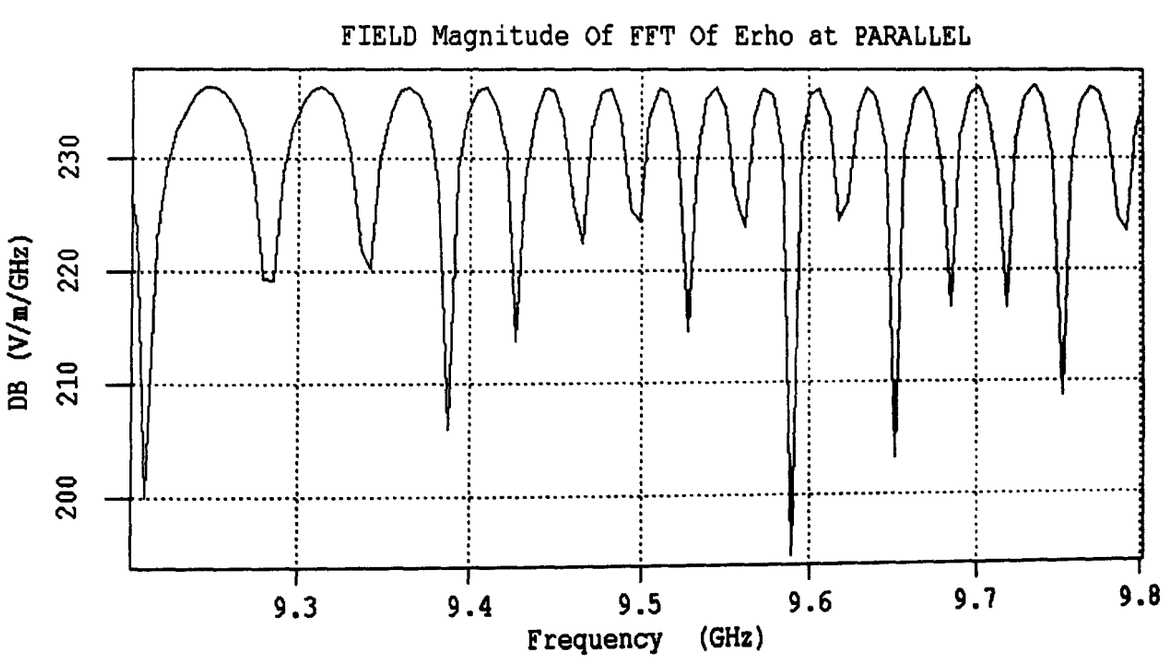

Figure 6-29 Fourier transform of a radial electric field measurement of a linearly polarised wave propagating through a 64 period length of aluminium helix with two 4 period tapers, between 9.2 and 9.8GHz, obtained using MAGIC.

A 64 period section of the modified aluminium helix was used in both the simulation and experiment and two 4 period sections of helical taper were used to reduce reflections in each case. The frequency bandwidth of the plots covers the range between 9.2GHz to 9.8GHz, which was split into two plots, one from 9.2GHz to 9.5GHz and the other from 9.5GHz to 9.8GHz.

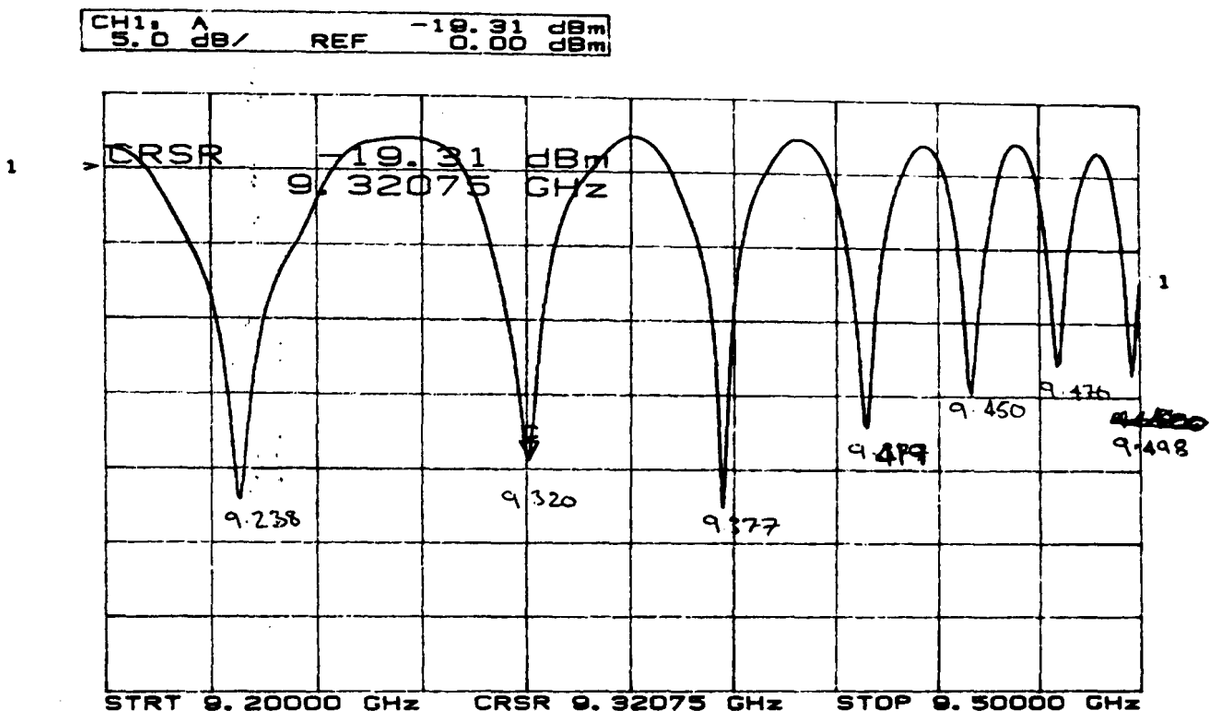

Figure 6-30 Transmission measurement of a linearly polarised wave propagating through a 64 period length of modified helix with two 4 period tapers, between 9.2 and 9.5GHz, measured using a scalar network analyser.

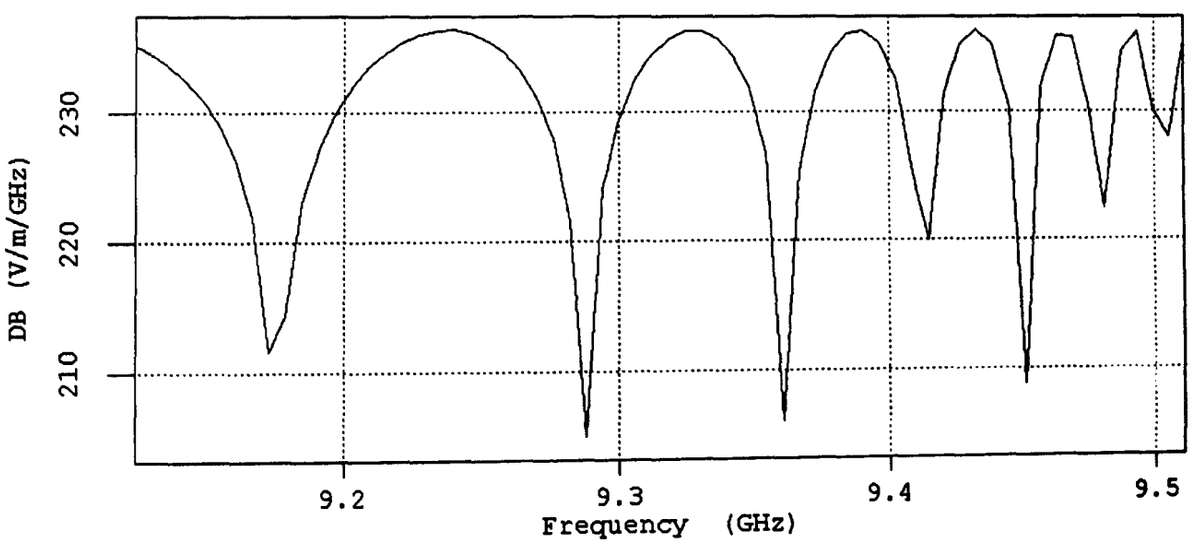

Figure 6-31 Fourier transform of a radial electric field measurement of a linearly polarised wave propagating through a 64 period length of modified helix with two 4 period tapers, between 9.12 and 9.51GHz, obtained using MAGIC.

Figure 6-30 and Figure 6-31 show the experimental and numerical transmission plots for the modified helix respectively, between the frequency range from 9.2GHz

to 9.5GHz. The experimental and numerical transmission plots between the frequencies 9.5GHz and 9.8GHz are shown in Figure 6-32 and Figure 6-33.

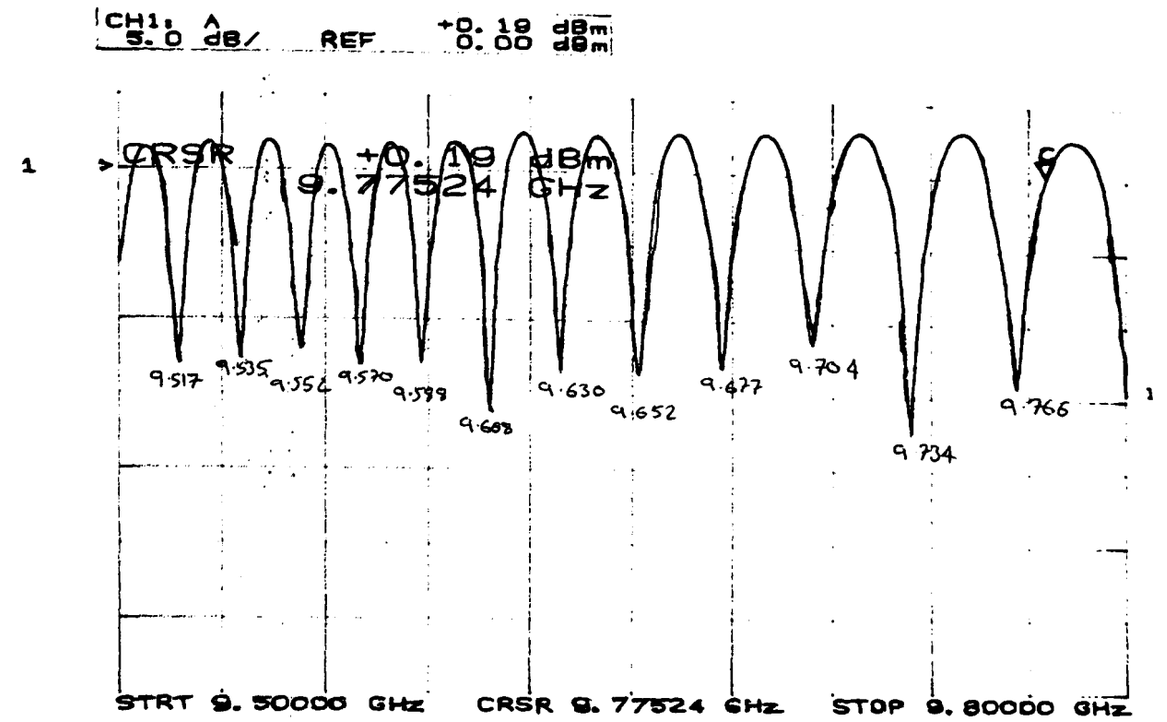

Figure 6-32 Transmission measurement of a linearly polarised wave propagating through a 64 period length of modified aluminium helix with two 4 period tapers, between 9.5 and 9.8GHz, measured using a scalar network analyser.

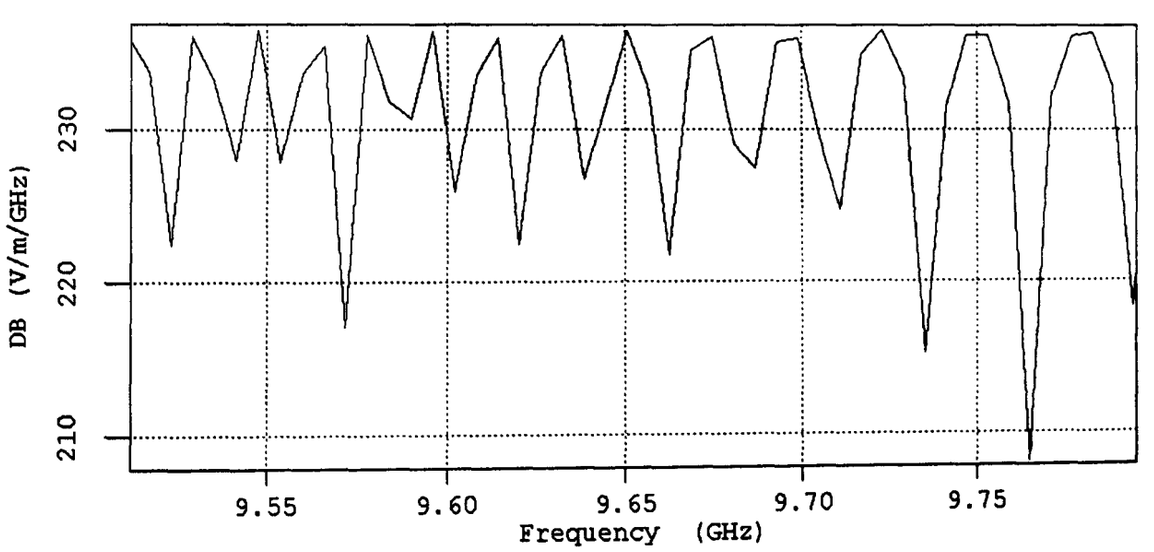

Figure 6-33 Fourier transform of a radial electric field measurement of a linearly polarised wave propagating through a 64 period length of modified helix with two 4 period tapers, between 9.51 and 9.8GHz, obtained using MAGIC.

The mean standard deviation of the frequencies at which minima occur for the modified helix was calculated to be 0.10%. The experimental and numerical dispersion plots for the modified helically corrugated waveguide are shown in Figure 6-34. The experimental SNA and SNA MAGIC dispersion characteristics gave good

agreement with each other, however a slight deviation between these two dispersion plots and the dispersion plot calculated using the vector network analyser was present.

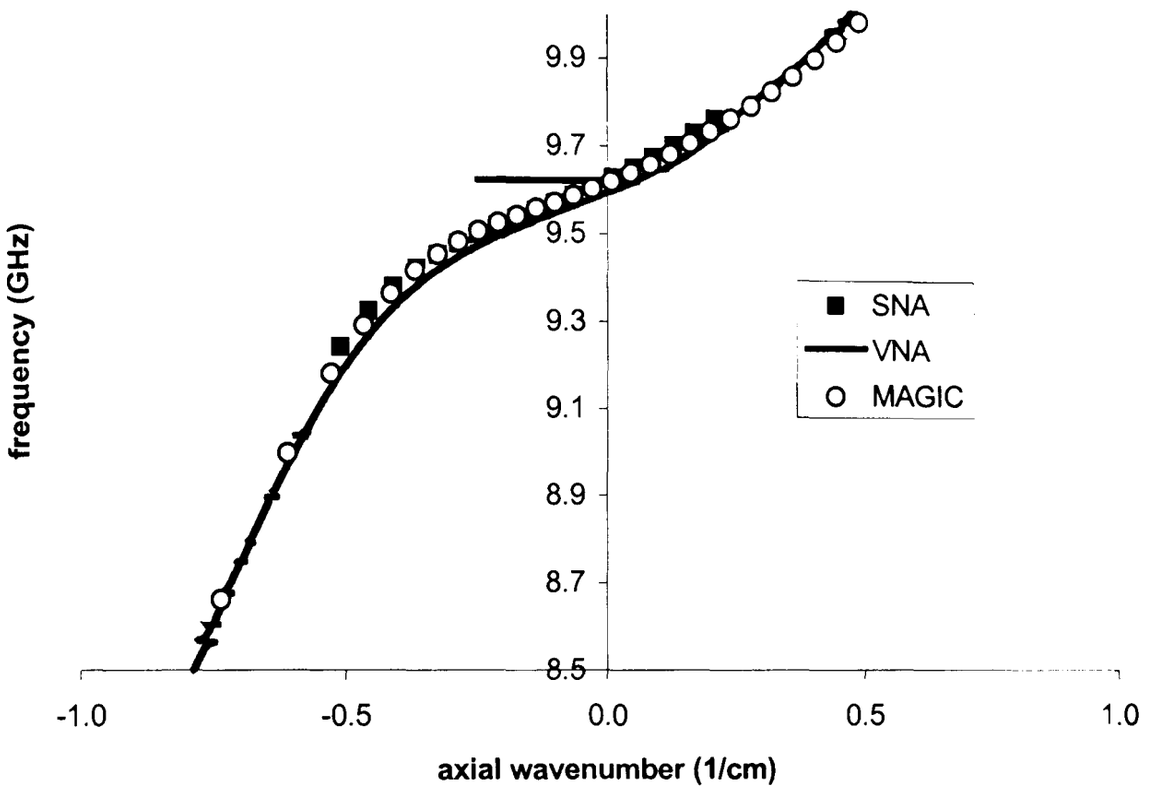

Figure 6-34 Dispersion plots of the modified aluminium helix showing the experimental SNA and VNA plots and the SNA MAGIC plot.

The group velocity dispersion characteristics calculated using the experimental SNA and SNA MAGIC results are shown in Figure 6-35.

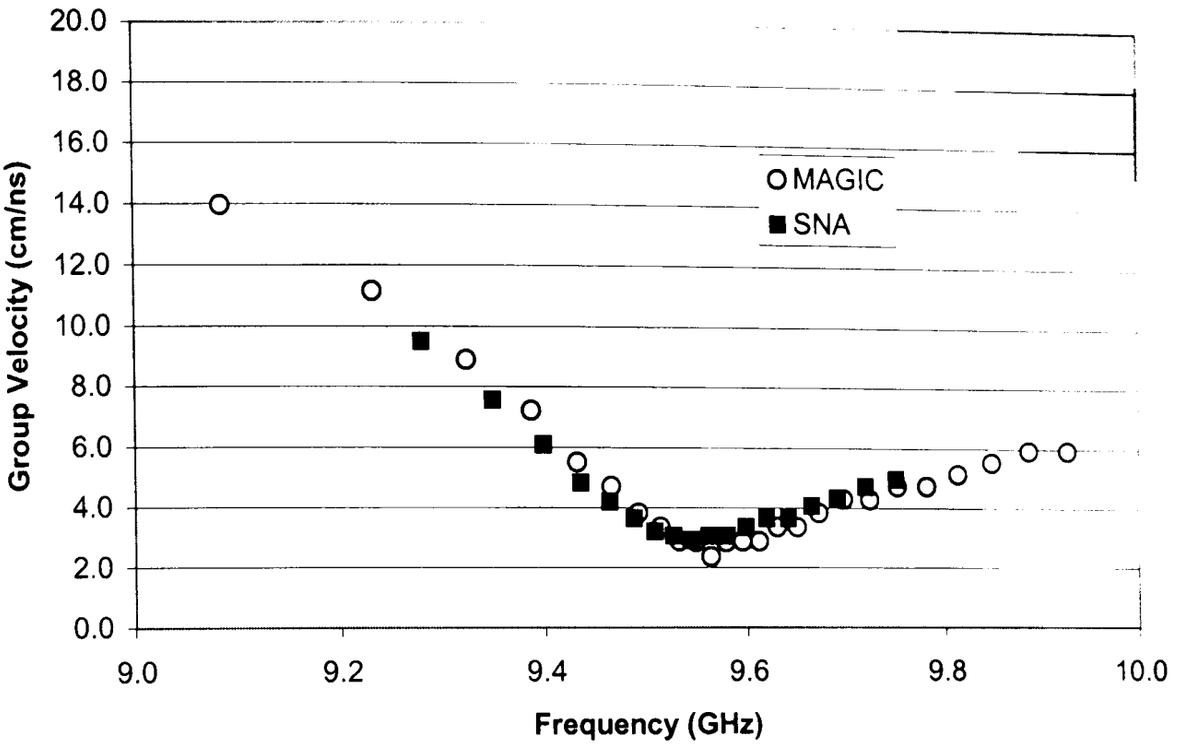

Figure 6-35 Group velocity dispersion plot for the modified aluminium helix showing the group velocity versus frequency curves calculated using the experimental SNA, and SNA MAGIC techniques.

A 72 period section of copper helix was used in both the simulation and experiment and two 4 period sections of helical taper were used to reduce reflections in each case. In the SNA MAGIC simulations the tapers had the parameters of the copper helical corrugation and the modified tapers were used in the experiment. The transmission measurements were made across the frequency range from 8.0GHz to 10.0GHz for the copper helically corrugated waveguide.

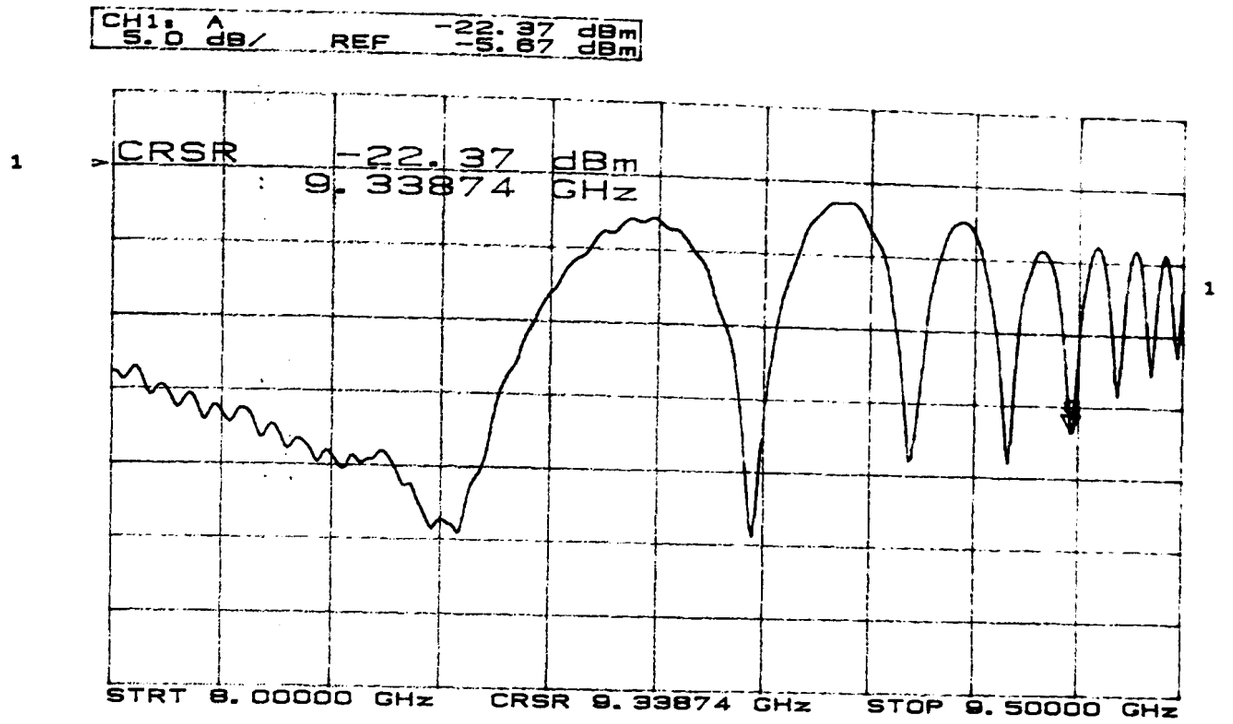

Figure 6-36 Transmission measurement of a linearly polarised wave propagating through a 72 period length of copper helix with two 4 period tapers, between 8.0 and 9.5GHz, measured using a scalar network analyser.

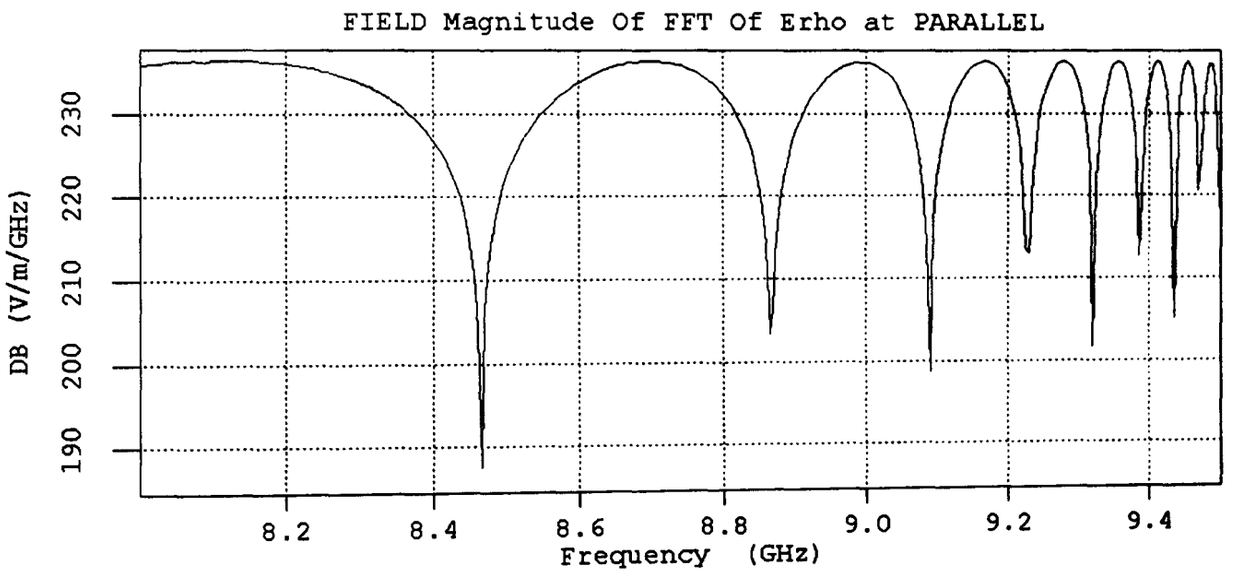

Figure 6-37 Fourier transform of a radial electric field measurement of a linearly polarised wave propagating through a 72 period length of copper helix with two 4 period tapers, between 8.0 and 9.5GHz, obtained using MAGIC.

Figure 6-36 and Figure 6-37 show the experimental and numerical transmission plots respectively of a linearly polarised TE_{11} propagating through the copper helix, in the frequency range from 8.0GHz and 9.5GHz.

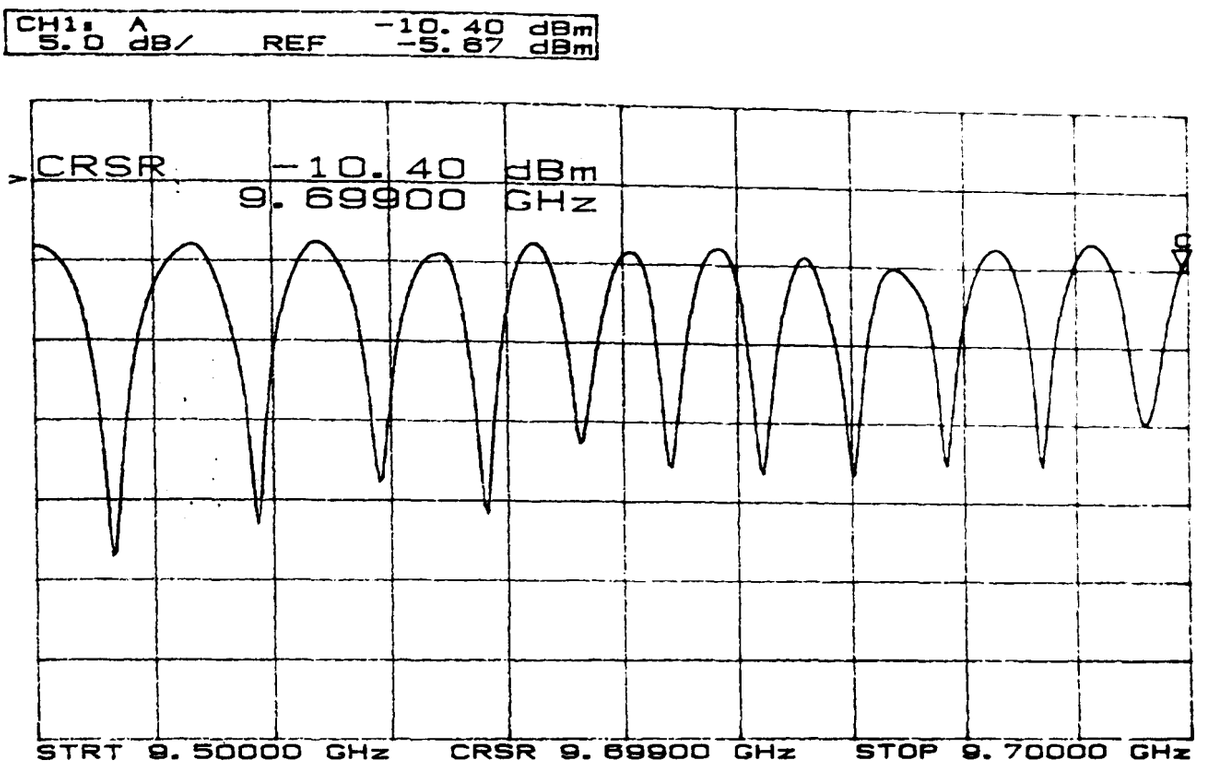

Figure 6-38 Transmission measurement of a linearly polarised wave propagating through a 72 period length of copper helix with two 4 period tapers, between 9.5 and 9.7GHz, measured using a scalar network analyser.

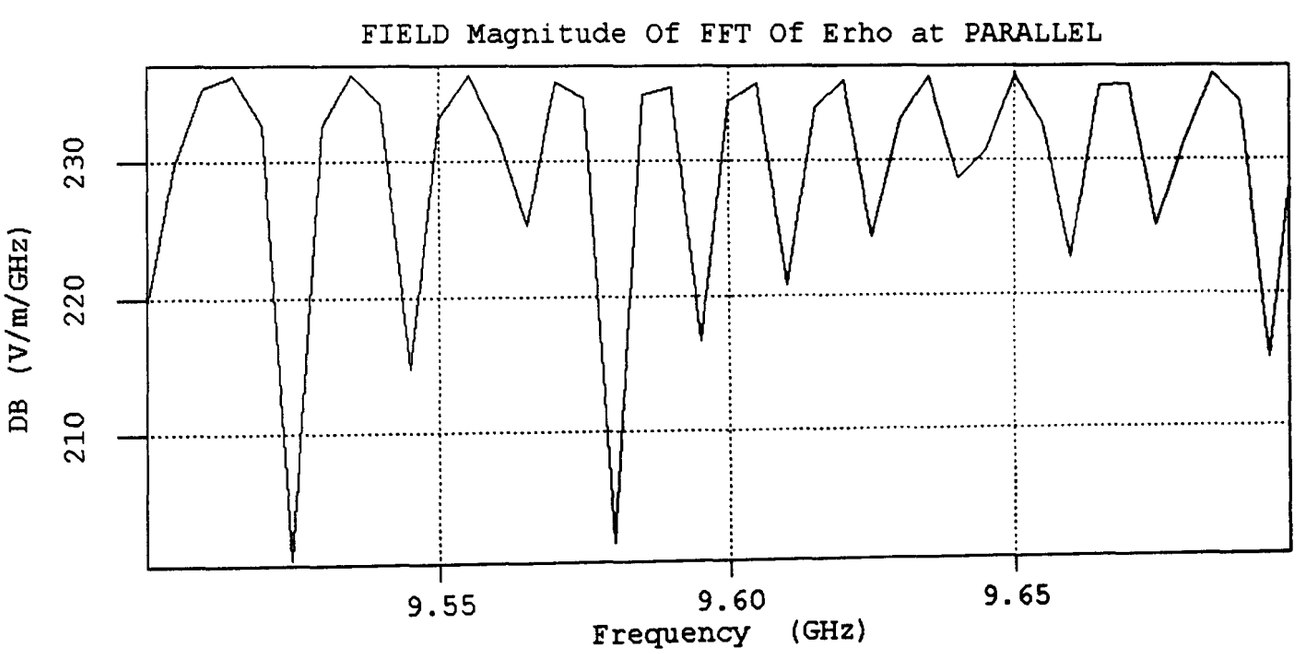

Figure 6-39 Fourier transform of a radial electric field measurement of a linearly polarised wave propagating through a 72 period length of copper helix with two 4 period tapers, between 9.5 and 9.7GHz, obtained using MAGIC.

Figure 6-38 shows the experimental transmission of the copper helix as a function of frequency taken using a SNA. Figure 6-39 shows the Fourier transform of the variation of the radial electric field with respect to time, as described in Chapter 4. Both plots cover the frequency bandwidth from 9.5GHz to 9.7GHz.

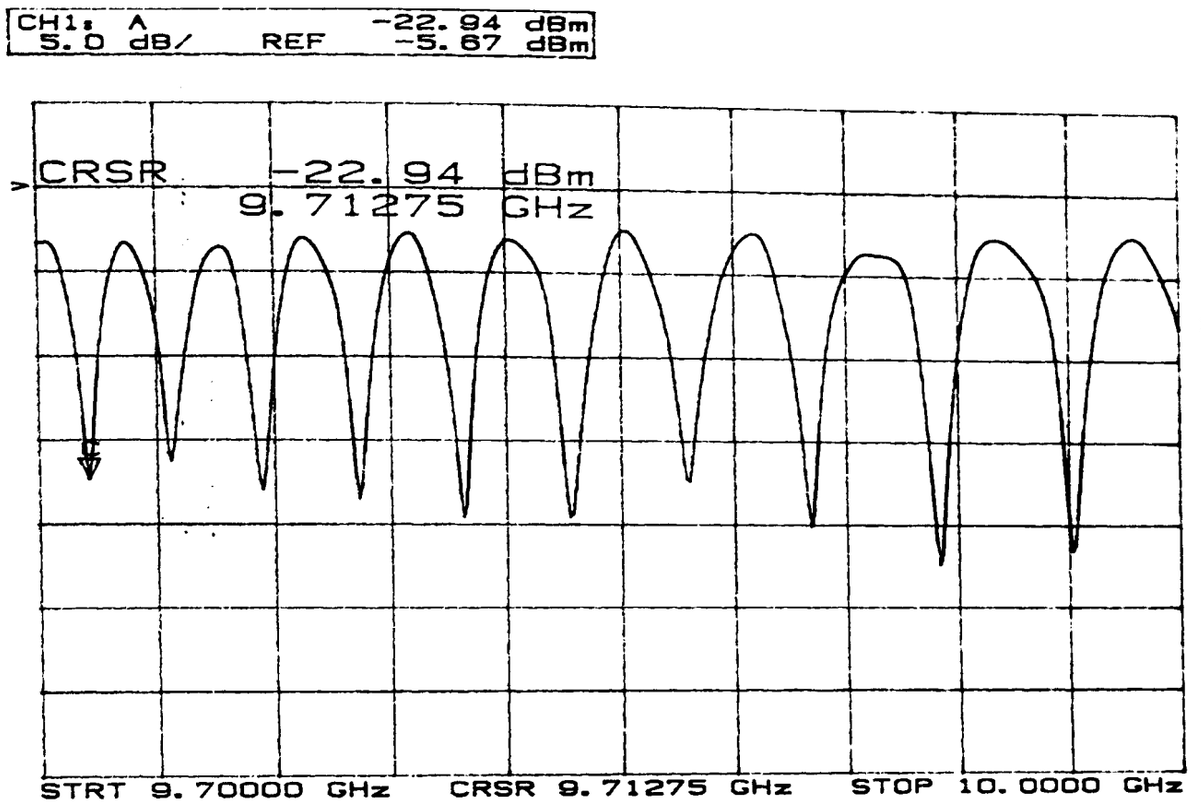

Figure 6-40 Transmission measurement of a linearly polarised wave propagating through a 72 period length of copper helix with two 4 period tapers, between 9.7 and 10.0GHz, measured using a scalar network analyser.

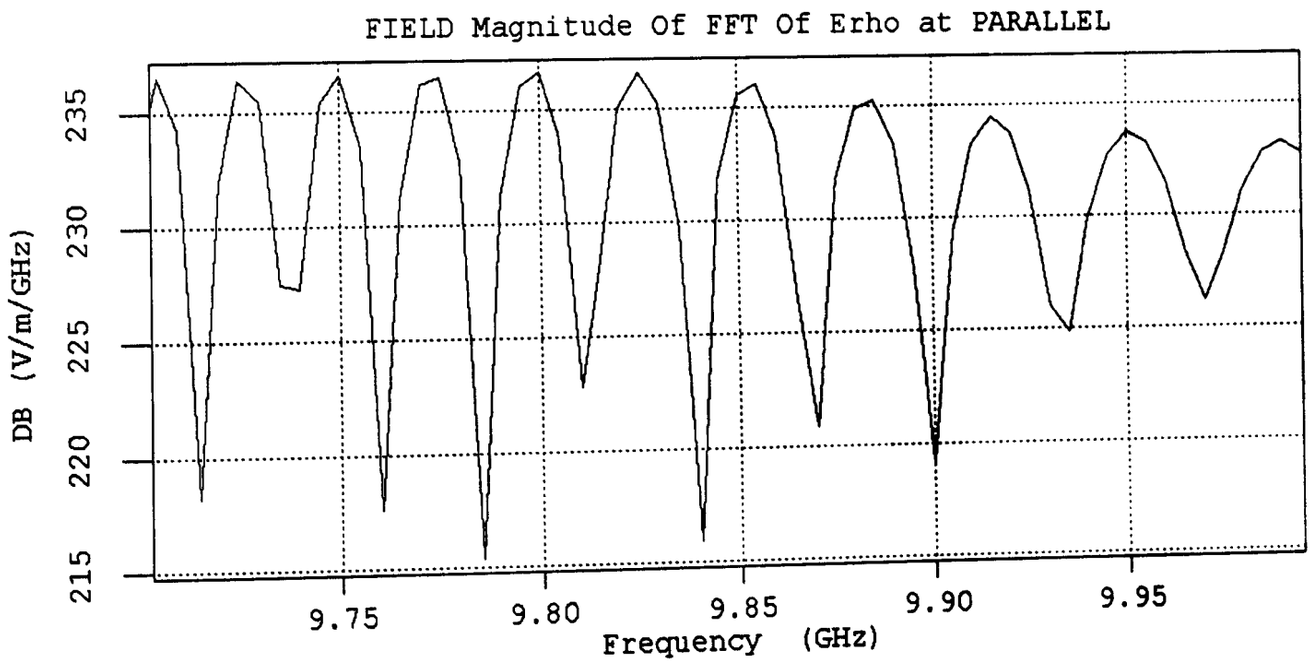

Figure 6-41 Fourier transform of a radial electric field measurement of a linearly polarised wave propagating through a 72 period length of copper helix with two 4 period tapers, between 9.7 and 10.0GHz, obtained using MAGIC.

Figure 6-40 and Figure 6-41 show the experimental SNA and MAGIC SNA plots from 9.7GHz to 10GHz. The mean standard deviation of the frequencies at which minima occur for the copper helix was calculated to be 0.15%.

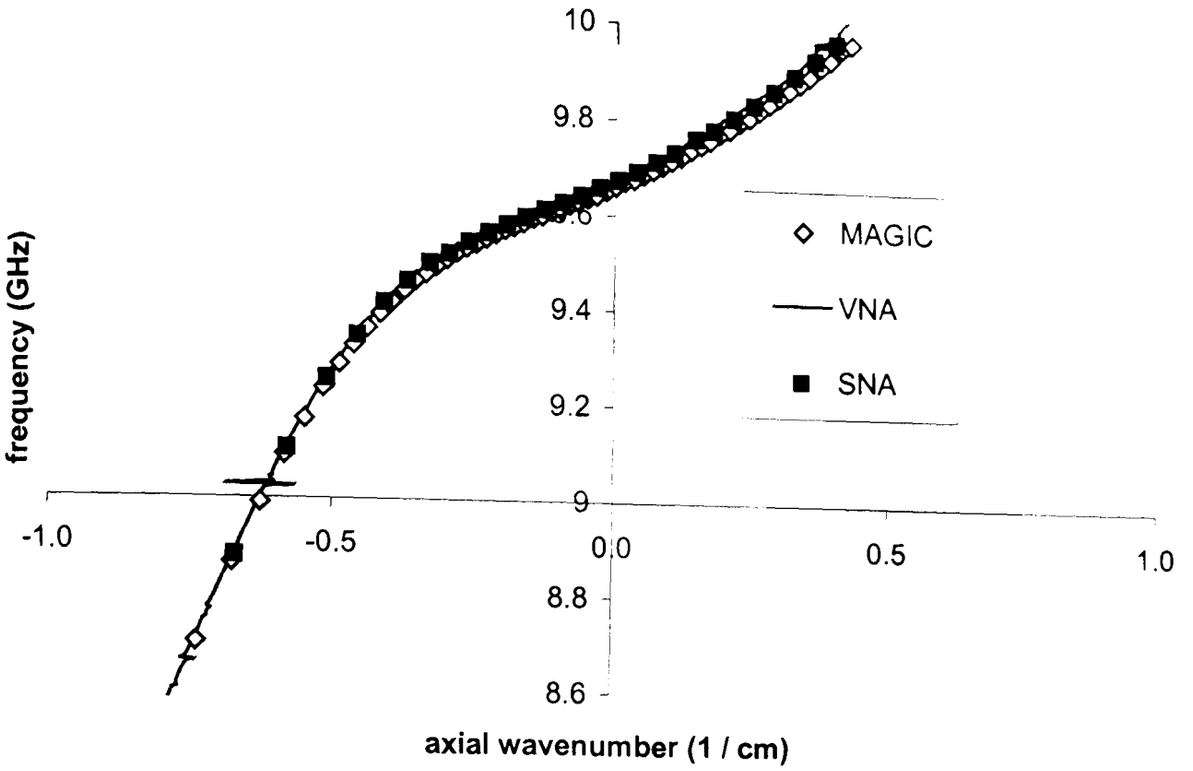

Figure 6-42 Dispersion plots of the Copper helix showing the experimental SNA and VNA plots and the SNA MAGIC plot.

Figure 6-42 shows the dispersion characteristics calculated using the experimental SNA and the SNA MAGIC results for the copper helically corrugated waveguide.

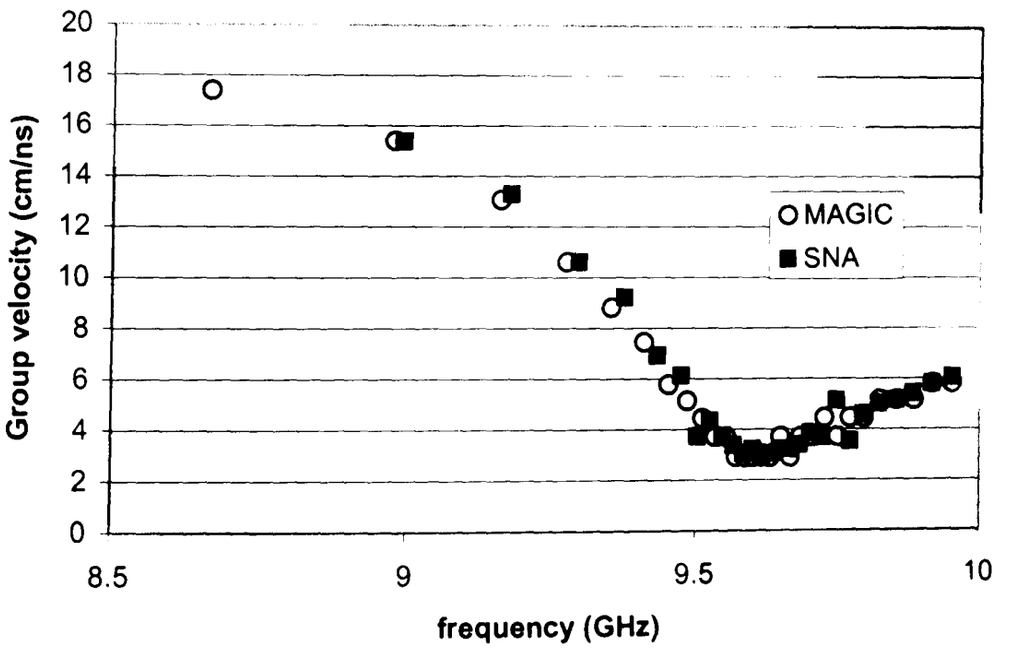

Figure 6-43 Group velocity dispersion plot for the Copper helix showing the group velocity versus frequency curves calculated using the experimental SNA, and SNA MAGIC techniques.

The group velocity dispersion plots calculated using the experimental and numerical polarisation turn measurements for the copper helix are shown in Figure 6-43.

6.7 Comparison between the experimental losses and the losses calculated using the method of perturbations.

The imaginary component of the axial wavenumber, alpha, which is responsible for losses in the helically corrugated waveguides, can be found theoretically using the method of perturbations or can be calculated from the transmission measurements taken using the SNA, assuming transmission decays exponentially with length. These two methods were compared by looking at plots of alpha versus frequency, using both methods, for the full length of each helix. As the exact electrical conductivities of each of the helically corrugated waveguides were unknown, the electrical conductivity was chosen so that both methods had the same peak value of alpha for each helix.

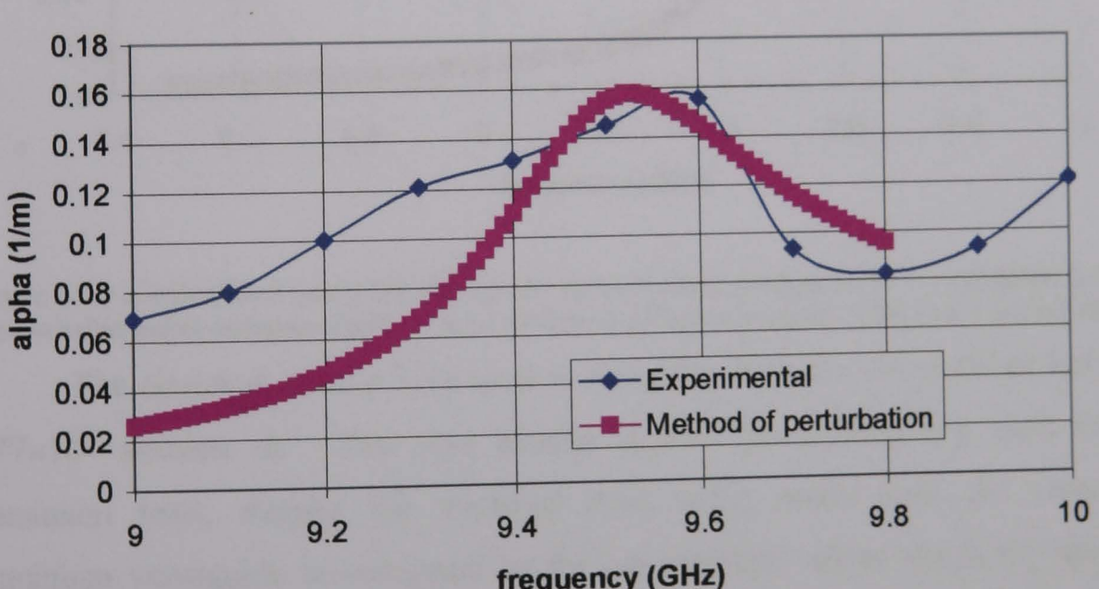

Figure 6-44 α calculated using the method of perturbations compared to α calculated from the transmission measurements made on a 64 period aluminium waveguide with two 4 period tapers.

The aluminium helix was simulated using an electrical conductivity of 8.85×10^{6} siemens m^{-1}, shown in Figure 6-44. This value was 25% of the expected value, and was due to the method of perturbations calculating alpha due only to

ohmic losses and not taking into account losses from connections. The two methods have maximum values of α at different frequencies, with the experiment giving the maximum value at 9.59GHz and the theory predicting its maximum at 9.53GHz. The two plots do not match precisely as the aluminium helix is relatively deep grooved. In order to calculate the value of α using the experimental transmission it was assumed that the transmission decays exponentially with helix length however some of the losses, such as reflections at the input and output to the waveguide due to impedance matching, do not increase with helix length.

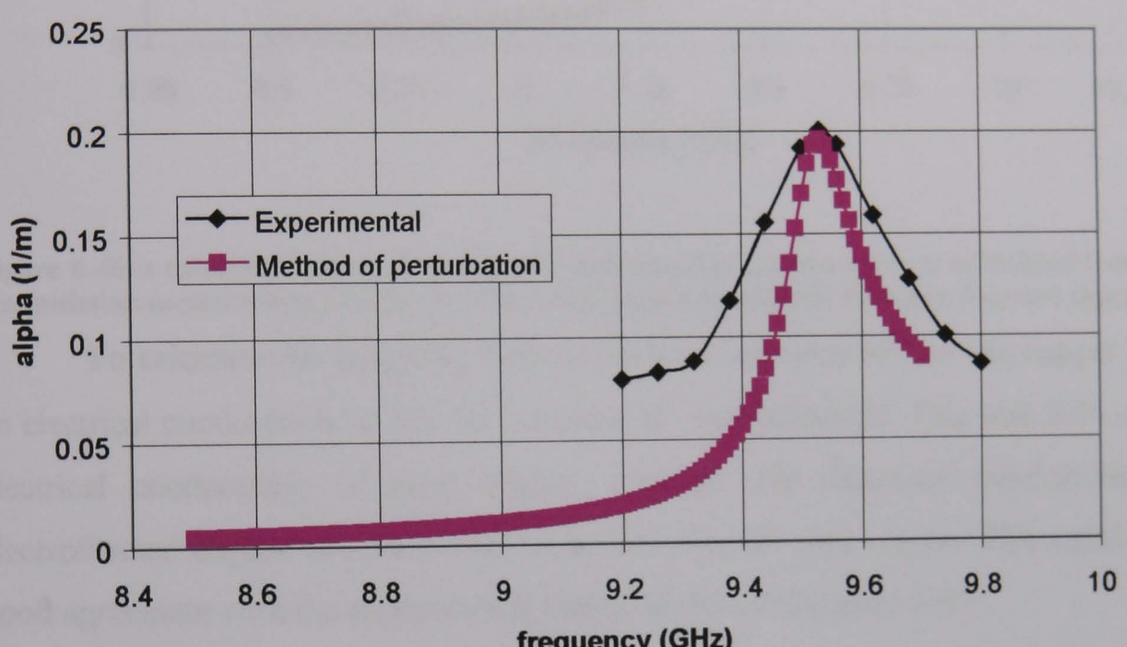

Figure 6-45 α calculated using the method of perturbations compared to α calculated from the transmission measurements made on a 64 period modified waveguide with two 4 period tapers.

The electrical conductivity used to simulate alpha for the modified helix was 1.77×10^{7} siemens m^{-1}. This was exactly double the conductivity used for the aluminium helix, despite the modified helix being made from the corrugated aluminium waveguide as compared to the experimental values which are shown in Figure 6-45. Both the method of perturbation and the transmission measurement give a maximum value of the imaginary component of the axial wavenumber at a frequency of 9.53GHz.

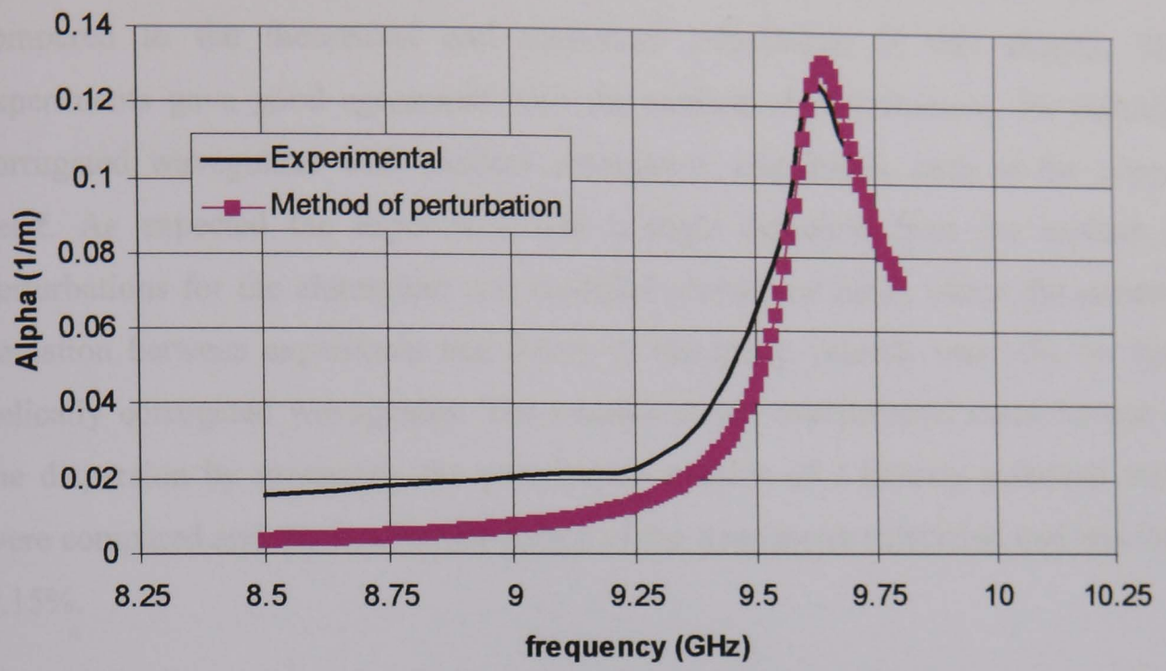

Figure 6-46 α calculated using the method of perturbations compared to α calculated from the transmission measurements made on a 72 period copper waveguide with two 4 period tapers.

To calculate the imaginary part of the axial wavenumber for the copper helix an electrical conductivity of 2.9×10^{7} siemens m^{-1} was estimated. This was 50% of the electrical conductivity of pure copper, however the electrical conductivity of electroformed copper structures tend to be less than for pure copper. This resulted in good agreement with the experimental values as shown in Figure 6-46.

6.8 Discussion

In this chapter the experimental measurement of the dispersion characteristics of a helically corrugated waveguide was investigated. Two methods were proposed for measurement of the lower eigenwave dispersion. One method involved the measurement of the polarisation rotation of a linearly polarised TE_{11} due to its propagation through a helically corrugated waveguide. The other method measured the change in phase of a circularly polarised TE_{11} wave due to its propagation through a helically corrugated waveguide using a VNA. The transmission coefficient of the operating eigenwave as a function of frequency was also measured for each of the helically corrugated waveguides.

The experimental measurement of the dispersion characteristics was compared to the theoretical and numerical calculations in this chapter. The experiments gave good agreement with the method of perturbations, for helically corrugated waveguides with shallow corrugation amplitudes, such as the copper helix. As expected the experiment had a slight deviation from the method of perturbations for the aluminium and modified aluminium helix, where the standard deviation between experiment and theory of the group velocity was 10% for both helically corrugated waveguides. The numerical and experimental measurement of the dispersion by measuring the polarisation rotation of a linearly polarised wave were compared and the standard deviation of the frequencies calculated was less than 0.15%.

7 Compression Experiments

7.1 Introduction

A helically corrugated waveguide, can, with the correct choice of parameters provide an ideal dispersion for sweep-frequency based microwave pulse compression. In Chapter 7 the proof-of-principle experimental results of the measurement of compressed microwave pulses are presented.

In section 7.2 the solid state microwave source used to produce the frequency swept microwave pulse was tested and a heterodyne technique for frequency measurement undertaken. In section 7.3 compression of a continuous wave pulse signal was performed using the circular and modified aluminium helix compressors. Section 7.4 contains the results of microwave pulse compression using smooth circular waveguides and all 3 helically corrugated waveguides. A numerical simulation of each of these experiments is presented in Section 7.5.

7.2 The driving RF oscillator

The driving oscillator should produce almost constant power in the range of tens of milliwatts within an 8.5 to 10.5 GHz frequency range and permit fast, smooth frequency tuning at a rate of at least 5 MHz/ns by applying an external sweep voltage. A solid state RF source was ideal for this purpose and had the added advantage of compactness, low operating voltage and long lifetime.

A solid state source, presented in Figure 7-1, was obtained from Istok Company (Fryazino, Moscow region, Russia) for the experiments. This source, relied for its operation on a bipolar transistor, and was compact with a coaxial RF output and had two points of contact, one for the CW drive voltage, +12 DCV and 115mA, and the second for the control voltage (0-20V) with the frequency of the output radiation dependent on the control voltage.

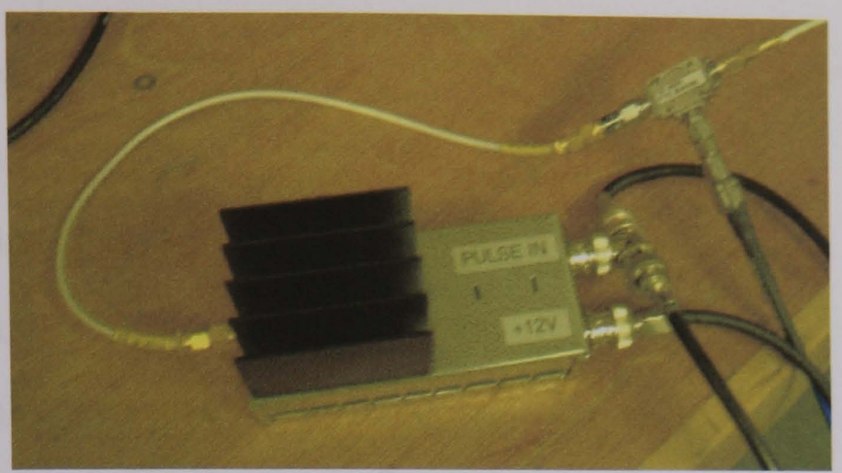

Figure 7-1 The solid-state microwave oscillator shown with the microwave mixer.

Analysis of the performance of the solid-state microwave source was carried out using a constant drive voltage with the output frequency and power measured as a function of the DC control voltage. The control voltage was stepped between 0 and 20 DCV at 0.5V steps and the frequency and power of the output radiation was monitored on a spectrum analyser (HP 8559A) and a power meter (HP 437B) respectively as shown in Figure 7-2.

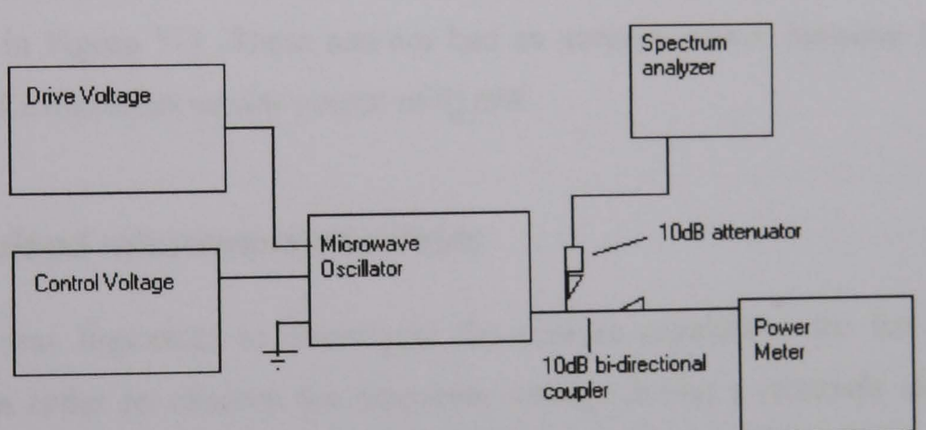

Figure 7-2 Using an HP437B power meter and head and an HP8559A spectrum analyser the frequency and power were measured as a function of control voltage, in the set-up shown.

The maximum power output of the oscillator was ~17dBm. The output was connected to the spectrum analyser through a 10dB bi-directional coupler and a 10dB attenuator, which limited the power input at the spectrum analyser to ~0.17dBm well below its damage threshold of 20dBm.

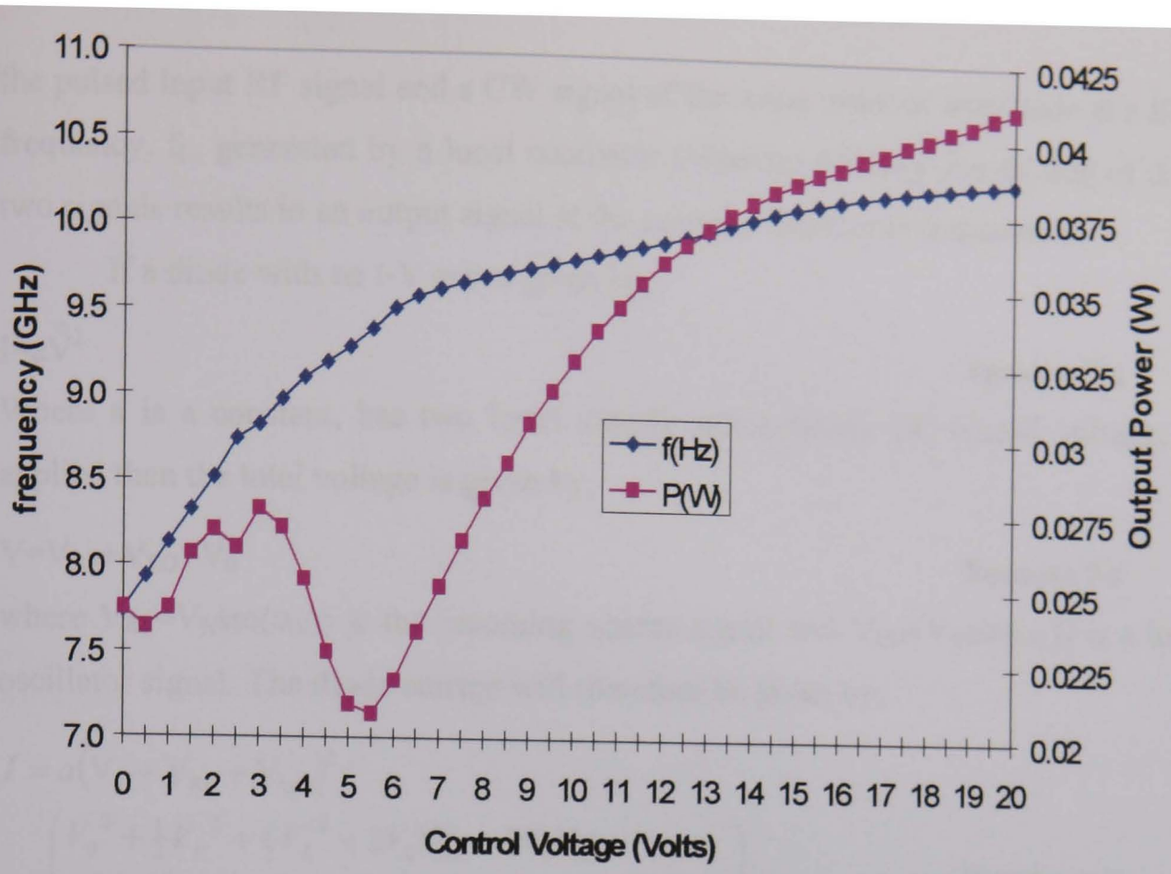

Figure 7-3 Frequency and power against control voltage for microwave source 127117

There were three solid-state sources available identified by their serial numbers as follows 127117, 127124 and 127125. The calibration chart of 127117 is presented in Figure 7-3. These sources had an average power between 15mW and 30mW and a maximum power output of 41mW.

7.2.1 Pulsed microwave oscillator

It was important to investigate the sources capabilities for fast frequency sweeps. In order to observe the frequency change during a relatively short sweep voltage pulse a heterodyne technique with a fast digital oscilloscope was used to analyse the output as opposed to a spectrum analyser which is better suited to CW radiation.

The control voltage pin was connected to a pulse generator which provided a swept voltage pulse to fast tune the frequency on the rising/falling edge of the pulse. The output frequency of the microwave oscillator was about 8-11 GHz but the oscilloscope used could only resolve a maximum frequency of ±750MHz. To see the output on the oscilloscope, the output RF was applied to the input port of a microwave mixer (Farran TB-MXR FTL845B), as shown in Figure 7-4. A mixer is a device that forms the product of two waveforms. A mixer accepts two input signals,

the pulsed input RF signal and a CW signal of the same order of amplitude at a fixed frequency, f_L, generated by a local oscillator (Marconi 6158A), the mixing of these two signals results in an output signal at the sum and difference frequencies.

If a diode with an I-V curve given by,

$$I=aV^2 \qquad \textbf{Equation 7-1}$$

Where a is a constant, has two input signals and a steady DC biased voltage, V_0 applied then the total voltage is given by,

$$V=V_{RF}+V_{LO}+V_0 \qquad \textbf{Equation 7-2}$$

where $V_{RF}=V_R\sin(\omega_R t)$ is the incoming source signal and $V_{LO}=V_L\sin(\omega_L t)$ is a local oscillator signal. The diode current will therefore be given by,

$$I = a(V_0 + V_{RF} + V_{LO})^2$$
$$= a\begin{pmatrix} V_0^2 + \frac{1}{2}V_R^2 + \frac{1}{2}V_L^2 + 2V_0V_{LO} + 2V_0V_{RF} \\ + \frac{1}{2}V_R^2\cos(2\omega_R t) + \frac{1}{2}V_L^2\cos(2\omega_L t) \\ + V_LV_R\cos((\omega_R - \omega_L)t) + V_LV_R\cos((\omega_R + \omega_L)t) \end{pmatrix} \qquad \textbf{Equation 7-3}$$

the DC terms can be ignored, and all frequencies except for the difference frequency will be filtered out. The difference frequency of the incoming signal and the local oscillator is known as the intermediate frequency (IF), $\omega_{IF}=\omega_R-\omega_L$.[76]

The intermediate frequency from the IF port of the mixer was then monitored on the oscilloscope. The oscilloscope has a 1.5 GHz bandwidth and could therefore resolve frequencies of up to ±750 MHz. If the local oscillator frequency was within 750MHz of the input frequency, then the oscilloscope could resolve the intermediate frequency and hence the frequency of the pulsed RF input signal could be ascertained.

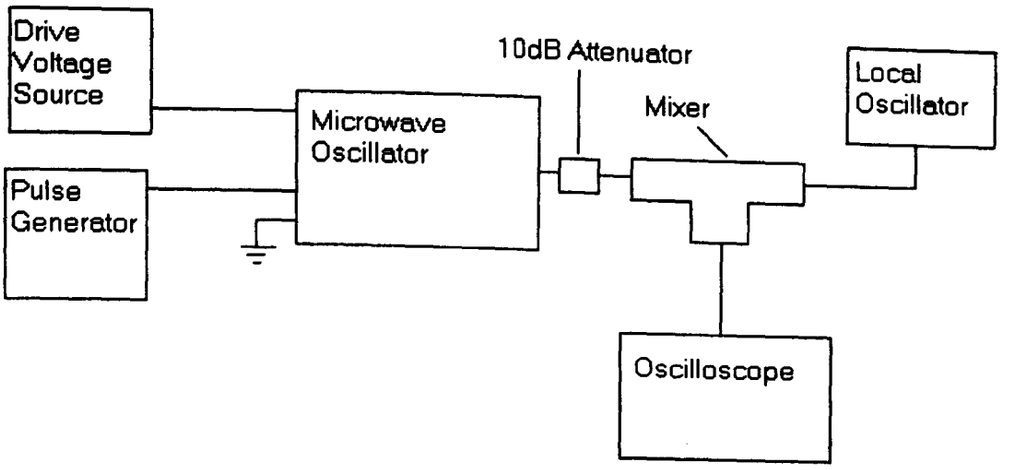

Figure 7-4 Swept source frequency measurement for high frequencies, using a heterodyne technique.

A fast Fourier transform applied to digitised data from such an experiment provides a very powerful method of signal analysis, particularly the recognition of weak signals of well-defined periodicity buried in interfering signals of noise. Such a technique was applied to the IF data received from the digital oscilloscope.

The signal generator was set to produce the frequency tunable input voltage pulse, shown in Figure 7-5, which varied from 0.35 to 3.6 V.

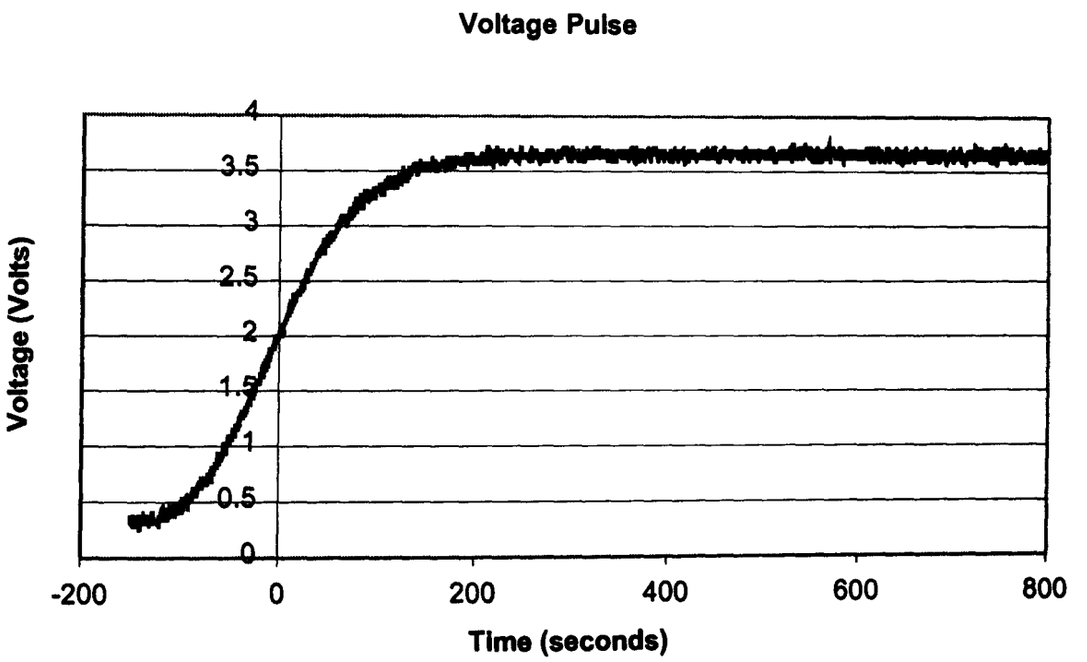

Figure 7-5 The swept voltage pulse used to demonstrate the heterodyne technique.

This voltage sweep corresponds to a frequency sweep of 7.9 to 9.0 GHz. The local oscillator was set to 8.47 GHz. Figure 7-6 show a photograph of the experimental set-up.

Figure 7-6 Experimental set-up showing from left to right, Systron Donner Pulsed generator swept voltage source, Thurlby power supply to drive microwave oscillator, solid-state microwave oscillator, Marconi local oscillator, mixer, fast digitising oscilloscope and spectrum analyser.

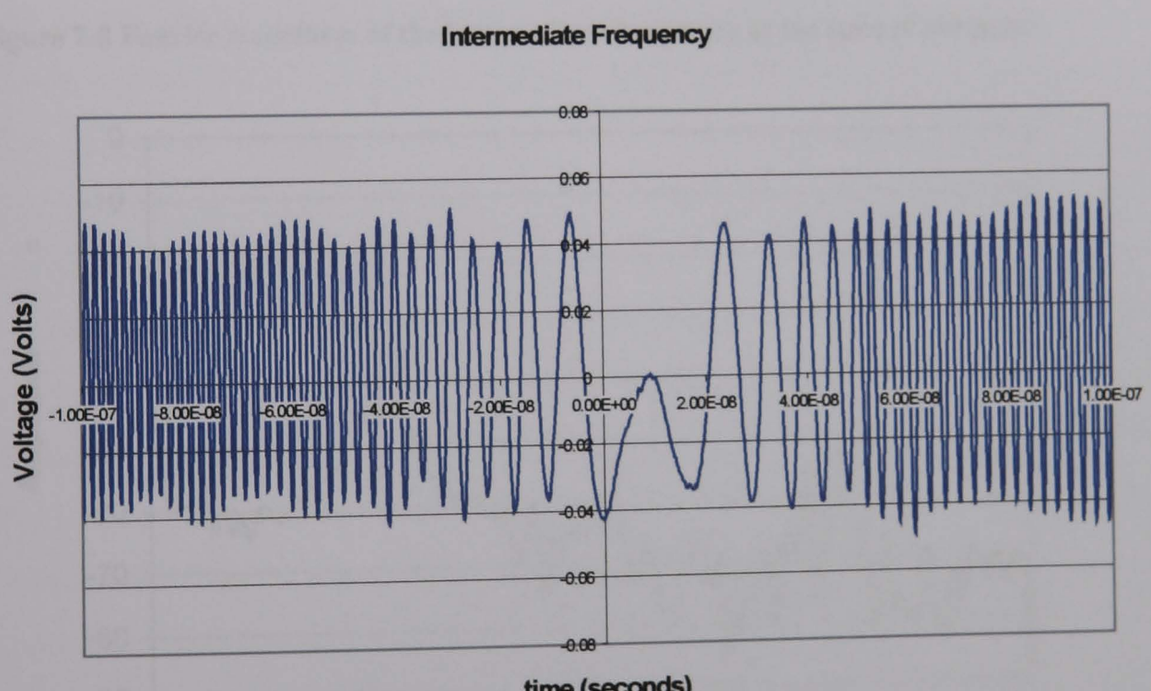

Figure 7-7 The intermediate frequency from the microwave mixer.

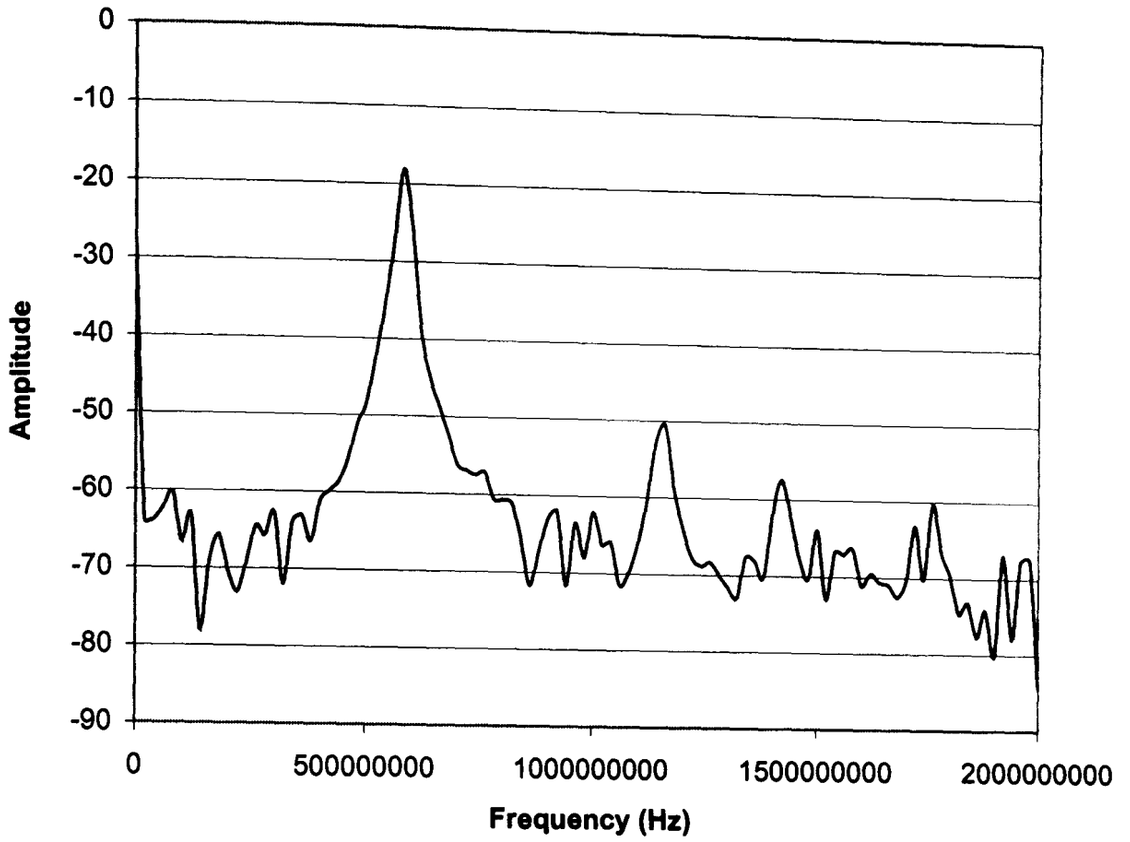

Figure 7-8 Fourier transform of the intermediate frequency at the start of the pulse.

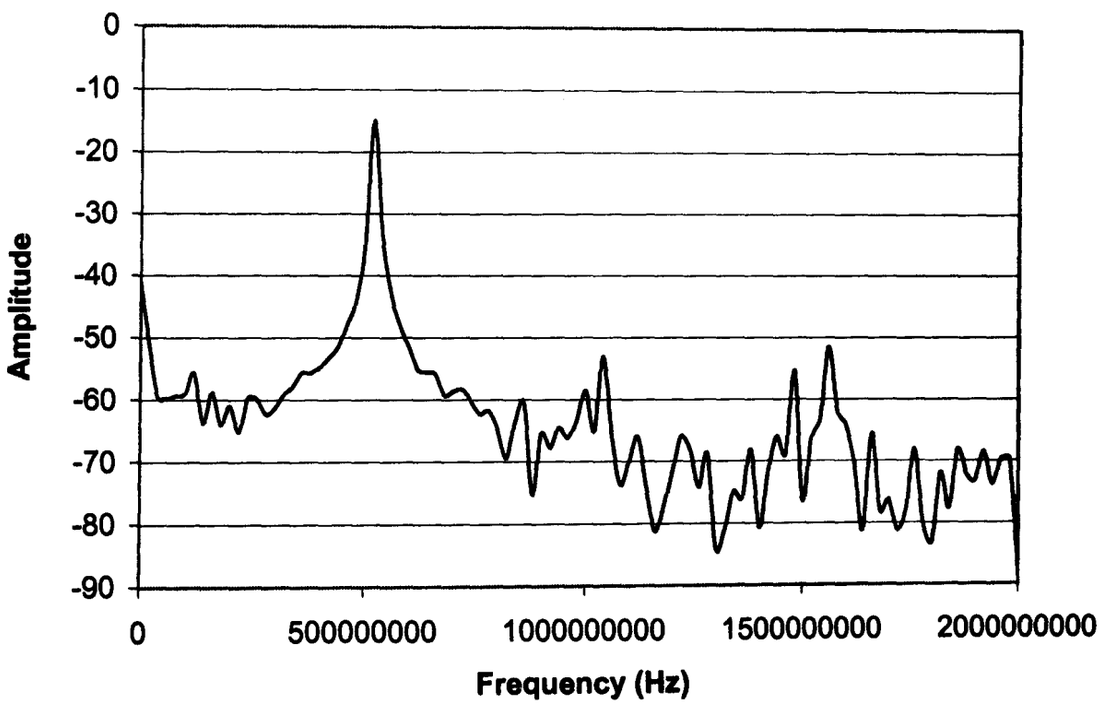

Figure 7-9 Fourier transform of the intermediate frequency at the tail of the pulse.

The output from the mixer (Figure 7-7) was a wave of IF frequency 570MHz (Figure 7-8) slowly sweeping its IF frequency down to zero and up to 530 MHz (Figure 7-9). The sources had a maximum sweep rate of 10 MHz/ns. This shows an input source

frequency sweep from 7.9GHz to 9GHz which is in good agreement with the sweep calculated from the voltage sweep.

7.3 Long pulse duration compression

The compressors were studied in a series of experiments. First a low power long pulse duration compression was performed using a solid-state source as the swept input source, where the pulse duration is much longer than the sweep time and only part of the pulse is compressed. A pulse generator (Systron Donner 110C) produced a sweep voltage, which was applied to a special pin of the solid-state oscillator to control its oscillation frequency. The solid-state source had a maximum sweep rate of about 10MHz/ns. The input radiation was launched into WG16 waveguide from a co-axial to waveguide adapter and passed through a circular-to-rectangular waveguide converter. A 10MHz to 18GHz crystal detector (Narda 9610), and a waveguide attenuator (Flann 16020) were used to measure the power and display it as a voltage on a 1.5GHz single shot bandwidth digitising oscilloscope (Le Croy LC684D). The attenuator was used to set the output power to protect the solid-state microwave crystal detectors. This wave was then compressed in a dispersive medium and displayed on a fast digital oscilloscope as shown below in Figure 7-10. To obtain the power compression ratio, the attenuation of the pulse was set so that the crystal detector displayed an output of 50mV. The experiment was repeated with the dispersive medium removed and the couplers directly connected together with the attenuation decreased until the 50mV signal was again observed on the digital oscilloscope. The power compression ratio was then found from the ratio of the attenuation used for the compressed and uncompressed pulses. To obtain the pulse shapes the calibration chart of the crystal detector was used. The frequency modulation of the input wave was monitored using a heterodyne technique and a fast digital oscilloscope. A fraction of the pulse was mixed with a signal from a cw local oscillator with a set frequency, f_{lo}, to produce an intermediate frequency pulse with a maximum frequency difference of ±750MHz which was displayed on the digital oscilloscope.

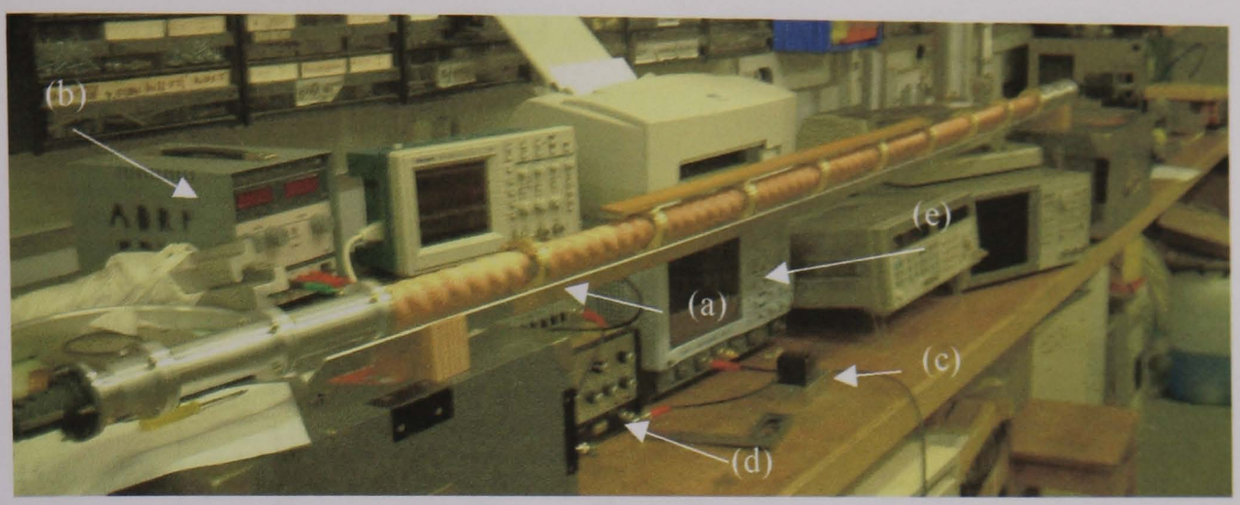

Figure 7-10 A picture of the experimental set-up for the measurement of microwave pulse compression, showing (a) the copper helically corrugated waveguide, (b) Thurlby power supply, (c) Solid-state oscillator, (d) Systron Donnor frequency control voltage, (e) 1.5GHz LeCroy Digitising Oscilloscope.

Two dispersive medium geometries were studied a cylindrical waveguide with circular cross-section, and 3 different circular waveguides with a 3-fold helically corrugated groove on the inside surface of the cylindrical waveguide (Figure 7-10). The maximum pulse compression ratio in these experiments was limited by the maximum sweep rate of the solid state oscillator.

7.3.1 Circular compressor

The optimised compression ratios of various lengths of circular waveguide, using a TE_{11} mode were studied. The waveguide had a length between 3.1m and 9.7m and diameter of 19.2mm. The compressor was modular and could be made from up to 4 separate sections of circular waveguide. For each length of smooth-waveguide compressor, three parameters of the input pulse (start frequency, stop frequency and pulse width) were optimised at a pulse repetition rate of 20-50 Hz. The optimised power compression factor varied slightly (within ±15%) for different lengths between 4.95 m and 9.9 m, as shown in Figure 7-11, and a maximum power compression ratio of 8.7 was achieved at a length of 6.6 m.

This resulted in a compressed pulse with a duration of 2.5 ns with a power compression ratio of 7. The transition region before the linear part of the swept voltage pulse modulating the frequency provided close to the optimum frequency

sweep. The experimentally achieved power compression factor was mainly limited by the frequency sweep rate, available.

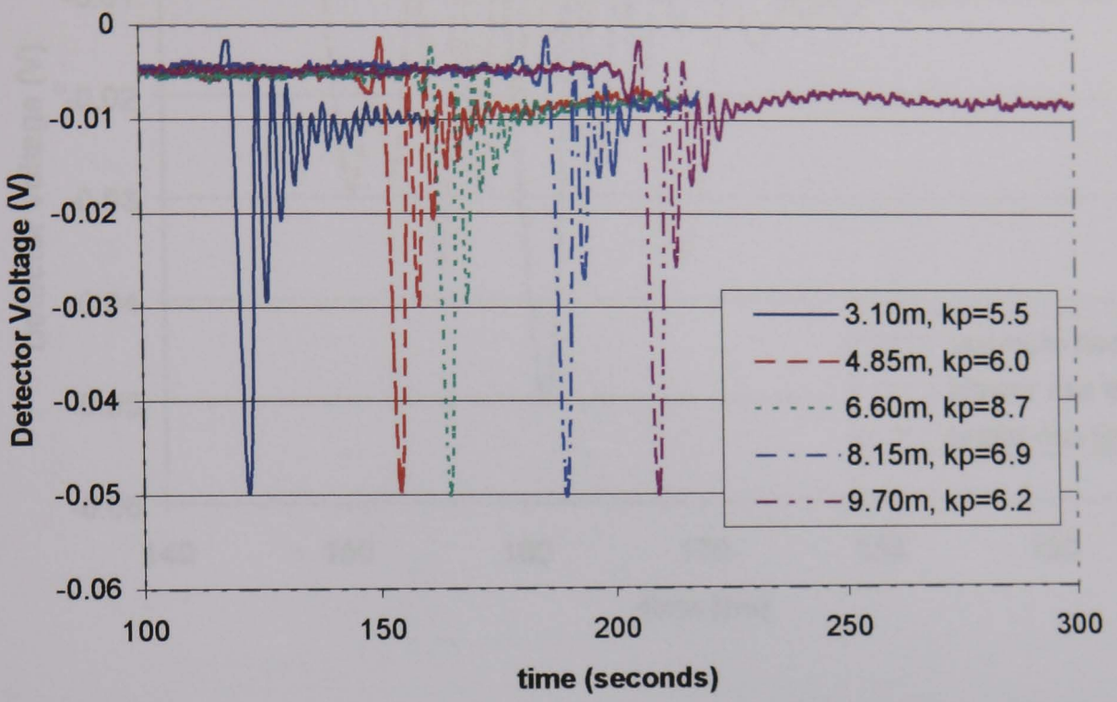

Figure 7-11 Pulses compressed in various lengths of circular waveguide.

In order to observe the sensitivity to small changes in the frequency sweep the time it took to sweep from the minimum frequency to the maximum frequency, known as the rise time, was varied slightly by ±10ns. Figure 7-12 shows a series of compressed pulses having the optimum rise time, a faster rise time and a slower rise time respectively. In both cases the peak power was 73% less than the optimum case.

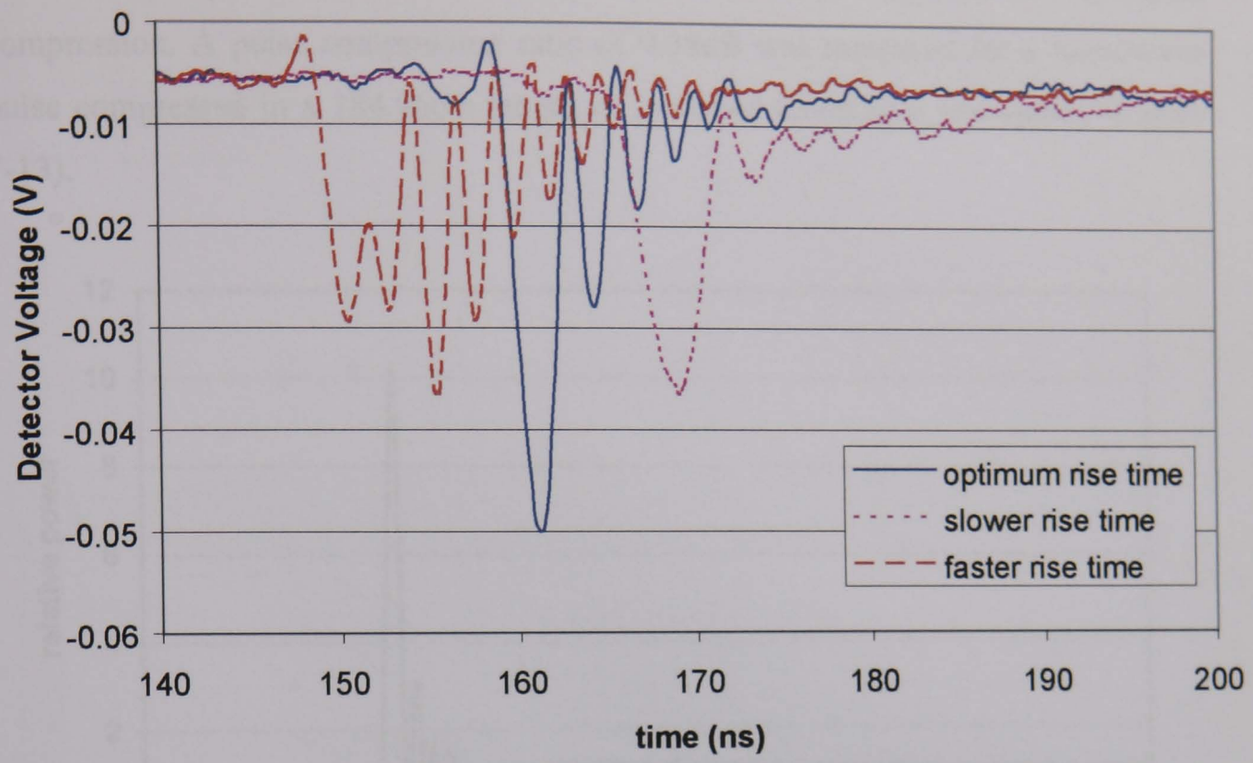

Figure 7-12 Faster and slower sweep of a pulse compressed in a 6.6m long smooth circular waveguide.

7.3.2 Modified aluminium helix

In the next series of experiments, a helically corrugated waveguide was used as a pulse compressor. A 3-fold sinusoidal corrugation coupled a circularly polarized $TE_{1,1}$ mode having large group velocity with a near-cut-off counter-rotating $TE_{2,1}$ mode resulting in a frequency region of 5-6% where the eigenwave group velocity changed from about $0.1c$ to $0.5c$.

The input radiation was launched from the circular waveguide through a polariser having elliptical cross-section in the middle, which converted the linearly polarised $TE_{1,1}$ mode to a circularly polarized mode. Two modified helical tapers were used to minimise reflections from either end of the helical compressor, which were 4 periods long. The most favourable region for pulse compression in the helically corrugated waveguide was the part of the dispersion characteristic where the group velocity has a negative gradient as a function of frequency. Correspondingly, the frequency modulation in the input pulse should have a negative slope in contrast to the case when a smooth waveguide was used. The minimum and

maximum frequencies as well as the fall time were adjusted for optimum compression. A pulse compression ratio of 9.38dB was measured for a microwave pulse compressed in a 184.96cm length of modified aluminium waveguide (Figure 7-13).

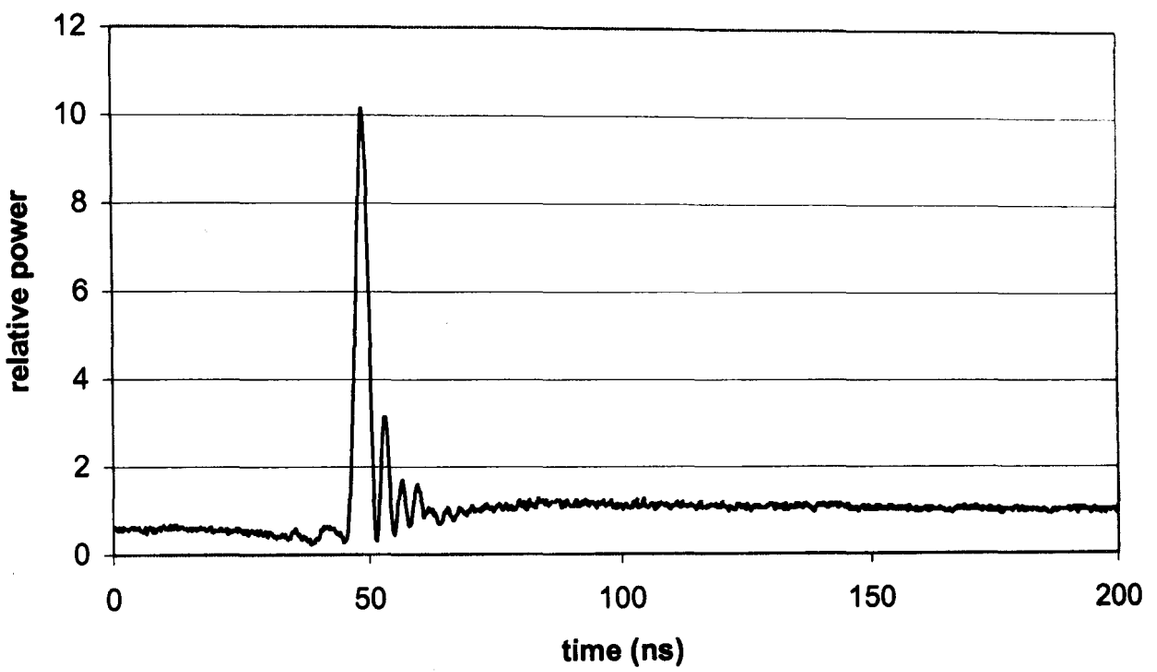

Figure 7-13 Pulse compression in the full length modified aluminium helix using a long pulse duration input pulse.

7.4 Pulsed

A conventional X-band TWT (TMD PTC6358) with an output power of about 1kW driven by a solid-state frequency-tuneable oscillator was used for generating an input pulse for the compressors. An external trigger for the TWT set the pulse width, allowed the time compression ratio of the pulse to be measured and hence the compression efficiency to be found. The experimental set-up used is shown in Figure 7-14.

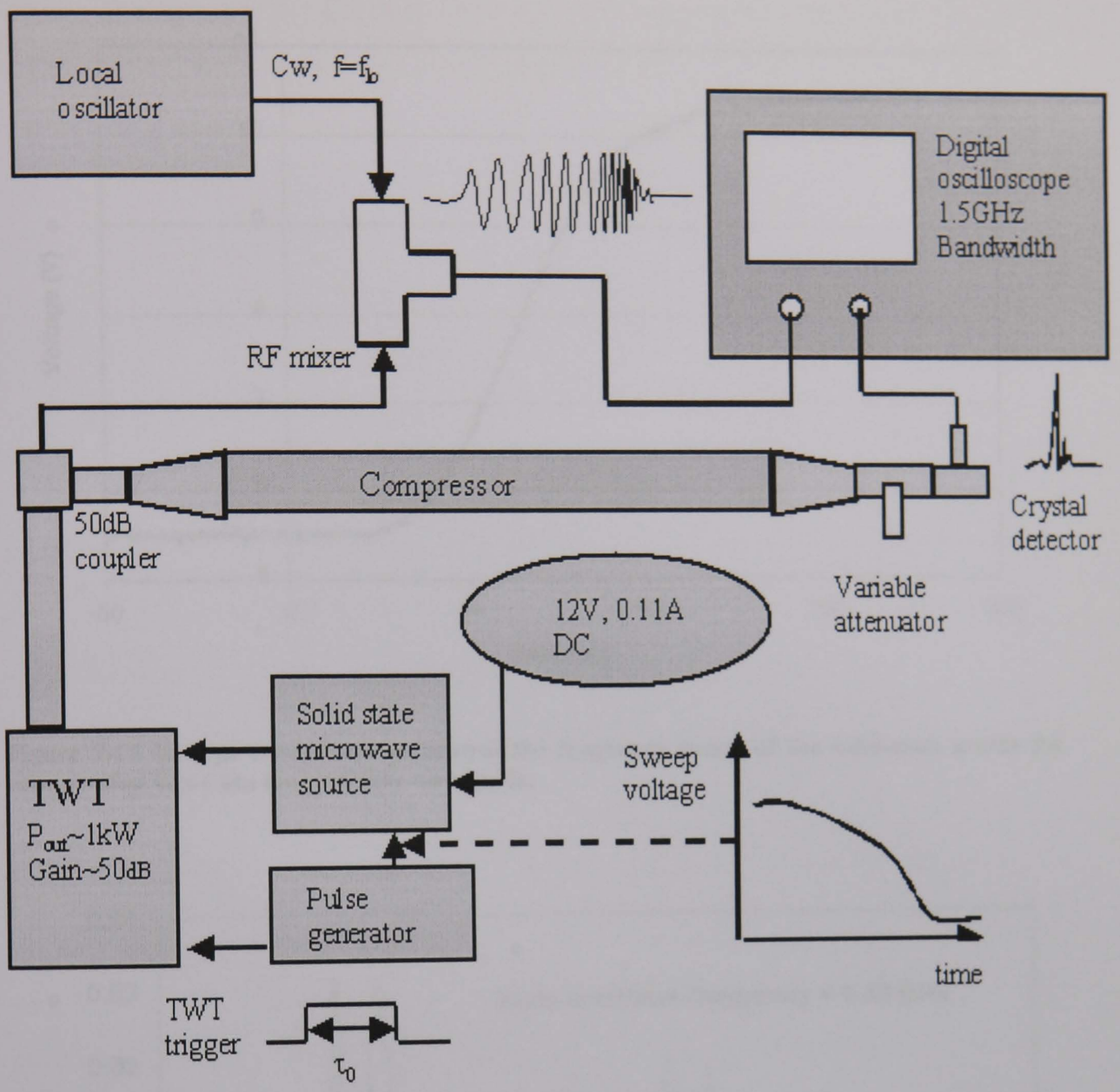

Figure 7-14 The experimental set-up for the measurement of power compression ratio, of pulses from a TWT.

7.4.1 Circular compressor

A 9.6 mm radius aluminium circular waveguide consisting of two 3.3 metre long straight circular waveguides and a U-bend of average length of 25cm was used as a sweep-frequency based pulse compressor. A voltage ramp (Figure 7-15) from 5.5 to 10.5 Volts in about 100ns applied to the driving pin of the solid state source was used to produce the necessary frequency sweep for sweep-frequency based pulse compression in a circular waveguide.

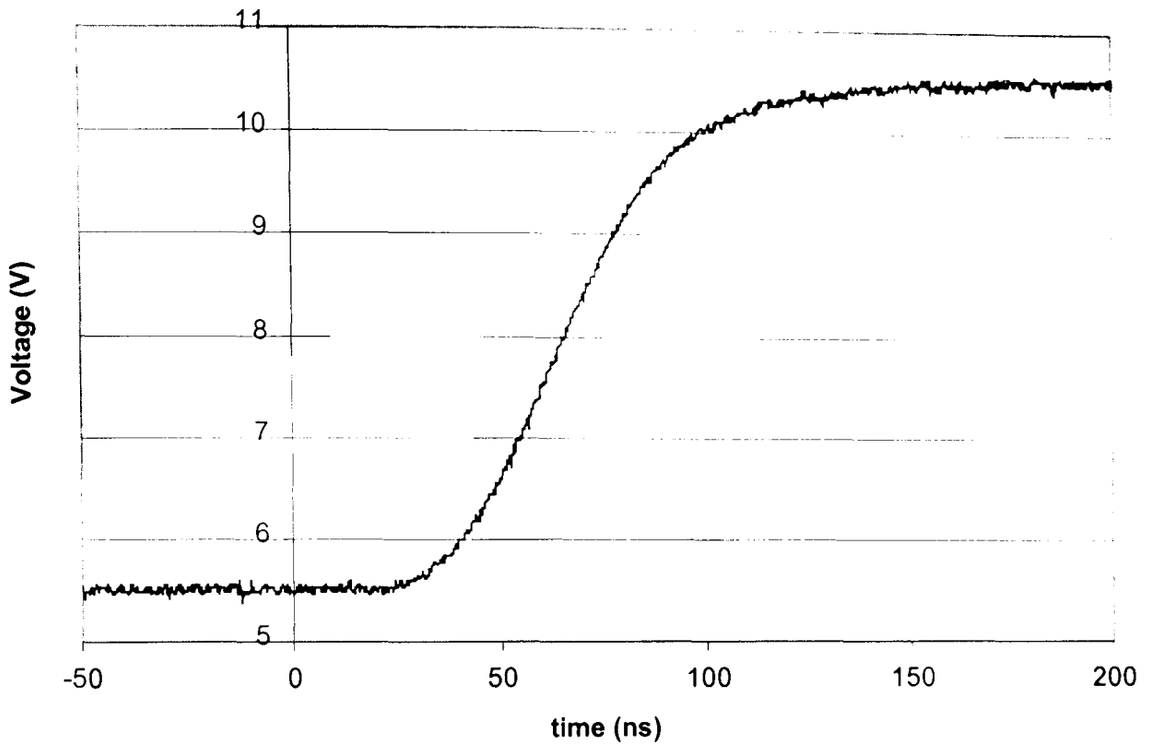

Figure 7-15 Voltage sweep used to control the frequency sweep of the solid-state source for compression in a 6.6m long circular waveguide.

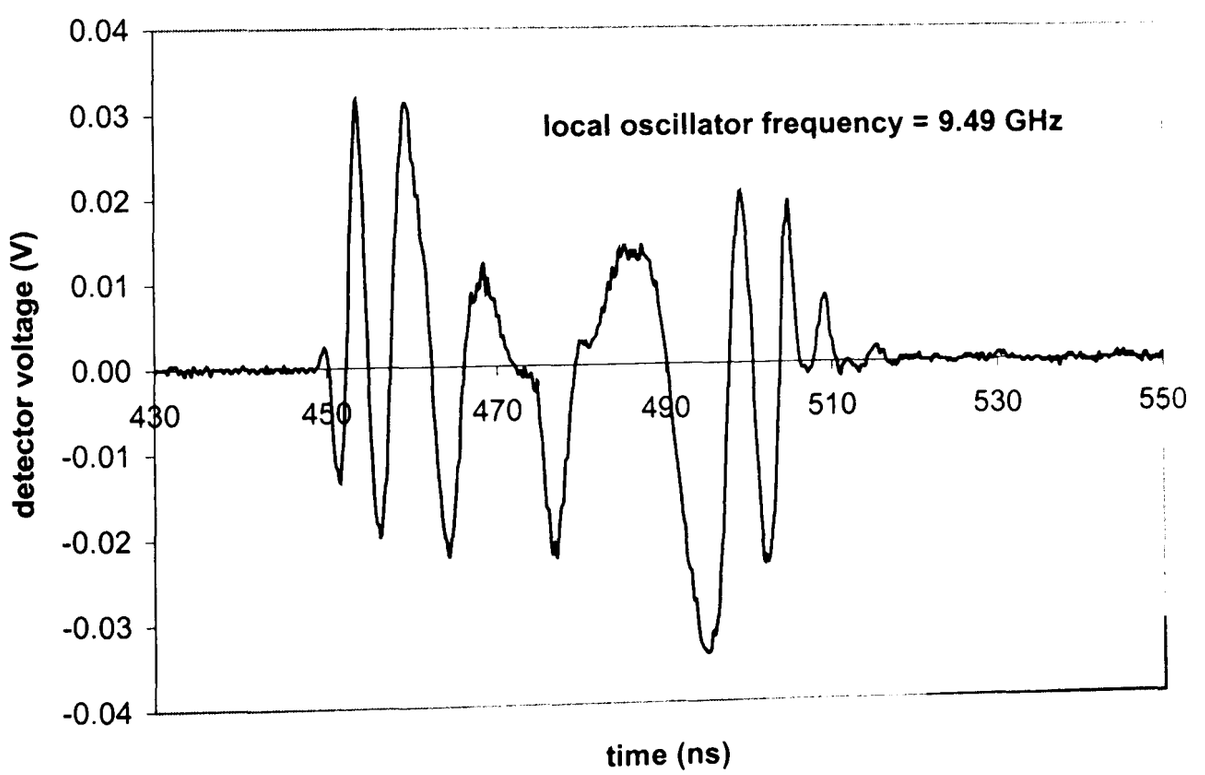

Figure 7-16 Mixed output from the travelling wave tube, of the pulse to be compressed in the circular waveguide.

The frequency sweep was found by measuring the period of each oscillation in the mixed pulse (Figure 7-16), and is shown in Figure 7-17.

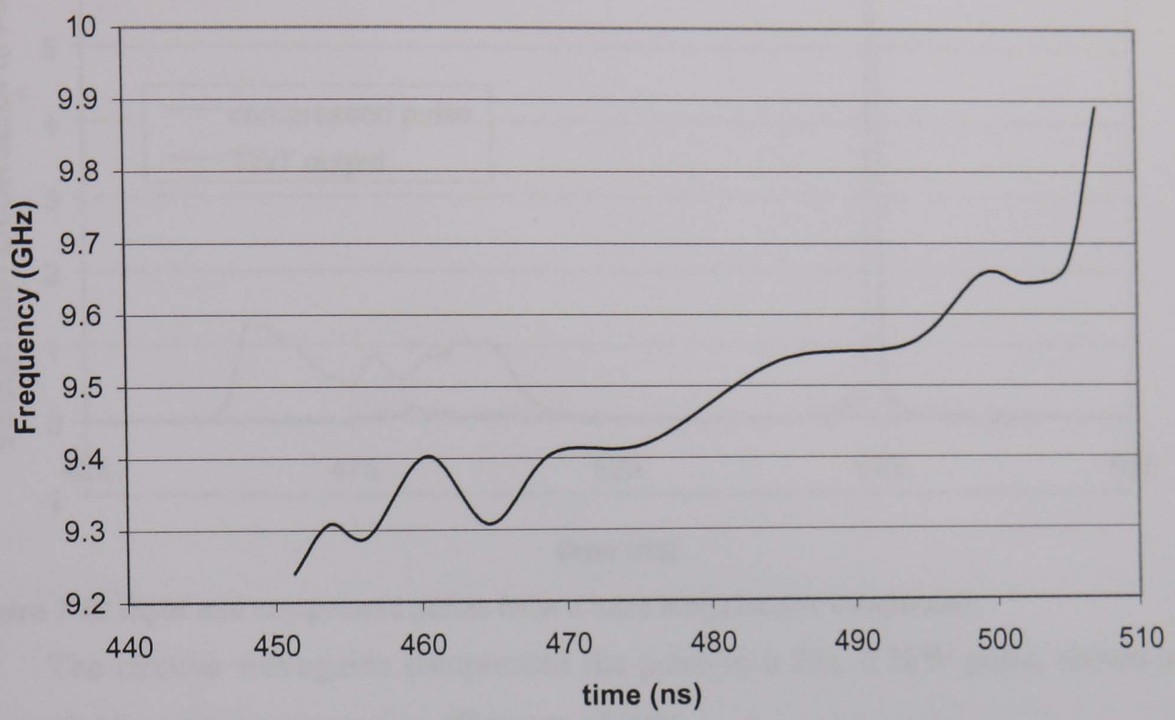

Figure 7-17 Frequency sweep calculated from the mixed pulse from the circular waveguide compression experiment.

The TWT was used to produce a 1kW pulse with a pulse duration of 54ns, in which time the microwave source was swept from 9.2–9.9GHz which was propagated through a circular waveguide in order to compress its duration.

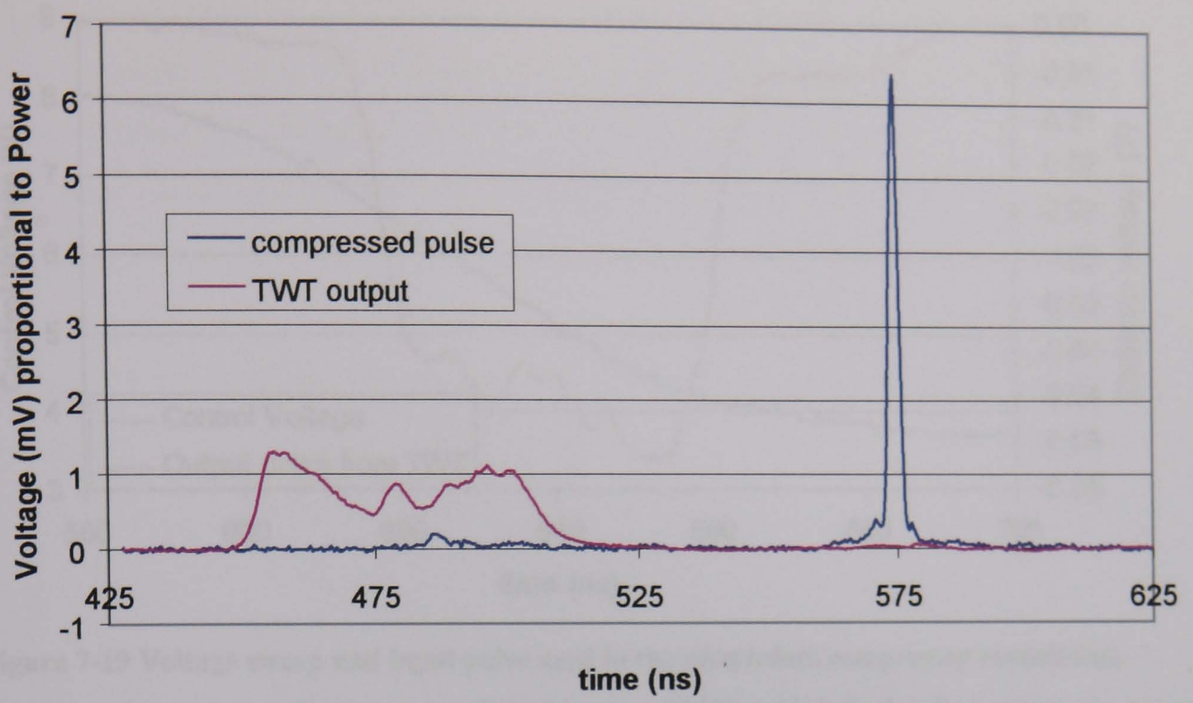

Figure 7-18 Input and compressed pulses from a 6.6m long circular compressor.

The circular waveguide compressed the pulse to a 2ns, 6.3kW pulse, shown in Figure 7-18, with a compression efficiency of 23%.

7.4.2 1st aluminium compressor

The first experiments of sweep-frequency based pulse compression using a helically corrugated waveguide were undertaken using the 1st aluminium helix. The experiment was set up using a length of waveguide made from 64 periods and two 4 period aluminium tapers. A voltage pulse of 100ns duration was swept from 8 volts to 3.7 volts (Figure 7-19), which corresponded to a frequency sweep from 9.95 to 9.05 GHz.

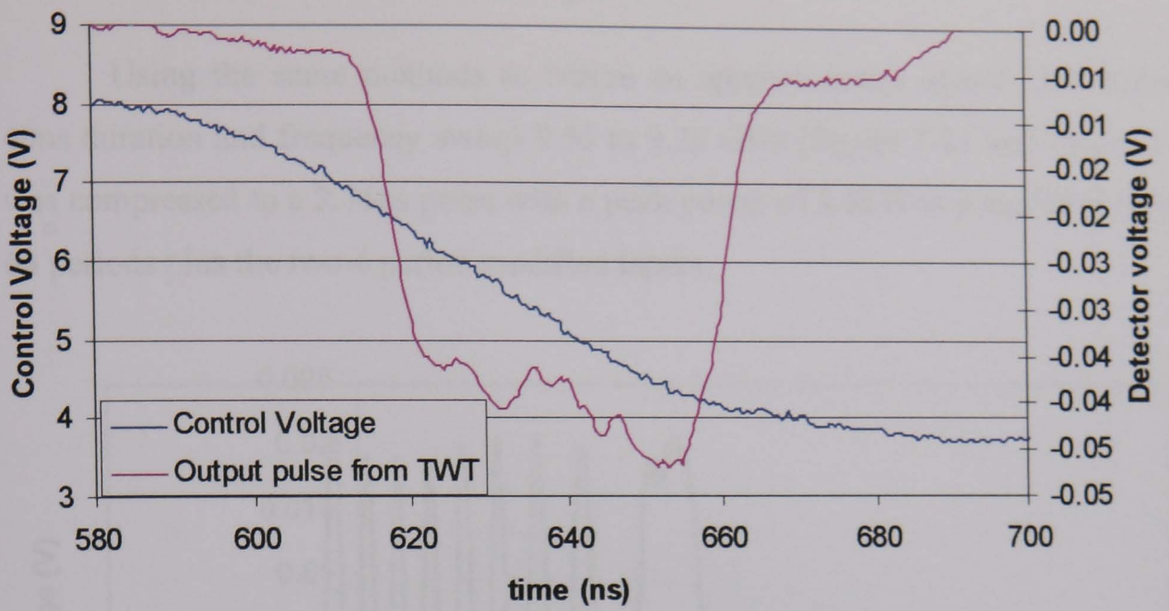

Figure 7-19 Voltage sweep and input pulse used in the aluminium compressor experiment.

A 45ns microwave pulse was amplified by the TWT which had a frequency sweep of 9.6 to 9.1GHz, which was compressed to a 4.5ns pulse with a power compression ratio of 3.5, as shown in Figure 7-20. The compressed pulse, excluding the side lobes, had a compression efficiency of 35%.

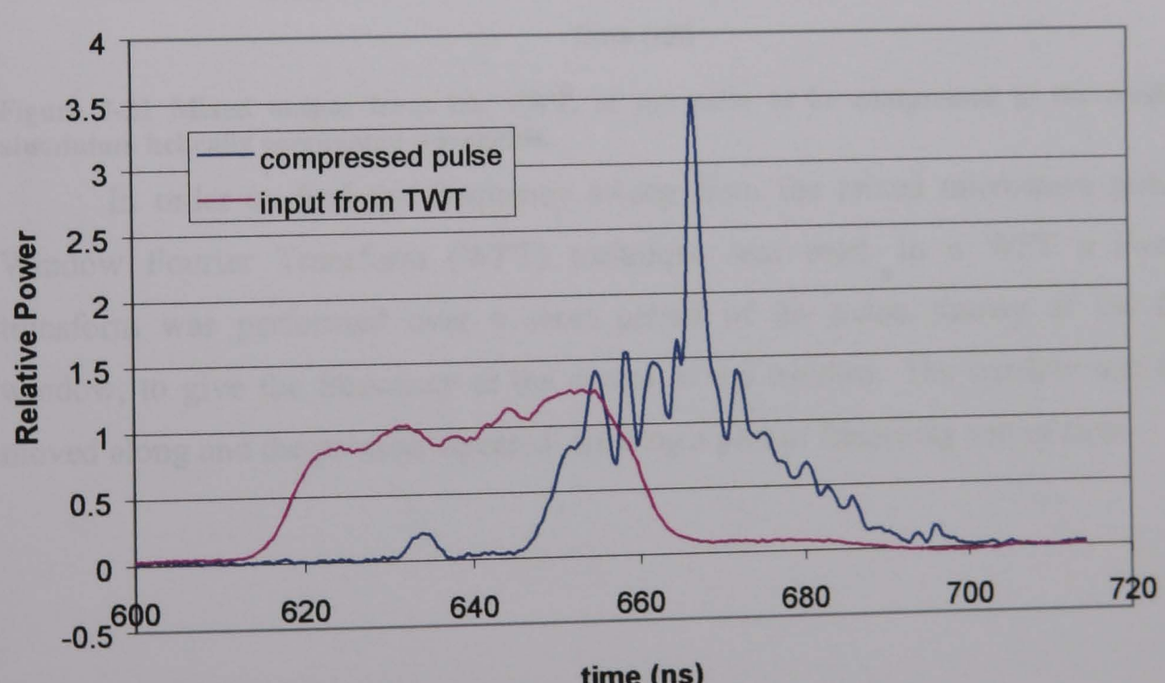

Figure 7-20 Experimental measurement of optimum pulse compression in the aluminium helix

7.4.3 Modified aluminium compressor

Using the same methods as before an approximately square 1kW pulse of 40ns duration and frequency sweep 9.55 to 9.25 GHz (Figure 7-21 and Figure 7-22) was compressed to a 2.75ns pulse with a peak power of 8.5kW in a modified helix of 64 periods plus the two 4 period modified tapers.

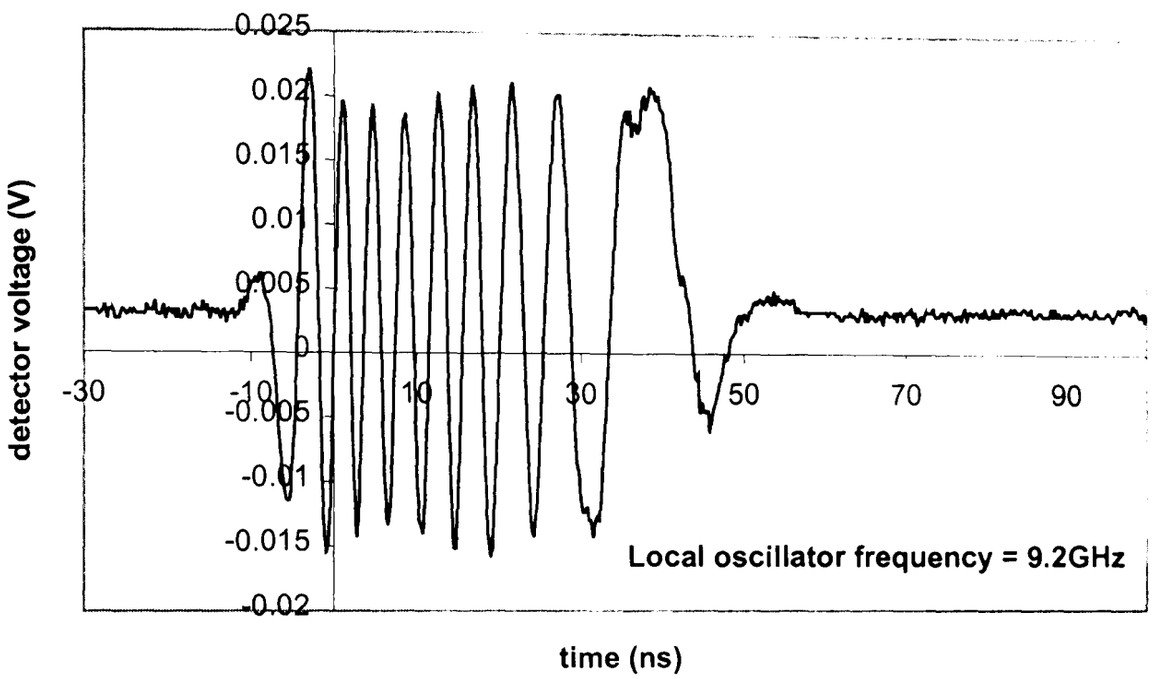

Figure 7-21 Mixed output from the TWT, of the pulse to be compressed in the modified aluminium helically corrugated waveguide.

In order to find the frequency sweep from the mixed microwave pulse a Window Fourier Transform (WFT) technique was used. In a WFT a Fourier transform was performed over a short period of the pulse, known as the time window, to give the frequency at the centre of the window. The window was then moved along and the process repeated, creating a plot of frequency versus time.

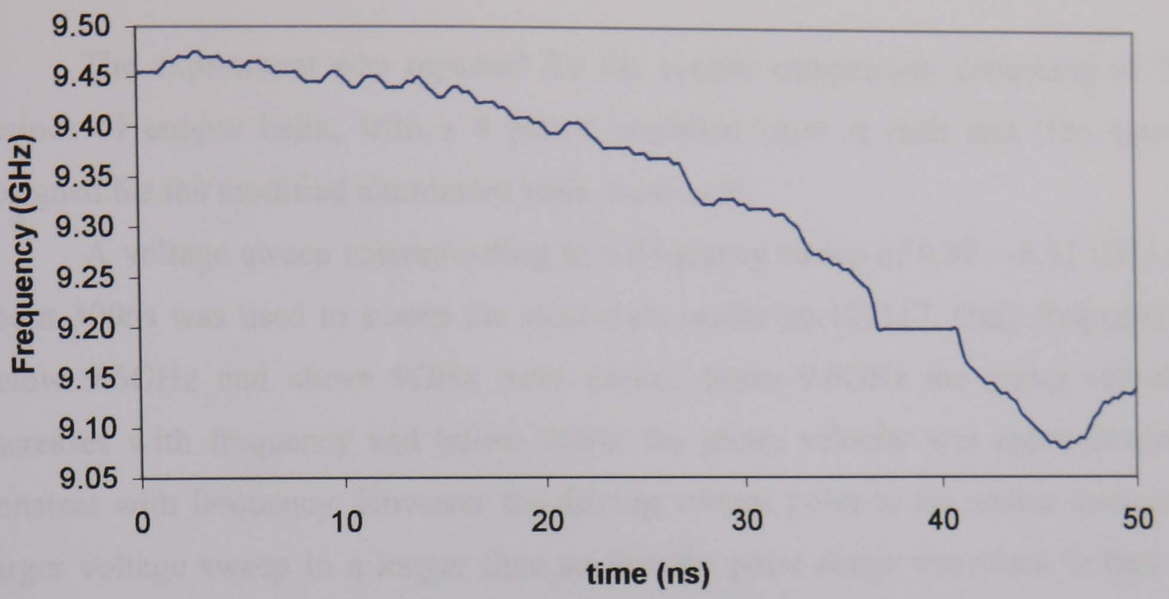

Figure 7-22 Frequency sweep used in the modified aluminium helix compression, found using a Window Fourier Transform.

This compressed pulse, shown in Figure 7-23, excluding the side lobes contained 52% of energy of the input pulse.

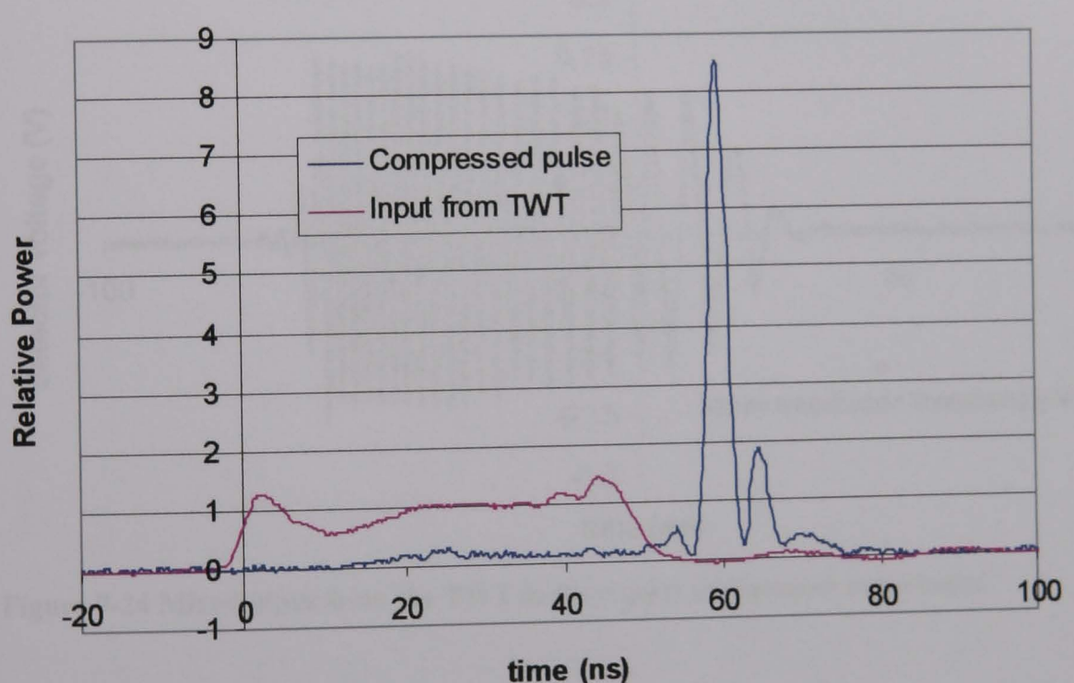

Figure 7-23 Experimental measurement of the maximum pulse compression in the modified helix.

7.4.4 Copper compressor

The experiment was repeated for the copper compressor, consisting of 72 periods of copper helix, with a 4 period modified taper at each end. The tapers designed for the modified aluminium helix were used.

A voltage sweep corresponding to a frequency sweep of 9.87 – 8.51 GHz in about 300ns was used to sweep the solid-state source no.127117. Only frequencies below 9.6GHz and above 9GHz were useful, above 9.6GHz the group velocity increases with frequency and below 9GHz the group velocity was approximately constant with frequency. However the driving voltage pulse to the source sweeps a larger voltage sweep in a longer time so that the pulse shape was close to that of optimum compression. A 70ns pulse was amplified by the TWT (Figure 7-24), giving a frequency sweep of 9.6 to 9.35GHz, as shown in Figure 7-25.

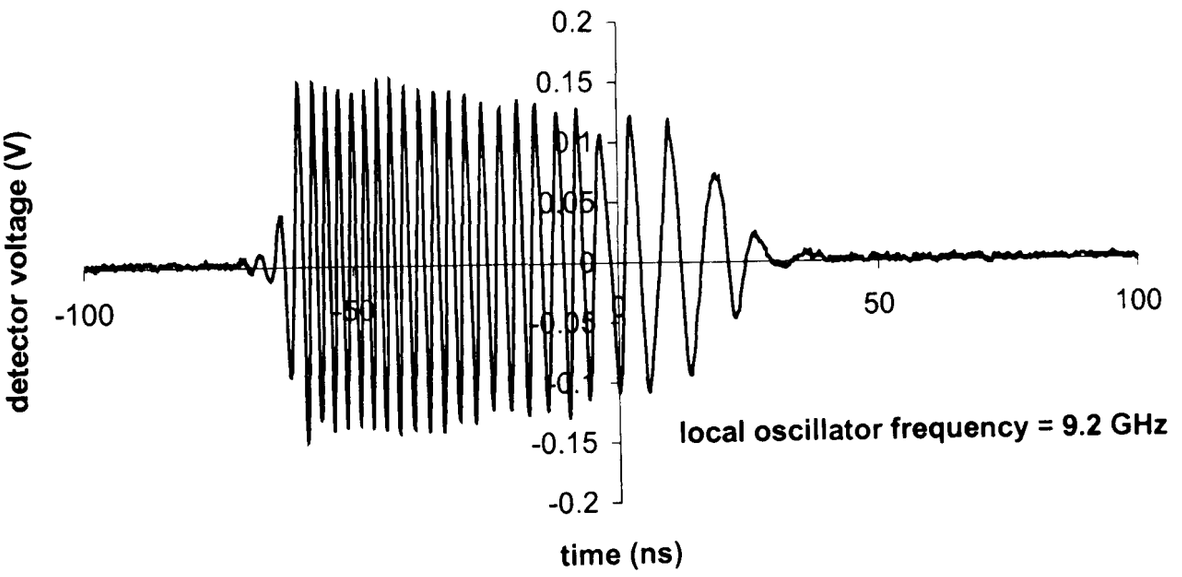

Figure 7-24 Mixed input from the TWT in the copper compressor experiment.

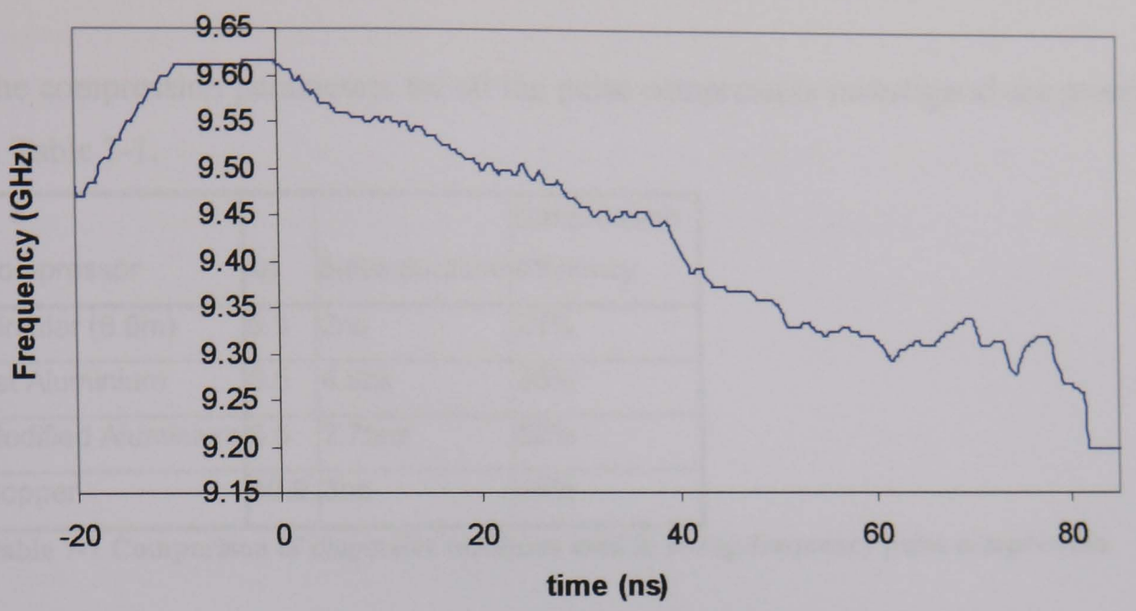

Figure 7-25 The frequency sweep of the pulse compressed in the copper helix, calculated from the mixed output using a Window Fourier Transform.

Experimental optimisation resulted in a compressed pulse of 3 ns duration with a peak power compression ratio of 10.9 (10.4 dB). This pulse, shown in Figure 7-26, excluding the side lobes contained 44% of energy of the input pulse.

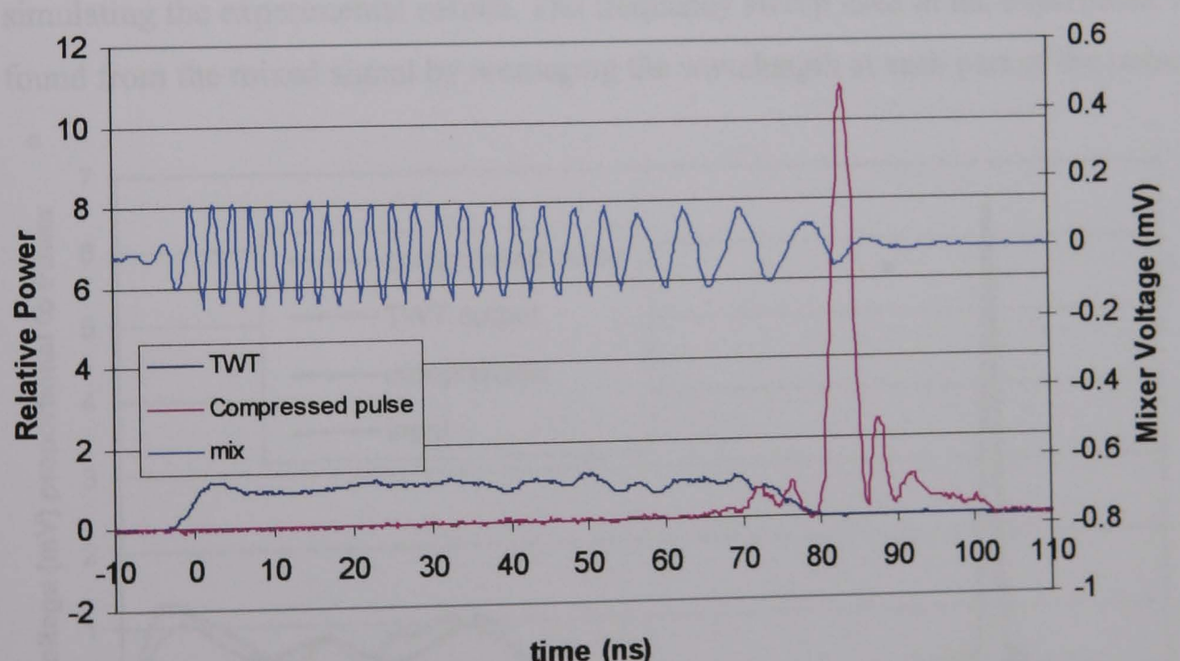

Figure 7-26 Optimised pulse compression in the copper helix, showing input and compressed pulses and the mixed input signal

7.4.5 Comparison between the different pulse compressors

The compression parameters for all the pulse compressors investigated are presented in Table 7-1.

Compressor	kp	pulse duration	compression efficiency
Circular (6.6m)	6.3	2ns	23%
1st Aluminium	3.5	4.5ns	35%
Modified Aluminium	8.5	2.75ns	52%
Copper	10.9	3ns	44%

Table 7-1 Comparison of dispersive mediums used in sweep-frequency pulse compression.

7.5 Numerical simulation of experiments

7.5.1 Circular compressor

The theoretical model simulating the compression of pulses was verified by simulating the experimental results. The frequency sweep used in the experiment was found from the mixed signal by measuring the wavelength at each part of the pulse.

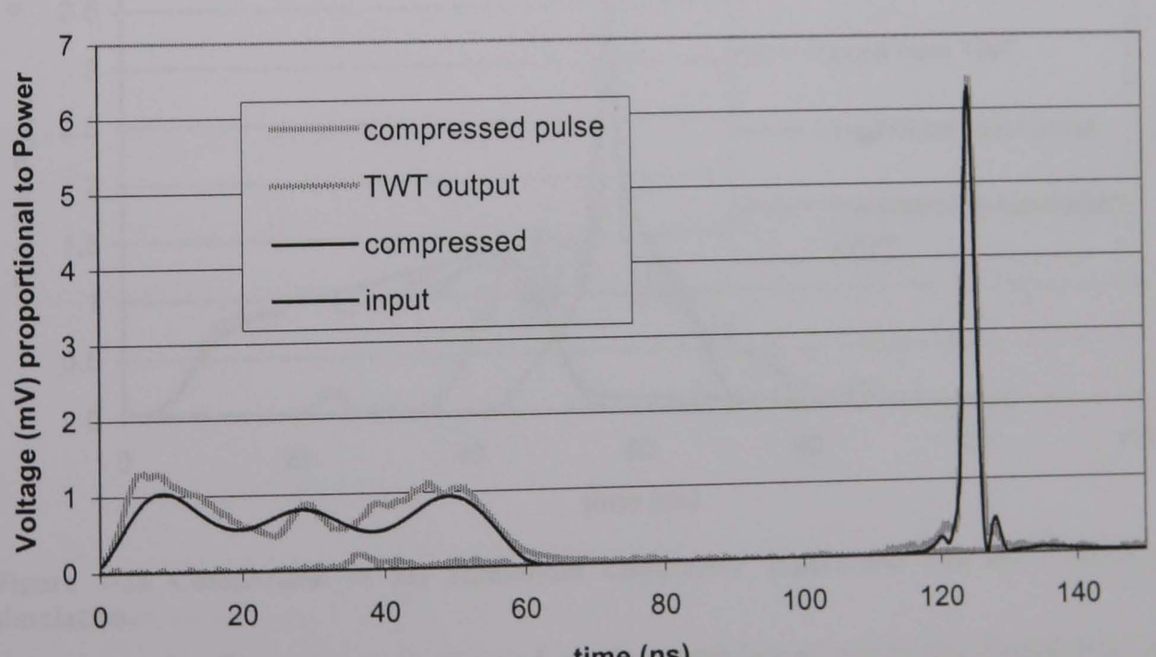

Figure 7-27 Experimental measurement of pulse compression in a 6.6m circular waveguide and Fourier optic simulation.

A similar input pulse shape to the TWTs output pulse was used with this frequency sweep in the model to obtain a simulation of the compressed pulse. The length of the circular waveguide was given as 6.85 metres. This was found from the 6.6 metre circular waveguide plus 25cm for the U-bend. The experiment gave a maximum power compression ratio of 6.3 and a pulse duration of 2ns. The model also gave a maximum power compression ratio of 6.3 and a pulse duration of 2ns as can be seen in Figure 7-27. The theory gave good agreement with the pulse shape obtained in the experimental results.

7.5.2 Aluminium compressor

As the method of perturbations was unable to accurately calculate the dispersive characteristics of either the aluminium or modified aluminium helix, the simulation was adapted to take this into account. A best fit 6^{th} order polynomial of the dispersion modelled using MAGIC was used as the dispersion relation of the aluminium helix in the simulation.

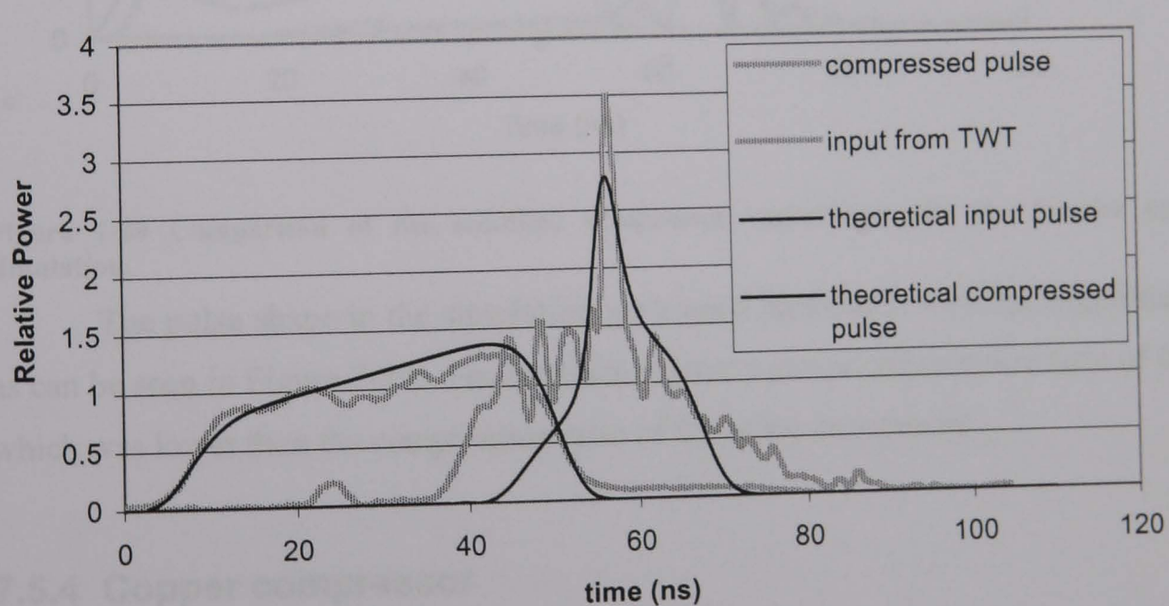

Figure 7-28 Comparison of the aluminium compressor experiment and the Fourier optic simulation.

As the frequency sweep used in the experiment using the aluminium helix was not measured, the frequency sweep was found using the voltage sweep used to control the solid state oscillator. This method was not as accurate as compared to measuring the real frequency sweep of the compressed pulse with the simulation

deviating slightly from the experimental results. The simulation gave a power compression ratio of 2.78, where as the experiment gave a power compression ratio of 3.5, as shown in Figure 7-28.

7.5.3 Modified aluminium compressor

For the simulation of the compression of the modified helix, the dispersion characteristics measured using the VNA were used by inserting a best fit 6th order polynomial.

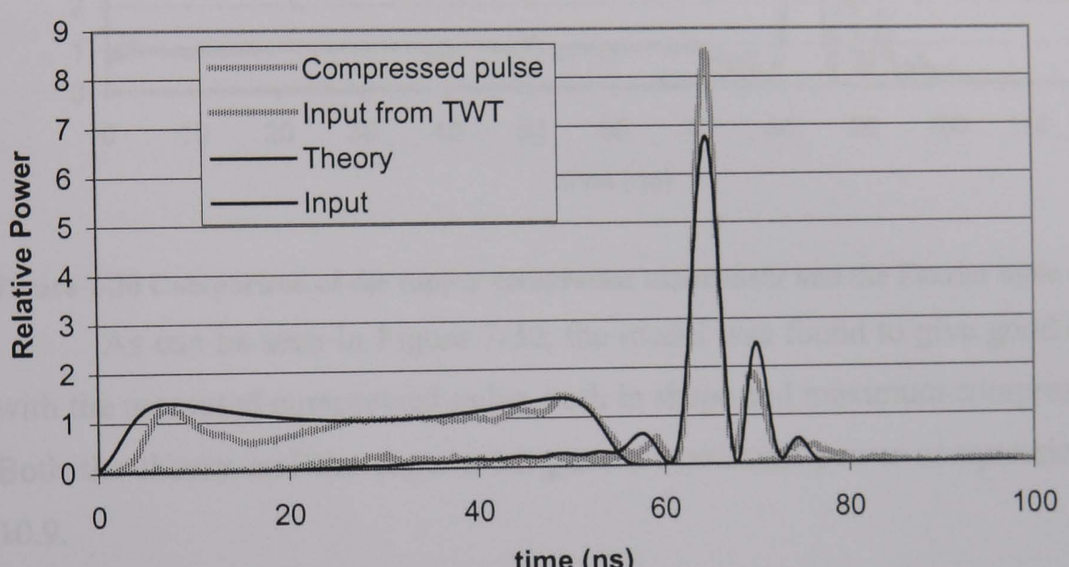

Figure 7-29 Comparison of the modified compressor experiment and the Fourier optic simulation.

The pulse shape in the simulation gave good agreement with the experiment, as can be seen in Figure 7-29. The simulation gave a power compression ratio of 6.8, which was lower than the compression ratio of 8.5 in the experiment.

7.5.4 Copper compressor

The experiment had a length of 72 periods and 4 tapered sections, in the simulation the tapers were approximated to have an effective length of half their actual length, so a length of 76 periods was used. The frequency sweep was again found from the mixed pulse. As the dispersion found using the method of perturbations gave good agreement with all other results for the copper helix, the

dispersion characteristics can be calculated in the numerical model with out the use of best fit polynomials.

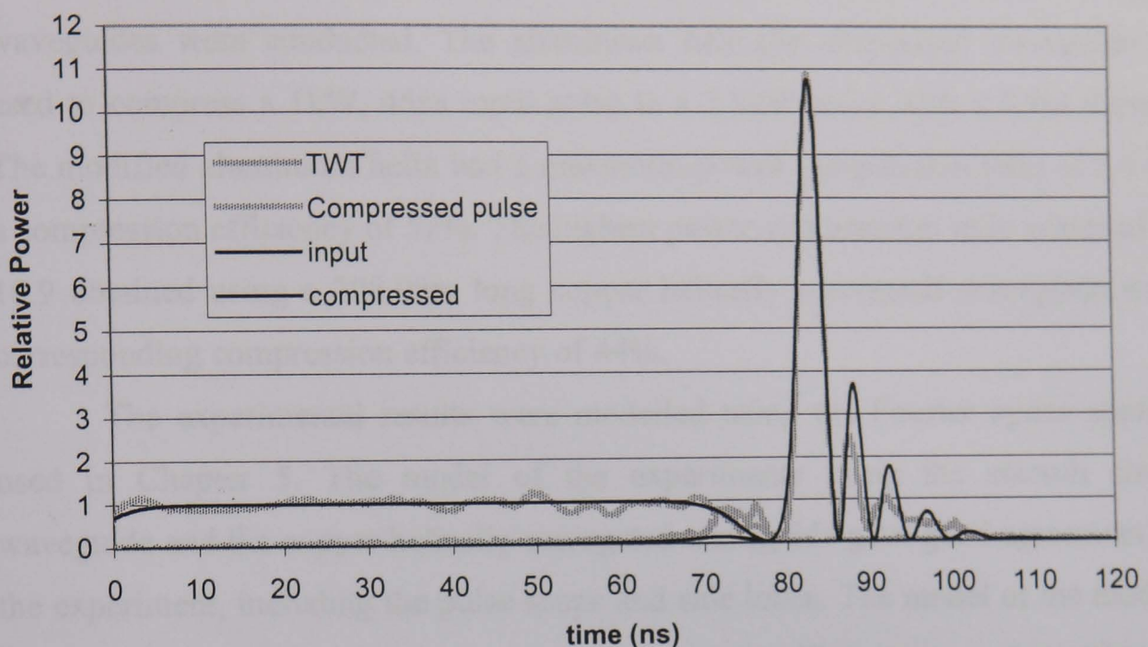

Figure 7-30 Comparison of the copper compressor experiment and the Fourier optic simulation.

As can be seen in Figure 7-30, the model was found to give good agreement with the measured compressed pulse, both in shape and maximum compression ratio. Both the theory and the experiment gave a maximum power compression ratio of 10.9.

7.6 Discussion

In this chapter the concept of sweep-frequency based pulse compression using a helically corrugated waveguide was experimentally studied. The solid state microwave source was investigated, and was found to have a maximum sweep rate of 10MHz/ns. Sweep-frequency based compression using a smooth circular waveguide was first investigated using the low power solid state oscillator. Several lengths of circular waveguide was used to find the optimum length of waveguide. The optimum power compression ratio of 8.7 was obtained using a 6.6m length of smooth waveguide. Next a 1kW conventional TWT was used to amplify the output from the solid state oscillator for the duration of the frequency sweep. Using a 6.6m

length of smooth circular waveguide a power compression ratio of 6.3 was obtained with a compression efficiency of 23%.

The first ever pulse compression experiments using helically corrugated waveguides were conducted. The aluminium helically corrugated waveguide was used to compress a 1kW, 45ns input pulse to a 3.5kW pulse with a 4.5ns duration. The modified aluminium helix had a maximum power compression ratio of 8.5 with a compression efficiency of 52%. The highest power compression ratio achieved was 10.9 obtained using a 208.08m long copper helically corrugated waveguide with a corresponding compression efficiency of 44%.

The experimental results were modelled using the Fourier optics approach used in Chapter 5. The model of the experiments using the smooth circular waveguide and the copper helically corrugated waveguide gave good agreement with the experiment, including the pulse shape and side lobes. The model of the modified aluminium helically corrugated waveguide gave a smaller power compression ratio of 6.8, but gave good agreement with the pulse shape. The model of the experiment using the aluminium helically corrugated waveguide gave a smaller power compression ratio than the experiment, of 2.78, due to an uncertainty in the measured frequency sweep for this experiment.

8 Conclusion

8.1 Overview

A relatively shallow helical corrugation of the inner surface of an oversized circular waveguide can radically change it's dispersion characteristics. Such a corrugation can be designed to provide an ideal dispersion for swept frequency pulse compression, as shown in Figure 8-1. Theoretical simulations using three separate helically corrugated waveguides as dispersive mediums were used to demonstrate this concept for the first time. The helical compressor experiment conducted was the first of its kind to be carried out.

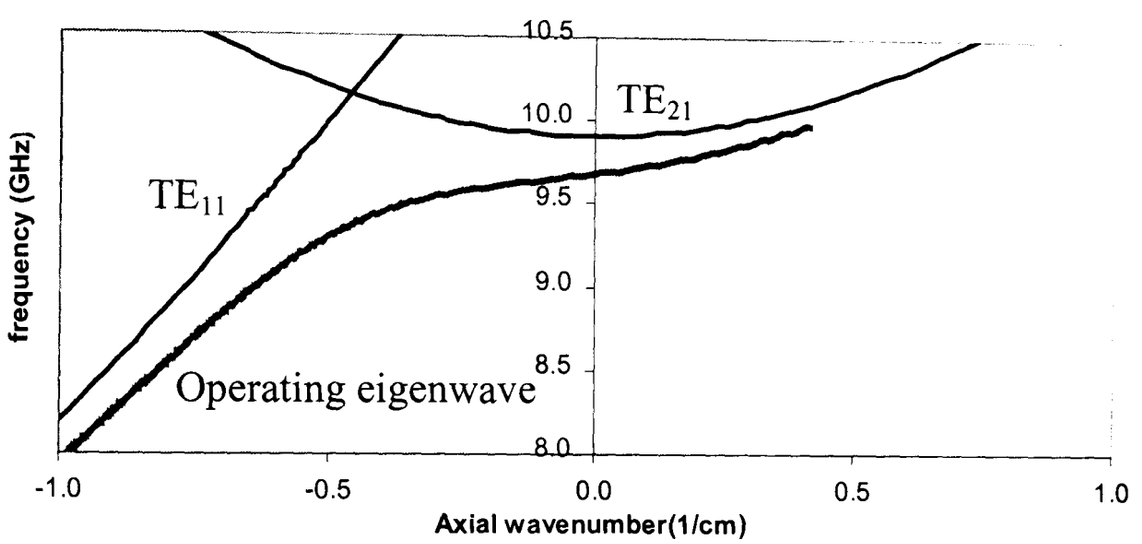

Figure 8-1 Dispersion curve of the operating eigenwave of a helically corrugated waveguide and the TE_{11} and TE_{21} modes of a smooth circular waveguide.

The main advantage of a helical compressor over a smooth circular compressor is its reduced reflections. In a circular compressor the optimum range of operation is close to cut-off, therefore if any stray part of the incident pulse was below cut-off it would be reflected. The helical compressor works far from cut-off and hence the input pulse is less prone to reflection. Due to its low reflection properties a helical compressor can be used effectively at the output of a powerful amplifier.

Another main advantage is the optimum sweep used. In a helically corrugated compressor the optimum sweep is from a higher frequency to a lower frequency, which is easier to obtain for BWO's than a sweep from a lower frequency to a higher

frequency. The flexibility of the dispersive properties also allows the group velocity dispersion to be matched to the frequency sweep from the BWO in order to achieve the optimum power compression ratio.

As the major limiting factor in the maximum possible compression ratio is the maximum possible sweep rate of the source used it is beneficial to have a large change in group velocity with frequency so that smaller sweep rates can produce higher power compression ratios. The large change in group velocity with frequency also allows shorter compressor lengths to be utilized, hence reducing ohmic losses.

8.2 Pulse compression experiments

Measurements of microwave pulse compression from a helically corrugated waveguide obtained a power compression ratio of 10.9 for a copper helically corrugated waveguide with a length equal to 208.08cm and a small corrugation depth of 1.4mm, with two 11.56cm tapers at each end. The frequency sweep was 9.6 to 9.35GHz in 70ns resulting in a compressed pulse at the output, of duration of 3ns and 44% compression efficiency.

A second helix with a deeper corrugation was constructed from aluminium, and had a length equal to 64 of its periods. A microwave pulse of 45ns duration was swept from 9.6 to 9.16 GHz and propagated through the compressor. This was compressed to a 4.5ns pulse with a power compression ratio of 3.5. The compressed pulse excluding the side lobes contained 35% of the pulse energy. Boring a 27.68mm hole down this waveguide, hence reducing the coupling coefficient, created the third helix. A maximum power compression ratio of 8.5 was observed for this compressor. The input pulse had a frequency sweep from 9.55GHz to 9.25GHz and a pulse duration of 40ns. The compressed pulse had a pulse duration of 2.75ns and contained 52% of the input energy. The maximum power compression ratios possible was limited by the maximum sweep rate of the microwave oscillator. The copper waveguide had the highest power compression ratio due to its low minimum group velocity and its high conductivity.

Various lengths of smooth circular waveguide were also used as dispersive mediums. This circular waveguide had a 19.2mm diameter, and lengths between

3.1m and 9.7m were used. The highest power compression ratio achieved in this circular waveguide was 7, at a length of 6.6m. Using the approximation that the optimum length of compressor, L_c, is equal to the inverse of the maximum plus the minimum imaginary part of the axial wavenumber, it was calculated that the optimum length of smooth circular compressor was 7.4m.

The helically corrugated compressors were found to have on average higher power compression ratios and higher efficiency than smooth circular compressors.

8.3 Simulations of pulse compression

Two theoretical simulations of sweep-frequency based microwave pulse compression were studied in this thesis. The first method involved a simple kinetic approximation where all the energy in the pulse was contained within a square wave of the minimum pulse duration. The second method used a Fourier optics approach to simulate the compression of a frequency-swept pulse in a dispersive medium. The difference between the maximum compression ratios calculated by these two approaches never exceeded 16%.

The theoretical simulation of pulse compression using the copper helix gives the same power compression ratio, 10.9, with similar pulse shape and compression efficiency. A simulation of the optimum compression in the modified helically corrugated waveguide also gave good agreement with pulse shape however a lower power compression ratio of 6.8 was achieved. The simulation of the pulse compression in the aluminium helix gave a power compression ratio of 2.78 compared to the value of 3.5 obtained in the experiment, the sidelobe shapes for these two results did not agree, but the peak of the pulses did give good agreement in shape and time of arrival at the output of the waveguide. The disagreement was due to the uncertainty in the frequency sweep used in the experiment for the aluminium helix. In the aluminium helix experiment the frequency sweep was derived from the voltage sweep, however the relationship between input voltage and output frequency for the solid-state oscillator was measured at constant voltage. This relationship will be slightly varied when the voltage was quickly swept. The frequency sweep for the aluminium helix was not measured directly using the heterodyne frequency

diagnostic because at the time of the experiment the Farran mixers were not available.

It is found that the simulations using the optimum kinematic sweep rate give significantly lower power compression ratio's than the simulations of the experimental results. For example, the theoretical calculations using an optimum kinematic sweep gave a maximum power compression ratio of 6.83, however the same simulation gave a power compression ratio of 10.9 for the sweep used in the experiment. The optimum kinematic sweep was calculated for the condition that optimum compression occurs when all parts of the pulse meet at the same point in time and space, however as the microwave pulse has a finite minimum duration, parts of the pulse arriving just before or after this can still contribute to the peak power, which means that the optimum sweep does not give the optimum power compression ratio.

The simulations also predict that with a maximum sweep rate of 20MHz/ns the maximum power pulse compression ratio should increase by 40% from a 10MHz/ns sweep. The Fourier optic simulation was also tested on the smooth circular waveguide compression experiment. The simulation gave excellent agreement with the experiment in both pulse shape and power compression ratio.

A simple kinematic approximation was developed that gave a power compression ratio based on the optimum frequency sweep, using the start and end frequency of the pulse, the helix parameters, and the helix length. This simple approximation was found to give good agreement with the Fourier optics simulation to within 16%.

8.4 Overview of dispersion characteristics

In previous work the dispersion characteristics had been calculated using the method of perturbations and experimentally verified by measuring the polarisation turn of a linearly polarised mode propagating through the helix[51]. In this thesis a method of calculating the dispersion characteristics of a helically corrugated waveguide using a numerical computer code has been developed. An improved

experimental technique for measuring the dispersion characteristics has also been studied.

The method of perturbation of Maxwell's equations is only able to calculate the dispersion characteristics of periodic structures for small perturbations. This means for helical structures with deep corrugations the method of perturbation is unable to calculate the dispersion accurately. To calculate the dispersion characteristics of deep grooved waveguides a numerical code must be used. For the aluminium helix, the group velocity dispersion measured using the experimental approach has a mean standard deviation of 9.92% from the group velocity dispersion calculated from the method of perturbations compared to a mean standard deviation of 6.25% for the shallower corrugation of the copper corrugated waveguide.

In this thesis the experimental approach used by Denisov[51] was simulated using the PIC code MAGIC. The dispersion plots found using MAGIC gave good agreement with the experimental approach. The frequencies where the wave was rotated by $\pi/2+2n\pi$ radians, simulated using the numerical code, were found to deviate by no more than 0.15% from the frequencies measured in the experiment. Increasing the spatial resolution by a factor of 1.5 gave a deviation of less than 0.5% on the frequencies where the minima occur. In order to introduce the wave into the corrugated waveguide without significant reflections, helical tapers were used. The polarisation rotation due to the tapers was approximated as half the rotation due to an equal length of regular helical waveguide. This approximation can introduce a deviation on the dispersion calculated, however if $L_{reg} >> L_{tap}$ this deviation can be made negligible.

MAGIC was also used to look at the wavenumber spectrum of a microwave pulse with a very narrow bandwidth inside the helically corrugated waveguide. This shows how much of the wave is propagating in the operating eigenwave and helps to find the number of full turns in the SNA MAGIC technique.

In order to measure the dispersion characteristic of the operating eigenwave in the helically corrugated waveguide from the polarisation turn of a linearly polarised wave an assumption about the dispersion of a TE_{11} wave co-rotating with the helix must be made. This assumption provides a small inaccuracy in the measurement technique. To improve the accuracy of experimental measurement of the dispersion

characteristics the dispersion of the operating eigenmode was directly measured. Using a Vector Network Analyser the phase shift of a circularly polarised TE_{11} wave, due to its propagation through a helically corrugated waveguide was measured. The change in phase due to the tapers was also removed from the results and the phase change due to the regular helically corrugated section alone was used to find the dispersion characteristics.

This method was found to give good agreement with previous experimental and numerical results for the copper waveguide, where the dispersion of the TE_{11} mode co-rotating with the helix was the same as a TE_{11} mode in a smooth circular waveguide. However in the modified waveguide there was a small deviation from the experimental SNA and SNA MAGIC results, as the TE_{11} mode co-rotating with the helix had a slightly different dispersion curve from that in a smooth circular waveguide.

A comparison of all the methods used to calculate the Group Velocity Dispersion (GVD) of the helically corrugated waveguides is presented in Table 8-1 by comparing the minimum group velocity in the operating bandwidth using each method.

	Minimum Group velocity (cm /ns)		
	Aluminium	Modified aluminium	Copper
Method of perturbations	3.78	2.10	2.49
SNA MAGIC	4.56	2.50	3.00
Experimental SNA	4.56	2.94	3.10
Experimental VNA	NA	2.96	2.90

Table 8-1 Comparison of minimum group velocity in the operating bandwidth calculated using the various methods, for each corrugated waveguide.

The method of perturbations calculated the lowest minimum group velocity for each helical waveguide. The other three methods all give good agreement with each other except for the MAGIC calculation for the modified aluminium helix. The experimental VNA method gives the most accurate results as it has less sources of error than the other methods.

Of all the methods used to calculate the dispersion characteristics of the lower eigenwave of the helically corrugated waveguide only the method of perturbations and the single-frequency MAGIC simulation are able to calculate the dispersion of the upper eigenwave.

8.5 Possible applications

The output from the sweep-frequency based pulse compressor has a high peak-power and short pulse duration, hence a low average power. The main exploitation of pulse compressors is in linear accelerators, requiring a pulse duration longer than is possible from a sweep-frequency based pulse, and a very narrow bandwidth, this means a helically corrugated compressor cannot be used for this application. However, several applications specifically need either very high peak powers, for instance non-linear testing, or very short pulse durations, such as nanosecond RaDAR.

The range resolution, δ, of RaDAR is given by $\delta \sim c\tau/2$, hence to increase the resolution the pulse duration, τ, must be reduced[5]. However, target detection is a function of total energy, hence peak power and repetition rate have to be sufficiently high to compensate for the small pulse duration. This concept has been tested using an X-band BWO with a 500MW pulse with a pulse duration of 5ns and a repetition rate of 150Hz[3]. With a power compression ratio of 20 a similar pulse could be produced using a smaller 25MW source, with a higher repetition rate.

8.6 Future work

8.6.1 High-power pulse compression

In this work the highest power input pulse used was 1kW from a conventional TWT. However, a helically corrugated waveguide can be used to compress pulses of 1MW power and above. A possible experiment to test the operation of the compressor at higher powers would be to compress the output of the Strathclyde Gyro-Travelling Wave Amplifier. Such an amplifier is sufficiently broadband and can produce pulses in the order of 1MW in the X-band, and has the added advantage of using circularly polarised TE_{11} waves for its operation.

8.6.2 Frequency-swept BWO

Electromagnetic radiation from electrons in a periodic slow-wave structure is known as Smith-Purcell radiation. Two well-known types of microwave tubes based on Smith-Purcell radiation are the Travelling-wave Tube (TWT) and the Backward Wave Oscillator (BWO)[10]. An electron beam guided by a strong axial magnetic field is injected into a slow-wave structure. Microwave generation occurs at resonances between the waves on the slow wave structure and the slow space-charge waves on the beam.[5,66]

One of the most likely sources to produce a high power microwave pulse with the necessary frequency sweep is the Backward-Wave Oscillator (BWO). As the beam interacts only with waves of the same phase velocity the BWO mode can be voltage tuned over a reasonable broad range of frequencies, and can easily produce a microwave pulse with a power of over 100MW. A BWO can also produce very fast frequency sweeps that can be closely modulated.

The optimum frequency sweep required for sweep-frequency based microwave pulse compression in a helically corrugated waveguide has a decreasing ramp. As the frequency of interaction increases with voltage in a BWO, this means the beam voltage should also decrease with time. For a helical compressor the optimum negative frequency sweep can quite naturally be realized at the falling edge of a X-band relativistic BWO pulse using the decay of a Marx bank. As it is much easier to produce a falling edge than a rising edge on a high power voltage pulse the helical compressor has a major advantage over the circular waveguide.

However, it is not clear if a BWO can be made to cover the necessary frequency bandwidth with one mode, which would be required for pulse compression. In order to prove that it is possible, a BWO was designed to produce an output microwave pulse with the necessary frequency sweep in the TE_{11} mode.

It is also important to design a new helically corrugated waveguide with a group velocity dispersion that complements the frequency sweep at the output of the BWO to allow higher power compression ratios to be realized.

If a BWO generates hundreds of MW during 50 ns over a voltage drop from 600 kV to 300 kV, the frequency modulated radiation can be compressed up to 10-20

times in power with an efficiency higher than 50%. The potential of this set-up to produce multi-Gigawatt microwave pulses is presented.

In order for the output from a relativistic BWO to be compressed using a 2metre long helical compressor the output pulse should be about 100ns in duration and have a 2-3% negative frequency sweep. The possibility of such frequency tuning by modulation of the electron energy is clearly evident from the BWO dispersion relation. A sinusoidal slow wave structure having a period of 1.55cm a mean radius of 1.4cm and a corrugation depth of 0.15cm was modelled using the method of perturbations, shown in Figure 8-2. The slow wave structure designed should be able to produce the required frequency bandwidth using a voltage pulse that drops from 600kV to 300kV over 70ns using the TM_{01} mode.

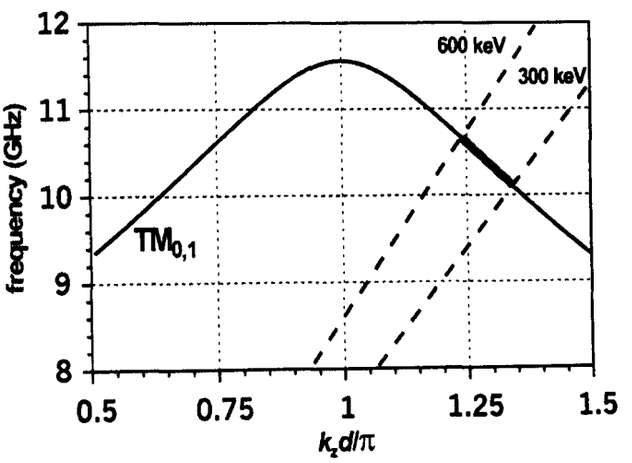

Figure 8-2 "Cold" dispersion diagram for the optimized frequency-swept BWO.

The BWO was optimised in the 2D time-domain PIC code KARAT[77], and was checked with 3D KARAT. The Slow Wave Structure (SWS) length was 10 periods and had two 2 period sinusoidal tapers at either side. A resonant reflector[78] providing more than 98% power reflection of the TM_{01} mode for frequencies between 9.2GHz and 10.7GHz was used so that an electron beam with a 1.1cm outer radius could be used.

The resonant reflector was made up of a circular cavity, stepped down to a section of regular circular waveguide with a smaller radius on either side. The radiuses of the two sections are calculated so that the TE_{01} mode was cut-off in the regular waveguide at the operating frequency and the axial wavenumber of a TM_{01} mode in the regular waveguide was the same as that of a TE_{01} mode in the cavity. This means that a TM_{01} mode propagating in the regular waveguide will be

completely converted to the TE_{01} mode at the step to the cavity due to conservation of momentum.

Similar to previous theoretical and experimental studies[79] it was found that the BWO operation is quite critical to the length of small drift section between the reflector and SWS. The KARAT simulations show that an optimum length of the drift section (2 cm for the discussed configuration) can provide both high BWO efficiency (more than 30%) and frequency modulation sufficient for the pulse compression. The geometry of the BWO is shown in Figure 8-3.

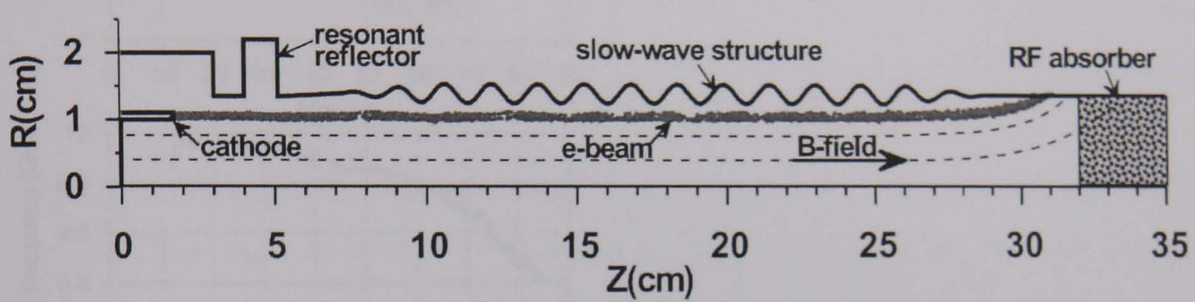

Figure 8-3 Relativistic BWO configuration optimized for frequency tuning by voltage.

As a result of the optimisation a BWO configuration was found which combines high output power, high efficiency and sufficiently wide frequency tuning for a moderately relativistic electron beam. The output pulse had a maximum power output of 800MW at 10ns and drops to 300MW at 70ns over which time the frequency has dropped from 10GHz to 9.5GHz, as shown in Figure 8-4. With a power compression ratio of 10, a peak power of 4-6GW would be produced at the output of a helical compressor.

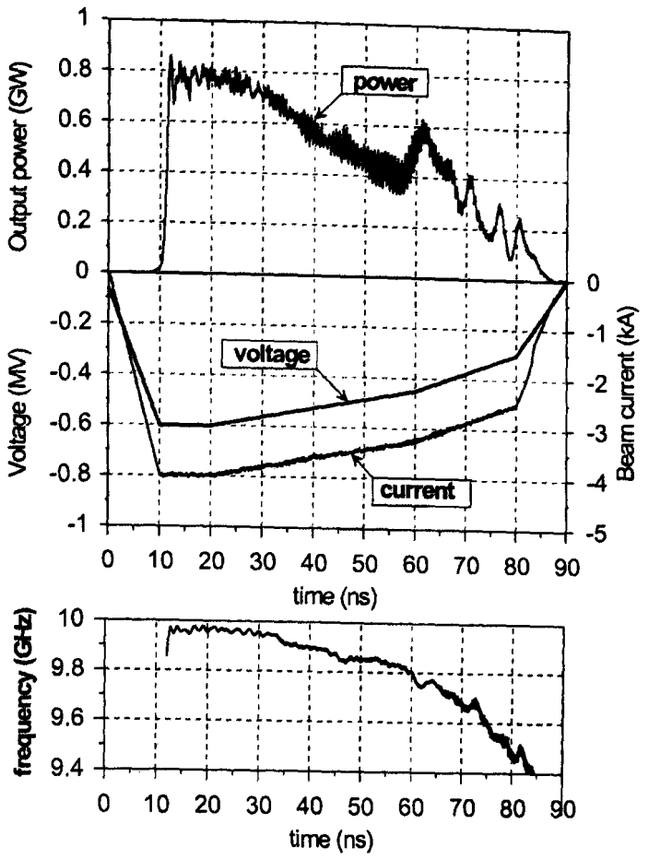

Figure 8-4 Results of KARAT simulations for a frequency-swept BWO.

8.6.3 Higher-order mode coupling

A favourable wave dispersion can be also synthesized for higher-order modes resulting in an increase of the helical waveguide diameter by 1.5-2 times (without significant overlapping of the coupling bands) and correspondingly in an enhancement of its RF breakdown strength. Higher order modes could also be used to produce a compressor for higher frequency operation in a waveguide of roughly the same size as the current helix. Such a helix would have a 4 or 5-fold azimuthal corrugation, coupling the TE_{31} mode to the TE_{11} or TE_{21}, respectively, and would have a mean radius of about 2.0cm. This would involve using an overmoded waveguide, with the TE_{11}, TM_{01}, TE_{01}, and TM_{11} modes all above cut-off at the operating frequency. A 4-fold helix has the advantage of using the fundamental mode of a smooth circular waveguide, the TE_{11} mode. The 5-fold helix would couple the TE_{21} and the TE_{31} at the operational frequency, however some difficulties arise in converting the input mode completely into the required mode without attenuating the pulse too much and affecting the frequency sweep.

Another option would be to use a 3-fold helix to couple a TM_{11} and a TM_{21} mode, with a mean radius of about 2.45cm which would also couple the TE_{11} and TE_{21} as has already been shown in this thesis. The advantage of this configuration is that most linear beam devices work using TM modes, and the TE_{11} mode can also be easily converted into the TM_{11} mode.

The method of perturbations and numerical PIC code MAGIC have been used to study a 4-fold helically corrugated waveguide where coupling the TE_{11} and the TE_{31} modes takes place. In order to work between 9.0GHz and 9.5GHz the mean radius was increased to 2.08cm making the TE_{31} cut-off below 9.645GHz. A period of 3.00cm was chosen, which makes the two modes intersect at 9.725GHz. This is an increase in the mean diameter by a factor of 1.415. A corrugation depth of 2.1mm gives the helically corrugated waveguide the dispersion characteristics required for pulse compression, shown in Figure 8-5. This waveguide has a small coupling coefficient but a large ratio of corrugation depth to mean radius which causes a small deviation between the dispersion calculated using method of perturbations and MAGIC.

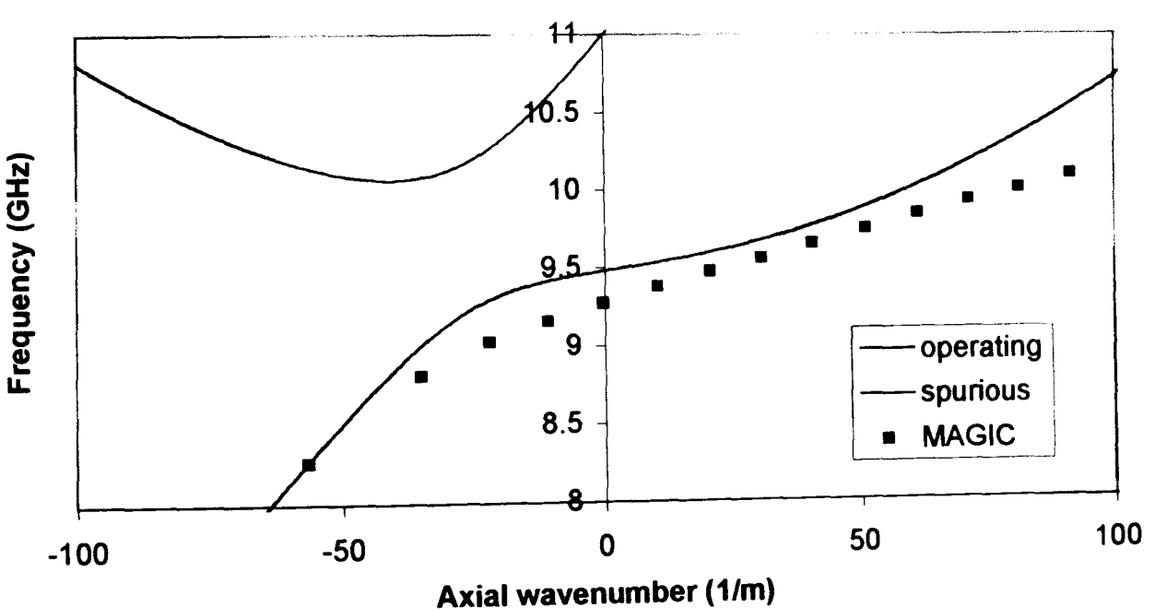

Figure 8-5 Dispersion characteristics of the 4-fold helically corrugated waveguide calculated using the method of perturbations and MAGIC.

Due to this waveguide being overmoded, it is possible that a large percentage of the input energy could propagate in modes other than the operating eigenmode. In order to investigate this, single-frequency MAGIC was used to look at axial wavenumber spectrum for a given frequency. It was found that in the range of

operation most of the microwaves stay in the operating eigenmode, a small amount was converted to the TE_{01} mode and virtually none of the pulse was converted to the TE_{21} mode.

8.6.4 Maximum power handling

In order to realize ultra high power pulses the maximum power handling of the helically corrugated waveguide before breakdown occurs needs to be calculated. To achieve an accurate estimate of the power handling capability detailed knowledge of the field structure of the eigenmode in the helically corrugated is required.

However, at present it is difficult to calculate the maximum power handling of a helically corrugated waveguide, as there is limited knowledge of its field structure. It is simpler to calculate the maximum power handling of a smooth circular waveguide of similar dimensions. The maximum power handling of a TE11 wave propagating in a circular waveguide of radius equal to the mean radius of the helix was calculated as a function of frequency. As a first order estimate the maximum electric field in air was taken to be 30kV/cm and was assumed to be constant with frequency.

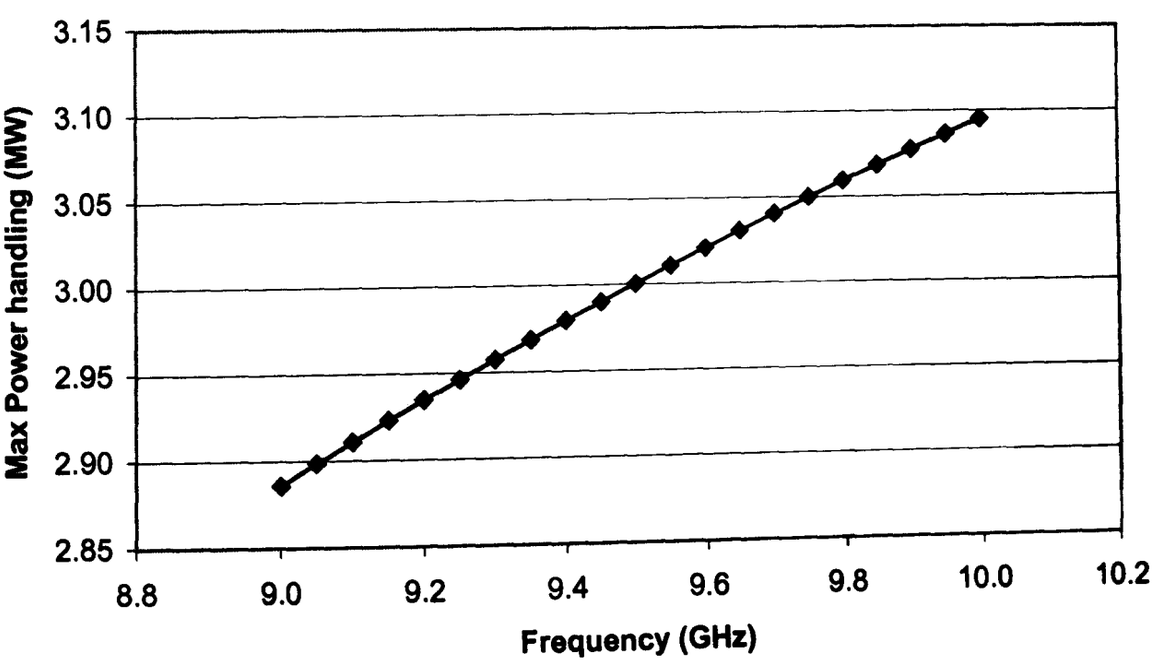

Figure 8-6 Maximum power handling as a function of frequency for a smooth circular waveguide with the same mean radius as the aluminium and copper helically corrugated waveguides in air.

A maximum power handling at 9 GHz was calculated to be 2.89MW, shown in Figure 8-6.

As mentioned previously it takes time for a gas to breakdown and the power handling increases as a result. If a pulse of 3ns was obtained the maximum electric field was expected to double[80]. This allows a power handling 4 times greater allowing a maximum power handling of 11.5MW. If the power handling of a helically corrugated waveguide is assumed to be similar to that of a smooth circular waveguide then a 1MW pulse can be compressed in the copper corrugated waveguide to a 3ns, 10.9MW pulse without breakdown.

If the Gigawatt potential of the helical compressor is to be achieved the compressor must either be evacuated to vacuum or be filled with an electronegative gas such as SF_6. The molecules in electronegative gases require one or two electrons to fill the outer shell. As a result they can easily capture free electrons[8].

8.7 Discussion

In this thesis the use of a helically corrugated waveguide for use as a dispersive medium for sweep-frequency based pulse compression was proposed and investigated. Such a system can produce compressed pulses with a power compression ratio greater than 10 and a pulse duration of about 3ns. Commercially available broadband sources, such as tuneable TWTs, are limited to a maximum power output of 10kW, the use of a helically corrugated compressor could increase the peak power output of such a source to 100kW. Such a set-up could be implemented for use in Radar without the requirement for further X-ray shielding. If such a compressor is to be used for RaDAR then it's modest weigh and size become important for use in an airborne applications.

Ultimately, such a compressor could be used at the output of a high power BWO producing a multi-Gigawatt pulse of 3ns duration. Current microwave sources which can produce this type of pulse are often bulky and require significant shielding from X-rays due to the high energy electron beams used. The helically corrugated pulse compressor is logistically much better requiring a much smaller microwave source. If the compressor is used to produce very high power microwave pulses as a research tool then its reduced cost becomes a significant factor.

References

[1] B.I. Cohen, R. H. Cohen, W. M. Nevins, T. D. Rognlien, Theory of free-electron-laser heating and current drive in magnetized plasmas, Rev. Mod. Phys, **63**, 1991 p. 949-990

[2] V.L. Granetstein, W. Lawson, Gyro-Amplifiers as Candidate RF Drivers for TeV Linear Colliders, IEEE Trans. Plasma Sci. **24**, 1996, p. 648-665

[3] B. Wardrop, A Russian Experimental High-Power, short-pulse radar, GEC Journal, **14**, 1997, p. 141

[4] M.K. Thumm, Generation and Applications of High Power Microwaves, Applications of High Power Microwave Devices, SUSSP Publications, Institute of Physics Publishing, 1997, ISBN 0-7503-0-451-0

[5] J. Benford and J. Swegle, High-Power Microwaves, Artech House Inc 1992, Norwood, MA

[6] D. M. Pozar, Microwave Engineering, 2nd Ed., John Wiley and sons, New York, 1998, ISBN 0 471 17096 8

[7] J. T. Randall, The Cavity Magnetron, An address on the occasion of the presentation of the 22nd Duddell Medal to Prof. Randall, 1946

[8] A. S. Gilmour Jr, Microwave Tubes, Artech House, 1986, Norwood, MA, ISBN 0-89006-181-5

[9] G. Bekefi, T.T. Ozrechowski, Giant Microwave Bursts Emitted from a Field-Emission, relativistic-Electron-Beam Magnetron, Phys. Rev. Lett. **37** (6), 1976

[10] S. H. Gold, G. S. Nusinovich, Review of high-power microwave source research, Rev. Sci. Instrum. **68** (11), 1997

[11] M. Friedman, Automodulation of an Intense relativistic Electron Beam, Phys. Rev. Lett., **32** (3), 1974, p. 92

[12] M. Friedman, V. Serlin, Modulation of Intense Relativistic Electron Beams by an External Microwave Source, Phys. Rev. Letters, **55** (266), (1985), p. 2860

[13] H. Motz, Applications of the radiation from fast electrons, J. Appl. Phys., **22**, 1951, p. 257

[14] R. M. Philips, The ubitron, a high-power travelling-wave tube based on a periodic beam interaction in unloaded waveguide, IRE Trans., Electron. Dev. **7**, 1960, p.231

[15] C.W. Robertson, P. Sprangle, A review of free-electron lasers, Phys. Fluids B, **1** (1), 1989, pp.3

[16] M. Thumm, State-of-the-art of High Power Gyro-Devices and Free-Electron Masers Update 2003, institut für Hochleistungsimpuls- und Mikrowellentechnik, Programm Kernfusion

[17] J.M.J Madey, Stimulated Emission of Bremsstrahlung in a Periodic Magnetic field, Journal of Applied Physics, **42** (5), 1971, p. 1906

[18] L. H. Yu, L. DiMauro, A. Doyuran, W. S. Graves, E. D. Johnson, R. Heese, S. Krinsky, H. Loos, J. B. Murphy, G. Rakowsky, J. Rose, T. Shaftan, B. Sheehy, J. Skaritka, X. J. Wang, Z. Wu, First Ultraviolet High-Gain Harmonic-Generation Free-Electron Laser, Phys. Rev. Lett. **91,** 2003, 074801

[19] R. Q. Twiss, Radiation Transfer and the possibility of negative absorption in radio astronomy, *Aust. Journal Phys.*, **11**, 1958

[20] J. Schnieder, Stimulated Emission of Radiation bt relativistic electrons in a magnetic field, Phys. Rev. Letters, **2** (12), 1959, p. 504-505

[21] V. Gaponov, Interaction of irrectilinear electron flows with electromagnetic waves in waveguides, - Addendum *ISV. VUZov, Radiofiz*,. **2**, 1959

[22] R. H. Pantell, Backward-Wave Oscillations in an unloaded waveguide, Proceedings of the IRE, **47**, 1959, p. 1146

[23] J. L. Hirshfield, V. L. Granetstein, The Electron Cyclotron Maser- An historical SurveyIEEE trans. Microwave Theory and Techniquies, MTT-**25** (6), 1977, p. 522-527

[24] J. L. Hirshfield, J.M. Wachtel, Phys. Rev. Letters, **12** (19), 1964, 533-536

[25] G. Dammertz, E. Borie, C.T. Iatrou, M. Kuntze, B. Piosczyk, M.K. Thumm, 140-GHz gyrotron with multimegawatt output power, IEEE Trans. Plasma Sci., **28** (3), (2000), p. 561–566

[26] J. R. Pierce. Theory of the beam-type traveling-wave tube. *Proceedings of the I.R.E.*, **35**, 1947, p. 111-123

[27] R. Kompfner. The traveling-wave tube as Amplifier at Microwaves. *Proceedings of the I.R.E.*, **35**, 1947, p, 124-127

[28] R. J. Barker, E. Schamiloglu editors, High-power microwave sources and technologies Ch 5. IEEE Press, New York, 2001, ISBN 0-7803-6006-0

[29] J. A. Nation. On the Coupling of an high-current relativistic electron beam to a slow wave structure, Appl. Phys. Lett. **17** (11), 1970, p. 491

[30] E. B. Abubakirov, A. N. Denisenko, M. I. Fuks, N. G. Kolganov, N. F. Kovalev, M. I. Petelin, A. V. Savelyev, E. Schamiloglu, E. I. Soluyanov, V. V. Yastrebov, An X-Band Gigawatt Amplifier, IEEE Trans. Plasma Science, **30**.(3), 2002, p. 1041-1052

[31] R.A. Alvarez, D. Byrne, and R.M. Johnson, Prepulse suppression in microwave pulse-compression cavities, Rev. Sci. Instrum. , **57** (10), 1986, p. 2475-2480

[32] R.A. Alvarez, Some properties of microwave resonant cavities relevant to pulse-compression power amplification, Rev. Sci. Instrum. , **57** (10), 1986, p. 2481-2488

[33] R.A Bromley, B.E. Callan, Use of a waveguide dispersive line in an f.m. pulse-compression system, Proc. IEE, **114**, 1967. p. 1213-1218

[34] D. Birx, G.J. Dick, W.A. Little, J.E. Mercereau, and D. J. Scalapino, Microwave power gain utilizing superconductiong resonant energy storage, Appl. Phys. Lett., **32** (1), 1978, p. 68-70

[35] R.A. Alvarez, D. Birx, D. Byrne, M. Mendonca, and R.M. Johnson, Generation of High-Power Microwave pulses using a spherical superconducting cavity and interference-type switch, IEE Trans. Magn., MAG-**17** (1), 1981, p. 935- 938

[36] Z. D. Farkas, H.A. Hogg, G.A. Loew and P.B. Wilson, SLED: A method of doubling SLACs energy, SLAC-PUB-1453, 1974, Stanford Linear Accelerator Center, Palo Alto, Calif.

[37] P.B. Wilson, Z. D. Farkas and R.D. Ruth, SLED II: A mew method of RF pulse compression, SLAC-PUB-5330, September 1990, Stanford Linear Accelerator Center, Palo Alto, Calif.

[38] S.G. Tantawi, R.D.Ruth, A.E.Vlieks, M. Zolotorev, Active High-Power RF Pulse compression using optically switched resonant delay lines, IEEE Trans. Microwave Theory Tech., MTT-**45** (8), 1997, p. 1486-1491

[39] Z.D. Farkas, Binary Peak Power Multiplier and its Application to Linear Accelerator Design, IEEE Trans. Microwave Theory Tech., MTT-**34** (10), 1986, p. 1036-1043

[40] A. L. Vikarev, A. M. Gorbachev, O.A. Inanov, V.A. Isaev, S. V. Kuzikov, L. Kolysko, A.G. Litvak, M. I. Petelin, J.L. Hirshfield, O.A.Nezhevenko, S.H. Gold, 100MW Active X-band Pulse compressor, Proceedings of the 1999 Particle Accelerator Conference, New York, 1999, p. 1474-1476

[41] M. K. Thumm, W. Kasparek, Passive High-Power Microwave Components, IEEE Transactions on Plasma Science, **30** (3), 2002, p. 755-786

[42] S. N. Vlasov, N.G. Kazakova, E.V. Koposova, Microwave pulse compression using diffraction gratings, Technical Physics, **43** (2), 1998, p. 209

[43] A. L. Vikharev, Yu. Yu. Danilov, A. M. Gorbachev, S. V. Kuzikov, Yu. I. Koshurinov, V.G. Paveliev, M. I. Petelin, J.L. Hirshfield, Quasi-Optical Microwave Pulse Compressor at 34 GHz, Advanced Accelerator concepts: Tenth Workshop, Edited by C.E.Clayton and P. Muggli, pp 448-458

[44] Yu. Yu. Danilov and M.L.Tai, Microwave Pulse compression in a Chain of Ring-Type Resonators, Technical Physics, **46** (4), 2001, p. 460-462

[45] R. M. Bevensee, Electromagnetic Slow Wave Systems, John Wiley and Son, Inc., New York, 1964

[46] T. M. Antonsen, Jr.,P. Safier, D. P. Chernin, B. Levush, Stability of Travelling-Wave Amplifiers with reflections, IEEE Trans. Plasma Science, **30**.(3), 2002, p. 1089-1107

[47] J. F. Gittins, Power Travelling-wave tubes, The English Universities Press, London, 1965,

[48] M.I. Fuks, N. F. Kovalev, Selective Multichannel Feedback, IEEE Trans Plasma Science, **30**, 2002, 1147

[49] He W., Cross A.W., Whyte C.G., Young A.R., Phelps A.D.R., Ronald K., Rafferty E.G. , Thomson J., Robertson C.W., Speirs D.C., Samsonov S.V., Bratman V.L. and Denisov G.G., Gyro-BWO experiment using a helical interaction waveguide, IVEC 2004, Monterey (USA), p. 206-207

[50] S. J. Cooke and G. G. Denisov, Linear Theory of a Wide-Band Gyro-TWT Amplifier Using Spiral Waveguide, IEEE Transactions on Plasma Science, **26** (3), 1998, p. 519-530

[51] G.G Denisov, V.L. Bratman, A.D.R.Phelps, and S.V.Samsonov, Gyro-TWT with a helical Operating Waveguide: New Possibilities to Enhance Efficiency and Frequency Bandwidth, IEEE Transactions on Plasma Science, **26** (3), 1998, p. 508

[52] G.G Denisov, V.L. Bratman, A.W.Cross, W.He, A.D.R.Phelps, K.Ronald, S.V.Samsonov, and C.G.Whyte, Gyrotron Travelling Wave amplifier with a Helical interaction Waveguide, Physical review letters, **25**, 1998, p. 5680

[53] V.L. Bratman, A.W.Cross, G.G Denisov, W.He, A.D.R.Phelps, K.Ronald, S.V.Samsonov, C.G.Whyte and A.R. Young, High-Gain Wide-Band Gyrotron

Travelling Wave Amplifier with a Helically Corrugated Waveguide, Physical review letters, **32** (12), 2000, p. 2746

[54] V. L. Granatstein, Igor Alexeff, High-Power microwave sources, ISBN 0-89006-241-2, Artech House 1987

[55] A.W. Cross, Electron Cyclotron maser Experiments Using Cold and Thermionic Cathodes, 1993, PhD

[56] K. R. Chu, The electron cyclotron maser, Rev. Mod. Phys., **76** (2), 2004, p. 489-540

[57] H. Benson, University Physics revised edition, John Wiley and sons, New York 1995, ISBN 0 471 00689 0

[58] P. Lorrain, D.R. Corson, and F. Lorrain, Electromagnetic fields and Waves 3rd Ed, W. H. Freeman and Company, New York, 1985, ISBN 0-716-71825-5

[59] A.W Cross, Experimental Microwaves, Sanders Ltd, England, 1977

[60] R. Dobbs, Electromagnetic Waves, Routledge & Kegan Paul, London, 1985

[61] Hecht, Optics 2nd Ed, ISBN 0-201-11611-1, Addison-Wesley Publishing Company, 1987

[62] J. Vanderlinde, Classical Electromagnetic Theory, John wiley and Sons, Singapore, 1993, ISBN 0 471 30587 1

[63] S. F. Mahmoud, Electromagnetic Waveguides theory and applications, Peter Peregrinus Ltd, London, UK, 1991, ISBN 0 86341 232 7

[64] J. Jackson, Classical Electrodynamics 2nd Ed.,1975, John wiley and Sons, New York, ISBN 0 471 43132 X

[65] N. Marcuvitz, Waveguide Handbook, Peter Peregrinus, 1986, IEE Electromagnetic Wave series

[66] A. S. Gilmour Jr, Principles of Travelling Wave Tubes, ISBN 0-89006-720-1, Artech House, 1994, Norwood, MA

[67] B.Z. Katsenelenbaum, L. Mercader del Rio, M. Pereyaslavets, M. Sorolla Ayza, M. Thumm, Theory of Nonuniform Waveguides the cross-section method, 1998, ISBN 0-85296-918-X, IEE, 1998, London UK

[68] P.V. Petrov, The Theory of Planar Bragg Resonators, Technical Physics, **47** (2), 2002, p. 141-147

[69] L. A. Vainshtein, Electromagnetic Waves [in Russian], izd. Sov. Radio, Moscow, section 82, 1957

[70] N. F. Kovalev, I. M. Orlova and M. I. Petelin, Wave transformation in a multimode waveguide with corrugated walls, Izv. Vyssh. Ucheb. Zaved. Radiofiz., **11** (5), 1968, p. 783-789

[71] G. G. Denisov and M. G. Reznikov, Corrugated cylindrical resonators for short-wavelength relativistic microwave oscillators, Izv. Vyssh. Ucheb. Zaved. Radiofiz., **25** (5), 1982, pp 562-569

[72] L. Ludeking, D. Smithe, T. Gray, Introduction to MAGIC,Mission Research Corporation, Virginia, 2003

[73] M.C. Booth, M.Atature, G.D. Giuseppe, B.E.A. Saleh, A.V. Sergienko and M.C. Teich, Physical Review A, **66**, 023815/ 1-8, 2002

[74] H. Ino, K. Tajiri, K. Kabeya, T. Nakamura, Y. Yamanka, K. Yoshino, F. Naito, T. Kato, E. Takasaki, Y. Yamazaki, Advanced copper lining for accelerator components, XX International Linac Conference, Monterey, California, THE20, p. 1015-1017

[75] Anritsu, Series 373XXA Vector Network Analyser operation manual, Anritsu, California, 1996

[76] J. Lesurf, Millimetre-wave Optics, Devices and systems, Adam Hilger, Bristol, 1990, ISBN 0-85274-129-4

[77] V.P. Tarakanov, *User's Manual for Code KARAT.* Springfield, VA: BRA, 1992.

[78] G.G. Denisov, D.A. Lukovnikov, S.V. Samsonov, Resonant reflectors for free electron masers, G.G Denisov, D.A. Lukovnikov, S.V. Samsonov, Int. J. Infrared Millimeter Waves, **16** (4), p. 745-752, 1995

[79] A.V. Gunin, A.I. Klimov, S.D. Korovin, I.K. Kurkan, I.V. Pegel, S.D. Polevin, A.M. Roitman, A.A. Rostov, A.S. Stepchenko, E.M. Totmeninov, Relativisric X-Band BWO with 3-GW Output power, *IEEE Trans. Plasma Sci.* **26**, 1998, p. 326-331

[80] N. S. Ginzburg, N. Yu. Novozhilova, A.S. Sergeev, N. Yu. Peskov, A.D.R. Phelps, S.M. Wiggins, A.W. Cross, K. Ronald, W. He, V.G Shpak, M.I. Yalandin, S.A. Shunailov, M.R. Ulmaskulov, V. P. Tarakanov, Generation of powerful subnanosecond microwave pulses by intense electron bunches moving in a periodic backward wave structure in the superradiative regime, Phys. Rev. E, **60** (3), 1999, p. 3297-3303

Appendix

Appendix A- Computer codes

Examples of the numerical code used to calculate dispersion of the helically corrugated waveguides and to calculated pulse compression are presented. The first two codes, SNA MAGIC and single-frequency MAGIC are written in MAGIC and are used for dispersion calculations, and are discussed in Chapter 4. The last code is written in MATLAB and is used to calculated compressed pulse shapes from frequency swept input pulses, this code is discussed in Chapter 5.

```
HEADER  DEVICE  "SNA MAGIC" ;
graphics pause ;
!-------------------------------------------------------------------------
-----------
! Problem definition.
! Construct an oversized cylindrical waveguide with a helical corrugation on
the inner surface.
!
! Parameters defining the chamber.

       CYL_RADIUS = 1.65_CM ;                                  ! Cylinder inner
radius.
       TAP_RADIUS = 2.35_CM ;                                  ! Cylinder inner
radius.
       circular_length=6cm;
                                                               ! Azimuthal component
      m=3;
      period=2.89_CM;          ! Period
      h=2.PI/period;
                                                               ! Mean Radius
      a0=1.47_CM;
       tap_r1=0.4cm;
      enter=a0 +2*tap_r1;
      Ext_Radius =enter ;
                                                               ! Corragation depth
      a1=0.14_CM;
      TAPER_LENGTH = 1*period;
      TAPER_START =12*period+TAPER_LENGTH;
      CYL_LENGTH = TAPER_LENGTH+TAPER_START;                   ! Cylinder length.
      FUNCTION helixpara(Z,R,PHI) =R- a0 - a1*SIN(h*Z-m*PHI); ! Helical
shaped hole
      FUNCTION helixtaper(Z,R,PHI)=R- a0 - a1*Z/TAPER_LENGTH*SIN(h*Z-m*PHI);
! Taper hole
      FUNCTION helixtaper2(Z,R,PHI)=R -a0 + (a1*(Z-CYL_LENGTH)*SIN(h*Z-
m*PHI)/TAPER_LENGTH);

! Mesh resolution parameters.
       DELTA.Z = period/30 ;                                   ! Axial resolution.
       DELTA.R = a1/7;                                         ! Radial resolution.

      Delta.ro = 3*Delta.R ;
      Delta.rc = 5*Delta.R ;

                                                               ! Azimuthal
       DELTA.PHI = 2.PI/36 ;
Resolution
      TIME_OF_RUN = 65.0NANOSECONDS ;

!  Select the coordinate system and create the OBJECTS

       SYSTEM  CYL ;

! Define the endcaps.
```

```
      Point endcap2.lo  CYL_LENGTH,0.0cm,0.0 ;
      Point endcap2.hi  CYL_LENGTH,tap_radius,2pi ;
      AREA ENDCAP2 CONFORMAL ENDCAP2.LO ENDCAP2.HI ;

! Define the confining shell.
      CONVERTER_END=CYL_LENGTH+circular_length;
       POINT CIRSHELL.LO -circular_length,0,0PI ;
       POINT CIRSHELL.HI  0.0cm,TAP_RADIUS,2.PI ;
       POINT SHELL.LO 0.0cm,0,0PI ;
       POINT TAPER.HI  TAPER_LENGTH,CYL_RADIUS,2.PI ;
       POINT HSHELL.LO TAPER_LENGTH,0,0PI ;
       POINT TAPER2.HI  TAPER_START,CYL_RADIUS,2.PI ;
       POINT TAPER2.LO TAPER_START,0,0PI ;
       POINT SHELL.HI  CYL_LENGTH,CYL_RADIUS,2.PI ;
       POINT CONSHELL.LO CYL_LENGTH,0,0PI ;
       POINT CONSHELL.HI  CONVERTER_END,TAP_RADIUS,2.PI ;

      VOLUME SHELL CONFORMAL CIRSHELL.LO CIRSHELL.HI ;
       VOLUME SHELL2 CONFORMAL SHELL.LO SHELL.HI ;
       VOLUME SHELL3 CONFORMAL CONSHELL.LO CONSHELL.H ;

! *** Add forward and trailing Cyl guide so Ports are not ill-conditioned.

      ZForward = -circular_length - 3*Ext_Radius ;
       POINT Forward.SHELL.LO Zforward,Ext_Radius,0PI ;
       POINT Forward.SHELL.HI -circular_length,TAP_RADIUS,2.PI ;
      Volume Forward.Shell Conformal Forward.SHELL.LO Forward.SHELL.hi ;

      ZTrailing = CONVERTER_END + 3*Ext_Radius ;
       POINT  Trailing.SHELL.LO CONVERTER_END,Ext_Radius,0PI ;
       POINT  Trailing.SHELL.HI Ztrailing,TAP_RADIUS,2.PI ;
      Volume Trailing.Shell Conformal Trailing.SHELL.LO Trailing.SHELL.hi ;

!Define the taper
      VOLUME taper FUNCTIONAL helixtaper SHELL.LO TAPER.HI;
      VOLUME helix FUNCTIONAL helixpara HSHELL.LO TAPER2.HI;
      VOLUME taperend FUNCTIONAL helixtaper2 TAPER2.LO SHELL.HI;

! Define the cir converter
      FUNCTION output(Z,R,PHI)=R -a0 -tap_r1 - tap_r1*COS(1.PI*(Z-
CONVERTER_END)/circular_length);
      VOLUME conshell FUNCTIONAL output CONSHELL.LO CONSHELL.HI;

! Define the input WG
      FUNCTION input(Z,R,PHI)=R -a0 -tap_r1 +
tap_r1*COS(1.PI*Z/circular_length);
      VOLUME cirshell FUNCTIONAL input CIRSHELL.LO CIRSHELL.HI;


!-------------------------------------------------------------------------
------------
! MARK the objects for AUTOGRID and create the grid.

       MARK  SHELL  X1  SIZE Delta.Z ;

       MARK  SHELL  X2  Min SIZE Delta.RC ;
       MARK  SHELL  X2  Mid Max SIZE Delta.R ;

       MARK  SHELL  X3  SIZE Delta.PHI ;
       MARK  SHELL2  X1 SIZE Delta.Z ;

       MARK  SHELL2  X2  min SIZE Delta.Rc ;
       MARK  SHELL2  X2  mid SIZE Delta.Ro ;
       MARK  SHELL2  X2  max SIZE Delta.R ;

       MARK  SHELL2  X3  SIZE Delta.PHI ;
      MARK  SHELL3  X1  SIZE Delta.Z ;

      MARK  SHELL3  X2  min SIZE Delta.Rc ;
      MARK  SHELL3  X2  mid max SIZE Delta.R ;
       MARK  SHELL3  X3  SIZE Delta.PHI ;

       MARK  CONSHELL  X1  SIZE Delta.Z ;
```

```
      MARK  CONSHELL  X2  min SIZE Delta.Rc ;
      MARK  CONSHELL  X2  mid max SIZE Delta.R ;

      MARK  CONSHELL  X3  SIZE Delta.PHI;

      MARK  CIRSHELL  X1  SIZE Delta.Z ;

      MARK  CIRSHELL  X2  min SIZE Delta.Rc ;
      MARK  CIRSHELL  X2  mid max SIZE Delta.R ;

      MARK  CIRSHELL  X3  SIZE Delta.PHI ;

     Mark Forward.Shell X1 Size Delta.z ;
     Mark Trailing.Shell X1 Size Delta.z ;

      AUTOGRID ;

!-------------------------------------------------------------------------
-----------
! Define outlet port plane.

      POINT OUTLET.LO Zforward,0.0,0.0 ;
      POINT OUTLET.HI Zforward,tap_radius,2pi ;
     AREA  OUTLET   CONFORMAL OUTLET.LO OUTLET.HI ;

!-------------------------------------------------------------------------
-----------
! Set simulation duration.

      duration Time_OF_run ;

!-------------------------------------------------------------------------
-----------
! Assign material properties, boundary conditions, and drive applications.

     Conductor Forward.Shell  Material Brass ;
     Conductor Trailing.Shell  Material Brass ;

      CONDUCTOR SHELL MATERIAL COPPER SOLID TRANSPARENCY 50;
      CONDUCTOR SHELL2 MATERIAL COPPER SOLID TRANSPARENCY 50;
      CONDUCTOR SHELL3 MATERIAL COPPER SOLID TRANSPARENCY 50;
     VOID CONSHELL;
     VOID CIRSHELL;
     VOID HELIX;
     VOID TAPER;
     VOID TAPEREND;

! *** Turn this off initially, first verify proper behavior.

     ! *** SURFACE_LOSS 9.65GHz;

! Electromagnetic Wave.

     Parameter Transit_time = 2*(SYS$X1MX)/1.c ;
     Parameter TEND_SIGNAL = TIME_OF_RUN - 10.*TRANSIT_TIME ; ! this is
important
     TPULSE = (NINT(.5*TEND_SIGNAL/SYS$DTIME)+0.5)*SYS$DTIME ; ! avoid zero
over zero form

     FREQLO=6.0GHz;
     FREQHI=10.5GHz;
     ! *** Freqmd = 0.5*(FreqLo+Freqhi).
     Parameter_GHZ  FREQmd=9.65GHz;

     ! *** Set Frequency window of FFT, slightly broader than the lo,hi
range

     Parameter_GHZ      FWlo = FreqLO - 0.5ghz ;
     Parameter_GHZ      FWhi = FreqHI + 0.5ghz ;

     OMEGALO = 2PI*FREQLO;
     OMEGAHI = 2PI*FREQHI;
     OMEGAMD = 2PI*FREQmd;
     Parameter xKT = 1.841/enter;
```

```
      Parameter CutFreq = xKT*1.c/2.PI;

      ! Find range of Phase velocity for frequency range of interest.
      Parameter VphaseLo = 1/sqrt(1-(CutFreq/FREQLo)**2) ;
      Parameter Vphase   = 1/sqrt(1-(CutFreq/FREQmd)**2) ;
      Parameter VphaseHi = 1/sqrt(1-(CutFreq/FREQHi)**2) ;

      FUNCTION TE_Er(Z,R,PHI) = SIN(PHI)/R*BESSELJ1(1.841*R/enter);
      FUNCTION TE_Ep(Z,R,PHI) =
1.841/enter*COS(PHI)*BESSELJP(1,1.841*R/enter);
      FUNCTION f(t)= (sin(OMEGALO*(t-Tpulse))-sin(OMEGAHI*(t-Tpulse)))/(t-
Tpulse)*sqrt(2.PI) ;
      ! FUNCTION f(t)= sin(OMEGAMD*t);

      ! *** Take integral from r=0 to outer radius only.
      ! *** Line NORMALIZATIONLINE Oblique  Zforward,-enter,0.5PI
ZForward,enter,0.5PI ;
      Line NORMALIZATIONLINE   Oblique  Zforward,0,0.5PI
ZForward,enter,0.5PI ;

      Port outlet Positive
           PHASE_VELOCITY Vphase Incoming f
           FUNCTION E2 TE_Er E3 TE_Ep
           Normalization Voltage NORMALIZATIONLINE;

       POINT rec.P0 Ztrailing,0.0,0.0 ;
       POINT rec.P1 Ztrailing,enter,2.PI ;
      AREA  OUTPUT  CONFORMAL rec.P0 rec.P1;
      Port OUTPUT Negative;

      !Vector Field E2 E3 OutLet Tsys$last ;
      !Vector Field E1 E2 osys$midplane3 Tsys$last ;
      !Vector Field B1 B2 osys$midplane3 Tsys$last ;

      !Contour Field E2 Outlet Tsys$last shade;
      !Contour Field E3 Outlet Tsys$last shade;
      !Contour Field |E| Outlet Tsys$last shade ;
      !Contour Field E2 Osys$midplane3 Tsys$last shade ;
      !Contour Field E3 Osys$midplane3 Tsys$last shade;

!-------------------------------------------------------------------------
------------
! Define diagnostics.

      POINT RECEND1  ZTrailing,enter,90deg;
      POINT RECEND2  ZTrailing,0,90deg;
      POINT RECEND3  ZTrailing,enter,180deg;
      POINT RECEND4  ZTrailing,0,180deg;
      POINT START.LO -6.0cm,enter,90deg;
      POINT START.HI -6.0cm,0,90deg;
      LINE parallel oblique RECEND1 RECEND2;
      LINE perpendicular oblique RECEND3 RECEND4;
      LINE START oblique START.LO START.HI;
      OBSERVE FIELD E2 parallel
                       FFT MAGNITUDE DB_SCALE 10
                       ! WINDOW Time 15.0NANOSECONDS Time_OF_run
                       WINDOW FREQUENCY FWLo FwHi DUMP;
      OBSERVE FIELD E2 perpendicular
                       FFT MAGNITUDE DB_SCALE 10
                       ! WINDOW Time 15.0NANOSECONDS Time_OF_run
                       WINDOW FREQUENCY FWLo FwHi DUMP;

      DISPLAY ;
      START ;
      STOP ;
```

```
HEADER  DEVICE  "Single frequency MAGIC" ;

graphics pause ;

!-------------------------------------------------------------------------------
-----------
! Problem definition.
!
! Construct an oversized cylindrical waveguide with a helical corrugation on
the inner surface.
!
! Parameters defining the chamber.

       CYL_RADIUS = 1.7_CM ;        ! Cylinder inner radius.
       m=3;                         ! Azimuthal component
       d=2.89_CM;                   ! Period
       h=2.PI/d;
       a0=1.47_CM;                  ! Mean Radius
       a1=0.14_CM;                  ! Corragation depth
       TAPER_LENGTH = 1*d;
       TAPER_START =  6*d+TAPER_LENGTH;
       CYL_LENGTH = TAPER_LENGTH+TAPER_START;          ! Cylinder length.
       FUNCTION helixpara(Z,R,PHI) =R- a0 - a1*SIN(h*Z-m*PHI); ! Helical
shaped hole
       FUNCTION helixtaper(Z,R,PHI)=R- a0 - a1*Z/TAPER_LENGTH*SIN(h*Z-m*PHI);
! Taper hole
       FUNCTION helixtaper2(Z,R,PHI)=R -a0 + (a1*(Z-CYL_LENGTH)*SIN(h*Z-
m*PHI)/TAPER_LENGTH);
! Mesh resolution parameters.
       DELTA.Z = d/30 ;                                  ! Axial resolution.
       DELTA.R = a1/15;                                   ! Radial resolution.

      Delta.ro = 3*Delta.R ;
      Delta.rc = 5*Delta.R ;

       DELTA.PHI = 2.PI/90 ;                             ! Azimuthal
Resolution

! Parameters defining the electron beam.

      TIME_OF_RUN = 10.00NANOSECONDS ;


! Useful constants.

       CLIGHT=1.c;
       PIRA = 1.pi;
       XMU0 = PIRA*4.E-7 ;
       TWOPI = 2.PI ;
       EPS0 = 8.8544E-12 ;

!  Select the coordinate system and create the OBJECTS

       SYSTEM  CYL ;

! Define the output region.

     Point endcap2.lo  CYL_LENGTH,0.0cm,0.0 ;
     Point endcap2.hi  CYL_LENGTH,cyl_radius,2pi ;
     AREA ENDCAP2 CONFORMAL ENDCAP2.LO ENDCAP2.HI ;

! Define the confining shell.
       POINT SHELL.LO  0.0,0.0,0.0PI ;
       POINT TAPER.HI  TAPER_LENGTH,CYL_RADIUS,2.PI ;
       POINT HSHELL.LO TAPER_LENGTH,0.0,0PI ;
       POINT TAPER2.HI  TAPER_START,CYL_RADIUS,2.PI ;
       POINT TAPER2.LO TAPER_START,0.0,0PI ;
       POINT SHELL.HI  CYL_LENGTH,CYL_RADIUS,2.PI ;
       VOLUME SHELL CONFORMAL SHELL.LO SHELL.HI ;

! Define the helix
     VOLUME taper FUNCTIONAL helixtaper SHELL.LO TAPER.HI;
     VOLUME helix FUNCTIONAL helixpara HSHELL.LO TAPER2.HI;
     VOLUME taperend FUNCTIONAL helixtaper2 TAPER2.LO SHELL.HI;
```

```
!Define the taper

!-------------------------------------------------------------------------------
------------
! MARK the objects for AUTOGRID and create the grid.

       MARK  SHELL  X1  SIZE Delta.Z ;

       MARK  SHELL  X2  Min SIZE Delta.RC ;
       MARK  SHELL  X2  Mid Max SIZE Delta.R ;

       MARK  SHELL  X3  SIZE Delta.PHI ;



       AUTOGRID ;

!-------------------------------------------------------------------------------
------------
! Define outlet port plane.

       POINT OUTLET.LO 0.0,0.0,0.0 ;
       POINT OUTLET.HI 0.0,cyl_radius,2pi ;
      AREA  OUTLET   CONFORMAL OUTLET.LO OUTLET.HI ;



!-------------------------------------------------------------------------------
------------


! Set simulation duration.

       duration Time_OF_run ;

!-------------------------------------------------------------------------------
------------
! Assign material properties, boundary conditions, and drive applications.

       CONDUCTOR SHELL MATERIAL COPPER SOLID TRANSPARENCY 50;
      VOID HELIX;
      VOID TAPER;
      VOID TAPEREND;

! Electromagnetic Wave.
       POINT3 DRIVE.LO -ELL_LNTH, 0.0, 0.PI ;
      POINT3 DRIVE.HI -ELL_LNTH, a0, 2.PI ;
       AREA DRIVE_LOCATION  CONFORMAL DRIVE.LO DRIVE.HI ;
      Area DRIVE_LOCATION1 CONFORMAL DRIVE.LO DRIVE.HI ;

      Parameter DrvFreq = 11.0GHZ ;
      Parameter xKT = 1.841/a0;
      Parameter CutFreq = xKT*CLIGHT/2.PI;
      Parameter Vphase = 1/sqrt(1-(CutFreq/DrvFreq)**2) ;


      ! *** Adjust strength to be largely independant of dz resolution.

      FUNCTION f(t)= SIN(2.PI*t*DrvFreq) ;
      FUNCTION f1(t)= SIN(2.PI*t*DrvFreq+0.5PI) ;

      FUNCTION TE_Er(t,Z,R,PHI) = SIN(PHI)/R*BESSELJ1(1.841*R/a0)*f(t)
                                + SIN(PHI-
0.5PI)/R*BESSELJ1(1.841*R/a0)*f1(t) ;
      FUNCTION TE_Ep(t,Z,R,PHI) =
1.841/a0*COS(PHI)*BESSELJP(1,1.841*R/a0)*f(t)
                                + 1.841/a0*COS(PHI-
0.5PI)*BESSELJP(1,1.841*R/a0)*f1(t);

       Port outlet Positive PHASE_VELOCITY Vphase ;
      Port Endcap2 Negative PHASE_VELOCITY Vphase;
```

```
       DRIVER J2 TE_Er  DRIVE_LOCATION ;
       DRIVER J3 TE_Ep  DRIVE_LOCATION1 ;


!-------------------------------------------------------------------------------
------------
!Output
      AREA  OUTCross11   CONFORMAL TAPER2.LO TAPER2.HI ;
      TIMER showat periodic 100000 150000 1000;
       VECTOR FIELD E2 E3 OUTCross11 showat movie DENSITY 10 10;

DISPLAY;
START ;
STOP ;
```

```
% Fourier optic simulation of pulse compression
clear;
% variables ns GHz cm
pulseduration=67;
%for 10MHz t=60.73 f=9.425 for 20MHz t=67 f=9.345
dt1=.1;
df=.001;
dt=.1;
t1=[-5:dt1:75];
f=[-2:df:2]';
t=[0:dt:120]';   % Maximum time is 500
t0=pulseduration/2;
tau=t0+.3;
z=76*2.89;
%z=0;
c=30;
%variables for helix
period=2.89;
a0=1.47;
a1=.14;
m1=1;
m2=2;
X1=1.841;
X2=3.054;
wc2=3.054*c/a0;
hbar=2*pi/period;
sigSI=5.8E7;
sig=0.3*c*sigSI;
k0=X2/a0;

% Input pulse
f0=9.0;
s6=-3.5311E-11;
s5=5.5222E-9;
s4=-3.0242E-7;
s3=5.2954E-6;
s2=4.663E-5;
s1=-3.8788E-3;
s0=6.3206E-1;
sweep=s6*t1.^6/7 +s5*t1.^5/6 +s4*t1.^4/5 +s3*t1.^3/4 +s2*t1.^2/3 +s1*t1/2 +s0;
phase=sweep*2*pi.*t1;
%input=exp(i*(phase));
input=exp(-((t1-t0).^100/tau^100)).*exp(i*(phase));
TWT=[t1',abs(input)'.^2];
Mixed=[t1',input'];
save inputcop10.txt  TWT -ascii -tabs
save mix.txt Mixed -ascii -tabs
```

```
% Fourier Transform
F=(exp(i*2*pi*f*t1)*input')*dt1;
%four=[f,abs(F)];
%save spectrum.txt  four -ascii -tabs

% Helix Dispersion
fk = 2*pi*(f'+f0)/c;
%Calculate h
hp = [];
for k=fk,
   k1=X1/a0;
   k2=X2/a0;
   hBfB=(k2^2-k1^2+hbar^2)/(2*hbar);
   sigma=0.5*(X1^2*X2^2+2*a0^2*(k1^2+hbar*hBfB))/(sqrt(X1^2-1)*sqrt(X2^2-
4))*(a1/a0^3);
   N1=(m1^2/(X1^2-m1^2)+(X1/(k*a0))^2)*k/a0;
   N2=(m2^2/(X2^2-m2^2)+(X2/(k*a0))^2)*k/a0;
   l1=i*sqrt(k*c/(2*pi*sig))*(1-i)*N1;
   l2=i*sqrt(k*c/(2*pi*sig))*(1-i)*N2;
   c1 = 1;
   c2 = 2*hbar;
   c3 =-2*k^2 +k2^2 +hbar^2   -l1   +k1^2;
   c4 = 2*hbar*(k2^2-k^2-l2);
   c5=k^2*(k^2-hbar^2-k1^2-k2^2+l1+l2)     +k2^2*(hbar^2+k1^2-l1)     +l2*(l1-
k1^2-hbar^2)   -4*sigma^2;
   ch = [c1 c2 c3 c4 c5];
   x = roots(ch);
   hp = [hp x];
end;
h = hp;
% Inverse Fourier transform
O=length(t);
K=h(4,:)';
%plot(h(4,:)',f');
X=abs((exp(i*z*ones(O,1)*K'-i*2*pi*t*f')*F)*df).^2;
kp=max(X);
kp
dB=10*log10(kp);
dB
excel=[t,X];
save modelcop10.txt  excel -ascii -tabs
hold on;
plot(t1',abs(input)'.^2)
plot(t,X,'r')
```

Appendix B- Publications

1. Samsonov, S.V., Phelps, A.D.R., Bratman, V.L., Burt, G., Denisov, G.G. et al., Compression of frequency modulated pulses using helically corrugated waveguides and its potential for generating multi-gigawatt RF radiation, *Phys. Rev. Letters* **92**, 118301 (2004).

2. G. Burt, S.V. Samsonov, K. Ronald, G.G. Denisov, A.R. Young, V.L. Bratman, A.D.R. Phelps, A.W. Cross, I.V. Konoplev, W. He, J. Thomson and C.G. Whyte' Dispersion of helically corrugated waveguides: analytical, numerical and experimental study, Phys. Rev. E

APPENDIX B
NOT DIGITISED AT THE REQUEST OF THE UNIVERSITY.